Experimental Investigation of a Low-NO_x Swirl-Assisted and Jet-Stabilized Gas Turbine Combustor Concept

A thesis accepted by the Faculty of Aerospace Engineering
and Geodesy of the University of Stuttgart
in partial fulfillment of the requirements for the degree of
Doctor of Engineering Sciences (Dr.-Ing.)

By

MSc Saeed Izadi

born in Larestan, Iran

Main referee:	Prof. Dr.-Ing. Manfred Aigner
Co-referee:	Prof. Dr.-Ing. Hans-Jörg Bauer

Date of defense: 30.01.2025

Institute of Combustion Technology for Aerospace Engineering
University of Stuttgart

2025

Danksagung

Die vorliegende Arbeit ist während meiner Tätigkeit als wissenschaftlicher Mitarbeiter am Institut für Verbrennungstechnik des Deutschen Zentrums für Luft- und Raumfahrt (DLR) in Stuttgart entstanden. Es war eine unglaubliche Reise, und ich bin den vielen Menschen, die mich unterstützt haben, zutiefst dankbar.

Zuallererst möchte ich Prof. Dr.-Ing. Manfred Aigner, meinem Doktorvater und Hauptbetreuer, meinen tief empfundenen Dank aussprechen. Ohne seine Ermutigung, Unterstützung, Geduld, seinen unschätzbaren Rat und sein unvergleichliches Wissen wäre diese Dissertation nicht möglich gewesen. Herrn Prof. Dr.-Ing. Hans-Jörg Bauer danke ich für die Übernahme des Mitberichts und das große Interesse an meiner Arbeit.

Meinem Abteilungsleiter, Dr. Peter Kutne, danke ich sehr für sein Vertrauen, seine hervorragende Unterstützung und Anleitung bei der Überwindung schwieriger Hindernisse während meiner Forschung. Dr. Jan Zanger, meinem fachlichen Betreuer, bin ich äußerst dankbar für seine wertvolle Beratung und Freundschaft, sowohl auf akademischer als auch auf persönlicher Ebene. Die unzähligen Stunden, die er in Diskussionen und Korrekturen investierte, sowie seine konstruktiven und zügigen Rückmeldungen waren für meine Doktorarbeit unerlässlich.

Für die technische und wissenschaftliche Unterstützung sowie ihre ständige Ermutigung und wertvolle Beratung danke ich Hannah Seliger-Ost, Nina Gaiser, Tobias Grein, Zhiyao Yin, Stefanie Werner, Trupti Kathrotia, Patrick Oßwald, Torsten Methling und Oliver Kislat. Besonders dankbar bin ich Jürgen Roth, Timo Wagner und Stefan Fiedler für ihre unschätzbare Unterstützung, die meine Forschung am Laufen hielt. Ein besonderer Dank gilt der VT-DLR Werkstatt, Jens Kreeb, Ralph Bruhn, Sven Schober und Michael Gröninger für die schnelle Konstruktion und Anfertigung der Brenner- und Prüfstandteile.

Meinen früheren Studenten und Praktikanten, Cedric Kraus, Simon Müller, Tim Rörig, Jean-Jacques Fischer und Aditya Kurup, danke ich für ihre Hilfsbereitschaft und Unterstützung.

Schließlich bin ich meiner geliebten Frau Anna zu großem Dank verpflichtet. Ihre unerschütterliche Unterstützung, unglaubliche Geduld und Fürsorge während dieser Jahre haben diese Reise viel einfacher gemacht. Dafür kann ich ihr nicht genug danken.

Saeed Izadi

Februar 2025

Contents

List of Figures

List of Tables

List of Acronyms and Symbols

Acronyms

ATM	Air Traffic Management
CAEP	Committee on Aviation Environmental Protection
CFD	Computational Fluid Dynamics
DAC	Direct Air Capture
DAC	Double Annular Combustor
DLE	Dry Low Emissions
DLR	German Aerospace Center
DOE	Design of Experiments
DPSS	Diode-Pumped Solid-State
EI	Emissions Index
ETC	Easy-to-Change Factor
FF	Future Fuel
FL	Flame Length
FLOX	Flameless Oxidation
FN	Flow Number
GE	General Electric
GT	Gas Turbine
HAB	Height Above Burner
HEFA	Hydroprocessed Esters and Fatty Acids
HEL	Heating Oil Extra Light
HHV	Higher Heating Value
HTC	Hard-to-Change Factor
ICAO	International Civil Aviation Organization
IDT	Ignition Delay Time
LBO	Lean Blowout
LDI	Lean Direct Injection
LES	Large Eddy Simulation
LHV	Lower Heating Value
LIF	Laser-Induced Fluorescence
LPP	Lean Premixed Prevaporized
LTO	Landing and take-off
MCPC	Mixing Condensed Particle Counter
MW	Molecular Weight
NG	Natural Gas
OH*	Hydroxyl Radical
PM	Particulate Matter
ppmvd	Parts Per Million by Volume, Dry
PtL	Power-to-Liquid
PVC	Precessing Vortex Cores

RGB	Red Green and Blue
RQL	Rich-Burn Quick-Quench Lean-Burn
SAF	Sustainable Aviation Fuel
SCA	Spray Cone Angle
SMD	Sauter Mean Diameter
SP	Subplot
Std Dev	Standard Deviation
TALON	Technology for Affordable Low NO_x
TAPS	Twin Annular Premixing Swirler
TRL	Technology Readiness Level
VABP	Volume Average Boiling Point
WET	Water-Enhanced Turbofan
WGR	Water-to-Gas Ratio
WP	Whole Plot

Symbols

A/F	Air Fuel Ratio [-]
c	Vane Length [m]
D	Diameter [m]
Dp	Mass of any gaseous pollutant emitted during the reference emissions LTO cycle [g]
Foo	Maximum power/ thrust under normal operating conditions [kN]
p	Pressure [bar]
PM2.5	Particulate Matter Equal to or Smaller Than 2.5 microns [$\mu m/m^3$]
p_{sat}	Saturated Pressure [bar]
P_{th}	Thermal Power [kW]
r	Correlation Coefficient [-]
R^2	Proportion of Variation Explained by a Model [-]
Re	Reynolds Number [-]
s	Vane Thickness [m]
S_L	Laminar Flame Speed [m/s]
S_N	Swirl Number [-]
T	Temperature [K]
T_{ad}	Adiabatic Flame Temperature [K]
T_{air}	Preheated Air Temperature [°C]
T_{fuel}	Preheated Fuel Temperature [°C]
T_{sat}	Saturated Temperature [K]
ΔT	Preheat Level of Fuel [K]
v_{bulk}	Bulk Velocity [m/s]
x	Radial Direction
y	Axial Direction
z	Vane Height [m]

Subscript

ad	Adiabatic
AN	Air Nozzle
FT	Flame Tube
L	Laminar
Sat	Saturation
Stoic	Stoichiometric
SW	Swirler

Chemical Species

CO	Carbon Monoxide
CO_2	Carbon Dioxide
H_2O	Water (Vapor)
N_2	Nitrogen
N_2O	Nitrous Oxide
NO	Nitric Oxide
NO_2	Nitrogen Dioxide
NO_x	Nitric Oxides (NO + NO_2)
OH*-CL	OH*-Chemiluminescence

Greek Symbols

α	Significance Level
λ	Air Equivalence Ratio / Wavelength
ν_i'	Stoichiometric Coefficient of a Reactant
ν_i''	Stoichiometric Coefficient of a Product
σ	Standard Deviation
ϑ	Temperature

Kurzfassung

Die heutigen Abgasnormen für Flugzeugtriebwerke legen unter anderem fest, wie viel Stickoxide (NO_x), Kohlenmonoxid (CO) und unverbrannte Kohlenwasserstoffe (UHC) in niedrigen Höhen – also während des Starts und der Landung – ausgestoßen werden dürfen. Es wird erwartet, dass internationale Luftfahrtbehörden diese Regeln in Zukunft auch auf Emissionen in großen Höhen ausweiten werden. Das Ziel ist es, die globalen Auswirkungen dieser Schadstoffe zu verringern. Besonders die NO_x-Emissionen sollen reduziert werden, da sie in großer Höhe eine wichtige Rolle im Treibhauseffekt spielen und neben Kohlendioxid (CO_2) zu den größten Klimatreibern gehören. Um diese strengeren Anforderungen zu erfüllen, ohne die Zuverlässigkeit, Wirtschaftlichkeit und Effizienz der Brennersysteme zu beeinträchtigen, sind innovative Konzepte gefragt.

Als vielversprechende Low-NO_x-Verbrennungstechnologie für zukünftige Gasturbinentriebwerke stellt ein Low-Swirl-, Lean-Premixed-Prevaporized-Konzept eine attraktive Alternative zu herkömmlichen Brennersystemen dar. Dieser Ansatz zeichnet sich durch ein mageres Brennstoff-Luft-Gemisch und einen hohen Durchmischungsgrad von Brennstoff und Luft vor der Reaktionszone aus. Dadurch werden lokale Hotspots minimiert und die Bildung von thermischem NO_x signifikant reduziert.

In dieser Arbeit wird ein neuartiges Konzept untersucht, das auf einer jet-stabilisierten Verbrennung basiert. Zunächst wurde ein jet-stabilisierter Einzeldüsenbrenner als Referenzbrenner getestet, wobei sowohl Drall-Druck-Zerstäubung als auch die thermische Zerstäubung von überhitztem Jet A-1 (Flash-Atomization) bei Atmosphärendruck untersucht wurden. Mithilfe von Mie-Streuung konnte in nicht-reaktiven Tests gezeigt werden, dass bei steigender Brennstofftemperatur das Spray sich allmählich auflöste und durch eine schnell verdampfende Brennstoffwolke ersetzt wurde. Die Brennstofftropfen wurden kleiner, und der Brennstoffdampf beschleunigte in axialer Richtung. Durch die überhitzte Einspritzung drang jedoch weniger Brennstoff in radialer Richtung ein. Dies führte zu einer unzureichenden Vermischung von Brennstoff und Luft, was eine Verschiebung der Flamme stromabwärts zur Folge hatte. Zusätzlich bildeten sich bei den hohen Temperaturen Ablagerungen in den Brennstoffleitungen und dem Injektor, was den Betrieb des Brenners einschränkte. Diese ersten Tests machten deutlich, dass die Auslegung des Brenners grundlegend überarbeitet werden musste, um eine überhitzte Brennstoffeinspritzung mit niedrigen Emissionen und einem breiten Betriebsbereich zu ermöglichen.

Da der Einzeldüsenbrenner unter Spraybedingungen lediglich einen begrenzten Betriebsbereich aufwies und die Flamme bei überhitzter Einspritzung äußerst instabil wurde, erfolgte eine schrittweise Weiterentwicklung des Designs. Zur Optimierung des Brennersystems wurden zusätzliche

Komponenten integriert, deren Einfluss auf die Brennstoffverdampfung und die Emissionsbildung detailliert analysiert wurde. Die Untersuchungen ergaben, dass diese Komponenten die Durchmischung von Brennstoff und Luft sowie die Zerstäubung und Verdampfung des Brennstoffs vor der Verbrennung signifikant verbesserten. Ein axialer Drallgeber wurde implementiert, um die schnelle Expansion des überhitzten Brennstoffs durch die Erzeugung einer leichten Drehbewegung zu kontrollieren. Der Drallgeber fungierte dabei als Umlenkplatte, welche die Vermischungseffizienz von Brennstoff und Luft steigerte. Zusätzlich wurde um den Drallgeber ein Prefilmer installiert, um die Strömungsgeschwindigkeit durch die Drallgeberschaufeln zu erhöhen. Dies ermöglichte eine verbesserte Zerstäubung des Brennstoffs durch einen Luftstrahl-Effekt.

In der folgenden Phase wurden systematisch verschiedene Betriebs- und Designparameter variiert, um deren Einfluss auf den neu entwickelten, drallunterstützten und jet-stabilisierten Brenner zu evaluieren. Zu den Betriebsparametern zählten die adiabatische Flammentemperatur, die thermische Leistung sowie die Temperaturen von Luft und Brennstoff. Bei den Designparametern wurden der Brennstoffinjektor, der Durchmesser des Flammrohrs (D_{FT}) und der Luftdüse (D_{AN}) angepasst. Darüber hinaus wurden vier verschiedene Flüssigbrennstoffe mit unterschiedlichen Eigenschaften getestet, um deren Verhalten unter Spray- und überhitzten Einspritzungsbedingungen zu vergleichen. Abschließend wurde Wasserdampf in das Brennstoff-Luft-Gemisch eingeleitet, um die Flammenstabilität bei Störungen wie Verdünnung zu untersuchen.

Zur Analyse der physikalischen Prozesse kamen etablierte Methoden der Verbrennungsdiagnostik zum Einsatz. Mittels Mie-Streuung wurde der Brennstoffspray in nicht-reaktiven und reaktiven Tests untersucht, um qualitativ die Eindringtiefe und den Verdampfungsgrad im Flammrohr zu bestimmen. Die Flammenlänge (FL) und die Position der Wärmefreisetzungszone wurden durch OH*-Chemilumineszenz ermittelt. Ein Emissionsanalysator diente zur Erfassung der Schadstoffemissionen, einschließlich NO_x, CO, UHC und Feinpartikel (PM).

Die Variation des Flammrohrdurchmessers beeinflusste die Verweilzeit, die Strömungsgeschwindigkeit und die Rezirkulation im Flammrohr, was sich wiederum auf die Abhebehöhe (HAB) und Länge der Flamme auswirkte. Die niedrigsten NO_x- und CO-Emissionen wurden bei dem kleinsten Luftdüsendurchmesser gemessen, was auf eine verbesserte Durchmischung von Brennstoff und Luft zurückzuführen war. Die Zugabe von Dampf reduzierte die NO_x-Emissionen bei der Verbrennung von Jet A-1 und Erdgas, da die adiabatische Flammentemperatur gesenkt wurde.

Das entwickelte Brennerkonzept ermöglicht eine emissionsarme Verbrennung verschiedener Flüssigbrennstoffe über einen breiten Betriebsbereich. Es zeigt eine hohe Robustheit gegenüber der Qualität des Brennstoffsprays, sodass auch einfachere Injektoren verwendet werden können. Die Tests ergaben jedoch, dass die überhitzte Brennstoffeinspritzung aufgrund der effizienten Brennstoffaufbereitung in diesem Brenner keine signifikanten Vorteile bietet.

Abstract

Today's aircraft engine emission standards regulate, among other aspects, the emissions of nitrogen oxides (NO_x), carbon monoxide (CO) and unburned hydrocarbons (UHC) at low altitudes, i.e. during the take-off and landing cycle. It is expected that international aviation regulatory bodies will extend the standards to include high-altitude emissions. This will reduce the global impact of these pollutants. In particular, NO_x emissions will need to be reduced due to their role in the greenhouse effect as one of the major non-CO_2 factors at higher altitudes. Therefore, in order to meet the upcoming stricter emission standards while maintaining optimal combustor reliability, affordability and efficiency, innovative combustor concepts are required.

As a low-NO_x combustion technology for future gas turbine engines, a low-swirl, lean premixed prevaporized concept can be an alternative to current conventional combustor systems. The concept is characterized by a lean-fuel and a high degree of mixing of the fuel with air prior to the reaction zone. This results in minimized hot spots and a significant reduction in thermal NO_x levels.

This work aims to investigate an innovative jet-stabilized concept. Initially, a single-nozzle jet-stabilized gas turbine combustor as a reference combustor was tested using both spray and superheated injection (flash atomization) of Jet A-1 at atmospheric pressure. Non-reactive tests using Mie scattering showed that as the fuel temperature increased, the fuel spray gradually vanished and was replaced by a rapidly evaporating fuel plume. The primary effect was a reduction in the size of the fuel droplets, but also a rapid axial acceleration of the fuel vapor. As a result of the superheated injection, the Jet A-1's radial penetration was significantly reduced. This resulted in poorer mixing of the fuel with the air and led to shifting flame downstream of the flow. Additionally, the high temperatures caused carbon deposits to form within the fuel lines and the injector, which limited the operation of the combustor. These initial tests showed that fundamental changes to the combustor design are required to utilize superheated fuel injection with low emissions and a wide operating range in the jet-stabilized single-nozzle combustor.

Due to the narrow operating range of the single-nozzle jet-stabilized combustor under spray conditions and the extremely unstable flame under superheated conditions, the combustor was iteratively developed to incorporate additional components. This was followed by a thorough study of how each component affected fuel vaporization and emissions. The results showed that, the additional components allowed for improved fuel-air mixing, fuel atomization, and evaporation prior to the reaction zone. The axial swirler slowed the rapidly expanding, high-velocity, superheated fuel by providing moderate swirling motion. The swirler hub proved to be an effective baffle, allowing the expanding and superheated fuel to mix better with the air. In addition, a prefilmer channel was installed around the axial swirler to increase the velocity through the swirler vanes, which allowed for improved secondary atomization of the fuel by means of an air-blast effect.

As a result, a systematic variation of combustor operational and geometric design parameters was experimentally performed to study their effects on a newly developed swirl-assisted jet-stabilized combustor. The operational parameters included the adiabatic flame temperature, the thermal power, and the air and fuel temperatures, while the geometric parameters were the type of fuel injector, swirl number, the flame tube and the air nozzle diameters. In addition, to evaluate their behavior under sprayed and superheated injection regimes, four different liquid fuels with different thermochemical properties were tested. Finally, water vapor was added to the fuel-air mixture for evaluation of flame resistance to perturbations such as dilution and combustion inhibitors.

For the characterization of the physical phenomena, established methods of combustion diagnostics have been applied. Mie scattering was used in non-reactive and reactive tests for qualitative analysis of fuel spray angle, penetration depth and degree of evaporation in the flame tube. Flame length (FL) and height above burner (HAB) of the heat release zone were determined using OH* chemiluminescence. Furthermore, an emission analyzer was used to evaluate the pollutants emitted from the flames. These pollutants include NO_x, CO, UHC and particulate matter (PM).

The mean residence time, bulk velocity, and recirculation rate and shape in the flame tube were primarily affected by variation of the flame tube diameter (D_{FT}). This led to a change in reaction zone's HAB and FL. The lowest NO_x and CO levels were consistently observed with the smallest air nozzle diameter (D_{AN}). This could be attributed to improved fuel-air mixing resulting from increased air dispersion at the nozzle exit, which led to increased turbulence at higher jet velocities. For both Jet A-1 and natural gas combustion, the injection of steam reduced NO_x emissions by lowering the adiabatic flame temperature.

The characterized combustor concept features very low-emission combustion of a variety of liquid fuels over a wide operating range. The combustor concept is insensitive to spray quality so that injectors with poorer spray characteristics can be used. For the presented concept it was also shown that the injection of superheated fuel does not offer significant advantages due to the fuel preparation in the combustor.

1 Introduction

1.1 Motivation

For developers of aviation gas turbine (GT) combustion systems, reducing the environmental impact of aviation remains a key objective. The need for cleaner and more sustainable GT combustion systems is growing as more stringent emissions standards are implemented worldwide.

Today's combustion engineers are faced with conflicting goals that make the development of GT combustion systems extremely challenging. On the one hand, there is a need to reduce pollutant emissions; on the other hand, there is a need to increase engine performance and efficiency, i.e., lower combustor pressure loss with better fuel-air mixing. Higher engine efficiency is achieved by increasing the pressure ratio and the turbine inlet temperature, which in turn leads to the formation of nitrogen oxide (NO) and nitrogen dioxide (NO_2) (collectively referred to as NO_x). Any combustion that uses air as an oxidizer will produce some amount of NO_x at higher temperatures, regardless of the fuel used [1].

Nevertheless, gas turbine combustor designers continue their efforts to develop low emission combustion systems to reduce environmental impact. A key emission performance of an engine is NO_x. Three possible trends of NO_x emitted from a full flight (in Mt) are modeled for 2010 to 2050 and shown in Figure 1.1 (ICAO [2]). These trends are calculated according to a technology freeze of the CAEP/12 standards (dark blue line), a range of NO_x reductions due to additional technology improvements (light blue area), and additional air traffic control (ATM) and infrastructure improvements (orange area). It is evident that by 2050, the estimated 9.06 Mt NO_x can be reduced to 6.50 Mt if future engine combustors and infrastructure use are improved.

In addition to other human health risks, such as respiratory diseases and allergies [3], NO_x emissions, as a non-CO_2 emission, from an aircraft can contribute to the global greenhouse effect by photochemical changes that increase global ozone formation [4]. In terms of human health risks associated with GT emissions at ground level during taxiing and takeoff, ozone (O_3) and particulate matter (PM) can also be hazardous, while in cruise these emissions are rather harmful to the climate. At the local scale, the health effects of NO_2 have been shown to outweigh the health effects of $PM_{2.5}$ (particulate matter equal to or smaller than 2.5 microns). [2]

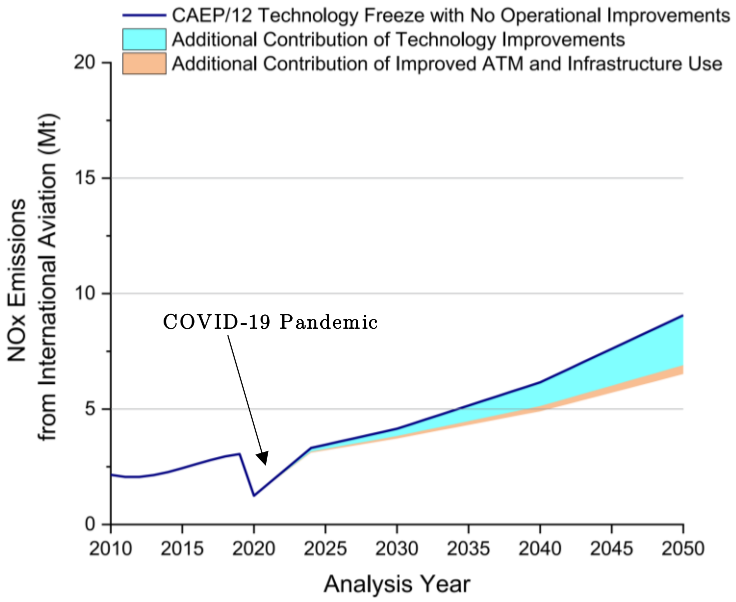

Figure 1.1: Full-Flight NO_x Emissions from International Aviation, 2010 to 2050 [2]

The design and development of a gas turbine combustion system is a multidisciplinary endeavor that seeks to achieve the optimum balance between efficiency, emissions, reliability and safety to meet the demands of modern aviation and environmental impact. The main requirements for an aero gas turbine, and to a large extent for an industrial gas turbine, can be summarized as follows [1] (see Figure 1.2):

- **Reduced Emissions:** The environmental impact of GT is currently a major driver for the development of alternative combustion concepts. Due in part to concerns about human health risks, a well-designed combustor tends to minimize the production of pollutant emissions.
- **Reliability and Durability:** Among long operational life, reduced maintenance requirements and their related costs, combustors need to operate reliably at various dynamic loads, high pressure and temperatures. Reliability and safety are paramount in aviation.
- **Stable Combustion:** A GT combustor must withstand a wide range of operating conditions due to rapid load changes. Any instability in the combustion chamber, e.g. due to thermoacoustic, can result in damage to the engine, failed high-altitude relight, flameout, reduced service life and performance.
- **Efficiency:** Combustor types can have a significant impact on the overall efficiency of a gas turbine. Efficient combustion of fuel is critical to maximizing power output for a given amount of fuel. Higher efficiency is directly correlated with lower fuel consumption and increased range, which is critical for commercial aircraft.

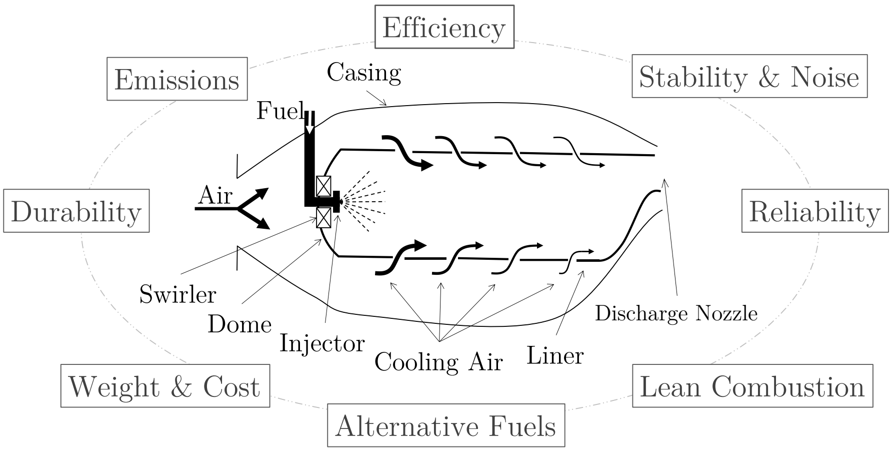

Figure 1.2: Schematic Drawing of a Common Gas Turbine Combustor with its Major Design Challenges. Adapted from [1]

- **Reduced Noise:** One of the main sources of loud noise from a gas turbine engine can come from its combustion chamber [5]. Quieter combustors can be a significant contributor to noise pollution reduction, especially in the vicinity of airports and for aircraft passengers.
- **Alternative Fuels Capability:** Due to the recent increased interest in sustainable aviation fuels (SAFs) for commercial aircraft, a combustor should be able to operate with the widest possible range of drop-in SAF's and potentially non-drop-in SAF's. It is important that the combustors achieve comparable or even better performance, efficiency and emissions when running with SAF.
- **Weight and Cost Reduction:** Reducing combustor material temperatures enables the use of less costly materials, such as lower-grade alloys, instead of high-temperature-resistant superalloys. Lower temperatures also extend service life by minimizing thermal degradation processes like oxidation, creep, and fatigue, thereby reducing maintenance and replacement needs.

1.2 Research Goals

The goal of the present work is to experimentally investigate a novel low-emission, swirl-assisted and jet-stabilized combustor. The experiments should be a general concept study for characterization of the most influential combustor design parameters. As a reference case, a previously characterized single-nozzle jet-stabilized combustor [6,7] was taken into consideration (see Section 6.1). The potential applications of the combustor are in aero and stationary gas turbine engines, that require the following boundary conditions:

- Low pollutant emissions: The combustor must emit low NO_x, PM, CO and UHC for a wide range of operation.

- Combustion stability: Under various operating conditions, the flame should provide a stable combustion without thermoacoustic instabilities, flashback and flameout.
- Compact reaction zone: The combustor system should produce an optimized mixture of fuel and air in order to obtain a rapid combustion and thus a compact flame. The combustor should be able to easily integrate into a desired GT combustor system.
- Fuel flexibility: The combustor should be able to operate with different liquid fuels of varying compositions and thermochemical properties without significant modification, while also maintaining high performance with gaseous fuels.

In addition, the objective is to gain insight into the underlying important mechanisms, i.e. fuel vaporization of the liquid fuel and important combustor design factors on NO_x formation in the combustor, by studying the flames under different combustor geometries, fuel properties, mixing techniques and other combustor operating conditions. Since the conventional jet-stabilized combustors for liquid fuels tend to produce a rather long flame, a major objective of the current work is to look for methods that can shorten the overall length of the flame in both the liquid spray and the superheated conditions. Finally, the results obtained through the modifications of the combustor are compared to the single-nozzle jet-stabilized reference combustor to evaluate the improvements.

1.3 Approach of Research

As a result of previous research demonstrating the potential of superheated injection for liquid fuel vaporization, many of the current design parameter variations include superheated injection to gain further insight into how this affects combustion performance, i.e., increasing flame operating range, reducing flame length and minimizing NO_x and CO emissions. Superheated injection is a process where a liquid fuel is heated above its boiling point before being injected, resulting in its conversion to a fine atomization or gaseous state. Atmospheric combustion tests are conducted at the DLR Institute of Combustion Technology to characterize the design parameters.

The novel swirl-assisted and jet-stabilized combustor's flame characterization is undertaken using gaseous emissions and particulate matter analysis, optical and laser diagnostic methods. The knowledge gained can be used to further optimize the liquid fuel combustor concept and to design a combustor for GT or other specific applications.

Two major series of tests (a preliminary and a deep-dive) were performed to comprehensively characterize the novel combustion concept. The results of the preliminary study to characterize six geometric and operational parameters of the combustor are given in sections 6.4 to 6.8. Subsequently, five follow-up (deep-dive) test series were conducted to gain a deeper insight into the combustion and physical phenomena occurring during the preliminary test campaign (see sections 6.4.1 to 6.4.5 for the results discussions). In the following, a brief description of the experimental tests (preliminary tests 1–5 and follow-up tests i–v) is given and how they have contributed to the previously mentioned research objectives.

1. The effect of superheated atomization of the liquid fuel on the combustion characteristics.
    - As shown in Section 6.4, by injecting the liquid fuel in both spray as well as superheated regimes, the effect of the fuel evaporation and atomization quality on lowering exhaust gas emissions and the heat release zone of the combustor was analyzed.
    - This test was necessary to detect any effects of the superheated atomization/evaporation of the fuel on the combustion performance of the novel combustor.
    - The results showed that the NO_x values increased with increasing preheat level of the fuel, which was contrary to the author's expectation. Therefore, a thorough experimental investigation was conducted as follow-up experiments (see sections 6.4.1 to 6.4.5) to understand the underlying combustion and physical phenomena of the developed combustor concept.
        1. The effect of jet velocity increase on the combustor performance indicators.
            - An insight into the interaction between the combustor jet velocity and level of superheat, emissions, operating range and flame shape, is provided by the results shown in Section 6.4.1.
            - The resulted two flame modes described in Section 6.2, which caused large changes in emissions and flame shape, could be eliminated by increasing the jet velocity. Furthermore, variation in the preheat level of the liquid fuel (ΔT) seemed to play a minor role in the emission values at higher jet velocities.
        2. The effect of fuel injector type: pressure-swirl and plain-orifice.
            - As shown in Section 6.4.2, experiments were conducted to analyze the effect of the primary fuel atomization quality on the combustor's performance.
            - The previous results in Section 6.4.1 had shown that by improving the quality of the fuel atomization by increasing the fuel preheating temperature, there was a small effect on the NO_x values.

        - These tests were necessary to detect the influence of the primary atomization quality on the combustor emissions and operating range.
    iii. The effect of fuel and air temperature on the evaporation of the liquid fuel.
        - The conducted tests shown in Section 6.4.3 allow for the evaluation of the difference in fuel evaporation through increasing the fuel and air temperatures.
        - These experiments showed, which of the fuel and air temperatures had a more dominant effect on fuel evaporation. Exhaust gas emission levels and compactness of the heat release zone position could be directly affected by the state in which the fuel was injected.
    iv. The effect of combustor core components.
        - As shown in Section 6.4.4, the effect of each combustor core component was analyzed in regard to their influence in fuel evaporation, heat release zone shape and location, exhaust gas emission and combustor operating range.
        - These tests allowed for a deeper understanding of the occurring physical phenomena in presence and absence of a specific combustor component. The NO_x and CO levels, heat release zone and combustor operating range were significantly affected by the combustor configuration variation.
    v. The effect of various liquid fuels with different saturation temperatures and thermochemical properties on the superheated atomization.
        - As shown in Section 6.4.5, the effect of varying the fuel saturation temperature on fuel vaporization, exhaust emissions, and flame shape was analyzed.
        - Furthermore, the fuel flexibility of the developed combustor concept with different fuels was analyzed at spray and superheated atomization conditions.
        - The saturation temperature of the fuel directly correlated with the evaporation time of a fuel droplet.
2. The effect of the combustor thermal power.
    - The results shown in Section 6.5 allow for characterizing the combustor at different power loads and the affiliated changes in combustor operation and performance.

  - Increasing the thermal power of a combustor leads to a higher fuel mass flow rate. To keep the adiabatic flame temperature constant, the air mass flow rate must also increase to maintain the proper air-to-fuel ratio. This results in greater momentum of the air-fuel mixture, increasing the jet velocity. Additionally, the increased fuel mass flow rate raises the backpressure in pressure swirl atomizers, which improves atomization quality by producing finer and more uniform fuel droplets.

3. The effect of the swirl number.
   - The results shown in Section 6.6 provide insight into the effect of the vane angle of the axial swirler on the fuel-air mixing quality and the recirculation zone.
   - Their effects on the exhaust gas emissions, heat release zone position and combustor operating range could be thus assessed.
4. The effect of the flame tube diameter.
   - The variation of the flame tube diameter shown in Section 6.7 allowed for the analysis of the effect of bulk velocity variation within the flame tube and the consequent residence time change on the heat release zone position and exhaust gas emissions of the combustor.
5. Test the resistance of the combustor to external perturbations, such as the dilution effect of combustion air enriched with steam.
   - The results shown in Section 6.8 allow the evaluation of the thermal effects on NO_x and CO emissions due to the presence of steam in the reaction zone.
   - The results showed that a large part of the reduction in NOx levels can be attributed to a reduction in flame temperature due to steam injection as a combustion inhibitor.

All of the above steps lead to the development of a deeper understanding of the combustor design parameters and their effects on the goals set within this research.

2 Low-NO_x Combustion Technologies

In this chapter, a survey of the dominating combustor types for low NO_x emission is presented.

Over the past 40 years, considerable work has been done to improve the performance and emissions of the aero GT, reducing its fuel consumption by 70%, noise by 50%, and UHC and CO emissions by 90%. This improvement comes at the cost of an increase in turbine inlet temperature, which has a tendency to increase NO_x. [8]

When liquid droplets enter the reaction zone, the vapor produced by these droplets can burn at near stoichiometric conditions, provided local conditions are met [9]. Combustion of liquid fuels is inherently more complicated than gaseous fuels [10] as a few additional challenges are associated to their combustion [11]:

- Atomization and vaporization of the liquid fuel
- Distribution of the fuel
- Spray/mixing channel wall interaction
- Delayed ignition
- Coking and nozzle blockage

2.1 Rich-Burn Quick-Quench Lean-Burn Combustors (RQL)

The RQL concept is considered an important strategy for reducing NO_x emissions in GT engines. This strategy was developed and demonstrated in the late 1970s [12,13]. It provides increased combustor stability while maintaining relatively low NO_x levels. The stages, in which the combustor operates are briefly presented below: [14]

Rich Burn Zone: The RQL concept is commonly used in GT engines to primarily control the production of NO_x emissions. Typically, the air equivalence ratio (the ratio of the actual air-fuel ratio to the stoichiometric air-fuel ratio) ranges from 0.63 – 0.83 in the primary zone [1]. Rich flames tend to be more stable due to the presence of hydrocarbon radical species. In addition, NO_x emissions are minimized due to lower flame temperatures and lower oxygen-containing intermediate species. The primary source of NO_x formation is where the hot, reactive mixture comes into contact with the fresh air in the quench zone. If the mixture is not adequate, there are areas that are close to the stoichiometry that will increase the NO_x levels, as demonstrated in a study by Hatch et al. [12].

Quench Zone: Downstream of the primary zone, a quench section is used to oxidize the high concentrations of CO, UHC and soot in the exhaust gases by introducing a considerable amount of air into the combustion section (see Figure 2.1). In addition, this zone represents a critical stage for the formation of NO_x in the event of an insufficient mixing of the fuel-air mixture.

Lean Burn Zone: The transition from a rich burn to a lean burn is necessary to avoid high levels of thermal NO_x formation (see Section 3.2.1). While increasing the air equivalence ratio, this stage continues to consume CO and UHC gases. The typical air equivalence ratio in this section ranges from 1.4 – 2.0 at 100% load.

Control of Temperature Distribution: The lean section of the burner acts as a controlling factor in the distribution of the temperature within the combustion chamber by rapidly mixing air and exhaust gases [1].

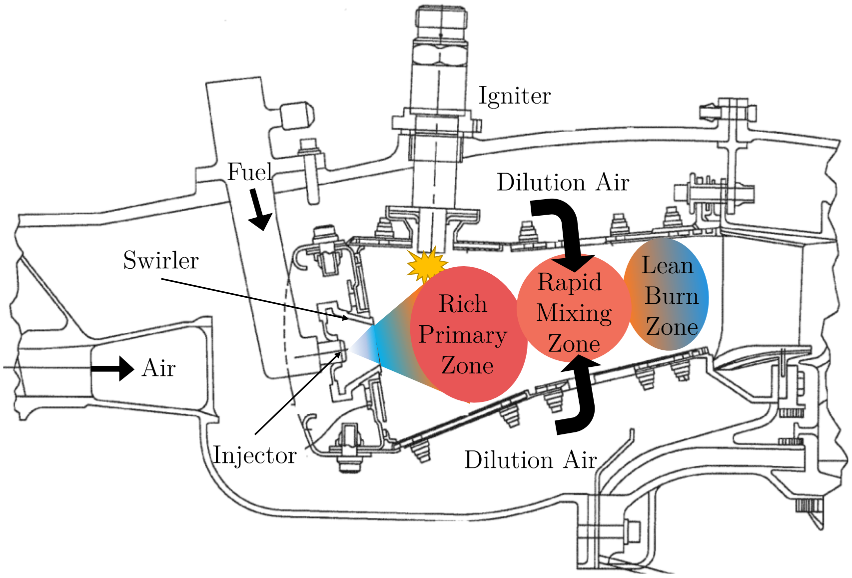

Figure 2.1: Cross-Sectional View of the RQL Combustor. Adapted from [15]

Among other applications, the RQL concept has been used in the TALON (Technology for Affordable Low NO_x) family of combustors on Pratt & Whitney's GT aircraft engines. The latest TALON X is used in PW1500, PW1130G, etc. It has demonstrated a 25% NO_x reduction over TALON II [3]. Extensive research has been conducted by Rosfjord et al. [16] on the emission control potential of the RQL combustor for high speed civil transport aircraft engines. Based on their findings, it was concluded that the RQL combustor can achieve a nitrogen oxide emission level of 121 ppm ($EI_{NOx} = 5$ at a combustor overall fuel-air ratio of 0.04) at supersonic cruise operating conditions while maintaining high combustion efficiency.

2.2 Double Annular Combustors (DAC)

The Double Annular Combustor (DAC) is another combustion control method developed by CFM in the early 1990s [17] and used in commercial engines such as the CFM56 and GE90-94B used in B777-200ER and 777F aircraft, respectively [18]. This concept uses a radial or axial staging strategy to control combustion stability and emission performance. Fuel is injected into the combustor at different locations to adjust temperature and combustion stoichiometry. Baklanov [19] studied fuel distribution between main/pilot stages and how it affects pollutant emissions. He found that combustion efficiency and emissions could be significantly affected by controlling fuel distribution.

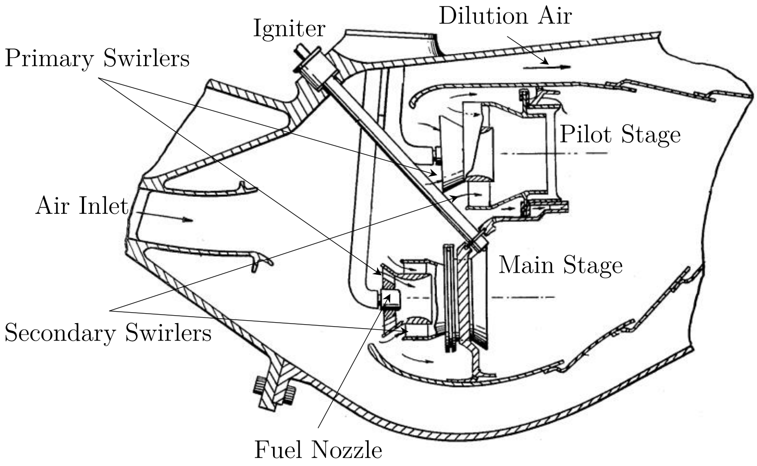

Figure 2.2: Schematic Illustration of a Radial Double Annular Combustor Configuration. Adapted from [20]

The outer stage, called the pilot stage, is primarily active at lower power loads (see Figure 2.2). This stage reduces CO and UHC and improves combustion efficiency by operating at an air equivalence ratio of approximately 1.25. The pilot stage operates at fuel-richer conditions than the main stage, which is activated at higher power loads, reducing the risk of lean-burn instability. The air equivalence ratio of the main stage is around 1.7. This allows lean-burn combustion for NO_x and soot reduction. In the mid-range, a portion of the main stage is fueled. This improves overall performance and emissions. [3]

A one-dimensional analysis of the DAC for reducing pollutant emissions is presented by Jeong et al. [21]. Their study discusses the key parameters to consider when upgrading a conventional single annular combustor to a DAC. In addition, the optimization of major design parameters to minimize NO_x and CO emissions was analyzed. The results showed that while the main stage combustion efficiency in taxi/idle was significantly reduced, NO_x emissions were reduced by adjusting some of the design parameters. It was concluded that by reducing the gas velocity in the pilot stage, CO emissions could be reduced at the expense of increasing NO_x.

A comprehensive study on the design, evaluation and performance analysis of the staged low emission combustors is conducted by Hegde et al. [22]. A developed design methodology is used to predict the performance of both radial and axial staged DAC types. Their results showed that although the radial staged combustor is shorter in length, it has a larger cross-sectional area. This could result in a larger engine casing diameter. The axial staged combustor showed some advantages in terms of emissions and efficiency. In the axial case, main stage ignition was faster and more reliable because the main stage is located downstream of the pilot stage. In addition, the combustion efficiency of the main stage was improved, even though it operated at a higher air equivalence ratio, because the hot exhaust gases from the pilot stage flow into the main stage. In general, for both radial and axial staged combustors, the NO_x emissions of the combustor models were in the range of 50 – 60 ppm, when the primary zone is operated between $\lambda = 1.25 - 1.67$

2.3 Twin Annular Premixing Swirler Combustors (TAPS)

In contrary to the traditional emission control concepts described above, which use a fuel-rich front end (e.g. RQL), lean-burn concepts have been proven to result in even lower NO_x emissions. By operating the combustor in a fuel-lean condition for the entire flight cycle, this offers a great potential for cleaner GT engines. [23]

Significant reductions are achieved at both low and cruising altitudes with a fourth generation, low-emission combustor developed by GE. The Twin Annular Premixing Swirler (TAPS) is essentially a product of accumulated experience with fuel staging of the DAC, including lessons learned with Dry Low Emissions (DLE) lean premixing combustors in industrial aero-derivative GTs [24]. In addition, Mongia's [25] research has shown that a 50% NO_x reduction over the DAC can be achieved without compromising other combustor design requirements such as performance, operability and durability.

Its working principle is based on a swirler built around a swirling cup mixer, hence the name: Twin. This creates a “flame-within-a-flame” (see Figure 2.3) that must operate from low to high load and maintain the characteristics of a modern GT combustor, i.e., combustion efficiency, low pressure drop, low gaseous and particulate emissions, rapid ignition, flame propagation, lean blowout prevention, stable combustion dynamics, desired exit temperature profile without dilution air, and improved premixing without risk of flashback. [8]

The TAPS concept uses internally staged, partially premixed technology. The combustor consists of concentric pilot and main stages. The pilot stage uses a simplex atomizer that produces a sheet of liquid fuel on a prefilmer where secondary atomization (air-blast) occurs through the jet streams. The atomized fuel then interacts with the swirling air to create a pilot recirculation zone. This stage provides sufficient combustion efficiency at low power in addition to ignition and idle operation. The main stage is activated at higher power requirements by partially premixing the injected liquid fuel in a jet cross-flow manner into the cyclone swirlers. (see Figure 2.3). The smaller pilot flame (orange region) is essential to the main flame (purple region) as it generates the swirling motion necessary to maintain a stable main flame. The GEnx TAPS combustor uses 70% of the airflow for the mixer and the remaining 30% for dome and liner wall cooling. The TAPS concept does not use dilution air. [3]

The TAPS I combustion concept has found its application in the GEnx engine for the B747-8 and B787 wide-body aircraft and entered service in 2010. The TAPS II and III versions have been deployed in LEAP (B737 MAX and A320 neo) engine and GE9X (Next-Gen B777), respectively [26]. Despite its significant improvement in NO_x emissions, there is still room for further development: [24]

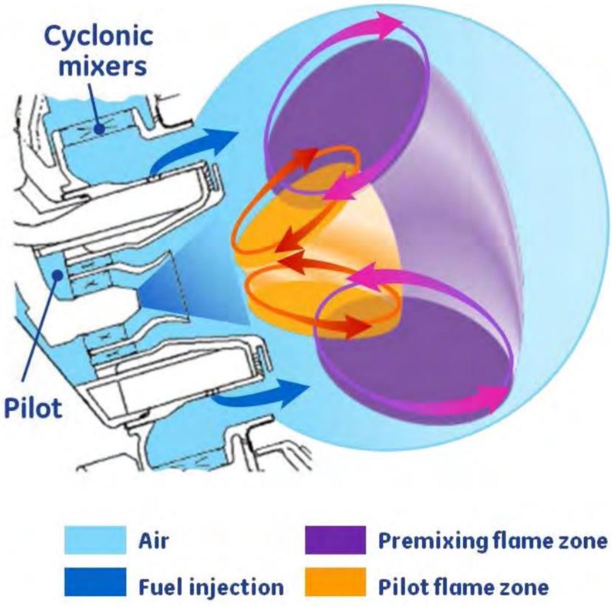

Figure 2.3: TAPS Fuel Injection Concept [24]

- **Simplification:** Efforts needed to simplify the combustion system and reduce costs.
- **Reduced combustion dynamics:** Due to the lean-burn concept, combustion dynamics require further improvement.
- **Operability:** Despite acceptable operability, there are still challenges related to the lean burning primary zone.
- **Autoignition and mixing:** As the ignition delay decreases at higher overall pressure ratios, the risk of autoignition must be further mitigated.

- **Fuel nozzle durability:** The fuel nozzle is a key component of the burner, providing the rich-burn at low power and the lean-burn at high power. Improved protection against radiant heat and minimized carbon deposits are necessary to extend its life.

2.4 Lean Direct Injection Combustors (LDI)

Similar to DAC, RQL and TAPS technologies, Lean Direct Injection (LDI), which is being developed by Rolls-Royce and CFD Research Corporation, among others, has the potential to significantly reduce NO_x emissions while maintaining other combustor requirements.

Research by Nickolaus et al. [27] on the LDI concept showed that because the fuel is injected directly into the combustion chamber along with a large amount of air, the need for dilution air is significantly reduced or eliminated. Their patented injector design utilizes a “bifurcated flow pattern” that produces low NO_x emissions at high/full power, CO and soot emissions at low power. Its design utilizes three swirlers, two separate fuel injectors (pilot and main), and a flow splitter that divides the airflow into two streams. The injectors are concentrically mounted and inject liquid fuel into the separated airstreams leading to two distinct flames (see Figure 2.4).

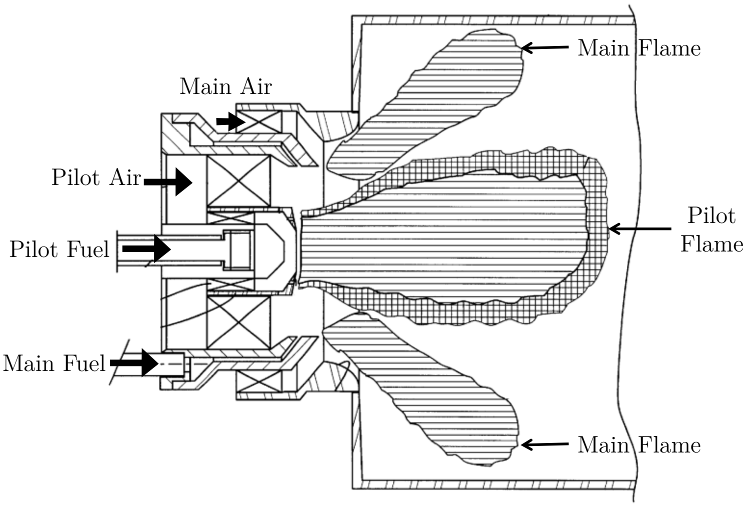

Figure 2.4: LDI Combustor Cross Sectional View. Adapted from [28]

In theory, any lean-burn concept has the potential in producing low NO_x emissions. In most cases, it is the staging issue that counterbalances the advantage of a flame burning at lean conditions. Since the LDI concept directly injects the fuel with a large amount of air, the rapid mixing and flashback risk is greatly mitigated. The concept heavily relies on fast vaporization and mixing and failing to adequately mix the air-fuel intake can result into near-stoichiometric regions with very high thermal NO_x production. [23]

In a study by Shen et al. [29], the vortex breakdown of the swirling flow in an LDI combustor was characterized numerically and experimentally. In their work, large eddy simulation (LES) and planar particle image velocimetry (PIV) were used to characterize the vortex flow of the LDI combustor under both confined and unconfined conditions. Their results showed that confinement significantly altered the flow characteristics. Compared to the unconfined case, the confined condition showed that the swirling jets exhibit an increased spreading angle, resulting in a larger central recirculation zone.

A comprehensive experimental study was performed by Marek et al. [30] on low emission hydrogen combustors GT using LDI. In order to better understand the underlying differences in combustion behavior, Jet-A was also used as a fuel in addition to hydrogen. The tests focused on measuring NO_x emissions and combustion performance at various inlet conditions and air equivalence ratios up to 2.1. Since hydrogen is seven times more reactive than Jet A-1, the flashback problem remained a major challenge. To counteract this problem, the mixing time was shortened and the jet velocities were kept high. The results showed that, in some cases, hydrogen NO_x emissions were comparable to those of the Jet A-1 LDI combustor system. For hydrogen and Jet-A combustion, the NO_x emissions were in the range of 50–60 and 50 ppm, respectively.

2.5 Lean Premix Prevaporized Combustor (LPP)

Similar to the operating principle of the LDI concept, the lean premix prevaporized (LPP) concept uses fuel-lean burn technique to minimize the pollutant emissions. A lean premixed combustion is any fuel-air mixture that is thoroughly mixed before entering the combustion chamber.

When burning liquid fuel, the fuel is first vaporized, then mixed with combustion air and finally fed to the combustor (see Figure 2.5). The air-fuel ratio of the mixture is typically close to the lean blowout limit, minimizing NO_x levels. Local hot spots within the reaction zone are largely eliminated, further improving emissions performance and elimination of soot formation. The LPP concept is subject to an increased risk of autoignition, particularly at lower power conditions. This risk arises due to the complete vaporization of fuel and thorough mixing of fuel and air in the premixing duct. Consequently, a highly reactive and homogeneous mixture is formed, which is more susceptible to premature ignition, especially when exposed to elevated temperatures and pressures for prolonged residence times. The LPP concept has found application in the GE LM6000 GT. [3]

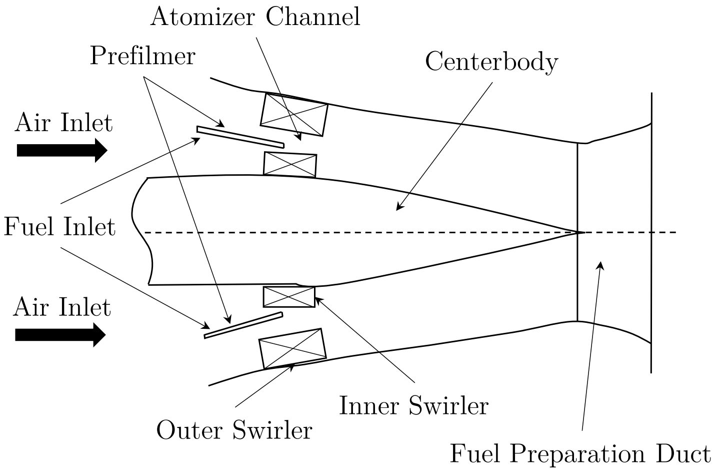

Figure 2.5: Schematic Illustration of a Lean, Premix and Prevaporize Nozzle. Adapted from [31]

In addition, the LPP concept has the advantage of operating at flame temperatures not exceeding 1900 K. At these temperatures, NO_x formation is also controlled by residence time. However, slightly longer residence times do not have as strong an effect because the NO_x formation reactions are very slow at these temperatures. Therefore, the LPP combustors can provide longer residence time, which is beneficial for CO and UHC reduction while keeping NO_x low. This is particularly interesting for industrial GT applications where the size of the combustor plays a lesser role in its design. [32]

In a study conducted by Behrendt et al. [31] on a LPP injector concept for high pressure aero engines, the NO_x and CO emissions showed a strong dependence on the air preheat temperature. In addition, as the evaporation rate, and therefore the preheat temperature, changed, so did the fuel placement and the resulting temperature distribution. Another study by Nakamura et al. [33] investigated the effect of liquid fuel preparation on GT engine emissions using an air-blast atomizer and an injector/premixer assembly to vaporize the fuel. Interestingly, at a prevaporized fuel condition, the NO_x emissions of the actual GT engines increased. This phenomenon means that the combustor design strategy must focus not only on minimizing atomization droplets, but also on the properties of the fuel-air mixture, such as the temporal and spatial distribution of homogeneity before and within the reaction zone. The measured CO concentration remained fairly constant in the prevaporized and liquid cases.

Harth [34] studied swirl-stabilized LPP kerosene flames, with a focus on characterizing flow fields at realistic Reynolds numbers and investigating vortex bursting mechanisms. By analyzing vortex transport and axial momentum equations, the study identified key factors influencing recirculation zone formation in combustion chambers. Using Large Eddy Simulation (LES) and laser-optical methods, it demonstrated how turbulent momentum exchange within the mixing tube impacts flame stability.

2.6 Jet-Stabilized Combustors (FLOX)

The previously mentioned flame stabilization methods utilize a swirling motion to create vortex breakdown for flame stabilization and fuel-air mixture enhancement. The use of aerodynamic flow techniques can also provide a proper mixing and profound recirculation zone.

The jet-stabilized combustors, or FLOX (Flameless Oxidation) [35], are designed to intensively mix the fuel and combustion air with the recirculating hot exhaust gases to produce a diluted mixture, which in turn results in fuel-lean combustion. The generic term “flameless oxidation” is derived from the fact that the fuel is burned without a visible flame. This means that as the flame spreads, the volume occupied by the reaction zone in the combustor increases significantly until the flame is distributed over almost the entire combustion chamber.

The developed concept for gas turbine applications is characterized by high momentum jets originating from circularly arranged air nozzles. These jets induce a strong recirculation zone that provides enhanced mixing and flame stabilization in the combustion chamber (see Figure 2.6). NO_x formation is greatly reduced by avoiding temperature peaks in the combustion chamber [36,37].

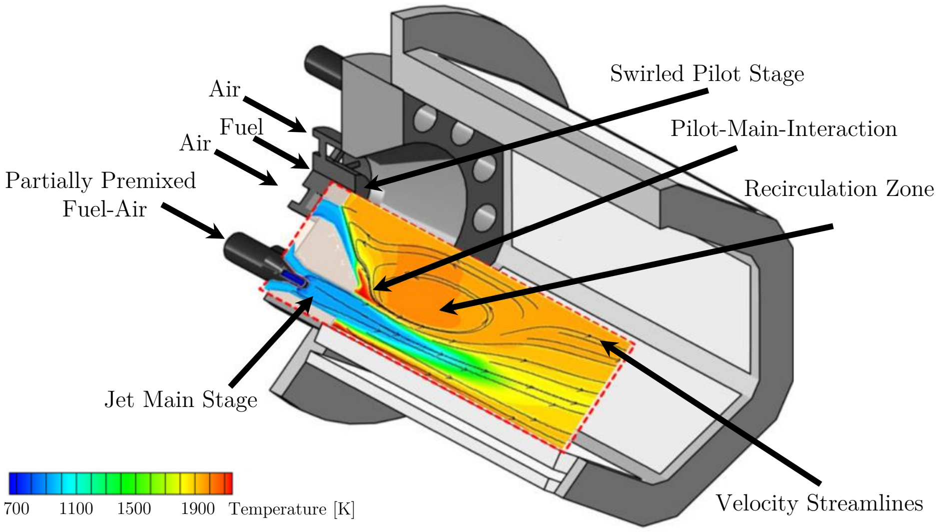

Figure 2.6: Piloted 12-Nozzle FLOX Based Combustor. Adapted from [38]

Due to its promising potential for reducing NO_x levels, many researchers have characterized the operability of this concept for both industrial firing and GT applications. In this respect, researchers at the Institute of Combustion Technology at the German Aerospace Center (DLR) have extensively investigated the concept for GT application. In a work by Lammel et al. [39], an eccentric single-jet burner was used as a generic jet-stabilized model combustor, which emulated the distinct recirculation zone within the combustion chamber, similar to the typical strong internal recirculation of the full-scale combustor. The tests were conducted at atmospheric pressure and elevated air temperatures using methane-air and hydrogen-air mixtures at high exit bulk velocities up to 150 m/s. The flame of methane was lifted and detached considerably, while the hydrogen flame was attached to the nozzle. The average flow fields of both flames showed comparable recirculation lengths.

Experimental analysis using synthetically blended fuel compositions was used in a study by Zornek et al. [40] where the performance of the combustion system and the Turbec T100 micro gas turbine were compared. The pressure loss across the FLOX combustion chamber was found to be less than 4%. In addition, over the entire operating range, the FLOX combustor demonstrated low pollutant emissions. Specifically, CO emissions were less than 30 ppm, NO_x emissions were less than 6 ppm, and unburned hydrocarbons were less than 1 ppm.

Lammel et al. [41] conducted research on a single-nozzle FLOX based burner to optimize injectors for low NO_x and CO emissions over a wide range of loads in a high-pressure combustion test. The resulted NO_x emissions over flame adiabatic temperatures for pressures of 4–10 bar is depicted in Figure 2.7. It is evident that as the flame temperature increases, so do the NO_x levels. The emissions from 4–8 bar show similar levels for the same flame temperatures with a tendency for greater NO_x increase with increase in flame temperature and pressure. The potential of FLOX based combustors for gas turbine applications is demonstrated by the relatively low NO_x levels.

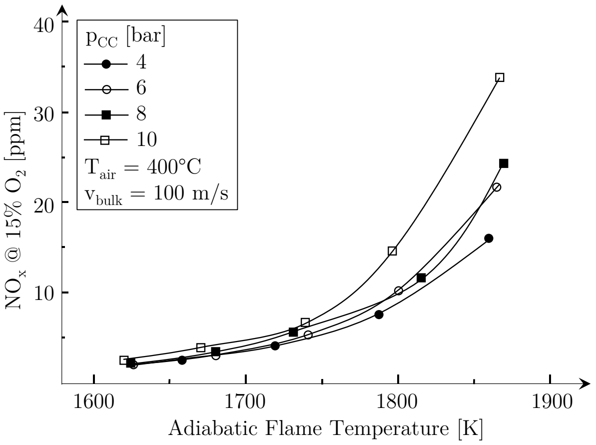

Figure 2.7: NO_x emissions of a FLOX Based Combustor at Different Pressure Levels. Adapted from [41]

The hydrogen capability of a jet-stabilized combustor designed to burn mixed biomass and natural gas was investigated in a study by Hohloch et al. [42] using a 10-nozzle pilot FLOX-based combustor. The system was operated with various natural gas/hydrogen blends, from pure natural gas to pure hydrogen. Figure 2.8 shows the resulting NO_x emissions.

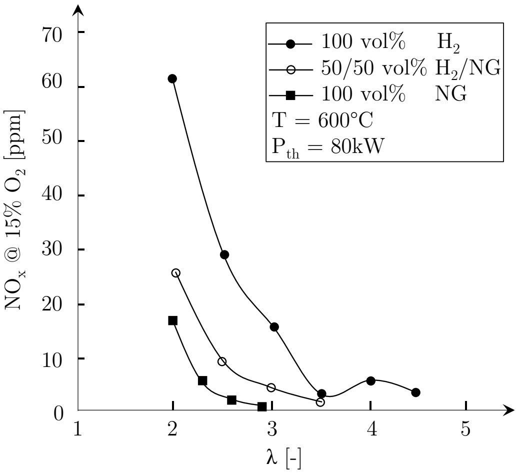

Figure 2.8: Resulted NO_x Emissions from a Piloted 10-Nozzle FLOX Based Combustor. Adapted from [42]

The jet-stabilized combustion concept has been shown to provide very good emission performance and operating range for gaseous fuels [43,44], but the number of liquid fuel combustion studies [6,45,46] is relatively limited. Using liquid heating oil and an oil-water mixture, Schäfer et al. [47] conducted research on a generic single-nozzle jet-stabilized combustor in a high-pressure test rig to gain a detailed insight into liquid fuel-air distribution, mixing and droplet distribution. The results showed that most of the liquid fuel evaporates near the hot gas region because a substantial fraction of the droplets is transported far downstream of the nozzle by the high-momentum jet.

Gounder et al. [48] studied the characteristics of light fuel oil sprays using laser diagnostic methods in flames at 3.5 bar pressure, 300°C preheated air temperature, 1.45 air equivalence ratio, and 120 m/s jet velocity. The combustor consisted of 8 evenly spaced nozzles on a circle. Despite the prediction of intense fuel evaporation using simulation tools, experimental observations showed that spray droplets penetrated deep into the combustion chamber ($x > 150$ mm) and droplets were still present downstream of the peak heat release zone. The chemiluminescence of the OH* images showed long flame lengths with a short flame lift-off height.

The technology has already been implemented in stationary gas turbines of various power classes [49] and MGTs [50]. However, it has not yet been integrated into gas turbine systems in aviation due to the larger combustion volume required.

2.7 Combustors' Performance Review

Performance aspects of the previously described combustor technologies are given in Table 2.1.

Table 2.1: Combustor Technologies Performance Aspects Reviewed in the Current Work [3]

	Performance Aspect			
Combustor	Strengths		Challenges	
RQL	High resistance to Flame out, particularly at low power	Relatively low/short development cost/time	Need for airflow distribution optimization for soot control	Need for advanced fuel spray system to improve fuel-air mixing
DAC	Radial configuration allows for attaining performance at shorter liner length	Lean combustion is made possible even at high power leading to reduced NO_x	Liner cooling issues due to larger surface area of the radial configuration / complexity	Undesired combustion efficiency at mid power range due to fuel split control difficulties
TAPS	Improved combustor exit temperature due to internally staged configuration	Reduced liner cooling air requirement due to ceramic matrix liner, which allows for leaner combustion	Issue with auto-ignition and flashback due to premixed combustion	Complex fuel injector nozzle requires improved thermal management
LDI	Local uniform fuel-air mixture can lead to shorter liner design and lower NO_x levels	Active control of the temperature distribution through regulating local fuel air ratio of each injector	Compact combustor design requires high injector manufacturing technology	Coking issues may occur due to close proximity of the reaction zone and the injectors
LPP	Lowest emissions can be attained due to elimination of fuel droplets	Due to elimination of soot and thus reduced flame radiation, liner durability is greatly improved	Risk of auto-ignition and flashback at higher overall pressure ratio due to premixed combustion	Higher lean blowout risk due to very fuel-lean combustion
FLOX	Homogenous reaction zone temperature is achieved by intensive and rapid fuel-air mixing in the recirculation zone	Minimized risk of flashback due to high jet velocity at the nozzle exit	Longer reaction zone, especially with liquid fuel combustion due to increased bulk velocity and lower residence time	Increased fuel droplet wall impingement due to very close proximity of the fuel injector and burner nozzle wall

Figure 2.9 provides an overview of some of the combustor technologies used in aircraft engines. Figure 2.9 *a* shows the NO_x emission index for two engine types each with a rated thrust of 130–150 kN for the DAC, TALON X (RQL) and TAPS II at takeoff flight stage. The NO_x emission index for the corresponding engine and combustor configurations under climb-out conditions is shown in Figure 2.9 *b*. Clearly, the DAC and TALON X combustors have comparable NO_x emissions at takeoff and climb out, while the TAPS II combustors have higher emissions at both flight cycles.

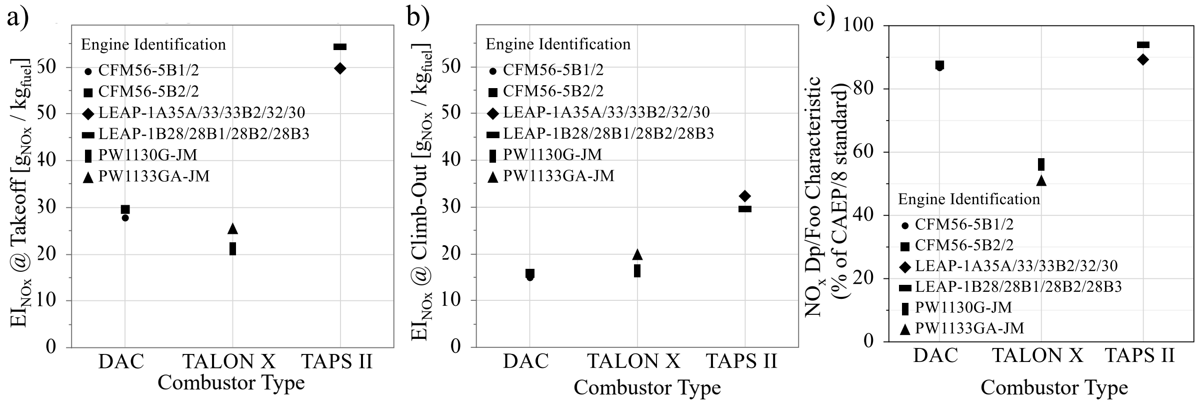

Figure 2.9: NO_x Emissions of Typical Engines with their Corresponding Combustor Technology at a) Takeoff Conditions, b) Climb-Out Conditions and c) charac. Dp/Foo expressed as % of the CAEP/8 NO_x regulatory limit [51]

The Figure 2.9 *c* compares NO_x Dp/Foo characteristics (as a percentage of the CAEP/8 standard) for six aircraft engines using three combustor types. Dp is the mass of NO_x emitted during the reference landing and take-off (LTO) cycle. Foo refers to the maximum power/thrust available for take-off at International Standard Atmosphere (ISA) sea level conditions [52]. To obtain certification approval, the Dp/Foo value of a pollutant species must remain below the specified threshold [53]. Engines with DAC combustors (CFM56-5B1/2 at 89% and CFM56-5B2/2 at 88%) utilize older technology, offering NO_x reduction through a two-stage combustion process. TAPS II combustors in LEAP engines (LEAP-1A35 at 89% and LEAP-1B28 at 94%) achieve lower NO_x levels. The TALON X combustor in PW1000G engines (PW1130G-JM at 56% and PW1133GA-JM at 51%) achieves the lowest NO_x emissions among the compared engines.

An ideal combustor would incorporate all of the strengths listed in Table 2.1 and would avoid, to a large extent, the challenges associated with the combustor technologies described above. Despite various physical and geometric constraints, this research, as described in Section 1.2, is aimed at combining the above-mentioned strengths, e.g., low NO_x, compact reaction zone, fuel flexibility, and stable combustion.

3 Fundamentals

This section provides an overview of the fundamentals necessary for comprehending the physical and chemical phenomena, including details of liquid fuel atomization and evaporation. It also includes a literature review of studies on steam injection, as well as a discussion of types of design of experiments (DOE) and its use in generation of multivariate models used within this work.

3.1 Gas Turbine Combustion Fundamentals

The development of gas turbine technology has shifted from prioritizing maximum thrust with little regard for environmental and operational efficiency, to a model where contemporary gas turbines must meet stringent combustion standards. This includes controlling emissions, improving fuel efficiency, and ensuring high operational performance to be suitable for modern applications [1]. In this section, an overview of the thermodynamic fundamentals behind combustion process is given.

3.1.1 Stoichiometry

In an ideal, complete and stoichiometric combustion of a liquid fuel (e.g. Jet A-1) and air, the products of combustion can only be CO_2, water vapor (H_2O) and atmospheric nitrogen (N_2). Regarding CO_2 and H_2O, these are natural products of a chemical oxidation of a hydrocarbon fuel molecule and any oxidizing agent (e.g. air) and are not considered as pollutants. However, CO_2 and water vapor contribute to global warming [2]. The most effective method to mitigate CO_2 and H_2O emissions involves decreasing the use of conventional hydrocarbon fuels or transitioning to carbon-neutral alternatives, such as sustainable aviation fuels (SAF). Nonetheless, it is important to acknowledge that these measures cannot entirely eliminate CO_2 and H_2O emissions, as they are intrinsic byproducts of hydrocarbon combustion. Using Fischer-Tropsch synthesis, power-to-liquid (PtL) kerosene can be produced. Direct air capture (DAC) technology and water electrolysis can be used to provide the carbon and hydrogen needed for the process.

The liquid fuels used in aviation today are primarily derived from fossil crude oil, and their thermochemistry varies to some extent depending on their origin and refining process. A typical Jet A-1 consists of hydrocarbon molecules with 8 to 18 carbon atoms [54]. For detailed thermochemical properties of Jet A-1 and other liquid fuels used in this study, see Section 6.4.5 and Appendix C. On average, however, 12 and 23 atoms ($C_{12}H_{23}$) can be assumed for carbon and hydrogen, respectively [55]. In the case of a hydrocarbon fuel expressed as C_xH_y, the stoichiometric relationship can be summed as:

$$C_xH_y + a(O_2 + \frac{79}{21} N_2) \rightarrow x\, CO_2 + \frac{y}{2} H_2O + \frac{79}{21} a\, N_2 \tag{3.1}$$

where:

$$a = x + \frac{y}{4} \tag{3.2}$$

For simplicity, the composition of air can be assumed to be 21% oxygen and 79% by volume nitrogen. Thus, the reaction equation for Jet A-1 and air is:

$$C_{12}H_{23} + 17.75\, (O_2 + \frac{79}{21} N_2) \rightarrow 12\, CO_2 + 11.5\, H_2O + 66.77\, N_2 \tag{3.3}$$

for Jet A-1 ($C_{12}H_{23}$), the constants are: x = 12 and y = 23 and therefore a = 17.75.

Assuming 1 mole of the fuel, the masses (m_i) of the air and fuel are calculated using the corresponding molecular weight (MW) of each species:

$m_{fuel} = 167.311\ g$ with $MW_{fuel} = 167.311\ \frac{g}{mole}$

$m_{O_2} = 567.964\ g$ with $MW_{O_2} = 31.998\ \frac{g}{mole}$

$m_{N_2} = 1870.535\ g$ with $MW_{N_2} = 28.013\ \frac{g}{mole}$

$m_{air} = m_{O_2} + m_{N_2} = 2438.499\ g$

The following equation can be used to calculate the stoichiometric air-fuel ratio $(A/F)_{stoic}$: [56]

$$(\mathrm{A/F})_{\mathrm{stoic}} = \left(\frac{m_{air}}{m_{fuel}}\right)_{stoic} \tag{3.4}$$

Assuming that Jet A-1 is simplified as $C_{12}H_{23}$, the A/F stoichiometry is 14.575 g_{air}/g_{fuel}. This ratio represents the stoichiometric amount of air (in grams) required to completely burn 1 gram of fuel. The Jet A-1 fuel ($C_{12}H_{22.6}$) used in this research has a hydrogen and carbon content of 13.65% and 86.35% (based on mass), respectively (see Section 6.4.5 for composition details of the tested liquid fuels). This leads to an A/F stoichiometry of 14.621 g_{air}/g_{fuel} assuming air consists of (Mole%): N_2 78.084, O_2 20.9476, Argon 0.9365 and CO_2 0.0319 [55]. The difference between $C_{12}H_{23}$ and $C_{12}H_{22.6}$ in terms of adiabatic flame temperature amounts to 0.04 K.

If the oxidizer exceeds the $(A/F)_{stoic}$, the mixture will burn at a fuel-lean condition, where the excess O_2 will exit the combustion chamber with other products: H_2O and CO_2. In the event of a lack of sufficient oxidizer in the reaction zone, the mixture is referred to as fuel-rich, in which case excess fuel will leave the combustion chamber.

A common and important quantitative indicator of rich, lean, or stoichiometric mixtures is the equivalence ratio Φ or air equivalence ratio λ. They are defined as:

$$\lambda = \frac{\left(\frac{A}{F}\right)}{\left(\frac{A}{F}\right)_{stoic}} = \frac{1}{\Phi} \tag{3.5}$$

For mixtures with $\lambda > 1$, $\lambda < 1$, and $\lambda = 1$, combustion is lean, rich, and stoichiometric, respectively. In a gas turbine combustor, this ratio is one of the most important factors in determining the emissions, efficiency and performance of the engine.

3.1.2 Heat of Combustion

A chemical reaction, such as a combustion process, releases a certain amount of heat that can be quantified using a steady-flow reactor. In the case of combustion of Jet A-1 with air, the enthalpy of combustion (Δh_c) is calculated on the assumption that the mixture enters and leaves the reactor under standard conditions (1 atm., 25°C). The combustion process is assumed to be complete (see Equation 3.1), i.e. all of the fuel carbon is converted to CO_2 and all of the fuel hydrogen is converted to H_2O [57]. Figure 3.1 shows the steady-flow reactor of a complete combustion of a hydrocarbon fuel with air. Since the reaction is isothermal ($T_{reactants} = T_{products}$), heat must be removed from the process.

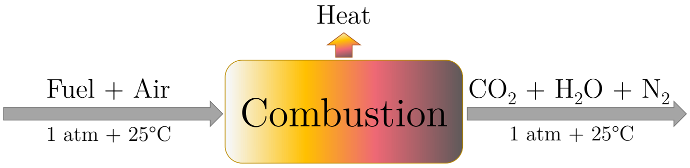

Figure 3.1: Steady-flow Reactor for a Hydrocarbon Fuel-air Mixture Combustion. Adapted from [56]

To estimate the molar enthalpy of combustion (= - heat of combustion Δh_c), the difference between the enthalpies of the reactants and products must be calculated. It is defined as [57]:

$$\Delta_R H_m^0 = \underbrace{\sum_{i=i}^{S} \nu_i'' \, \Delta_f H_i^0}_{products} - \underbrace{\sum_{i=i}^{S} \nu_i' \, \Delta_f H_i^0}_{reactants} \tag{3.6}$$

where $\Delta_f H_i^0$ [kJ/mol] is the enthalpy of formation of the species (see Table 3.2).

$$\Delta_R h^0 \left[\frac{kJ}{g_{fuel}}\right] = \frac{\Delta_R H_m^0}{MW_{fuel}} \tag{3.7}$$

By using the values in Table 3.2 the molar enthalpy of combustion $\Delta_R H_m^0$ [kJ/mol_{fuel}] for liquid Jet A-1 and liquid H_2O as the product equals to -7705.76 kJ/mol_{fuel}. This value can be formulated as per gram fuel (-46.14 kJ/g_{fuel}) using Equation 3.7 and MW_{fuel} = 167.311 g/ mol. The heat of combustion Δh_c [kJ/g_{fuel}] is numerically equal to the enthalpy of combustion. This value is referred to as the higher heating value (HHV) if the H_2O exits the reactor at 25°C and is thus condensed.

The heat generated includes the enthalpy of vaporization $\Delta_{vap}H_{H2O}$ of water. If the water exits the reactor in a gaseous state, then the value is referred to as the lower heating value (LHV). In this case, the heat of combustion is reduced by the $\Delta_{vap}H_{H2O}$ and is 43.11 kJ/g_{fuel} (about 7% less than HHV). In the case of vaporized Jet A-1, $\Delta_{vap}H^0_{Jet\,A}$ [kJ/g_{fuel}] is added to the heat of combustion. These values are summarized in Table 3.1. The relationships can be put into perspective by graphing the calculated values in Table 3.1. An h – T diagram illustrating the heat of combustion values of the four cases explained below is presented in Figure 3.2.

Table 3.1: Summary of Heat of Combustion Δh_c [kJ/$g_{Jet\ A\text{-}1}$] at Various Condition

Fuel	Product	Δh_c	Note
Jet A-1 (L)	H_2O (L)	46.14	Higher heating value / Spray fuel injection
Jet A-1 (L)	H_2O (g)	43.11	Lower heating value / Spray fuel injection
Jet A-1 (g)	H_2O (L)	46.46	Higher heating value / Prevaporized fuel injection
Jet A-1 (g)	H_2O (g)	43.43	Lower heating value / Prevaporized fuel injection

Table 3.2: Thermodynamic Properties of Selected Gaseous and Condensed Species

	Jet A-1* (g)	Jet A-1* (L)	O_2 (g)	N_2 (g)	CO_2 (g)	H_2O (g)	H_2O (L)
$\Delta_f H_i^0$	-249.657	-303.403	0	0	-393.5	-241.82	-285.83
Cp^{298K}	293.491	350.332	29.378	29.124	37.13	33.588	75.35
ν'	1	1	17.75	66.77	0	0	0
ν''	0	0	0	66.77	12	11.5	11.5

* Jet A-1 ($C_{12}H_{23}$) thermodynamic data are adapted from the NASA Thermal Library of Chemical Equilibrium for Application Software [55]

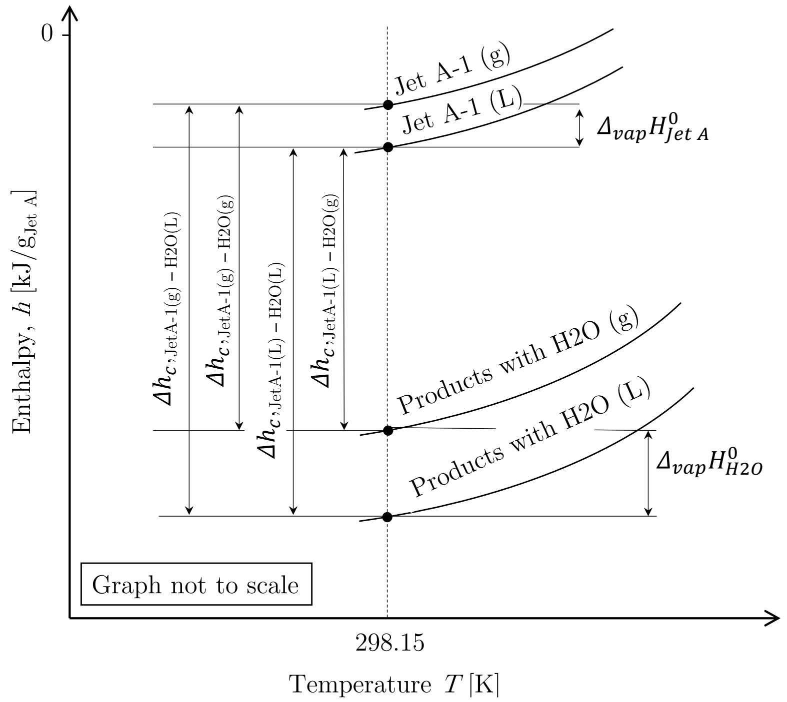

Figure 3.2: Enthalpy-Temperature Diagram Showing Heat of Combustion of Jet A-1 at Various Conditions. Adapted from [56]

3.1.3 Adiabatic Flame Temperature

Combustion in a gas turbine engine occurs at approximately constant pressure (isobaric). Therefore, the standardized enthalpy of the products at the end state ($T'' = T_{ad}$, $p''= 1$ atm) is equal to the standardized enthalpy of the reactants ($p' = 1$ atm). [56]

$$H'_{reactants}(T', p) = H''_{products}(T_{ad}, p) \tag{3.8}$$

reorganized, the equation would be:

$$0 = \sum_{i=i}^{S} H_i''\ (T_{ad}) - \sum_{i=i}^{S} H_i'\ (T') \tag{3.9}$$

where the temperature dependent molar enthalpy $H_i\ (T)$ for each (i) species (S) is defined as:

$$H_{m,i}(T) = \Delta_f H_i^0 + \int_{T^0}^{T} C_{p,m,i}\ (\vartheta)\ d\vartheta \tag{3.10}$$

The thermodynamic library of the NASA CEA software [55] is used to calculate the molar heat capacity of the species $C_{p,m,i}(\vartheta)$, which is temperature (ϑ) dependent. The library uses the NASA 9-coefficient polynomial parameterization for the molar heat capacity and the molar enthalpy, which is defined as follows:

$$\frac{C_{p,m,i}(T)}{R_m} = a_1T^{-2} + a_2T^{-1} + a_3 + a_4T^1 + a_5T^2 + a_6T^3 + a_7T^4 \tag{3.11}$$

$$\frac{H_{m,i}(T)}{R_m} = -a_1T^{-2} + a_2\frac{\ln T}{T} + a_3 + a_4\frac{T}{2} + a_5\frac{T^2}{3} + a_6\frac{T^3}{4} + a_7\frac{T^4}{5} + \frac{b_1}{T} \tag{3.12}$$

where $R_m = 8.314$ J/(mol K) is the universal gas constant, a_i and b_i are NASA 9-coefficients.

For Jet A-1 combustion with air, T_{ad} can be calculated using equations 3.8 through 3.12, assuming stoichiometric and complete combustion with no dissociation (products consist of only CO_2, H_2O, and N_2). As shown in Table 3.3, the T_{ad} for liquid Jet A-1 with air is 2402.5 K and for vaporized Jet A is 2416.64 K (about 0.6 % higher than liquid fuel combustion) for a reactant temperature of 298.15 K.

Table 3.3: Calculated Adiabatic Temperatures for Liquid and Vaporized Jet A-1 with Air

			Products Mol Fraction		
Variable	**T_{ad} [K]**	**T' [K]**	**CO_2**	**H_2O**	**N_2**
Jet A-1 (L) / air	2402.5	298.15	0.13293	0.12739	0.73968
Jet A-1 (g) / air	2416.64	298.15	0.13293	0.12739	0.73968

Heat capacity values play a role in the calculation of the adiabatic flame temperature, as shown in Equation 3.10. Although the Cp values of the trivial species are readily available in any thermodynamic table, finding the Cp values of the liquid constituents of Jet A-1 in their liquid state can be challenging. Therefore, only the Cp values of the fuels in their gaseous state are used for all four different liquid fuels characterized in this study. It is assumed that the fuel Cp has a negligible influence on the calculation of the adiabatic temperature.

Assessing this assumption requires a sensitivity analysis that measures the effect of fuel Cp on T_{ad} at different fuel temperatures. As a result, the fuel Cp is varied by +50% and -50% (see Figure 3.3 *a*). Jet A-1 (L) Cp values at liquid phase temperatures (220–550 K) are shown in Figure 3.3 *a*. Next to the original Cp values are their ±50% variations. All three Cp variations are used to calculate the corresponding T_{ad} at different fuel temperatures (see Figure 3.3 *b*).

There is no effect of the fuel Cp on the T_{ad} at $T'_{fuel} = 298.15$ K as shown in Equation 3.10. As the temperature of the fuel increases, the integral term in Equation 3.10 will have a greater effect on the calculated T_{ad}. As shown in Figure 3.3 *b*, the T_{ad} differences between the fuel at 298.15 K and $T'_{fuel} = 400$ K are ±5.25 K and ±11.4 K for $T'_{fuel} = 500$ K. This indicates a marginal influence of the fuel Cp on the T_{ad} over a wide fuel temperature range.

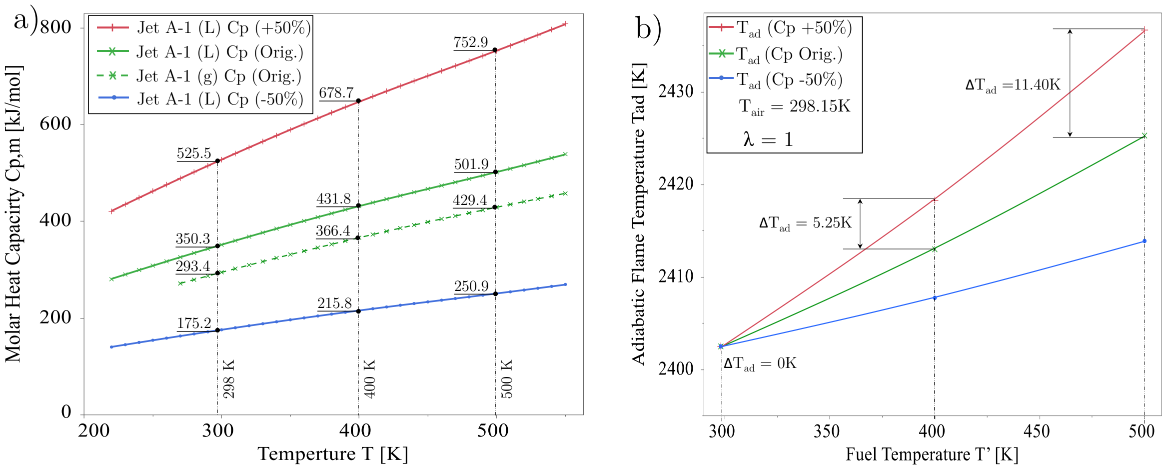

Figure 3.3: a) Molar Cp Values of Jet A-1 (L) in Three Variations, b) Corresponding Adiabatic Temperatures

Although it is unlikely that the Cp values of the same species would vary by up to ±50% in both the liquid and gaseous states (compare green dashed and continuous lines in Figure 3.3 *a*: ≈ 20% difference). Since the Cp values for the fuels in their liquid state is not available and the deviation of the calculated T_{ad} for different Cp values is marginal, in this work the Cp values of the gaseous fuel are used for the calculation of the adiabatic temperature of the liquid fuel. However, by considering the correct enthalpy of formation for each gaseous and liquid fuel, the enthalpy of vaporization is considered, which will affect the T_{ad}.

3.2 Emission Formation Mechanism

Ideally, a hydrocarbon combustion process with air proceeds to form only the CO_2, H_2O and N_2 in the exhaust gas. However, the exhaust gas of a combustion process contains several other species, most of which are undesirable. The continuous nature of gas turbine combustion leads to relatively cleaner emissions compared to the intermittent combustion process in an internal combustion engine. However, to protect public's health and the environment, the amount of NO_x, CO, UHC and C emitted from a GT engine must be further reduced. There is a lot of research on minimizing such emissions in the literature [58–61]. The purpose of this section is to provide an overview of the main mechanisms involved in the emission of pollutants in a gas turbine combustion process.

The major pollutants such as NO_x, CO, UHC and soot (C) are produced in a combustion process where the major species dissociate to form a group of minor species. The dissociation of the reactants and the subsequent reaction between the dissociated species results in the formation of H_2, H, OH, CO, NO, and O [56]. The key to avoiding the CO and UHC emissions produced in the exhaust gas is to provide sufficient residence time and temperature at which they are oxidized to CO_2. However, contrary to the previous argument, both residence time and very high temperatures support NO_x production. By introducing some complexity, i.e. fuel staging and lean premixed combustion, an emissions optimum can be found (refer to sections 1.1 and 2). [1]

In a liquid-fueled combustor, the number of undesirable products (NO_x, CO, UHC and C) depends on several factors, including the following: [1]

- Air equivalence ratio and flame temperature
- Combustion chamber pressure
- Air and fuel temperature
- Fuel atomization quality
- Fuel type

In order to compare the emission levels of different combustor systems, it would be important to correct the emissions to certain reference conditions. For this purpose, there are two main correction methods used for GT combustion emissions: (1) corrected concentrations to 15% by volume O_2 and (2) emission index.

Corrected Concentrations to 15% O_2

The reason for correcting an emission level to a certain percentage of O_2 is to remove the dilution effect while maintaining similar emission concentrations. By correcting the emission level, it is also specified that if the combustors burn less fuel, they are likely to produce less NO_x [1]. This allows a true comparison between different combustors. Also, depending on the application, H_2O is retained or removed from the exhaust prior to analyzing it, which is expressed as wet or dry. Emission concentrations are corrected to 15% O_2 and dried prior to analysis in a gas turbine application. [56]

For example, the wet NO_x emissions [in ppm] can be dried and corrected to 15% O_2 by:

$$[NO_x]_{dry} = [NO_x]_{wet} \times \frac{100}{100 - [H_2O]_{in\,\%\,vol}} \tag{3.13}$$

$$[NO_x]_{ref15\%O2} = [NO_x]_{dry} \times \frac{21 - 15}{21 - O_{2\,measured\,in\,\%\,vol}} \tag{3.14}$$

By drying and then correcting, the concentration can be expressed as “NO_x @ 15% O_2 dry”, which is primarily used to compare emission values in stationary gas turbines:

$$[NO_x]_{dry,ref15\%O2} = [NO_x]_{wet} \times \frac{100}{100-[H_2O]_{in\,\%\,vol}} \times \frac{21-15}{21-O_{2\,measured\,in\,\%\,vol}} \tag{3.15}$$

Emission Index (EI)

The Emission Index (EI) is a quantity that is defined as the ratio of the mass of a species (i) to the mass of the fuel used in the combustion. The unit used for minor emissions such as NO_x is

[g_{NO_x}/kg_{fuel}] and for major emissions such as CO_2 etc. the unit used is [g_{CO2}/g_{fuel}]. It is worth mentioning that all emissions must be used in wet condition to include the water vapor. [1]

$$EI_i = \frac{m_{emission,i}}{m_{fuel}} \left[\frac{g_i}{(k)g_{fuel}}\right] \tag{3.16}$$

Correspondingly, using the emission in ppm by volume, the fuel and air mass flow rates in g or kg per second, and the molecular weights (MW), the equation can be rewritten as:

$$EI_i = \frac{Emissions_{wet\ in\ [ppm\ by\ volume]} \times 10^{-3} \times \frac{MW_i}{MW_{Exhaust\ Gas}} \times (\dot{m}_{fuel}+\dot{m}_{air})}{\dot{m}_{fuel}} \left[\frac{g_i}{kg_{fuel}}\right] \tag{3.17}$$

The main purpose of the emissions index, which is primarily used in aircraft engine emissions analysis, is the comparison of emissions from different gas turbine engines and has been the regulatory emissions standard unit. It is particularly interesting because it is a clear indication of the amount of pollutant produced by the combustion of a given amount of fuel, regardless of the dilution of the products. It can also be used as a measure of the efficiency of a particular combustor. It does not take into account the application. [56]

3.2.1 Nitrogen Oxides (NO_x)

The majority of the nitric oxide (NO) molecules produced in a combustion process react with the oxygen radicals to form NO_2. Therefore, it is common to add NO and NO_2 together and refer to them as $NO_x = NO + NO_2$. Nitric oxide is oxidized to nitrogen dioxide in the atmosphere. Both NO and NO_2 are precursors to acid rain and contribute to photochemical smog, while nitrous oxide (N_2O) is a greenhouse gas. In addition, the formation of NO_x in a combustion process is strongly influenced by the O/H radicals. [62]

According to Lee et al. [4], the main effect is that NO_x briefly increases atmospheric ozone, which negatively affects the radiative budget. There are other effects involved, some of which are also climatically beneficial, but are dominated by the effect described above. It should be noted that due to the altitude at which the emissions are emitted, the release in aviation applications is particularly problematic.

Nitrogen oxides can be divided into four categories based on their formation mechanism:

- NO_x formation from free nitrogen in combustion air
    - Thermal nitric oxides (Zeldovich NO)
    - Prompt nitric oxide (Fenimore-NO)
    - Nitrous oxide (N_2O)
- NO_x formation from organically fuel-bound nitrogen “organic NO_x”

A typical behavior of the pathways for the formation of NO_x is shown in Figure 3.4. The tendency for thermal NO_x formation is near stoichiometric and lean conditions where flame temperature is high and O_2 is available. The prompt NO is formed primarily in the fuel rich conditions. The N_2O radicals are formed under lean fuel conditions, with the N_2O being formed under high pressure in the combustion chamber. [63]

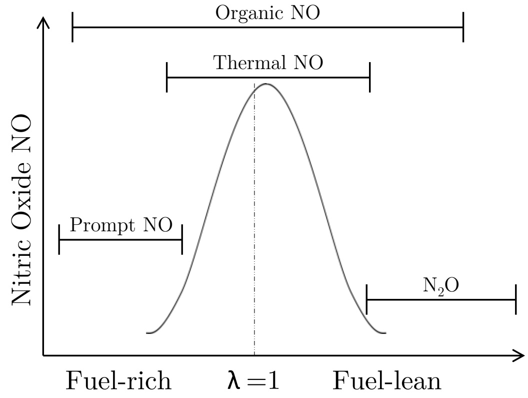

Figure 3.4: Dominant Pathways for each NO Formation Mechanisms. Adapted from [63]

The levels of NO_x emissions as a function of the flame temperature for both liquid and gaseous fuels are shown in Figure 3.5 *a*. The graph shows (based on experimental data from Snyder et al. [64]) that the flame temperature dependence is slightly weaker for the liquid fuel (#2 fuel oil). Even at identical flame temperatures for both liquid and gaseous fuels, the NO_x emissions of liquid fuels appear to be higher than those of gaseous fuels. This may be due to the near stoichiometric combustion temperatures of the liquid fuel around droplets. An increase in thermal NO formation could be the result. The graph also shows that the difference in the level of NO_x decreases as the conditions become more fuel-rich (higher flame temperatures). The bulk flame temperature approaches stoichiometry as the air equivalence ratio decreases. This approximates the combustion conditions of both liquid and gaseous fuels by reducing the effect of localized near-stoichiometric burning of liquid fuels. [1]

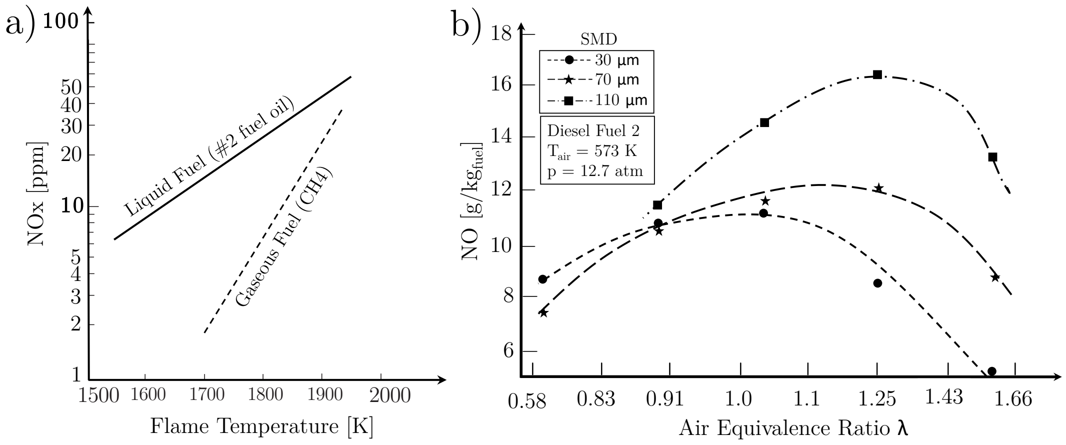

Figure 3.5: a) NO_x Emissions on Flame Temperature for Liquid and Gaseous Fuels, B) Effect of Atomization Quality on NO Emissions. Adapted from [1,64]

The behavior of the different Sauter Mean Diameter (SMD) on NO levels at different air equivalence ratios is described as such by Lefebvre et al. [65]: The equivalence ratio strongly influences how and to what degree NO_x is affected by the fuel spray SMD. NO emissions increase with increasing mean droplet size, especially at fuel-lean conditions, as shown in Figure 3.5 *b*. Increasing the SMD, though, means that more of the fuel droplets in the spray help create the "envelope" flames. These envelope flames formed around the larger droplets burn in a diffusion mode at near stoichiometric fuel-air ratios, resulting in multiple local high temperature pockets where significant levels of NO_x are formed. Decreasing the SMD makes it more difficult for envelope flames to form, so larger portion of the overall combustion process is in a rather premixed mode, which produces less NO_x. As a result, the NO_x emissions of gaseous and liquid fuels can become more similar the better the liquid fuel is atomized (see Figure 3.5 *a*).

In the absence of hot pockets, the size of fuel droplets can still have an effect on combustion. As the size of the fuel droplets grows, a greater proportion of the fuel burns in the fuel-rich regions created as a result of the moving large droplets. As fuel droplets move through the combustion zone, they create wake areas behind them. These wake areas have a higher fuel concentration than the surrounding air. Because of the higher fuel concentration, combustion can occur more readily in these fuel-rich regions. Consequently, more of the fuel burns in these fuel-rich regions than in the surrounding air.

The local air equivalence ratio becomes similar to the global air equivalence ratio as combustion approaches fuel-rich conditions. This proposition that is generally confirmed by the results shown in Figure 3.5 *b*, means that the SMD should have no effect on NO_x emissions for stoichiometric mixtures. This is significant because it indicates that the presence of fuel droplets in the combustion zone creates conditions where combustion can and does occur at near stoichiometric equivalence ratios, irrespective of the global equivalence ratio in the combustion zone.

In the case where the maximum NO level shifts into the lean range, it is typically due to the interaction between the fuel droplet size and the local fuel/air mixing quality. An increase in the droplet size will have an effect on the mixing process of the fuel and air in the combustion zone. Larger droplets have a slower rate of evaporation which leads to longer time for droplets to completely evaporate and mix with the air in the surrounding area.

This is the reason why increased levels of NO is still formed at fuel-lean conditions where the average combustion temperature is so low that theoretically very low levels of NO should be present. This is the basis for the various types of lean premix prevaporize combustors which rely heavily on the elimination of all fuel droplets from the combustion zone. [1]

Beck [66] analyzed nitrogen oxide formation in lean spray flames with incomplete pre-evaporation. The study proposed that single droplet combustion dominates these flames. Numerical simulations revealed key parameters affecting NO formation, such as extinguishing effects from droplet relative velocity. These predictions were validated experimentally using a generic gas turbine combustion system.

Thermal Nitric Oxides

The most important source of NO formation is the Zeldovich pathway, if the combustion is not extremely lean. Typically, the residence time in a gas turbine combustor is about 10 ms. This is not sufficient for NO to reach its chemical equilibrium, which takes hundreds of milliseconds [63].

The mechanism of thermal NO is well established. The initiating step is to attach an oxygen atom to the triple bond in N_2: [62]

$$N_2 + O \rightleftarrows NO + N \tag{R3.18}$$

This reaction is considered to be the rate-limiting step in thermal NO formation. In addition, the activation energy of R3.18 is very high (319.050 kJ/mol) and therefore requires very high temperatures. Therefore, the mechanism becomes unimportant at temperatures lower than 1800 K. Once the NO is formed in R3.18, the rapid oxidation of the nitrogen atom (N) is initiated and leads to the formation of NO by reaction with OH or O_2 (see R3.19 and R3.20). [56,62,67].

$$N + O_2 \rightleftarrows NO + O \tag{R3.19}$$

$$N + OH \rightleftarrows NO + H \tag{R3.20}$$

Compared to the rate at which fuel is oxidized, thermal NO formation is rather slow. As a result, NO is formed in a downstream region of the flame. As shown in Figure 3.4, thermal NO peaks on the fuel-lean side of the stoichiometry. This is because both fuel and nitrogen compete for more oxygen. The remaining oxygen atoms react with N_2 (see R3.18) once the fuel oxidation is satisfied. The oxygen radicals are preferentially consumed by the fuel rather than N_2, despite the higher temperature of the stoichiometry. [1]

Prompt Nitric Oxide (Fenimore-NO)

Under fuel-rich conditions ($0.63 < \lambda < 1.0$), where NO levels are minimized due to lower flame temperatures and abundance of CH radicals in the reaction zone, the prompt nitric oxide mechanism plays a more dominant role in NO formation [63]. The initiation of the mechanism is started by [63]:

$$N_2 + CH \rightleftarrows HCN + N \begin{cases} \rightarrow NO \\ \rightarrow N_2 \end{cases} \tag{R3.21}$$

where the intermediate species CH reacts with the air to form N_2 and thus hydrogen cyanide (HCN), which reacts rapidly to form NO. The activation energy of R3.21 is only 92 kJ/mol compared to about 319 kJ/mol of R3.18, resulting in NO formation at much lower flame temperatures. [57]

Nitrous Oxide (N_2O)

The pathway through nitrous oxide (N_2O), as described by [68], is initiated by:

$$N_2 + O + M \rightleftarrows N_2O + M \tag{R3.22}$$

where M is a collision partner. Once the nitrous oxide is formed, the next step is its oxidation to NO:

$$N_2O + O \rightleftarrows NO + NO \tag{R3.23}$$

$$N_2O + H \rightleftarrows NO + NH \tag{R3.24}$$

$$N_2O + CO \rightleftarrows NO + NCO \tag{R3.25}$$

Compared to the thermal NO pathway, R3.22 requires less activation energy (97 kJ/mol). This leads to NO formation at lower flame temperatures (fuel-leaner conditions) [69]. This mechanism becomes dominant in higher pressure and lean combustion conditions due to the presence of M as a collision partner. [63,70].

Fuel-bound Nitrogen "Organic NO_x"

When the fuel itself contains traces of N, organic NO_x is formed. Examples include the nitrogen found in coal, natural gas, and some liquid fuels. Typically, 1% nitrogen compounds are found in heavy oil and coal. Under stoichiometric and fuel-lean conditions, this nitrogen content is converted to NO. In the case of kerosene combustion, nitrogen is already removed during the refining process. Therefore, the nitrogen content is very low and this pathway leading to NO formation can be neglected for Jet A-1 combustion. [63,71]

3.2.2 Carbon Monoxide (CO)

Insufficient oxidation of fuel carbon compounds to complete the reaction to CO_2 is the primary cause of carbon monoxide (CO) formation in the exhaust gas. This is an indication of inadequate combustion or lack of efficiency. The possible causes of CO formation are [72]:

- Improper mixing of fuel and combustion air
- Short residence time in reaction zone
- Rapid quenching of exhaust gas

On the one hand, a high level of CO is formed at lower engine loads where the flame temperature is too low as a result of a high air to fuel ratio. On the other hand, CO is formed as a result of CO_2 dissociation under stoichiometric conditions where the flame temperature exceeds 1800 K. The combustor length of a gas turbine engine is affected by the oxidation reaction rate of CO and unburned hydrocarbons (UHC). This is especially true at different combustor loads where the bulk velocity and thus the residence time of the emitted species can vary greatly [63]. At very lean conditions, the residence times required to reach chemical equilibrium are higher due to the lower temperatures. As a result, the residence time in the combustor is not long enough to reach equilibrium, resulting in higher emissions of CO, whose oxidation to CO_2 has been quenched.

In general, CO formation can be divided between three combustion conditions [63]:

- **Fuel-rich condition**: A longer residence time is required for CO oxidation. The lack of oxygen in incomplete combustion results in CO emissions. In this case, CO (R3.26) and hydrogen (R3.27) are in competition for oxidation:

  $$CO + OH \rightleftarrows \mathrm{CO_2} + H \tag{R3.26}$$

  $$H + O_2 \rightleftarrows \mathrm{OH} + O \tag{R3.27}$$

  $$H_2 + OH \rightleftarrows \mathrm{H_2}O + H \tag{R3.28}$$

  Reaction R3.26 is a chain-propagating step. It produces H atoms that react with O_2 to form OH and O (R3.27). The rate of reaction of R3.28 is much faster than the rate of reaction of R3.26. Reaction R3.26 is kinetically controlled and slower. That is, its reaction rate controls the reaction, not the temperature.
- **Stoichiometric condition**: The reactions R3.26 to R3.28 can be summarized in terms of stoichiometric ratios:

  $$CO + H_2O \rightleftarrows \mathrm{CO_2} + H_2 \tag{R3.29}$$

- **Fuel-lean conditions**: CO oxidation is not counteracted by H_2 oxidation under lean conditions. The reactions are as follows:

  $$CO + OH \rightleftarrows \mathrm{CO_2} + H \tag{R3.30}$$

  $$O_2 + H \rightleftarrows \mathrm{OH} + O \tag{R3.31}$$

  Here, due to the non-equilibrium of R3.30, relatively more H and OH are present. This slows down the CO reaction.

For liquid fuel combustion, both the air equivalence ratio and the mean droplet diameter have an effect on CO, as shown in Figure 3.6. It is evident that atomization quality, which has a positive correlation with fuel vaporization rates, has a significant effect on CO reduction at fuel-rich conditions. The effect of droplet size is less pronounced at fuel-lean conditions. This is mainly due to the reduced effect of evaporation rates at higher air equivalence ratios, where the combustion rate is more dependent on chemical reaction rates than fuel evaporation rates. [65]

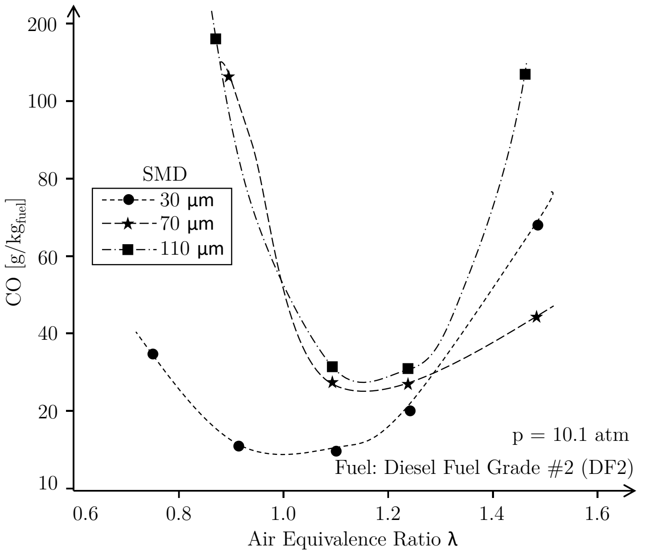

Figure 3.6: Effect of Mean Droplet Size and Air Equivalence Ratio on CO Emissions. Adapted from [65]

3.2.3 Unburned Hydrocarbons (UHC)

Another major pollutant in a GT combustion process is unburned hydrocarbons (UHC). Not only are they considered toxic, but they also form photochemical smog in combination with NO_x [65]. Unburned hydrocarbons are also associated with combustion inefficiency along with CO emissions. They are typically found as unburned fuel droplets or as the remains of thermal decomposition into lower molecular weight (volatile) species of the original fuel [1]. The chemical kinetics of UHC formation are more complex than that of CO. However, the main influencing factors are quite similar. [1]

The influence of air equivalence ratio and mean droplet size on UHC emissions is shown in Figure 3.7. Here, UHC emissions are significantly reduced by reducing the Sauter mean diameter, similar to the CO behavior. The main effect of average droplet size on emissions is its large influence on the volume of fuel vaporization. A significant portion of the total combustion volume is occupied by fuel vaporization at low power operation, where SMD increases. This is when CO and UHC emissions are at their highest concentrations. This results in less volume being available to react chemically. Under these conditions, any factor that affects the evaporation rate, such as fuel atomization and average droplet size, will directly affect the volume available for chemical reaction and, therefore, CO and UHC emissions. [65]

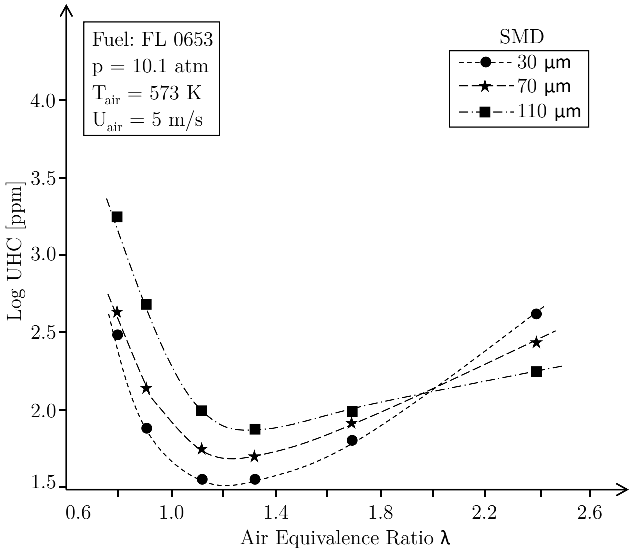

Figure 3.7: Effect of Mean Drop Size and Air Equivalence Ratio on UHC Emissions. Adapted from [65]

3.2.4 Soot Formation Mechanism

Hydrocarbon flames typically contain soot. It is formed on the fuel side of the reaction and progressively consumed (oxidized) as it flows into the rest of the flame. The soot may leave the flame area without oxidizing. This depends on some flame conditions, i.e., air inlet temperature, fuel spray characteristics, and combustion chamber pressure. The soot that leaves the flame is commonly referred to as smoke. [56]

The influence of fuel properties on soot formation can be divided into two parts. Firstly, the soot formation as a result of local fuel-rich regions and, secondly, by fuel chemical compositions, which are known to be soot formation precursors. The former is controlled rather by the physical properties of the fuel such as viscosity and volatility that have direct effect on mean droplet size, penetration depth and evaporation rate of the fuel, whereas the latter concerns the molecular structure of the fuel. The increasing tendency of the soot formation with decreasing hydrogen content is shown by Jones et al. [73]. However, the results from Naegeli et al. [74] show that fuels containing high concentration of polycyclic aromatics produced a higher amount of soot than it was predicted using correlation considering hydrogen content only. [75]

In the case of liquid fuels, the atomization behavior, and thus the mixture distribution in the soot formation zones, is influenced by several other mechanisms. In a GT combustor, the primary means of limiting soot formation is the reduction of local fuel-rich hot pockets. In addition, the effect of average droplet size on PM emissions is strongly influenced by the evaporation rate of individual droplets. The liquid fuel used in an aero GT combustor is typically multicomponent (e.g., Jet A-1). Each component has different physical and chemical properties. The chemical composition of a multicomponent fuel droplet changes through a simple batch distillation process as the evaporation process progresses. The volatile components of the fuel droplet evaporate first. This increases the concentration of the higher boiling components in the remaining liquid phase. As the larger droplets are exposed to heat during evaporation, their temperature rises, promoting the formation of carbon and soot in the center of the droplet. [65]

A study of the effect of fuel droplet size on exhaust soot was conducted by Rink and Lefebvre [76]. They used a tubular combustion chamber and kerosene fuel. Their results, which are shown in Figure 3.8, indicate that a reduction in the average drop size of the fuel leads to a reduction in the particulate matter in the exhaust gas. This is because smaller fuel droplets evaporate more quickly and burn more efficiently, resulting in less smoke and soot.

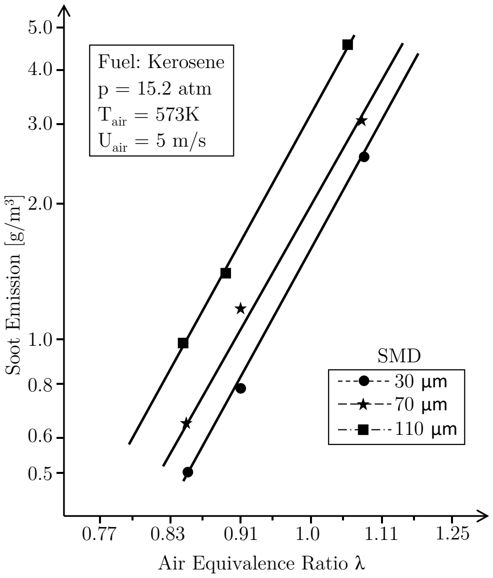

Figure 3.8: Influence of SMD of Kerosene. Adapted from [65,76]

As the size of the fuel droplets increases, there is less time for them to completely vaporize and mix with the air. Instead, they burn in what is known as a fuel-rich diffusion flame. Localized fuel-rich combustion is the primary cause of soot formation in the exhaust. Overall, as the average drop size of the fuel decreases, the amount of soot will decrease. However, soot output may actually increase if improved atomization results in reduced spray penetration, as seen with pressure atomizers. The cone angle of the fuel spray reduction, primarily by increasing the average size of the fuel droplets, can promote soot formation. [65]

3.3 Spray Atomization and Evaporation

In contrast to gaseous fuel injection, liquid fuel preparation tends to be more complex. The fuel must be atomized and vaporized. Sophisticated nozzles are required to inject liquid fuel into the combustor of a gas turbine engine. The fuel nozzles should also be designed to minimize coking or to prevent carbon buildup from impairing the function of the nozzle. These nozzles must be able to form a sufficient mixture that can be combusted. This section describes the process of liquid preparation in a combustion process using a fuel atomizer and the subsequent fuel evaporation.

3.3.1 Spray Atomization

Atomization refers to the process where a bulk volume of liquid fuel is broken down into smaller droplets. Fuels with higher viscosity generally result in larger droplet Sauter Mean Diameter (SMD), which can affect combustion performance. This is because higher viscosity fuels make it more challenging to overcome the liquid fuel's surface tension, which is essential for effective atomization. The principle of atomization involves applying sufficient disruptive forces to overcome the surface tension that holds the liquid together. The objective of atomization is to increase the surface area of the liquid fuel, thereby facilitating faster evaporation and promoting efficient mixing with air.

Some of the atomization techniques used to spray fuel are as follows:

- Air-blast atomization: This technique injects fuel into the combustion chamber with a stream of compressed air. The high velocity of the air causes the fuel to break up into small droplets.
- Pressure-swirl atomization: This technique injects fuel into the combustion chamber with a swirling motion.
- Pressure atomization (plain-orifice): Fuel is injected through a nozzle into the combustor at high pressure, accelerating it to high velocity. This interaction with air and instabilities from surface tension and aerodynamic forces breaks the fuel into small droplets.

Some of the most important aspects of the atomization process are mean drop diameter, droplet size distribution, drop penetration and spray angle [77]. In simple terms, the atomization process in a pressure swirl atomizer follows these steps (see Figure 3.9):

1. The fuel is pressurized and delivered into the atomizer. This high pressure provides the fuel with the energy needed to break into smaller fragments during the subsequent stages.
2. As the pressurized fuel exits the atomizer nozzle, it forms a thin, conical sheet. The swirling motion generated by the atomizer's design spreads the fuel into a thin film.
3. The fuel sheet becomes unstable and starts to break apart into elongated structures known as ligaments. These are thin, thread-like formations of fuel that are beginning to fragment.
4. The ligaments further break apart into individual droplets due to surface tension and aerodynamic forces. This step is essential in atomization, where the fuel is converted into a fine spray of small droplets.

5. The small droplets have a large surface area, which enables them to evaporate quickly when exposed to heat. This step is important for efficient combustion, as evaporated fuel mixes more readily with air.

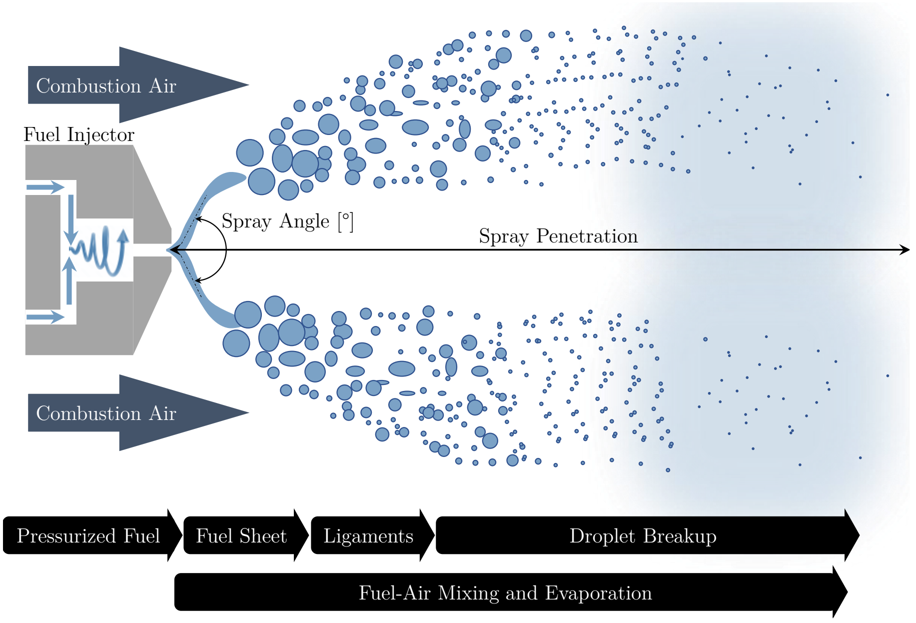

Figure 3.9: Schematic Illustration of Liquid Fuel Atomization and Evaporation Process

The outcome and quality of the atomization depends on the physical properties of the fuel, such as surface tension and viscosity. Fuel-air mixing, ignition rate and combustion performance can be greatly influenced by the injector and its atomization [78].

There is much research in the literature regarding the fundamentals of atomizing. From the mean droplet diameter, among other things, information about the spray quality can be extracted. The Sauter Mean drop Diameter (SMD) has a significant influence on the formation of major pollutants. This has been discussed previously (see sections 3.2.1 to 3.2.4). This characteristic droplet has the same volume to surface area ratio as the entire spray and is defined as [63]:

$$SMD = \sum_i^n \frac{D_i^3}{D_i^2} = d_{32} \tag{3.32}$$

Another characteristic that must be considered when evaluating the spray quality of an injector is the droplet size distribution. For example, to obtain information about the evaporation rate of the fuel, knowledge of the mean diameter size alone is not sufficient. The evaporation time of the spray for two spray distributions, both with a SMD of 50 µm but with different standard deviations, will not be the same.

Among the various atomization methods, such as air-blast, air-assist, and rotary, pressure atomizers are known for their simplicity and reliability, though their spray quality may vary depending on the design and operating conditions. In general, atomizers are required to deliver liquid fuels into the combustion chamber where they are properly mixed with the combustion air and ignited. To function properly, a fuel injector must have the following characteristics: [1]

- Ensure consistent and effective atomization across a wide range of operating conditions
- Provide rapid and precise adjustment to changes in mass flow rate
- Reduced instability
- Minimal required pressure or air flow
- Low cost, light weight and low maintenance
- Low sensitivity to blockage by contaminants and carbon deposits
- Uniform and symmetrical fuel distribution

The simplest pressure injectors are plain-orifice and simplex injectors (see Figure 3.10). In the case of the simplex injector, the primary design interest lies in the fuel sheet breakup, which leads to fuel dispersion and jet disintegration in the case of the plain-orifice injector.

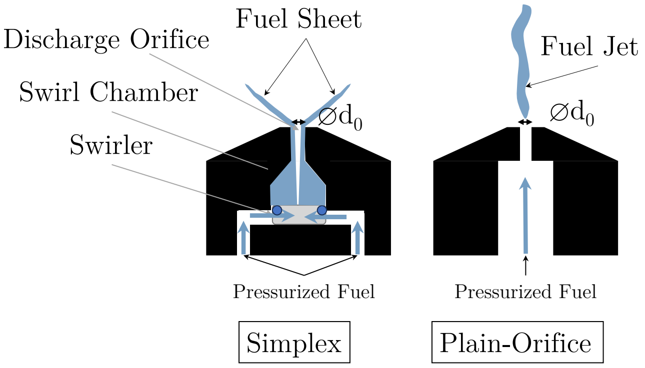

Figure 3.10: Schematics of Pressure Atomizers: Simplex and Plain-Orifice

The pressure-swirl atomizer (simplex) consists of a swirler, swirling chamber and orifice. Fuel passing through tangential slots on the nozzle swirler creates a conical sheet of the liquid fuel. This sheet of liquid expands radially as it exits the orifice (see Figure 3.10). A hollow, high-velocity and swirling sheet of liquid is the result. There are several correlations in the literature for the estimation of liquid sheet thickness. Many of these correlations are dependent on nozzle geometry. [77,79]

Plain-orifice atomizers use jet breakup of liquid fuel. Small disturbances cause the jet to break up into small droplets. As velocity increases, the relative motion between the jet surface and the surrounding air increases atomization quality [1,80].

In a study by Lorenzetto et al. [81] on the measurement of drop size of plain-jet air atomizers, the mean drop size increased with increasing viscosity and surface tension. Furthermore, their results showed that an increase in the density of the liquid results in a decrease in the mean drop size. Atomization quality is greatly affected by an increase in fuel pressure.

Spray angle is one of the most important factors in fuel atomization. It increases the interaction between the spray particles and the surrounding air or gas stream. The result is not only improved atomization, but also more effective mixing and heat transfer between the liquid and the air. Several studies on pressure-swirl atomizers have demonstrated the influence of nozzle geometry, fuel properties and air density on the spray cone angle [77]. The widest possible angle is advantageous for better spray quality (small droplet diameter). At the same time, attention must be paid to the surrounding combustor structure, which may be in contact with the spray liquid if the spray angle is wide.

Another important criterium for injectors is the depth of spray penetration. Spray penetration too deep will result in fuel contacting the combustor or combustion chamber walls, while penetration too short will result in inadequate mixing of the fuel with the air. Spray penetration is the maximum distance the spray will travel while atomizing. The depth of penetration is a function of the kinetic energy, the evaporation of the liquid fuel and the aerodynamic drag of the surrounding air. The droplet size, the movement of the surrounding air and gravity are the primary influences on the trajectories of the liquid fuel droplets as the droplets lose kinetic energy. For adequate mixing and evaporation rates, optimized atomization with a large spray cone angle is desirable. However, this results in low droplet penetration (decreased mixing quality) and possibly an increase of soot formation (see Section 3.2.4). This is because the spray encounters more resistance from the surrounding air. [82]

3.3.2 Spray Evaporation

Knowledge of the fuel droplet evaporation rate is critical to the design of a gas turbine combustor. Essentially, the droplet absorbs heat from the environment, which causes the liquid fuel to evaporate by diffusing the fuel vapor from the droplet surface into the ambient air. A residual droplet mass enters the reaction zone if the residence time of the droplet in the premixer is insufficient for complete vaporization. Unevaporated fuel droplets can form hot spots in the combustor, while burning at high temperatures near stoichiometric condition. These hot spots lead to high NO_x and if not evaporated completely, lead to increased CO and UHC levels.

In a Jet A-fueled gas turbine combustor, there are many complicated mechanisms surrounding vaporization and combustion of the liquid droplets. There are strong temperature and composition dependencies in many of the processes involved. Comparisons between different modeling techniques using various reference property schemes were performed by Hubbard et al. [83].

The physical properties of the liquid fuel are fundamental to its atomization, vaporization and mixing with the combustion air. Properties such as: [1]

- Density, which has an effect on the lower heating value in a fuel tank with a fixed volume.
- Vapor pressure, which determines the fuel partial pressure around the droplet of fuel at a given temperature. Rapid evaporation of fuel is possible at high vapor pressure.
- Distillation range, which is important because it affects how the fuel evaporates in the combustion chamber.
- Surface tension, which influences atomization and consequently on the evaporation rate of the liquid fuel. Lower surface tension leads to formation of smaller droplets.
- Viscosity, which varies at different fuel temperature. Atomization quality improves with lower viscosity. [1]
- Thermal conductivity, a measure of the fuel's ability to transfer heat from the hot ambient air to its core. This property also determines the rate of evaporation. Higher thermal conductivity leads to faster evaporation and improved fuel-air mixture.

Sahu et al. [84] experimentally investigated the interaction between fuel droplet dispersion and evaporation at ambient conditions. In their work, an acetone spray was used to investigate the correlation between the local vapor mass fraction and the droplet number density and velocity. For the acetone spray, the evaporation influence on the average droplet velocity was not significant. However, evaporation significantly reduced the SMD of the spray.

Another study by Pichard et al. [85], using n-heptane/air premixtures at ambient pressure and temperature, investigated the average droplet evaporation rates in partially vaporized turbulent spray flames. The effects of three main parameters were investigated: the equivalence ratio, the residence time of the droplets in the premixing channel, and the initial mean diameter of the droplets. The results showed that droplet diameter, spray turbulence intensity and droplet residence time in the premixer strongly influenced the average evaporation rate.

Spray Combustion requires understanding the multiple effects on droplet evaporation as it progresses through its lifetime to become gaseous. The droplet size, and jet co-flow velocity have a significant effect on the rate of liquid fuel evaporation. The auto-ignition delay time and consumption time were shown to be significantly affected by droplet size and jet velocity in a study by Abdelsamie et al. [86]. However, the effect of equivalence ratio was less pronounced. Evaporation, mixing and ignition were found to be significantly affected by high shear jets. Wolff et al. [87] studied autoignition-delay times of liquid fuel sprays in premixing ducts. They found that spray evaporation time significantly affects autoignition delay, especially in the negative temperature coefficient region. Smaller droplets and narrow size distributions improve the safety margin between autoignition and evaporation.

3.4 Liquid Fuel Coking

Combustion of liquid fuel presents a number of additional challenges, as discussed in Section 3.3.1. Essentially, the liquid fuel must be vaporized before it can react with the oxidizer. This is typically done with the help of an injector that creates a spray for better heat transfer between the fuel droplets and the surrounding hot combustion air.

It is common practice to moderately preheat fuel prior to injection to reduce fuel surface tension and viscosity. In gas turbine engines, the liquid fuel has become the primary heat sink for the waste heat produced by the aircraft and engine subsystems [88]. Improvements in fuel atomization and the combustion process result in higher fuel efficiency and lower emissions. Preheating of liquid fuel can result in the formation of carbonaceous particles, which can potentially lead to injector clogging/coking [89]. Coking is the build-up of hard carbon compounds in the fuel system when the fuel is heated to a temperature close to its saturation temperature in an oxygen-free environment. These compounds can have the effect of blocking or reducing the flow of fuel by adding additional pressure drop in the fuel line. [3]

Increased efforts are being invested to develop fuels that offer improved thermal stability, a property that decreases fuel system maintenance and fuel coking. In some conditions, the fuel is thermally stressed to temperatures above its thermal stability causing it to degrade and form varnishes, gums (oxidative instability products) and coke (thermal instability products.). Having a fuel injector coked, it can have fatal consequences (low frequency acoustic: rumble) and be very costly for the operation of a gas turbine engine. Other related issues can be increased difficulty in altitude relights, difficulty with cold starts and fuel control anomalies. [88]

Coke formation occurs when oxygen in fuel, either as a dissolved gas or in chemical forms, combines with hydrocarbons to form radicals. These radicals then bond together into larger molecules, usually composed of carbon, hydrogen, oxygen, sulfur and nitrogen. Certain aspects of the process are explained in references [90–92], although the exact process is not fully understood. Several factors, including temperature, pressure, velocity, composition, physical state of the fuel affect the rate of fuel decomposition and subsequent deposit formation. These variables affect the kinetics of the reaction as well as the diffusion, coagulation and decomposition processes. [93]

Coking of the fuel is generally undesirable because it can lead to reduced fuel delivery rate and component life, as well as undesirable fuel spray characteristics. But while developing the TAPS I combustor, GE discovered that carbon deposits on the pilot orifice outer wall actually increased lean-burn performance. This effect was called “good karma” or “good coke” [3,94]. This observation resulted in a patented design for the exterior of the pilot burner, aimed at replicating the benefits of carbon buildup. A detailed report can be found in [95]. Previous studies have examined Jet A thermal fuel reactions and found that temperature has a limiting effect on the rate of deposition, which peaks around 533–644 K [96].

In a study conducted by Szetela et al. [93] on liquid fuel evaporation, the composition of the deposit was analyzed using an electron microscope. It was found that the major elements were carbon and sulfur. Minor constituents were found to be iron, silicon, copper and oxygen. Deposit formation rates have been found to be increased by increasing the dissolved oxygen concentration in the fuel and by the presence of sulfur, nitrogen, and oxygen compounds. Deposit formation can also be affected by the chemical structure of the hydrocarbons, such as the presence of chain branching and alkyl substituents on the rings. Monocyclic hydrocarbons tend to behave better with respect to deposition. Experimental studies [97,98] have been conducted at elevated liquid fuel temperatures to find ways to mitigate the coking behavior of the liquid fuel.

The effect of wall material on deposition rates has been investigated in other studies [99–101]. In general, these studies have found that copper results in high deposition rates while aluminum, titanium and nickel result in lower deposition rates. In stainless steel, it is generally found that the rate of deposit formation is low, although there have been a few cases where higher rates have been observed. These discrepancies in published data suggest that the condition of the surface, including contamination and cleanliness, may need to be considered to obtain reliable data regarding the effect of wall material on scaling. Data from [102] showed that metallic contaminants in fuel such as copper, vanadium, cadmium, and lead can affect the thermal stability of fuel. In a fuel coking test, even a low concentration of 0.01 ppm of elemental copper significantly affected the results.

3.5 Superheated Injection (Flash Atomization)

It has been emphasized that the goal of fuel injection process is to improve a rapid mixing and evaporation of the liquid fuel in all of the dry low NO_x combustors presented in Section 2. This helps to eliminate hot spots in the reaction zone. The lean premixed prevaporized concept has shown the greatest potential in this regard. It provides a continuous homogeneous mixture of fuel and air to the combustor, allowing a very fuel-lean operating condition. The lack of carbon formation results in a reduction in soot emissions, which in turn greatly reduces radiation in the combustion chamber. This eliminates or reduces the need for wall cooling air, thus allowing more air to be supplied to the primary combustion zone for even fuel-leaner combustion.

As the flame temperature is kept below 1900 K, due to decreased reaction rate the effect of residence time on the NO_x formation decreases [1,103,104]. This is extremely important for the formation of CO and UHC. Both require longer residence times for their oxidation to CO_2. This means that the prevaporized and premixed combustors can be designed with a long residence time and still have a very low level of major emissions.

In reality, a very long residence time in the fuel-air premixing channel is required to achieve 100% pre-vaporization. This is a major challenge for the LPP concept. It is also susceptible to flashback, acoustic resonance, and autoignition at high air temperatures and pressures upstream of the flame.

Insufficient atomization and the resulting lack of proper vaporization of the liquid fuel can be mitigated by flash atomization. By heating the fuel close to its saturation temperature, a pressurized mixture of liquid and bubbles is created. By injecting the mixture into a lower pressure environment, the mixture undergoes expansion, resulting in a rapid disintegration of the liquid fuel bulk. Thus, very fine atomization and fast evaporation can be achieved [105]. Flash atomization can be used to produce a fine spray. The spray angle can be increased to reduce spray penetration. This can have a positive effect on fuel-air mixing, improving combustion efficiency and reducing pollutants [106].

In a study conducted by Rees et al. [107] on the velocity and diameter distribution of droplets in a flash atomization of liquid nitrogen jets, it was shown that the maximum of the vertical and horizontal velocity distributions occurred close to the exit of the injector. This was a result of high kinetic energy at the core of the liquid zone where internal energy is converted into kinetic energy during liquid expansion and evaporation. In addition, the spray pattern became more monodisperse with increasing axial distance from the injector. The mean droplet diameter distribution became more homogeneous.

One of the main causes of flash atomization is nucleate boiling. There are two main parameters to describe the level of superheat: [108]

$$\Delta T = T_{inj} - T_{sat}\,(p_\infty) \tag{3.33}$$

$$R_p = \frac{p_{sat}(T_{inj})}{p_\infty} \tag{3.34}$$

The first parameter, ΔT (Equation 3.33), describes the difference between the liquid temperature at the injector, T_{inj}, and the fuel saturation temperature, T_{sat}, at the corresponding back-pressure p_∞ (combustion chamber pressure). The saturation temperature T_{sat} of the fuel Jet A-1 used in the current study was calculated using the Antoine Equation 3.35 [109,110]:

$$T_{sat}\,[K] = \frac{4264.57763}{21.3176792 - \ln p_{sat}} + 43 \tag{3.35}$$

where, p_{sat} is the saturation pressure in [Pa].

The resulting T_{sat} at 1 atm (1.01325 bar) is 478.5 K (≈ 205°C).

The second parameter of the preheat level (Equation 3.34), R_p, is defined as the ratio between the saturation pressure at the fuel injection temperature and the corresponding back pressure. See Figure 3.11 for a graphical illustration of the described parameters using a p-T Diagram.

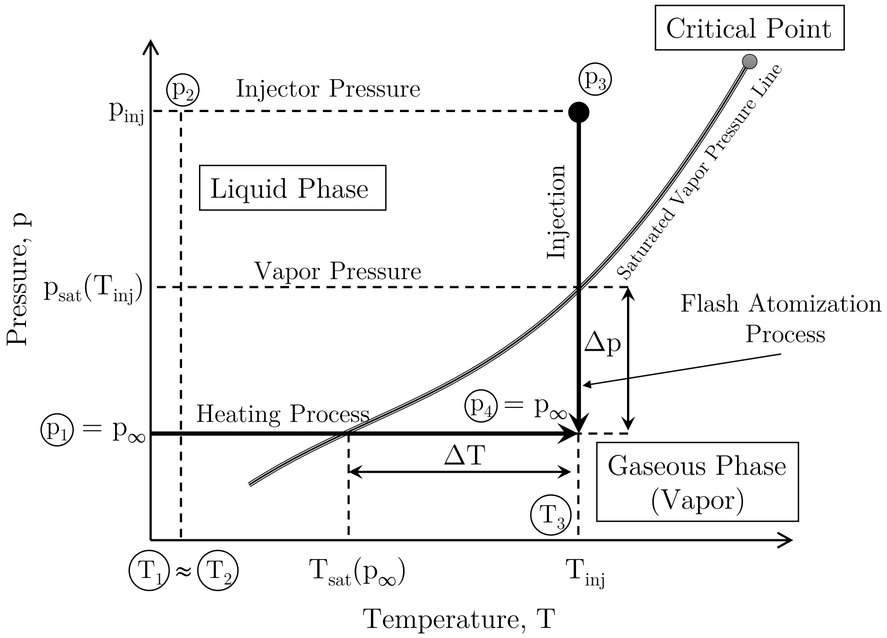

Figure 3.11: p-T Saturation Diagram for a Superheated Injection. Adapted from [106,108]

For this research, ΔT is primarily used to describe the level of superheat. This is because the back-pressure p_∞ is always 1 atm. For tests where the back-pressure is varied, the parameter R_p would be more useful.

The flash atomization process is described in the following steps (see Figure 3.11 and Figure 3.12 *a*): [111]

1 → 2: Liquid fuel is pumped by the liquid fuel supply system from p_1 and T_1 to pressure p_2 and T_2, whereas $T_1 \approx T_2$ and $p_2 > p_1$.

2 → 3: The fuel passes through a heat exchanger to increase its temperature to T_3. As the fuel heats up, its density decreases, which leads to higher pressure required to maintain a constant fuel mass flow rate $p_3 > p_2$. This increase in pressure is performed by the fuel pump.

3 → 4: The fuel reaches the injector (pressure-swirl or plain-orifice) while at p_3 and T_3. The kinetic energy (velocity) of the fuel is increased during the ejection from the nozzle as it expands from p_3 to p_4. At this point, p_3 is reduced to the surrounding (combustion chamber) pressure $p_4 = p_\infty$. Flash atomization occurs at the outlet of the nozzle when the pressure of the fuel drops below its saturation pressure p_{sat} but its temperature exceeds its saturation temperature Tsat. The difference between $T_{inj} = T_3$ and T_{sat} is then ΔT, the level of superheat.

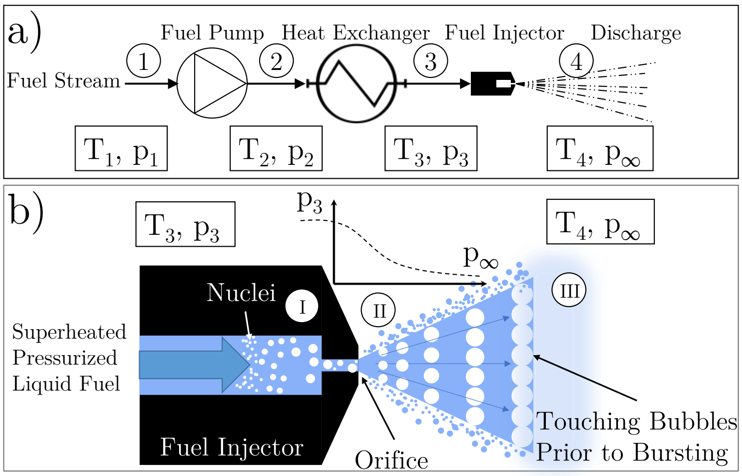

Figure 3.12: a) Schematic of the Flow Process, b) Illustration of the Physical Phenomena During a Flash Atomization. Adapted from [105,111]

The physical phenomena during a flash atomization is shown in Figure 3.12 *b*, where: I → II: As the static pressure of the fuel is reduced rapidly, but the temperature is close to its saturation temperature, very small bubbles (nucleation) are formed as the pressure drops below its saturation vapor point at fuel temperature.

II → III: The expansion of the bubbles continues as the mixture (bubbles and liquid fuel) exits the nozzle. The bubbles grow rapidly and will eventually touch each other. The bubbles burst at the interface between the liquid fuel and the surrounding environment. This results in rapid dispersion of the liquid fuel mass into fine droplets.

The superheated injection of liquid fuel is an approach that can reduce the required length and residence time for fuel evaporation within the premixing chamber. This method enhances the evaporation process, which helps to mitigate the risks of flashback and autoignition, thus improving the safety and efficiency of the combustion system. Increasing the fuel temperature can not only lead to NO reduction [112], it can also lead to flame length reduction. In a study conducted by Yin et al. [113] on superheated injection of liquid fuels, the effect of fuel temperature on spray behavior was characterized. It was shown that while the level of superheat effect (Equation 3.33) on the transition of spray morphology from mechanical breakup to superheated regime was minor, its significant effect on the jet-to-plume and fuel evaporation was quite visible. Although two different fuel injectors (pressure-swirl and plain-orifice) were used in their study, their liquid spray behaviors diminished at high levels of fuel preheat, which accounts for predominant thermal effect on spray morphology.

Wiest et al. [97] conducted experiments on a single can gas turbine combustor with Rolls-Royce 501K fuel injector at elevated liquid fuel (Jet A) temperatures. Here, a new fuel injector was designed that allowed for dual-phase fuel injection. The outcome of their analysis was improved evaporation and thus increased combustion efficiency as a result of heated liquid fuel. In contrast, at operating pressures lower than the Jet A vapor pressure, the combustion efficiency decreased due to changes in atomization and mixing from flashing. The increase in combustion efficiency was accompanied by reduction of CO and UHC, however, the NO_x levels were increased because of higher flame temperatures.

3.6 Steam Injection Mechanism

With the dry low NO_x techniques presented in Section 2, wet low NO_x offers similar benefits. Water or steam injection can be used either in addition to low-NO_x dry concepts to further reduce NO_x levels, or separately to minimize flame temperature and avoid thermal NO. The water-to-gas ratio (WGR: see Equation 3.36), previously used by [114,115], is a term used to quantify the amount of water or steam injected into the combustion zone:

$$WGR = \frac{\dot{m}_{water}}{\dot{m}_{water} + \dot{m}_{air}} \tag{3.36}$$

In terms of NO_x reduction, lowering the flame temperature can significantly reduce the rate of NO_x formation in the reaction zone, as shown in Section 3.2.1. Adding more air into the reaction zone will dilute the flame and lower the flame temperature, but it will also raise the velocity in the primary reaction zone, resulting in combustion performance issues. Water or steam injection, however, avoids the velocity profile alteration, which may negatively affect flame stability, while acting as a heat sink. [1]

A number of stationary gas turbines, such as the GE MS7001E [116], have adopted this concept. In a study by Kaiser et al. [117], a new concept for a water-enhanced turbofan (WET) for aviation is introduced. A comprehensive description of the WET configuration and cycle is provided in their work. In order to improve performance and emissions, the concept uses the injection of superheated steam into the combustor. In addition, a 13% improvement in engine specific fuel consumption could be achieved with the proposed cycle. The NO_x level is claimed to be reduced by as much as 90%.

The role of steam injection on the chemistry of hydrocarbon-oxygen mixtures was characterized in a study by Degges et al. [118] on the influence of steam on the flammability limits of premixed natural gas/oxygen and steam mixtures. The mixture with a higher adiabatic flame temperature was suppressed by the steam, where it lowered the reaction zone temperature. In the case of a premixed natural gas flame, the researchers found that water vapor, due to its high efficiency as a third collision partner, has an important influence on the chain ending reactions leading to the flammability limit. Depending on the water vapor content, either the physical effect (temperature reduction) or the chemical effect (support of the chain-terminating reactions) dominates.

Nonetheless, water injection into gas turbine combustors has practical limitations. For the additional thermal energy (fuel) required to heat the injected water, a penalty must be paid, if the waste heat of the exhaust gas is not used to vaporize the water. Reduced combustion performance due to water injection, increased levels of CO and UHC, in addition to increased thermo-acoustic risk, are some of the drawbacks. These problems have led to the development of dry low NO_x concepts as an alternative to water/steam injection.[65]

3.7 Axial Vane-Type Swirler

The swirling motion created by a radial or axial swirler plays an important role in the combustion process. Both are commonly used in gas turbines, where the latter has been widely used in dry low NO_x combustors. Experience has shown that flow fields of radial and axial swirlers are generally similar. At a high swirl number (S_N), the core of the flow expands and leads to the formation of a vortex breakdown. This improves the mixing between the fuel and the oxidant, thus increasing its combustion efficiency. The vortex breakdown further enhances the combustion process by acting as a flame stabilizer within the combustion chamber. Compared to non-swirling or free jets, swirling flows are known to improve mixing and propagation rates. [1,119]

The dimensionless parameter S_N describes the intensity of swirl in a combustor. It quantifies the ratio of the axial component of the angular momentum flow rate to the axial momentum flow rate [120]. Since the swirl number defines the swirling flow structure, it indicates to some extent the presence of a toroidal recirculation zone within the flow. The intensity of the swirl (weak or strong) depends heavily on the vane angle. Typically, swirl number less than 0.4 and greater than 0.6 are referred to as weak and strong swirl, respectively (see Figure 3.16 *b–d*). Like Reynolds number, the swirl number should be treated as a dimensionless parameter for comparing flows and is not to be added or subtracted [121].

The governing geometry based equation considers three main geometric properties: the hub diameter (D_{hub}), the swirler diameter (D_{SW}), and the vane angle θ [1]. Other parameters are vane thickness (*s*), height (*z*) and length (*c*) (see Figure 3.13). The geometric swirl number is defined as:

$$S_N = \frac{2}{3}\frac{1-(D_{hub}-D_{sw})^3}{1-(D_{hub}-D_{sw})^2}\tan\theta \qquad (3.37)$$

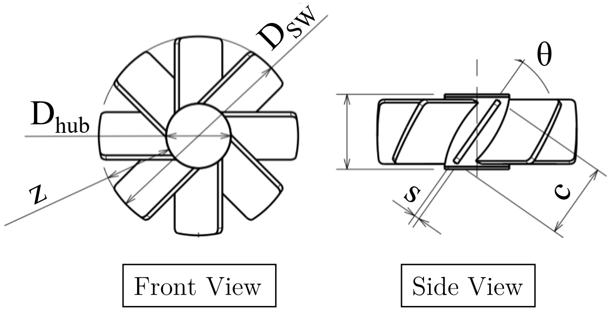

Figure 3.13: Front and Side Views of an Axial Vane-Type Swirler. Adapted from [122]

An important aspect of swirling flow fields is their ability to entrain the surrounding fuel-air mixture (see Figure 3.14). The swirl number and Reynolds number (Re) strongly influence the extent and intensity of entrainment of the hot exhaust gases. In swirling flows at high Reynolds numbers, large-scale periodic motion (helical vortex structure) can occur [123]. The motions lead to the formation of precessing vortex cores (PVC). These PVCs dominate the characteristics of a swirling flow [124].

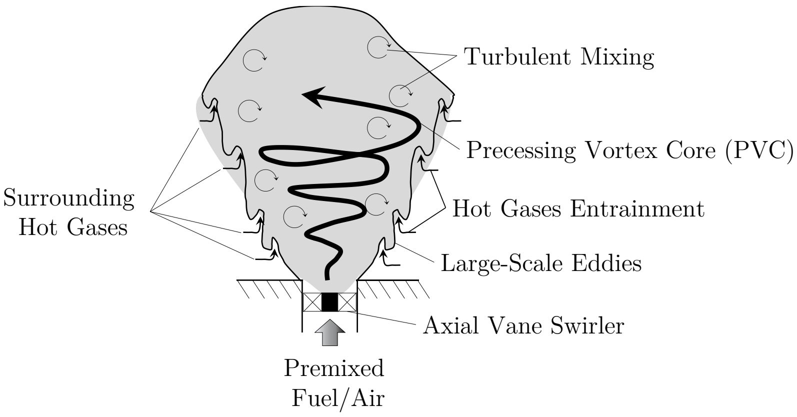

Figure 3.14: Schematic Overview of a Swirling Flow Field. Adapted from [125]

Qualitative flow characteristics for three different swirl numbers: 0, 0.6 and 1.87 at a constant Re = 20 500 are shown in Figure 3.15 *a–c*, respectively. It shows that increasing the S_N causes the cone angle to increase. It can be observed that as the S_N increases, the turbulent / non-turbulent boundary layer becomes more pronounced, with large scale protrusions in this region. These intense eddies lead to optimized mixing. They play an important role in the entrainment process and rate [126]. Furthermore, the figure shows that the large-scale eddy motion appears closer to the nozzle as the swirl number increases. [127]

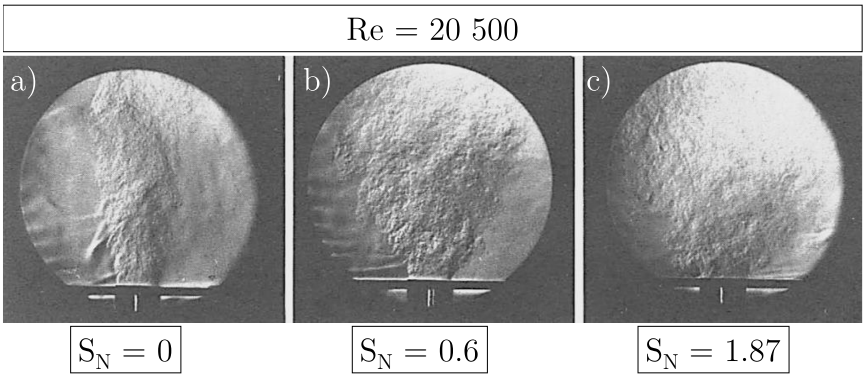

Figure 3.15: Schlieren Photographs of Swirling Jets. Adapted from [127]

The aerodynamic phenomena shown in Figure 3.15 *a–c* are shown schematically in Figure 3.16 *a*, *c* and *d* for a jet, a moderate and a strong swirl flow, respectively. The axial velocities of the various swirl intensities are shown. The vortex collapse that occurs as a result of a sufficiently high ratio of angular to axial velocity (swirl) can be seen in figures *b*, *c* and *d*. The relatively low velocity near the center axis in medium and strong swirl cases allow for stabilization of the flame, where the flow velocity and burning velocity of the fuel-air mixture are identical.

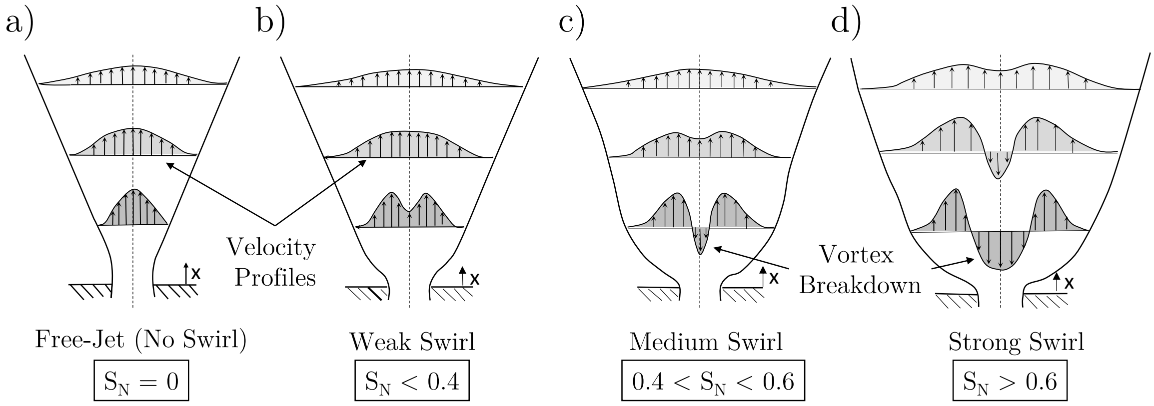

Figure 3.16: Axial Velocity Profiles for Free-Jet, Weak, Medium and Strong Swirl. Adapted from [128]

After a sudden expansion, the jet widens, causing the tangential velocity to decrease and the radial pressure gradient to decrease. This results in a negative axial pressure gradient close to the center and a reduction in axial velocity along the central axis. The reverse flow supplies hot gases and radicals that are needed for maintaining a stable flame. Due to the increasing jet angle and creation of a negative velocity in the axis center, the risk of flashback increases with increasing swirl number. [128]

3.8 Design of Experiments (DOE)

This section provides an overview of relevant concepts in experimental design. To this day, both classical and modern methods of DOE play a role in scientific experimentation. Classical methods are widely used and include Screening, Response Surface, Full and Fractional Factorial Designs. Modern methods, which are quite similar to classical designs, have been developed primarily to meet the special needs of some process developers who either have limited resources, restrictions on parameter variation, or simply do not require very high precision in prediction quality. These designs include Custom, Augment, Space Filling and Split-plot Designs.

There are a variety of designs that have been developed since the conception of DOE by R.A. Fisher [129]. The classical and modern designs use somewhat different approaches to how the design is created and analyzed. This is because the domains in which these designs are applied often have different characteristics. The classification of DOE methodologies is shown in Figure 3.17. For a comprehensive review of the following techniques, it is recommended to refer to Montgomery [130].

The definition of the denoted Classical Designs in Figure 3.17 are as follows [131]:

- **Screening Designs:** These designs are utilized at the beginning stages of the experiments, where a relatively large number of factors are suspected to have significant effect on the response.
- **Response Surface Designs:** The goal of response surface experiments is the determination of optimal values for a set of factors. They mathematically determine the maximum point (optimal response) on the surface using a curved surface model.
- **Full Factorial Designs:** All possible combinations of factor levels are run in a complete factorial experiment.
- **Fractional Factorial Designs:** A fraction of factorial design in which some factors are formed by interacting with other factors. Common use for screening designs.

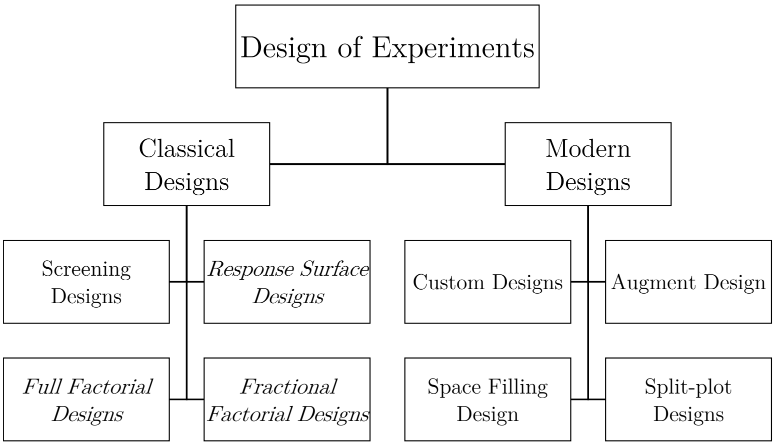

Figure 3.17: Classification of the Design of Experiments

Classical designs are defined as those techniques that have been established for decades. Although these designs are relatively simple and can be modeled and analyzed by any spreadsheet software, they offer extreme potential in terms of accuracy. These designs are primarily used to detect any factor effects or interaction effects between two or more factors (see Equation 3.38). Experiments with random error, relatively few factors, and few factor levels are among the types of experiments for which these methods are best suited. In addition, randomization, replication, and blocking are required for classical designs as they form the basis of the design. [131]

Randomizing is the most important principle in using statistical methods to design experiments. Statistical techniques assume the data (or errors) to be independently distributed random quantities. Randomizing usually allows this to become true. It helps to “average out” the effects of any non-essential factors that may be present. This is done by properly randomizing the experiment. [130]

Replication means an independent repetition of each factor combination. It is important because it allows the experimenter to obtain: [132]

- An estimate of the error of the experiment. This estimate of error becomes a basic unit of measurement for determining whether observed differences in the data are statistically different.
- A more accurate estimate of the factor effect if it is used to estimate the response for one of the factor levels in the experiment.

Blocking of an experiment is the division of the experimental units into similar groups (blocks). It is a method of controlling and compensating for the variability of the experimental unit. [133]

The more advanced Modern Designs are defined as follows: [134,135]

- **Custom Designs:** Customized and cost-effective experimental designs to address a wide range of objectives. It offers different design types. Even when standard designs do not fit, it can be tailored to fit their specific experimental situation.
- **Augment Design:** A design that can add more runs to its experiment and optimize the design for optimal results. It allows for the addition of new runs to take advantage of historical data or for the collection of more information.
- **Space Filling Design:** Alternative designs for deterministic experiments, such as computer simulations, are often used when standard experimental designs are not appropriate. These designs are used primarily when factors or conditions cannot be easily randomized or manipulated.
- **Split-plot Designs:** Certain factors are easier to vary than others in some experiments. While fully randomizing designs with easy-to-change factors is possible, experiments with hard-to-change factors are limited in their ability to randomize. This is where split-plot designs provide a great deal of flexibility in terms of randomization-restricted designs.

Regarding the current work, the procedure, in which the design factors were used in a design is described in Section 4.2.

3.9 Multivariate Data Analysis

As shown in Figure 4.4, more than two variables are involved in exerting their influence on the defined responses, such as NO_x, CO, etc. The basics of multivariate analysis, which has been used extensively in this thesis, are outlined in this section.

Multivariate data analysis is the analysis of multiple variables at the same time, rather than just one variable (univariate) or two variables (bivariate). This allows for a more complete understanding of how multiple variables relate and interact and how they affect the response variable. To uncover patterns, relationships, and trends in complex data sets, multivariate analysis techniques are often used [136].

In some situations, the term “multivariate” is used for problems where the assumption is that all variables have a multivariate normal distribution. However, for a study to be truly multivariate, all the variables must be random and must be related to each other in such a way that their individual effects cannot be interpreted in a meaningful way separately. This means that in order to understand the overall phenomena, it is essential to understand the relationships and interactions between the factors (variables).

Research results can be significantly affected by measurement error and poor reliability. Their effects are not immediately apparent; however, they are hidden in the observed variables. The aim of a researcher is to make his measurements more reliable and valid. Using multivariate analysis allow for a more accurate representation of the variables. While it is not always possible to attribute poor results solely to measurement error, it is certain that the presence of measurement error will distort the relationships that are observed and weaken the effectiveness of multivariate techniques. [137]

Often the relationship between the design factors and the response is not straightforward. This requires a more complex assessment of the existing behavior between the factors. For example, to account for possible nonlinearity in the factor-response function, a quadratic regression model can be used, which is shown in Equation 3.40 [130]:

$$y = \underbrace{\beta_0}_{interception} + \underbrace{\sum_{j=1}^{k} \beta_j \, x_j}_{main\,effects} + \underbrace{\sum \sum_{i<j} \beta_{ij} \, x_i \, x_j}_{factor\ interaction} + \underbrace{\sum_{j=1}^{k} \beta_{jj} \, {x_j}^2}_{second\ order} + \underbrace{\varepsilon}_{\text{random error}} \tag{3.38}$$

The β_0 is the grand average of all the effects (interception). The variables are x_i and x_j. The β_i are unknown coefficients for the linear term that will be calculated through the data in the experiment. The β_{ij} refers to the unknown coefficients for the factor interaction term of the equation. The β_{jj} refers to pure second-order or quadratic effects with *k*-many factors that are considered. The term ε represents a random error constant that accounts for the experimental error in the studied system [138]. These models are characterized as second–order response surface models (RSM).

4 Experimental Setup and Operating Condition

This section provides a detailed description of the experimental setup employed for characterizing the swirl-assisted jet-stabilized combustor. A comprehensive exploration of the combustor's design presented, highlighting the influence of key design and operational parameters.

4.1 Experimental Setup

The developed combustor investigated in the atmospheric test is a single-nozzle swirl-assisted jet-stabilized liquid fuel combustor with a concentric simplex pressure-swirl atomizer. To evaluate the effect of superheated injection of the liquid fuel Jet A-1 Ref. 3 (see Appendix C for fuel properties) on the combustion behavior, a modified liquid fuel combustor from a previous research [139] was used for a first experimental study with superheated fuel injection.

In this regard, a number of important combustor design parameters were selected and varied to investigate their contribution to combustion characteristics and to find an improved range of flame stability and exhaust gas emissions (see Section 4.2.1).

As shown in Figure 4.1 *a*, preheated jet A-1 ① is injected into the premix channel at various temperatures using a pressure-swirl atomizer ④. The premix channel consists of a prefilmer ⑤ and an axial vane swirler ⑥. The prefilmer is a simple DN40 pipe with a wall thickness of 0.75 mm and a length of 60 mm. The swirler consisted of eight each 1 mm thick straight stainless-steel vanes that were welded to a 12 mm pipe (swirler hub). Both ends of the hub were covered to prevent fuel and air passing through. The prefilmer and the swirler contribute significantly to improved atomization / vaporization of the liquid fuel. The preheated air ② is then partially mixed with sprayed or vaporized fuel before and after the swirler prior to exiting the air nozzle ⑦ into the quartz glass combustion chamber ⑧. For specific information on the geometry and dimensions of the combustor, refer to Appendix Figure E.1.

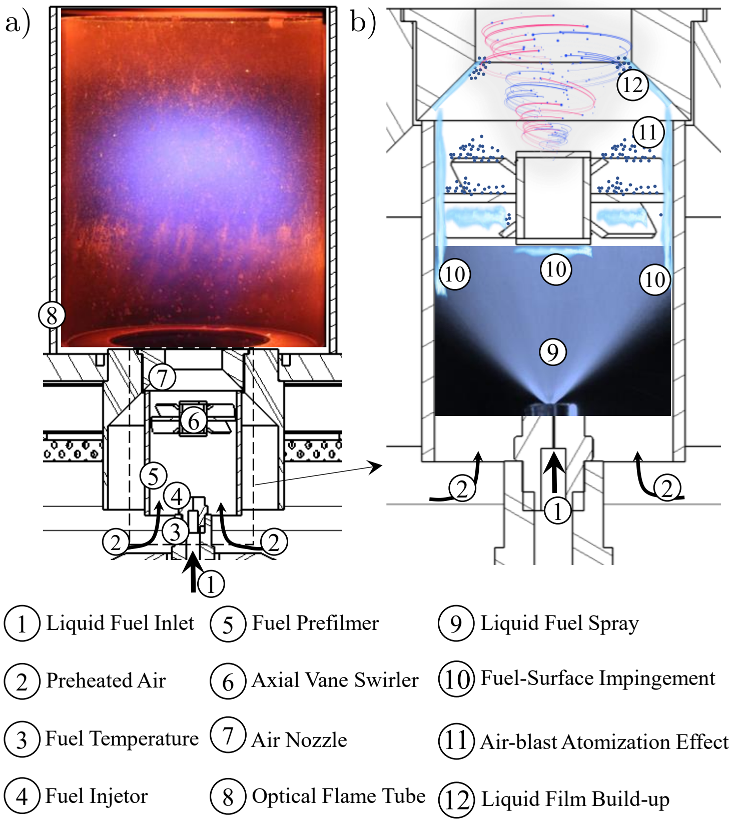

Figure 4.1: a) Sectional View of the Liquid Fuel Combustor Detailing Its Main Components, b) Schematic Illustration of the Combustor Core Components. Adapted from [122]

Figure 4.1 *b* shows a magnified view of the combustor core components where, in the case of spray injection of liquid fuel with the pressure-swirl atomizer, the swirler helps to form a thin film of fuel on ins vane surfaces which leads to secondary atomization (air blast effect) due to the high jet velocities downstream of the flow. The prefilmer, on the other hand, enhances the vaporization of the liquid fuel by creating a fine liquid film on its surface. This increases the residence time of the fuel on hot surfaces and maximizes conductive and convective heat transfer into the fuel. In addition, both prefilmer and swirler prevent most of the fuel from excessive accumulation on the inner wall of the air nozzle and provide optimized mixing through swirling and high-velocity jet. Without these components, spraying directly onto the inner walls of the air nozzle would result in fluid build-up and large droplets at the nozzle exit rim. In the case of superheated fuel injection, the swirler has two main functions: (1) to slow down the superheated fuel vapor using its hub, especially near to the central axis and (2) to improve the air-fuel mixture after the rapid expansion of the fuel as it transitions from the superheated liquid phase to the gaseous phase in the mixing channel.

A sectional view of the combustor operated in this study is shown in Figure 4.2. Here, preheated air enters a toroidal plenum where it is evenly distributed before entering the combustor. The redirection of air due to the toroidal plenum resembles the air flow path in a can combustor of micro GT. Four thermocouples (type N), distributed circumferentially, are installed in the plenum to measure an average temperature of the incoming combustion air. Concentric to the combustor outlet, liquid fuel is injected using a simplex pressure-swirl atomizer (see section 4.3.4). To measure the fuel temperature prior to injection, a type N thermocouple is mounted on the fuel lance.

To measure the static pressure, a pressure measurement was made inside the plenum through a 1 mm hole. At the other end of the hole, a NetScanner™ Model 9116 with an accuracy of ±4 mbar (manufactured by Pressure Systems, VA) was used to measure the variations in pressure caused by a variety of operating conditions and geometric variations. It is common to measure total pressure when measuring pressure drop in a combustion chamber. Total pressure includes both static and dynamic pressure, and thus more accurately represents the total pressure in the combustion chamber. However, due to the difficulty in accurately reading the total pressure (e.g. flow velocity) in the congested plenum, the static pressure loss is measured with the understanding that the accuracy of the measurement will be reduced.

The pressure drop across the combustor is calculated using the static pressure in Equation 4.1:

$$\Delta p\ [\%] = \frac{p_{plenum} - p_{atm}}{p_{plenum}} \cdot 100\ \% \tag{4.1}$$

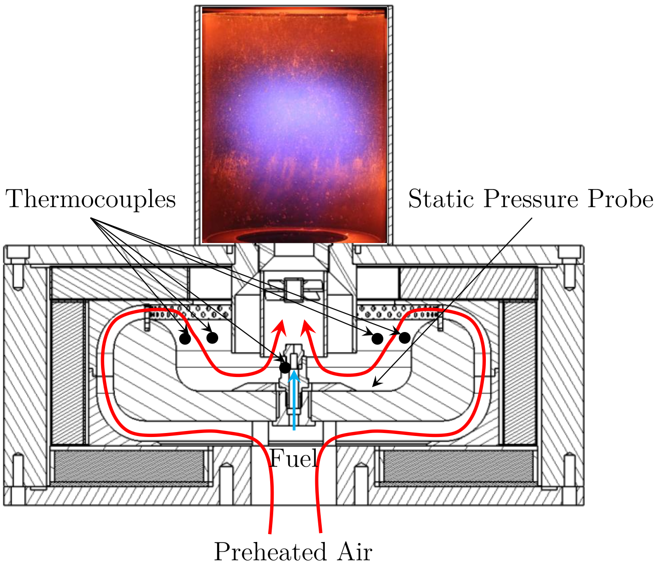

Figure 4.2: Sectional View of the Single Nozzle Combustor with Temperature and Pressure Measurements [140]

The data are recorded at a sampling rate of 1 Hz by a number of different modules from the Delphin Technology AG. Mass flow controllers (MFC) (manufactured by Bronkhorst, Ruurlo, the Netherlands) with accuracies of ±0.1%, ±0.2%, and ±0.2% of full scale were used to control combustion air, water, and liquid fuel flows, respectively. Fuel and water pressures were measured with a transducer manufactured by OMEGA, Bridgeport, NJ, with an accuracy of ±2.5% of full scale (±0.85 bar). All built-in temperature sensors were Type N, Class 1, manufactured by TC Mess- und Regeltechnik GmbH, Mönchengladbach, Germany, with an accuracy of ±1.5 K up to

375°C and ±0.4 % · |T| from 375 – 1000°C. A complete verification of the operating range of the instrumentation, including its accuracy, is given in Appendix D.

4.1.1 Atmospheric Test Rig

The test facilities of the DLR Institute of Combustion Technology were used for the experimental investigation of the developed combustor.

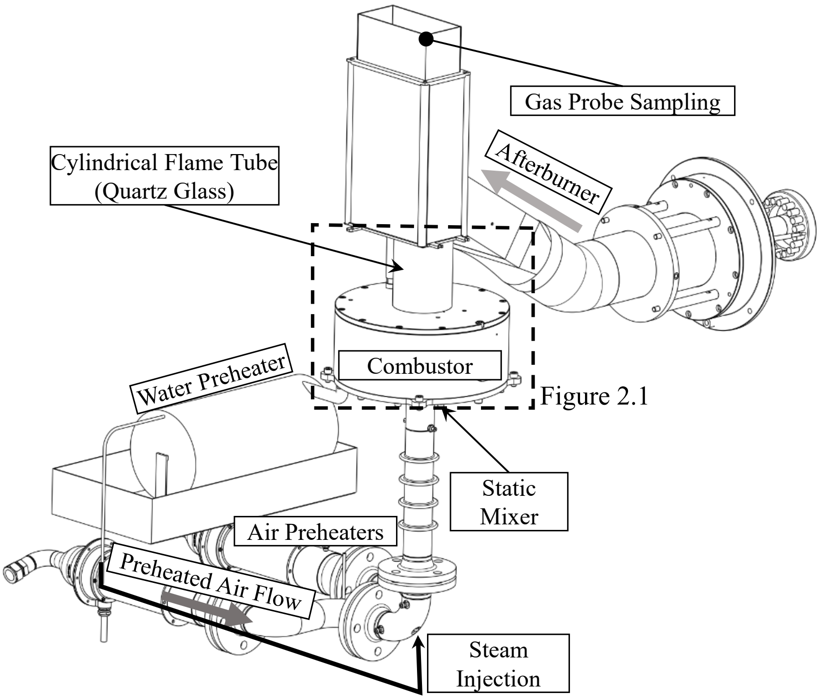

Figure 4.3: Schematic of the Experimental Setup: Test Rig and its Peripheral Equipment. Adapted from [140]

The general test setup is shown in Figure 4.3. The air was preheated by two electric heaters (each 15 kW_{el}) and passed through a T-junction to the liquid fuel combustor. The temperature of the preheated air was in the range of 155–255°C. Another electric heater (3.6 kW_{el}) preheated the fuel after it passed through a mass flow controller (Cori-Flow, manufactured by Bronkhorst, Ruurlo, the Netherlands). The fuel was fed to the plenum, where the fuel lance and injector were located, through a 3 mm tube. Approximately 1000 mm upstream of the combustor inlet, steam could be injected into the air. To improve the mixing quality of air and steam, a static mixer was installed at the plenum inlet.

Prior to ignition, combustor flameout and for the non-reactive tests, a natural gas-fired afterburner was used to combust the unburned liquid fuel. The hot (up to 900°C) exhaust gas from the natural gas burner was channeled into the combustion chamber above the quartz glass flame tube of the liquid fuel flame. The afterburner was off during all measurements of lean blowout, emissions, and OH*-CL. Concentric to the flame tube, a sample of the exhaust gas 566 mm downstream of the front plate of the combustor at a rate of 47.5 liters per minute (see Section 5.3 and Figure 5.8.)

4.2 Designing and Analysis of Experiments

The development and characterization of the combustor is carried out in an experiment that analyzes the effect of six design parameters (see Table 4.1). This experiment uses a custom design in combination with a split-plot design (see Section 3.8). This modern approach allows for a more efficient experiment, i.e., a good estimate of the factor and interaction effects with a fraction of the runs compared to a full factorial design.

4.2.1 Design Space Definition

Previous knowledge combined with a series of screening tests were used to define the boundaries of the current experiments. For the characterization of the flame, four responses were selected to indicate the combustion performance. These responses are NO_x, CO, flame height above burner (HAB) and flame length (FL). Six combustor design parameters were varied to obtain the largest changes in these responses. These factors are the combustion air temperature (T_{air}), superheat level of the fuel (ΔT) (see Section 3.5), axial vane swirl number (S_N) (see Section 4.3.3), flame tube diameter (D_{FT}) (see Section 4.3.1), thermal power (P_{th}) and finally the adiabatic flame temperature (T_{ad}) (see Table 4.1 for an overview of all the design parameters). For the present study, the use of the equivalence ratio is purposely disregarded and replaced by the adiabatic flame temperature. The adiabatic flame temperature considers the effect of several design parameters, such as T_{air} and ΔT, as well as fuel and air mass flow rates.

A subsequent and detailed characterization campaign was carried out to examine the effects of key parameters on combustion performance. The study included analyzing jet velocity, evaluating the performance of different fuel injector designs, testing various fuel types, and assessing the impact of fuel-air mixture dilution through steam injection. This approach provided insights into the system's behavior and the interactions that govern it (see Figure 4.4).

For the experiments described in Section 6.4.5 with different liquid fuels, it was necessary to use adiabatic flame temperature for comparing their combustion performance. This was due to the different chemical composition of the fuels. The results would have been misinterpreted if the air equivalence ratio had been used to compare the effects.

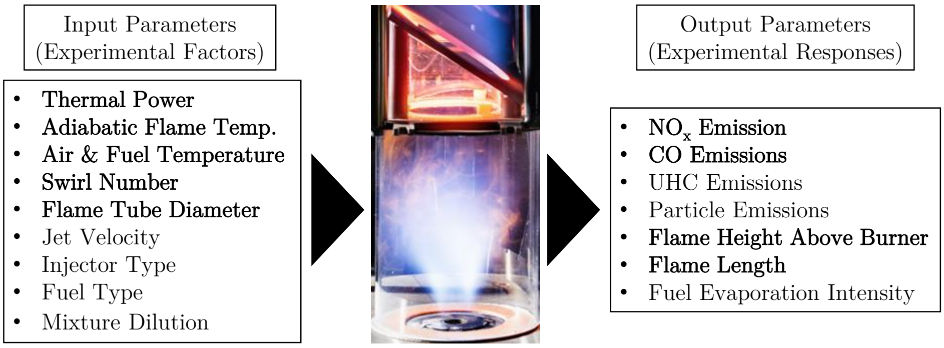

Figure 4.4: An Overview of the Experimental Factors and Responses of a Combustion Process

The air temperature range of 155, 205, and 255°C was chosen since they resemble the air temperature prior to the combustor of the M250 turboshaft helicopter engine [141] that are currently being tested at the DLR Institute of Combustion Technology. Based on a series of non-reactive tests [142], a range of level of superheat ΔT (-50, 0 and +50 K) was chosen as it includes liquid, saturated and superheated fuel conditions. This allows a deeper analysis of the ΔT effect on combustion behavior.

Table 4.1:Overview of the Studied Design Parameters and their Ranges

Factors	Unit	Lower level	Baseline	Higher Level	Factor Type
T_{air}	[°C]	155	205	255	HTC
ΔT	[K]	-50	0	50	HTC
S_N	[-]	0.5	0.6	0.7	HTC
D_{FT}	[mm]	80	95	120	HTC
P_{th}	[kW]	15	22.5	30	ETC
T_{ad}	[K]	1750	1900	2050	ETC

HTC: Hard-to-Change Factor, *ETC*: Easy-to-Change Factor

The axial swirl was intended to improve mixing, slow down the superheated fuel flow and optimize atomization, but not to create a strong toroidal recirculation zone inside the flame tube. Therefore, rather weak, moderate, and strong swirl were chosen, ranging from $S_N = 0.5$, 0.6, and 0.7, respectively. The flame tube diameter range of ⌀80, ⌀95, and ⌀120 mm was selected based on preliminary experiments that had resulted in a change in combustion performance. The thermal power range of 15, 22.5 and 30 kW was chosen due to infrastructure limitations of the test rig and laboratory. Finally, the adiabatic flame temperatures of 1750, 1900, and 2050 K were defined, which is similar to typical flame operating conditions in a GT combustor. For the consistency of the tests, the air nozzle diameter $D_{AN} = 25.2$ mm is kept constant throughout the preliminary characterization of the combustor design parameters.

4.2.2 Designing the Experiments

The current research uses the Design of Experiments (DOE) method to evaluate the effect of design parameters (also referred to as factors) on key performance indicators (also referred to as responses) of the combustor. In addition, statistical software (JMP 17, a subsidiary of SAS Institute, Cary, NC) was used to create multivariate models for each of the responses that best described the multidimensional data. The goal was to detect and estimate uncorrelated factor effects. Using the DOE, this was accomplished by creating a custom experimental design that allowed for a high degree of design orthogonality, i.e., the estimation of uncorrelated factor effects. By determining the factor effect estimates, statistical models are derived that can be used as a design tool for combustion system development.

When certain factors in an experiment are difficult or expensive to vary from run to run, split-plot designs are used. These factors are held constant across groups of runs. As a result, they are assigned to groups of units rather than randomly. The design and analysis of the experiment must account for this limitation of randomization. In a split-plot design, the design parameters (factors) (see Table 4.1) are divided into two types, Hard-to-Change (HTC) and Easy-to-Change (ETC) factors. The HTC factors can remain constant in an experiment, while the ETC factors are randomly varied throughout the experiments. The disadvantage of using HTC factors in an experimental design is that the prediction accuracy of these factors is significantly reduced due to the limited number of times in which they are varied. However, reasonable prediction accuracy can be achieved by increasing the number of times the HTC factors are varied.

In order to run a full factorial design using six factors each at three levels, it would require 729 test runs. Utilization of a custom design allows for systematically skipping few factors in the design space. It is not limited to testing all possible combinations of factor levels, and the selection of factor combinations is based on the specific objectives of the research. Custom designs are frequently employed where certain factors are uninteresting, or where practical constraints limit number of experiments. Customized experimental designs can optimize the experimental design for maximum information gain, taking into account statistical and practical considerations.

For the current study, the custom design reduced the number of test runs to 264. This contained 22 grouped experimental designs (whole plots WP) each consisting of 12 randomly varied operating points (subplots SP). A whole plot is an experimental design that contains two categories of factors: fixed factors that are held constant and changing factors that are randomly varied. The number of whole plots is positively correlated with the prediction accuracy of the hard-to-change (T_{air}, ΔT, S_N and D_{FT}) factors.

Figure 4.5 *a* shows an example of 9 groups of operating points (whole plots). In each whole plot, ΔT and D_{FT} are held constant while P_{th} and T_{ad} are randomly varied 12 times (12 subplots). Some of the design points are tested only once. Others are varied two or even three times to obtain an estimate of the experimental error. Figure 4.5 *b* shows another 9 whole plots. In each whole plot, T_{air} and S_N are kept constant and P_{th} and T_{ad} are varied randomly 12 times.

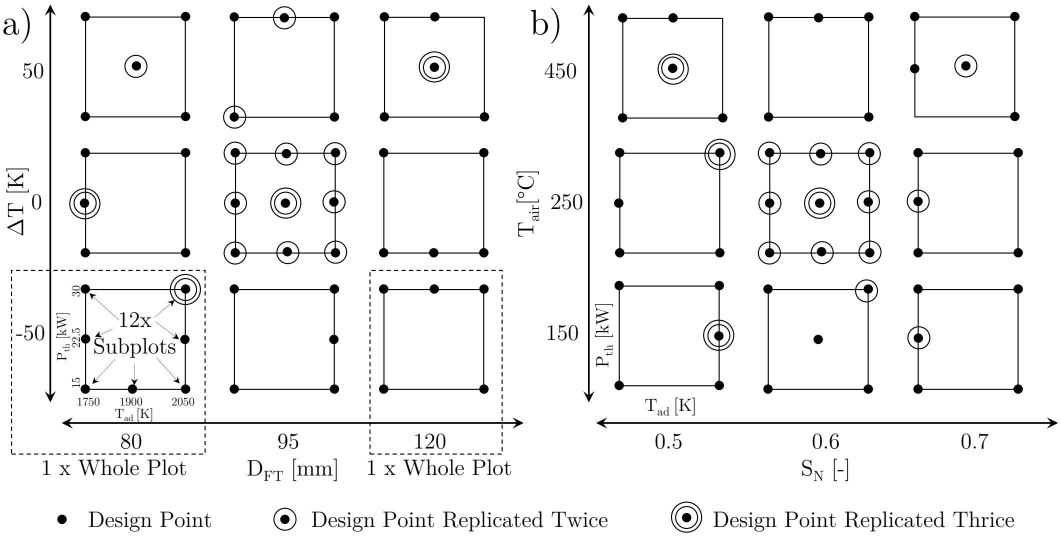

Figure 4.5: Graphical Representation of the Subplots (P_{th} x T_{ad}) within, a) ΔT x D_{FT} Whole Plots and b) T_{air} x S_N Whole Plots

Power analysis evaluates the ability of the current design to detect potential effects. It is the probability of detecting a factor effect in an experiment. The likelihood of detecting a significant effect is increased with higher power. Table 4.2 shows the power of estimation for a selected number of model terms. It is evident that, due to the randomization restriction imposed by the split-plot design on the HTC factors, the power of estimation for these factors is slightly lower than for the ETC factors.

Power can help determine whether additional runs are needed and is affected by the number of runs, significance level, and estimated error variation. The significance level (α) for the current analysis was set at 0.05 meaning there is 5% chance of failing to detect a significant factor effect, if there is one. The power of the design, i.e., the prediction accuracy, is affected by both the number of test runs and the significance level. Prediction accuracy increases with increasing significance level and number of runs. The estimated error variation is a measurement of the precision desired by the experimenter a design should deliver. For the current work, a desired precision (σ: standard deviation) of ±1 ppm for NO_x and CO was considered. The precision level of ±1 ppm was required because the majority of the design space was expected to have NO_x and CO levels of less than 10 ppm.

Table 4.2: Power Analysis for the Current Design for $\alpha = 0.05$ and $\sigma = 1$

Model Term	T_{air}	ΔT	S_N	D_{FT}	P_{th}	T_{ad}
Power	0.95	0.99	0.91	0.99	1.0	1.0
Factor Type	HTC	HTC	HTC	HTC	ETC	ETC

4.2.3 Model Validation and Test

An additional 58 operating points were performed for validation and testing purposes in addition to the 264 test runs generated by the design. As a result, the number of experimental points is increased to a total of 322 test runs.

Models based on multiple factors can easily be subject to overfitting. One way to prevent model overfitting is to test the model on data points that were not used to train the model. For this purpose, the random holdback method is used to fit, validate, and test the models. The data obtained from the combustion experiments were divided into 3 separate parts: training, validation and test sets, each containing 70, 15 and 15% of the total operating points, respectively.

Each of the models was fitted using the training data set. The validation dataset was used to determine if the model contained too much noise or if more complexity could be added to describe additional variation, as there is a variety of modeling types/techniques with varying degrees of complexity, such as factorial, response surface, partial cubic, neural network, etc. If the models perform adequately on the validation dataset and enough terms had been added, these models are reformed to accommodate both the training and validation datasets. The test dataset is then used to select an appropriate model by evaluating the model prediction independently of the training and validation sets.

The Actual by Predicted plot helps to visually assess the accuracy and fit of the regression model (see Figure 4.6 *a*–c). It is a graphical tool used to assess how well a regression model fits. It allows to compare the actual observations of the response variable with the predictions of the model. The graph plots the observed values on the y-axis. The predicted values are plotted on the x-axis. Each data point represents one observation in the data set. The model predictions align closely with the observed data, as indicated by the points being near the diagonal line ($y = x$). An optimal fit is shown by the points being evenly and randomly distributed around this diagonal, suggesting that the model accurately represents the underlying patterns in the data with minimal bias or systematic error.

For the characterized responses in this study, four different models were fitted, which provided quite reasonable model statistics. As shown in Table 4.3, the total variation explained by the models (R^2) is greater than 0.75, except for the fitted CO model, which could be due to its complex behavior in the experimental design space. However, as long as the model estimation against the test data set is acceptable, the R^2 value plays a minor role.

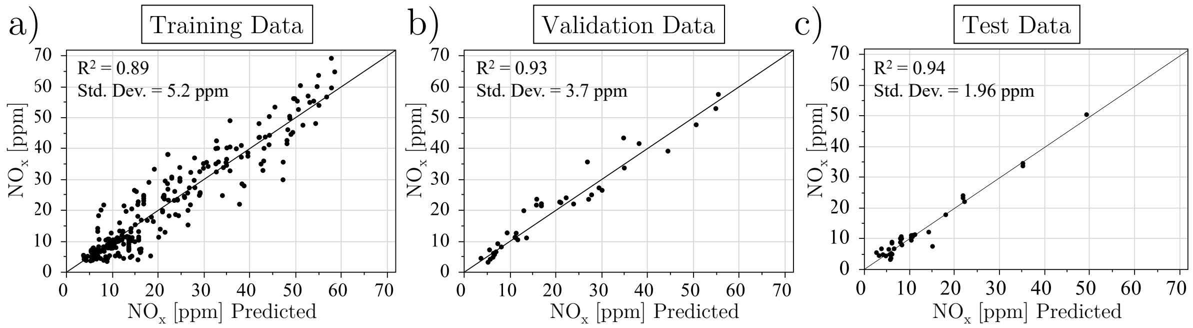

Figure 4.6: NO_x Actual by Predicted Plots for a) Training, b) Validation and c) Test Data

Other important statistics shown in Table 4.3 are the residual mean and the standard deviation, which explain the accuracy of the model in predicting the test data set. For the emission concentrations NO_x and CO, the residual means of the selected model are less than ± 0.5 ppm with a residual standard deviation of less than ±3 ppm, indicating acceptable accuracy of the fitted models. For the fitted models of the flame geometry parameters, HAB and FL, the corresponding model residual means are less than ±1.5 mm and their residual standard deviations are approximately ±5.5 mm.

The bimodal flame behavior (refer to the Section 6.2 for more information on this topic and the measures that were taken to resolve this flame behavior), which significantly distorted both the flame geometry and the emissions, is partly responsible for the relatively high standard deviation of ±5.5 mm. Only flame mode A was considered for data analysis. However, some of the flames could not be visually distinguished.

Table 4.3: Model Statistics for each Response Based on Test Dataset

Response	R^2	Residual Mean	Residual Std Dev
NO_x	0.94	0.15 ppm	1.96 ppm
CO	0.55	- 0.14 ppm	2.41 ppm
HAB	0.88	0.66 mm	5.57 mm
FL	0.76	1.25 mm	5.34 mm

Overall, the model statistics of HAB and FL also show acceptable results. For ease of understanding, the predictions of each model will be referred to simply by their designated names (NO_x, CO, FL and HAB), and the term “fit” will not be used.

4.3 Geometric Parameter Variation

The effects of various geometric design parameters on the swirl-assisted jet-stabilized combustor were investigated. The combustor was operated under superheated and spray atomization regimes. A series of flame tubes and air nozzles with different diameters and axial swirlers with different swirl numbers were taken into consideration. A cross-sectional view of the combustor with dimensions is given in Appendix Figure E.1.

4.3.1 Flame Tube

The current swirl-assisted jet-stabilized combustor relies to a large extent on recirculation zones for its flame stabilization. These recirculation zones are created by the sudden expansion of the area between the inlet port (air nozzle) and the combustion chamber (flame tube). The Figure 4.7 shows cross-sectional views of the combustor illustrating the dump area ratios, 3.17, 3.77 and 4.77 for D = 80 mm (D80), D = 95 mm (D95) and D = 120 mm (D120) flame tubes, respectively. These ratios lead to an area reduction of the flame tubes from D95 to D80 of 41% and an area increase of 37% for D95 to D120. It is expected that the combustion performance including emissions and flame operating range is influenced by the dump area ratio variation. In these tests, the bulk velocity in the air nozzle is held constant and only the volume available to the air-fuel mixture in the flame tube is varied. For the baseline condition, the decrease in flame tube diameter results in mean residence times increase of 39.5, 55.7, and 88.9 ms, respectively (see Table 6.4).

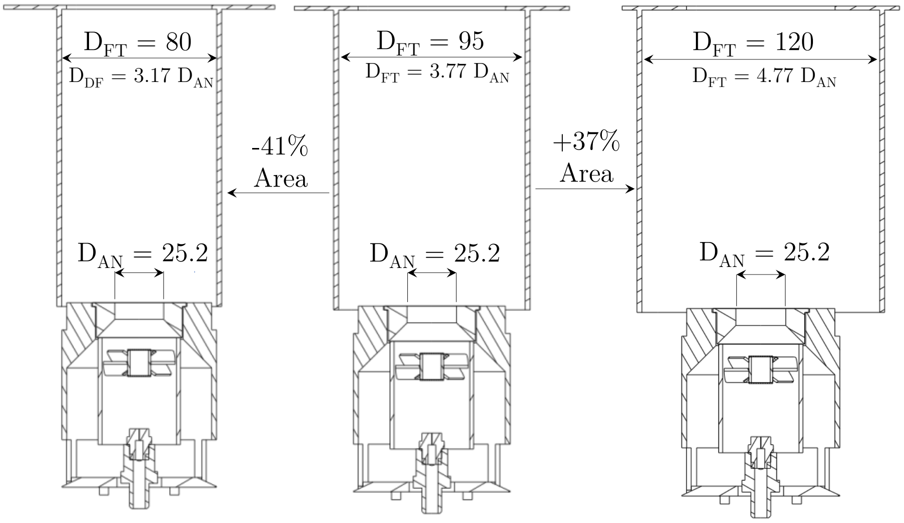

Figure 4.7: Overview of the Three Flame Tube Diameters and the Corresponding Dump Area Ratios

4.3.2 Air Nozzle

The air nozzle diameter (D_{AN}) was varied to better control the fuel-air mixture momentum into the flame tube, which directly influences the flow field in the downstream flow. A range of bulk velocities from 14.5–143 m/s can be achieved by varying the air nozzle diameter (16–25.2 mm) and air temperature (155–255°C). Dump area ratios of 7.5 and 4.77 were obtained for air nozzle diameters of 16 and 25.5 mm, respectively. The flame tube diameter was kept constant at 120 mm in order to achieve similar volumes available to the reaction zone (see Figure 4.8).

Here, the flame tube diameter was set to 120 mm instead of 95 mm to minimize reflection on the inner flame tube walls and facilitate laser Mie scattering measurements. The larger diameter reduces optical interference, providing a clearer and improved signal to noise ratio, thereby enhancing measurement accuracy. It also improves the alignment of diagnostic equipment, reducing experimental errors.

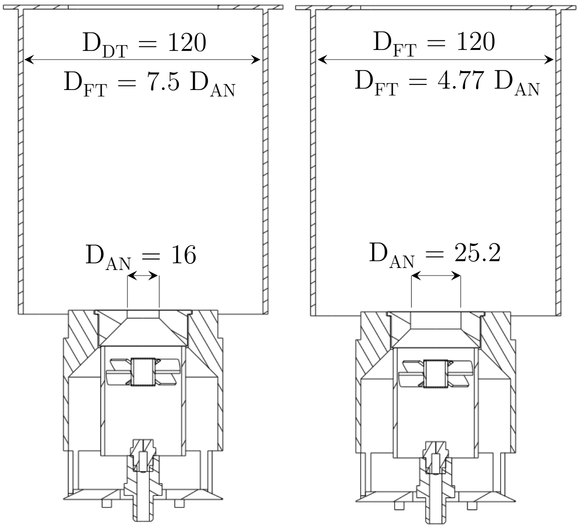

Figure 4.8: Overview of the Three Air Nozzle Diameters and the Corresponding Dump Area Ratios. Adapted from [122]

4.3.3 Axial Swirler

The axial vane swirler in the current study was selected from several mixing concepts because of its simple, yet very effective function as a decelerator of the expanding superheated and vaporized liquid fuel downstream of the fuel nozzle. Its ability to mix the air/fuel is very effective for both liquid and vaporized fuel combustion techniques.

One of the primary driving factors in combustor design is pressure loss. Since the current combustor concept uses high velocity jets, there is already some pressure drop across the combustor. Therefore, the pressure loss caused by the swirler should be kept low to avoid too high combustor pressure losses. For example, the currently tested swirlers had total pressure losses of 0.9, 1.1, and 1.3% at swirl numbers $S_N = 0.5$, 0.6, and 0.7, respectively, under baseline operating conditions and air nozzle D25.2. The low swirl axial vanes tend to have wider cavities for the air/fuel mixture to pass through. This results in minimized pressure losses, which can be beneficial to overall GT efficiencies.

As shown in Appendix Figure E.2 *a*, the swirler consists of 8 individual stainless-steel flat vanes and a solid core (hub). Appendix Figure E.2 *b–d* show an overview of the axial swirlers constructed for the tests. The core is made of a solid material and blocks the inflow of air and fuel. The values presented lead to the calculation of $S_N = 0.5$–0.7 for vane angles $\theta = 35°$, 40° and 44°, respectively. Using the vane height z and length *c*, the aspect ratio (*z/c*) can be calculated as another dimensionless factor. A constant aspect ratio of approximately 0.75 was chosen for the currently used swirlers for consistency of testing. This factor essentially defines the depth of the axial swirler and generally has a less profound effect on swirl generation and pressure loss than vane angle θ [143].

4.3.4 Fuel Injectors

An off-the-shelf simplex pressure-swirl atomizer with a spray angle of 80° at a pressure drop of 3 bar and at a fluid temperature of 20°C was used (Feinzerstäuberdüse TD, manufactured by DIVA Sprühtechnik GmbH, Hamburg, Germany). The fuel injector was made of EN 1.4305 (DIN X8CrNiS18-9, AISI 303) austenitic steel.

During the experiments, a total of two pressure injectors (hollow-cone pressure-swirl and plain-orifice) were used (see Section 6.4.2). The DIVA pressure swirl housing was used without its swirler as a plain-orifice injector, and for the pressure swirl injector, the swirler was reinstalled in the injector housing. The DIVA liquid fuel injector housing and its swirler are shown in Figure 4.9 *a–c*. Figure 4.9d and e show images of spray angles of 103 degrees with a pressure-swirl injector and 0 degree with the plain-orifice injector, respectively, at 0.52 g/s Jet A-1 mass flow rate. For this mass flow rate at $T_{fuel} = 155°C$, the pressure-swirl injector required a pressure drop of 4.5 bar and the plain-orifice injector required 2.5 bar.

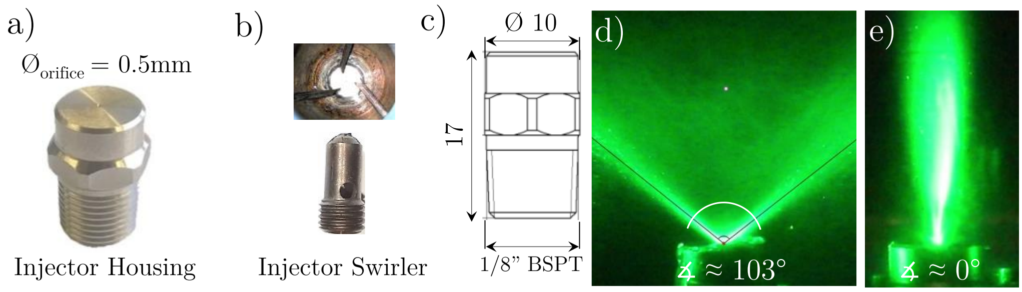

Figure 4.9: a) Liquid Fuel Injector Housing; b) Injector Swirler, c) Injector Geometrical Dimensions, Spray Angle Images of d) Pressure-Swirl and e) Plain-Orifice Injector. Adapted from [122]

5 Measurement Instrumentation

5.1 OH* Chemiluminescence

Reactive species are formed from energetic ground state species in the combustion zone. These excited species have short lifetimes. They emit energy in the form of light, known as luminescence. This luminescence is called chemiluminescence when it is caused by chemical excitation rather than thermal excitation. The intensity of chemiluminescence is a function of chemical composition and has a weaker dependence on temperature. In hydrocarbon flames, OH* and CH* produce the strongest chemiluminescence, while C_2* is less intense. [144,145]

A flame can be divided into two main zones: preheating and reacting. The pre-heat zone is the source of little heat release, while the reaction zone is where most of the chemical energy is released. The flame is very thin, about one millimeter thick, at atmospheric pressure. This thinness creates large temperature and species concentration gradients that drive flame self-sustainability, allowing heat and radical species to diffuse from reaction zone to preheating zone. The fast reaction zone appears blue when there is an excess of air. Excited CH radicals in the high temperature zone are responsible for this blue radiation. When the air is reduced to less than stoichiometric proportions, the zone appears blue-green. This is now due to radiation from excited C_2. In both cases, OH radicals also contribute visible radiation. [56]

Krishnamachari et al. [146] proposed the main reaction for the formation of OH* in hydrocarbon mixtures. They studied the emission spectra of oxygen-acetylene flames at low pressures. They found that the Reaction R5.1 plays a significant role in the formation of OH* in these flames.

$$CH + O_2 \rightarrow CO + OH^* \tag{R5.1}$$

$$OH^* \rightarrow OH + h\frac{c}{\lambda} \tag{R5.2}$$

In flame spectra, OH* emission wavelength λ is typically observed at 306.4 nm [147]. Here, *h* is the Planck constant and *c* represents the light speed. The fraction of OH* that is transferred to the ground state by the emission of radiation (R5.2) is so small that it is negligible in terms of reaction kinetics [148]. Nevertheless, radiation is sufficient for experimental detection as a qualitative marker of the heat release zone. The commonly accepted idea is that as a measure of total heat release in a flame, the chemiluminescence of species such as CH*, OH*, or C_2* can be used. This is because the total chemiluminescence is directly related to the total surface area of the primary flame, since the reaction zones in a flame are thin and sheet-like. [149]

OH*-Chemiluminescence Measurement Setup

In order to analyze the geometrical characteristics of the flame, i.e. flame length (FL) and height above burner (HAB), the OH*-Chemiluminescence (OH*-CL) intensities were recorded for all operating points using a charge-coupled device camera (LaVision Imager Pro Plus 2M, 1600 x 1200 pixels) in combination with an intensifier (LaVision: Intensified Relay Optics), a CERCO 100 mm UV lens F/2.8 and a UV interference filter (312 ± 15 nm). All OH*-CL images were acquired with a constant gain of 65% and a gate time of 400 µs. The signal intensity of each flame was analyzed by processing 200 single instantaneous images at a repetition rate of 26 Hz. In addition, a Canon EOS 70D single-lens reflex (SLR) with 55 mm lens was also used to observe the flames in a natural spectrum.

The OH* chemiluminescence images obtained in this work were analyzed using the commercial software Davis 10.2.0 from LaVision. During the analysis, the images were corrected for various influences. This is shown schematically in Figure 5.1, which shows the steps taken for camera signal corrections. First, from each individual white-field image, the time-averaged background noise generated by the camera sensor, the dark-field, is subtracted. The dark-field corrected white-field images are then averaged over time. The resulting average image is normalized to its intensity maximum.

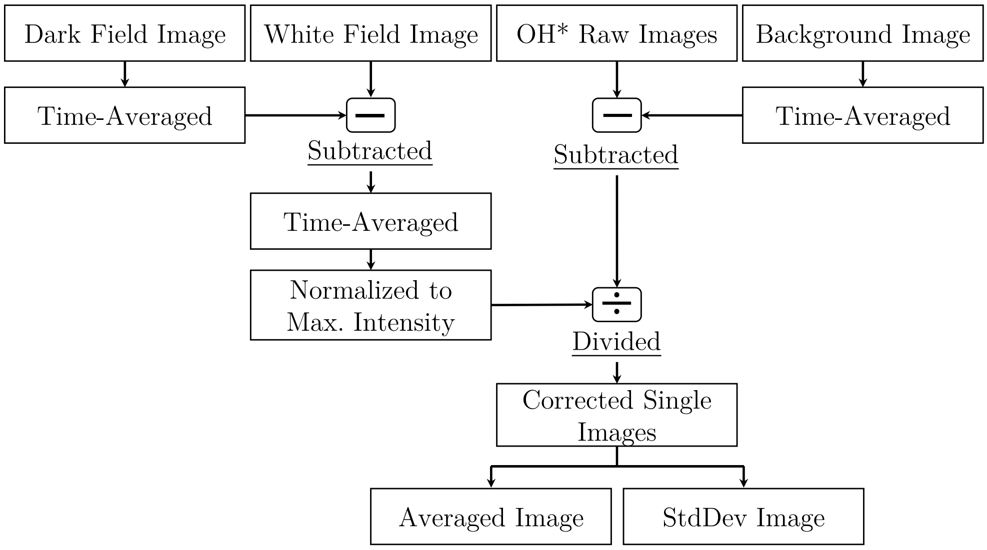

Figure 5.1: Correction and Evaluation Routine for the OH* Chemiluminescence Images

First, the mean value of the daily background is applied to the individual images of the measurement data. The next step is the white-field correction. From the corrected OH* chemiluminescence single images obtained in this way, the mean value over time can now be determined. The time average can be calculated from the resulting corrected OH* chemiluminescence images (see Figure 5.2 *a*). Figure 5.2 *c* shows a red-green-blue (RGB) color image taken with a Canon EOS 70D digital single-lens reflex (SLR) camera using a 55 mm lens for comparison.

The calculation of the HAB and FL was done by using a routine developed by Zanger [43] and is schematically illustrating in Figure 5.2 *b*.

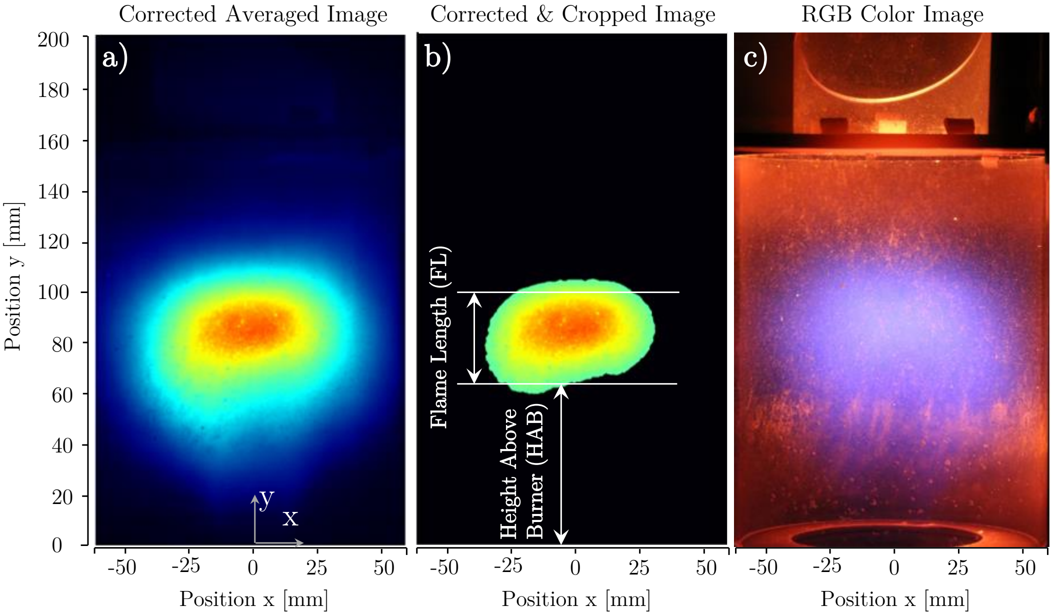

Figure 5.2: a) Corrected and Averaged OH*-CL Image, b) Illustration of the Reaction Zone with Reference to HAB and FL Locations and c) RGB Color Image of the Flame. Adapted from [140]

The general experimental setup is shown in Figure 5.3. Here, the field of view of the OH*-CL is centered axially on the liquid fuel combustor. Thus, the entire optically accessible flame tube could be observed. The camera system was placed approximately 1500 mm from the combustor, providing an image resolution of 5 pixels per mm.

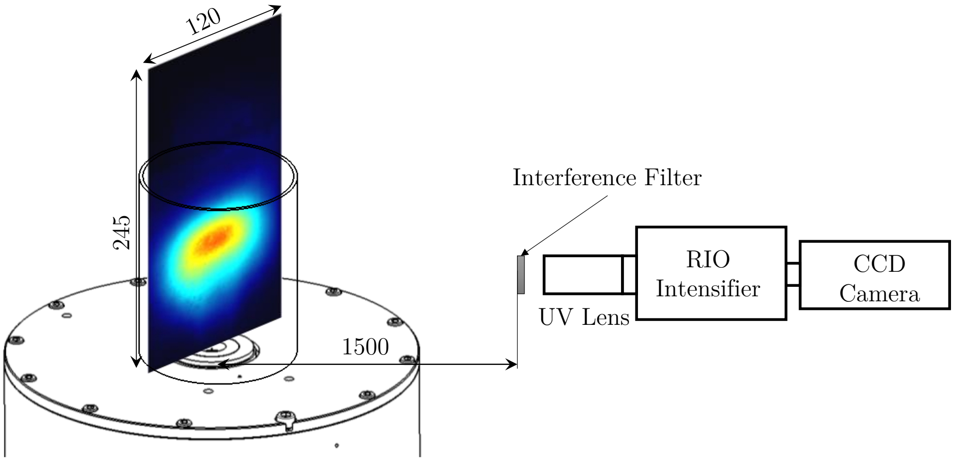

Figure 5.3: Schematic Illustration of OH*-CL Measurement Setup. Adapted from [140]

5.2 Mie Scattering

Scattering occurs when a photon of light encounters an irregularity in the medium through which it travels, and refers to the deflection of electromagnetic radiation from its original path. In this case, air is the medium and fuel droplets the irregularity. The wavelength of the light and the size of the particles in the medium determine the amount of scattering. Mie scattering occurs when the size of the particle is equal to or greater than the wavelength of the light. Since both Rayleigh and Mie scattering do not significantly change the energy, frequency, or wavelength of the photons, they are considered elastic scattering. [150]

The scattering particle has a dimensionless size parameter. It is usually expressed as x, see Equation 5.3.

$$x = \frac{2\pi R}{\lambda} \tag{5.3}$$

where R [m] is the droplet radius and λ [m] the wavelength of the laser.

The scattering intensity in the forward direction is higher than in the backward direction when the size of the particles is similar to or larger than the wavelength of the incoming light. This means that more light photons are scattered in the forward direction. Therefore, the intensity of the scattered light in this direction is higher [151].

Two different experimental setups (reactive and non-reactive) have been implemented in this dissertation in order to observe the individual fuel evaporation behavior and spray shape characteristics. These setups are described in the following.

In the reactive experiments presented in Section 6.4.3 and 6.4.4, fuel droplets were illuminated by a laser sheet of 1 mm thickness and 17 mm height created by a plano-concave and a plano-convex cylindrical lens. Using Mie scattering, their contours became visible to the high speed camera (LaVision HighSpeedStar 6) with a Nikon 50 mm f1.8 lens. An interference filter with a center wavelength of 532 nm allowed only the laser light to reach the camera sensor. A collimated diode pumped solid state (DPSS) continuous wave laser (Thorlabs CPS532) with a wavelength of 532 nm and a power of 4.5 mW was used to illuminate the observed spray.

In these reactive tests, the objective was to visualize the influence of the combustor core components on fuel atomization and evaporation and their effect on Combustion performance under various operating conditions. For this reason, the Mie scattering of the droplets was measured in a reactive mode during flame operation. A schematic of the Mie scattering setup is shown in Figure 5.4 *a*. For each image sequence, Mie scattering intensities were captured by 1000 instantaneous images at a repetition rate of 1kHz and an exposure time of 83 µs. The injector nozzle was in its original position at the combustor inlet (see Figure 5.4 *b*).

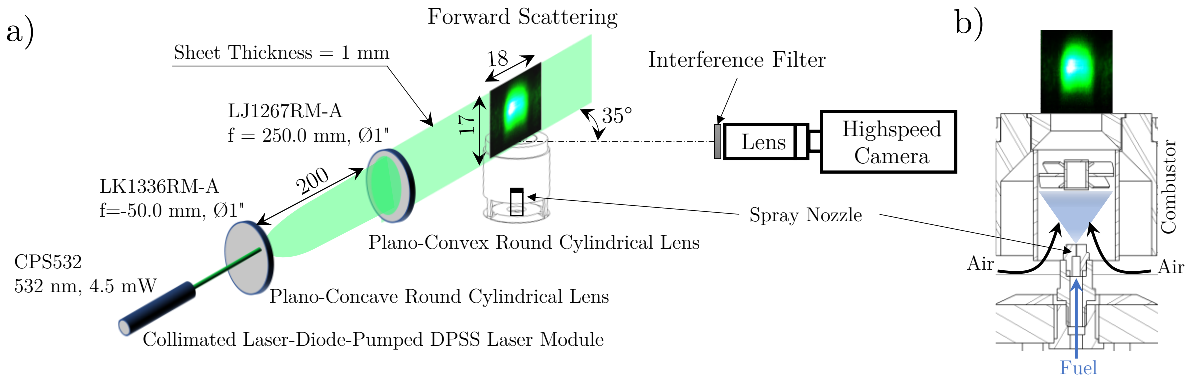

Figure 5.4: a) Schematic Illustration of the Mie Scattering Measurements for the Reactive Tests, b) Fuel Nozzle Position within the Combustor. Adapted from [122]

In a non-reactive Mie scattering measurement campaign presented in sections 6.4.2 and 6.4.5, the liquid spray was illuminated by a laser light sheet 1 mm thick and 25 mm high. The same high-speed camera was used as in the reactive tests but at a repetition rate of 50 kHz and an exposure time of 19.33 µs. However, a plano-convex cylindrical lens of H30 x L60 mm^2 was used to extend the axial length of the laser sheet. This made it possible to observe any changes in the axial penetration of the liquid phase along the combustor axis.

In the non-reactive tests, the objective was to analyze the behavior of the liquid fuel spray immediately after its injection and its evaporation at different fuel temperatures. For this reason, the Mie scattering of the droplets was measured in a non-reactive mode while the injector was moved to the combustor exit through the air nozzle (see Figure 5.5 *b*). The same continuous wave laser as in the non-reactive tests was used to illuminate the spray contour. A schematic of the Mie scattering measurement setup is shown in Figure 5.5 *a*.

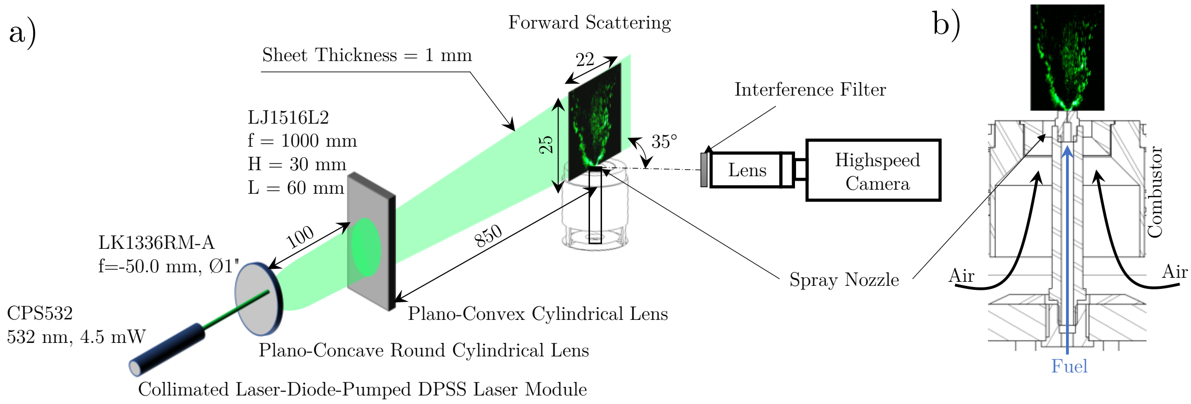

Figure 5.5: a) Schematic Illustration of the Mie Scattering Measurements for the non-Reactive Tests, b) Fuel Nozzle Position within the Combustor. Adapted from [142]

For both setups, the 1000 instantaneous raw images were corrected using a DaVis 10.2.0 software routine. In each of the images, all pixel intensities less than 10 counts were set to zero to remove any small laser light reflections on the combustion chamber quartz glass. The images were then time-averaged and each normalized to its maximum intensity to allow comparison of the evaporation behavior.

For quantitative analysis of the reactive Mie measurements, the sum of all pixel values was calculated column by column and plotted against the horizontal axis of the image to quantify the radial distribution of the liquid phase and therefore, the vaporization of the liquid fuel downstream of the flow (see Figure 5.6). In the right graph, the y-axis represents the sum of the pixel intensities column by column and the x-axis represents the horizontal position at which the intensities were calculated.

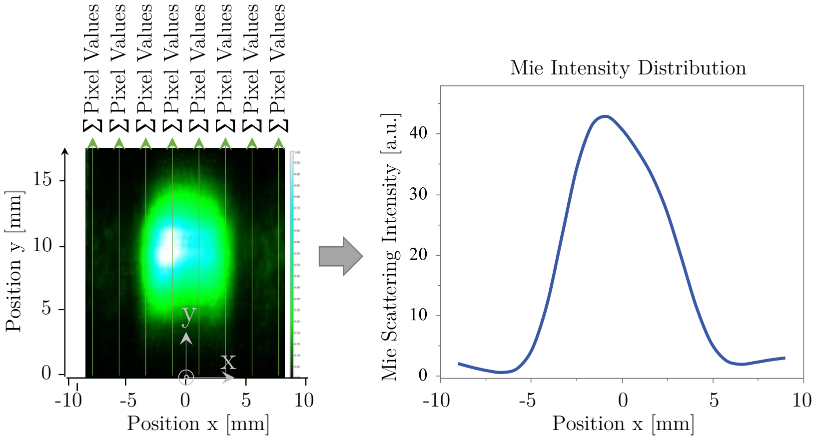

Figure 5.6: Procedure of Converting Pixel Data into Numerical Data for the Reactive Tests

Additionally, for quantitative analysis of the non-reactive Mie measurements, the sum of all pixel values was calculated line by line and plotted against the vertical axis of the image to quantify the axial penetration depth of the liquid phase downstream of the flow (see Figure 5.7). In the graph on the right, the x-axis of the graph represents the sum of the pixel intensities line by line and the y-axis represents the vertical position at which the intensities were calculated.

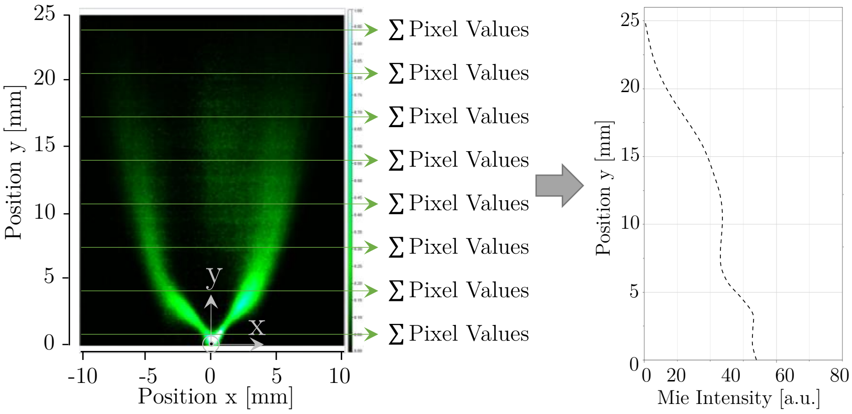

Figure 5.7: Procedure of Converting Pixel Data into Quantitative Numerical Data for non-Reactive Tests. Adapted from [142]

5.3 Exhaust Gas Emission

The exhaust gas concentrations for all operating points were measured using a commercially available emissions analyzer, ABB: Advanced Optima Process Gas Analyzer AO2000. Prior to every measurement day, all of the analyzer sensors were calibrated. An exhaust gas composition sampling probe was installed in the exhaust gas section at a single point concentric with the flame tube at a distance of 566 mm from the burner front plate (Figure 4.3). The probe is equipped with a coaxial air-cooling system to maintain a constant temperature of 120°C at the probe tip (see Figure 5.8). A thermocouple is passed through the probe to the inner wall of the probe tip, where the temperature of the wall is measured.

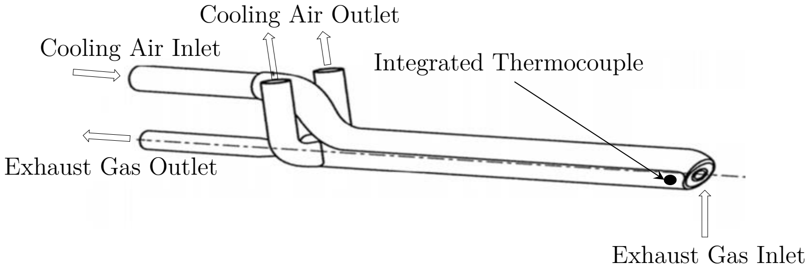

Figure 5.8: Schematic Illustration of the Incorporated Exhaust Gas Probe [152]

The use of a suction probe with a coaxial air-cooling system efficiently quenches reactions in the sampled exhaust gases that leads to freezing of the exhaust gas composition. This prevents excessively high temperatures on the outer wall of the probe, thus reducing surface reactions that could distort the gas composition. There are two effects that take place as a result of this. The first is the quenching of the reactions in the gas phase which is in the sample. At the same time, surface reactions on the outer wall of the probe are prevented by the cooler probe wall. In this way, it is possible to have defined measurement conditions for all the different operating points of the combustor when exhaust gas measurements are made. The exhaust gas from the probe is fed to the ABB via a heated hose to prevent condensation. The temperature of the heating hose is 180°C.

The gas analyzer is able to detect water vapor H_2O (Vaisala–HMT330), carbon dioxide CO_2 (ABB Uras26), and oxygen O_2 (ABB Magnos206) content, as well as carbon monoxide CO (ABB Uras26), unburnt hydrocarbons UHC (ABB MultiFID14 NMHC), and nitrogen oxide (NO_x: sum of the NO and NO_2) (ABB Limas11) concentrations. O_2, CO, and CO_2 are measured under dry conditions, while the other species are measured under wet conditions. The sensor type, measuring range and accuracies of the ABB gas analyzer are listed in Table 5.1.

For each operating point, a total of 180 measurements were taken over 3 minutes (at 1 Hz). The recording of the composition of the emission gases and the OH* images was started after a stationary state, i.e. the CO and NO_x emissions did not change noticeably over time. The measurements were averaged over time. The measured water vapor content was used to normalize the measured emission concentrations for all operating conditions to 15% residual O_2 and dry conditions using Equation 3.15 (see section 3.2 for details). The standard deviation of the calculation data is so small that it is not shown in the graphs. The emissions index (EI_i) of the NO_x and CO levels is calculated using the Equation 3.17.

Table 5.1: ABB Process Gas Analyzer Accuracies at Different Ranges

Species	**NO_x**	**CO**	**UHC**	**CO_2**	**O_2**
Unit	[ppm]	[ppm]	[ppm]	[vol.-%]	[vol.-%]
Sensor	Limas11	Uras26	MultiFID14	Uras26	Magnos206
Range 1	0–10	0–10	0–19	0–5	0–5
Accuracy	0.10	0.10	0.4	0.05	0.03
Range 2	0–20	0–100	0–187	0–20	0–15
Accuracy	0.20	1	3.7	0.20	0.08
Range 3	0–50	0–200	0–3733	N/A	0–25
Accuracy	0.50	2	74.7	N/A	0.13

5.4 Mixing Condensation Particle Counter

A mixing condensed particle counter (MCPC) is an instrument used to measure the number of particles in a gas sample. The principle of its operation is based on condensation growth. The MCPC consists of the saturating, condensing, and particle counting components.

Figure 5.9 shows a schematic of the MCPC setup used to count the particles emitted by the combustion of various liquid fuels and operating conditions in the current research. Initially, a cooled gas sample at 100°C is taken from the combustion chamber through a probe and sent to a diffusion dryer (Model 3062, manufacturer: TSI, Minnesota) to remove any water vapor from the aerosol containing desiccant material (silica). It is worth noting that the gas sample never comes in contact with the desiccant material, ensuring minimal particle loss. In a second stage, the gas sample is then introduced into the saturator (see Figure 5.10), where it is mixed with the saturated butanol vapor that is being produced. The saturated butanol/particle mixture is then passed to a condenser, where the saturated vapor condenses onto the particles present in the gas sample. This causes the particles to be enlarged.

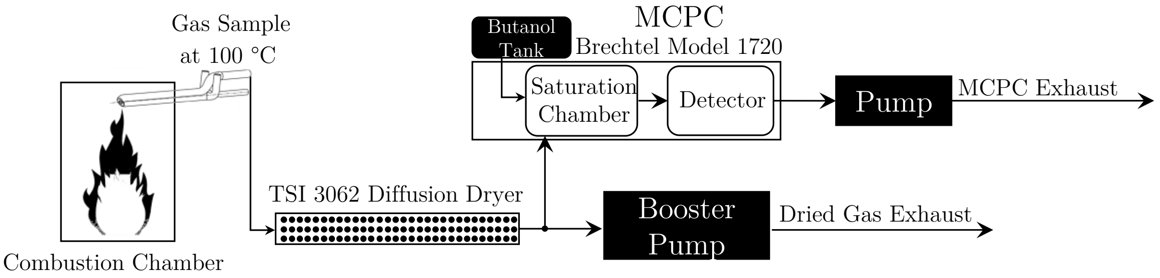

Figure 5.9: Schematic Representation of the Particle Measurement Equipment Used in the Current Work. Adapted from [142]

For rapid response of the MCPC, a booster pump was installed to draw gas sample at a rate of 4 liters per minute. A secondary pump then drew the desired 0.36 liters per minute for the MCPC from a T-junction downstream of the dryer. Both the MCPC and dryer exhausts were vented through the laboratory ventilation system.

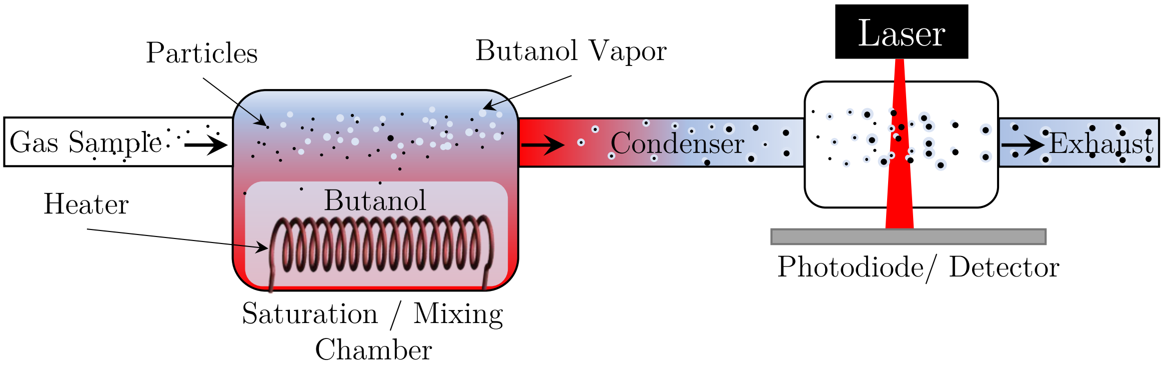

Figure 5.10: Schematic Illustration of MCPC Working Principle. Adapted from [153]

The third stage is the particle counter. The enlarged particles are then counted using a particle counter, typically a technique based on light scattering. The particle counter detects the light scattered or absorbed by the particles and converts it into an electrical signal. This signal is used to determine the number of particles. It's worth noting that the MCPC is best suited for measuring particles in the submicron size range. Typical particle sizes are in the range of a few nanometers to a few microns in diameter. Only particle count and no information about the particle size distribution can be measured by the used MCPC device. [154]

6 Results and Discussion

The purpose of this chapter is to examine the effect of various factors on the combustion performance of the swirl-assisted jet-stabilized combustor. The combustor produced low NO_x and CO emissions while maintaining a steady flame. The Jet A-1 was injected at both liquid and prevaporized conditions. Throughout the experiments, two fuel atomizer types were utilized: a pressure-swirl and plain-orifice atomizer. The effects on flame stability, flame shape and emission formation of the most influential combustor design parameters are evaluated.

These parameters include air temperature, swirl number, combustor flame tube diameter, thermal power, fuel preheat, and flame temperature (see Section 4.2.1). By varying these parameters, an improved design of the prototype combustor is obtained. Jet A-1 Ref. 3 (See Appendix Table C.2 for surrogate composition) was used as the fuel for the experiments.

6.1 Reference Case: FLOX Single-Nozzle Combustor

The reference case for this study is a single-nozzle jet-stabilized combustor (see Figure 6.1 *c*). Since the currently studied combustor is a derivative of the single-nozzle jet-stabilized combustor, their produced emissions and flame stability ranges are compared in later stages of the study. In this combustor, liquid fuel is atomized by a simplex pressure-swirl injector and partially premixed with incoming coaxial air before entering the combustor flame tube where the mixture is ignited. In previous work [7,46,139], a thorough characterization of this type of combustor using liquid fuel (Jet A-1) was performed. It should be noted that a typical circular multi-nozzle combustor with a pronounced inner recirculation zone will have a significantly different flame shape, emissions and operating range than a single-jet FLOX-based combustor.

As shown in Table 6.1, the flames show a narrow operating range ($\lambda_{LBO} = 1.6$) and therefore high NO_x emissions between 2140–2420 K ($\lambda = 1.1–1.5$) despite a relatively high preheated air temperature of 465°C and a 40 mm premix channel at 22 kW thermal power (see Figure 6.1 *a*). It appears that the CO emission remains relatively constant and low over the entire range due to the high flame temperatures as CO is oxidized to CO_2 within the stable range of combustion investigated. Due to thermal NO formation, NO_x levels increase from 20 to 90 ppm as flame temperatures increase from 2140 to 2420 K.

Table 6.1: Operating Conditions of the Reference FLOX Jet-Stabilized Combustor

Parameter	T_{air}	T_{ad}	S_N	D_{AN}	D_{FT}	P_{th}	NO_x	CO	HAB	FL
Unit	[°C]	[K]	[-]	[mm]	[mm]	[kW]	[ppm]	[ppm]	[mm]	[mm]
Range	465	2140–2420	0	25.2	80	22	20–90	5–10	65–90	120–150

In addition to emissions, another requirement for a combustion system, especially for an aero GT, is the size and volume of the combustor system. The reaction zone of a jet-stabilized combustor can generally have a larger axial extent compared to a typical swirl-stabilized flame. The application of a jet-stabilized combustion concept in an aero-GT combustor could be challenging [43]. A large flame requires a larger and/or longer combustor, which does not support aero-GT design criteria. Figure 6.1 *b* shows the OH* chemiluminescence images of the flame (OH*-CL), which describe the length and height above the burner of the reference combustor's flame flames with a range of 120–150 mm and 65–90 mm, respectively.

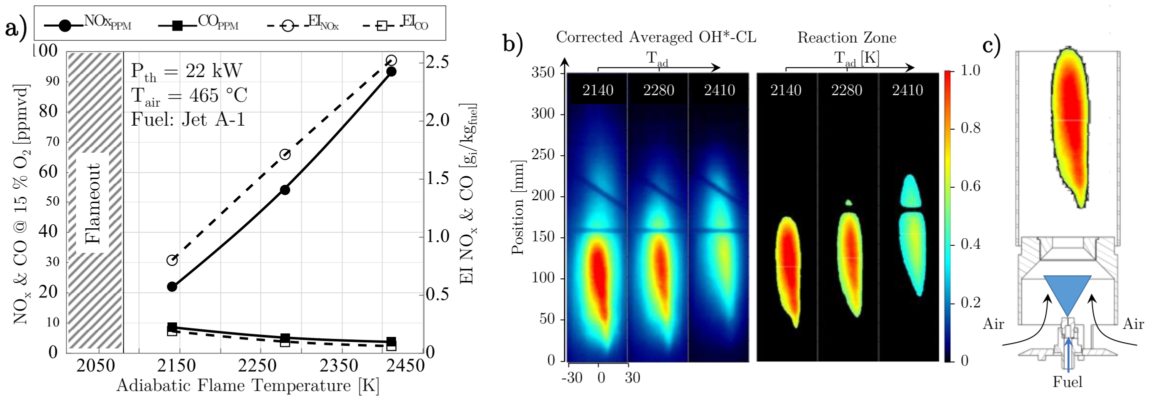

Figure 6.1: a) NO_x and CO Emissions over Flame Temperature of a Liquid Fuel Jet-Stabilized Combustor, b) OH*-CL Images of the Corresponding Flames; c) Cross-Sectional View of the Jet-Stabilized Combustor

Considering the data of the single-nozzle jest-stabilized combustor in Figure 6.1 *a*, it becomes clear that such narrow operating range, high NO_x, and long flame lengths would be unsuitable for aero GT applications.

6.2 Flame Behavior Hysteresis

One of the main objectives of the study was to develop a combustor concept with stable operation and low emission levels. However, while operating the novel swirl-assisted jet-stabilized combustor, a hysteresis behavior of some of the flames was observed. This was particularly interesting, since the flame exhaust gas emissions as well as the heat release zone positions were significantly influenced.

The reliability of the flame, and thus the predictive power of the regression models used to describe the combustion data, was reduced by hysteresis behavior of the flame during combustor operation. Addressing the occurrence of flame hysteresis and improving the quality of the collected data was therefore of critical importance.

A phenomenon occurred during the experiment. Under exactly the same operating conditions (all factors held constant), a different flame mode was established. The images taken with a Canon EOS 70D single-lens reflex (SLR) camera in Figure 6.2 *a–c* show the flame modes of *A* and *B* that occurred under certain identical operating conditions, such as constant $P_{th} = 22.5$ kW, $\Delta T = 0$ K, $T_{air} = 250°C$, $T_{ad} = 1900$ K, $S_N = 0.6$, and $v_{bulk} = 36$ m/s. The research conducted by Harth [34] and Blesinger [155] examines these phenomena within combustion systems.

It appears that there is a hysteresis in the operation of the combustor under certain conditions. As a result, the flame shape and emissions were very different for the same operating condition. Figure 6.2 *a–b* show a prime example of this behavior. For example, for the same combustion parameter settings, when the v_{bulk} was reduced from 60 m/s to 36 m/s, flame Mode *A* occurred, and when the v_{bulk} was increased from 25 to 36 m/s, flame Mode *B* occurred.

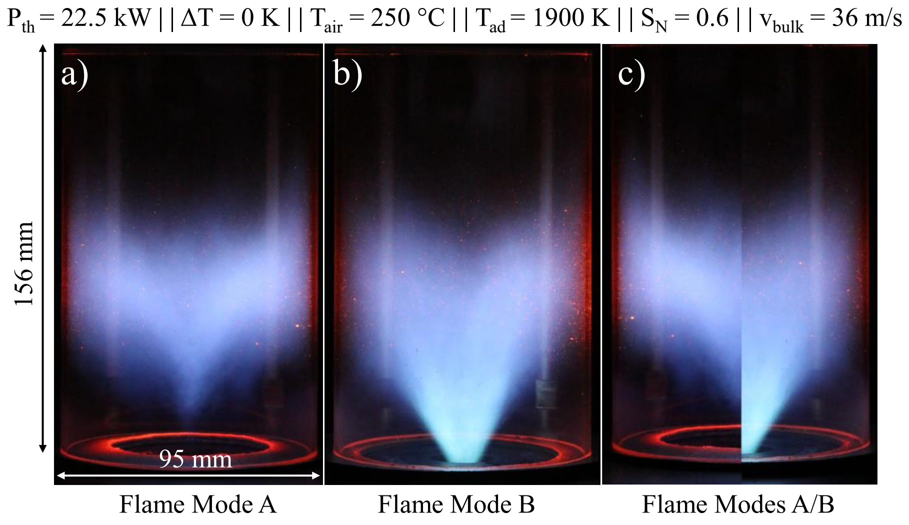

Flame Mode A Flame Mode B Flame Modes A/B

Figure 6.2: a) Flame Mode *A*, b) Flame Mode *B*, c) Joint Images of Both Flame Modes. Adapted from [156]

The flame Mode *A* appears to be detached from the burner nozzle, while the flame Mode *B* is already stabilized within the burner nozzle. Visual inspection of flame Mode *B* shows that the flame has no contact with either the swirler or the nozzle. Both the air nozzle and the swirler did not show any discoloration due to very high temperatures, which eliminates the risk of thermal degradation of the combustor components. Figure 6.2 *c* shows half of each flame modes (left: Mode *A*, right: Mode *B*). Here it appears that the downstream heights of the flames remain somewhat the same, but it is the flame root that is different. The flame Mode *B* had to be eliminated as it produced very high NO_x emissions compared to flame Mode *A*. The NO_x emissions difference ranged from 300–750% higher NO_x concentrations for Mode *B* compared to Mode *A*. In a GT operation, the presence of two different flame modes can result not only in increased pollutant emissions, but also in a reduction in combustor durability if the flame front contacts the liner wall.

The obtained experimental data were grouped into the two previously described flame modes *A* and *B*. Only flame Mode *A* was considered for further analysis of parameter/response correlation, factor effect on flame shape and emission concentration analysis. This decision meant that about 33% of the total 322 operating points had to be temporarily excluded (since they represented flame Mode *B*), as they caused severe errors in the prediction and analysis of the flame key performance indicators (NO_x, CO, HAB and FL).

A follow-up experiment was conducted to specifically address the influencing design factors in order to prevent the occurrence of flame mode *B* indefinitely (see Section 6.4.1). The analysis of the data showed that there are two major contributors to the bi-modal behavior of the flame: first, the bulk velocity and second, the level of fuel preheat ΔT. The bulk velocity is calculated using the fresh gas inlet conditions using continuity equation. Figure 6.3 *a* shows a box plot of all the tested operating points. The operating points are grouped into both flame modes, *A* and *B*, and their v_{bulk} quantiles are shown by the box plots whiskers. It appears that flame Mode *A* was more dominant at higher bulk velocities than 85 m/s, where flame Mode *B* no longer occurs. This indicates that the turbulent flame speed was far exceeded at the nozzle exit, so that no reaction could take place in the vicinity of the swirler inside the combustor's nozzle.

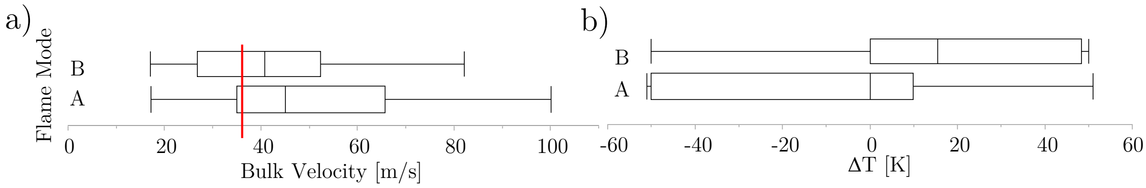

Figure 6.3: a) Box Plots of Both Flame Modes for Different a) Bulk Velocity, b) ΔT

Furthermore, the analysis showed that there is a correlation between ΔT and flame mode (see Figure 6.3 *b*). The probability of flame Mode *A* was higher at lower ΔT. As explained in Section 3.5, the superheat level quantifies the degree of fuel vaporization. As the fuel undergoes vaporization, its interaction with the surrounding air may become more homogeneous, potentially promoting a more reactive mixture. The significance of this effect likely depends on factors such as stoichiometric conditions and the prevailing combustion mechanism—whether primarily driven by autoignition or influenced by phenomena such as Combustion Induced Vortex Breakdown (CIVB). A comprehensive examination of these interactions is necessary to fully understand their role in the overall combustion process. This may well be the reason why the flame Mode *B* tends to dominate in the case of pre-evaporated premixed combustion. However, the bulk velocity had the greatest impact and therefore a follow-up experimental design (see Section 6.4.1) was created and conducted to eliminate flame Mode *B*.

6.3 Reproducibility of the Combustion Data

Throughout the experiments, it was essential to ensure the integrity of the measured data. It was critical that the measured data be reliable in order to draw the correct conclusions about the factor and geometric configuration effects for the characterized swirl-assisted jet-stabilized combustor. In this section, the reproducibility of the combustion data and flame behavior is analyzed. This is done to gain confidence in the observed trends and values.

During the experiments, some of the measurement points as well as the test matrices (subplots SP up to three times and whole plots WP once) were replicated. This was done to gain knowledge on the experimental error. Figure 6.4 *a* and *b* show the emitted NO_x and CO for different flame temperatures of the replicated operating points. Identical, operating points from two whole plots (WP1 and WP5), taken on two different measuring days, (day 13 and day 14) are analyzed. The symbols in the graphs represent actual measured operating points and the curves merely connect the data points.

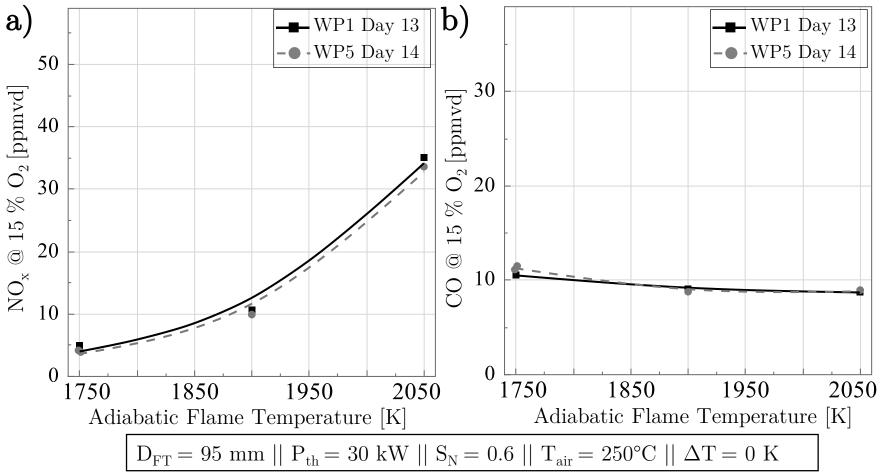

Figure 6.4: Emissions Reproducibility Test of Two Different Measurement Days for a) NO_x and b) CO

The NO_x values obtained from WP1 (solid curve with square symbols) show minimal deviation from those obtained from WP5 (dashed curve with round symbols). Over different measurement days, the maximum NO_x deviation was 0.4 ppm in the fuel-rich condition (T_{ad} = 2050 K). In addition, during the same day of measurement, replicates of the same operating points were made. Here, maximum deviation of 0.25 ppm NO_x was observed in the fuel rich condition. Considering the NO_x accuracy of the ABB gas analyzer of ±0.1 ppm and the maximum accumulated errors of the measurement instruments (see Appendix D) on the NO_x emissions of ±1.159, the measured deviations were to be predicted.

For both measurement days, the CO values also show good agreement. The maximum CO deviation for the same flame condition but different measurement days is also observed in the fuel-rich condition with 0.93 ppm. The maximum deviation measured between the same operating points on the same measurement day is 0.38 ppm. Considering the CO accuracy of the ABB gas analyzer of ±0.1 ppm and the maximum accumulated errors of the measurement instruments (see Appendix D) on the CO emissions of ±0.433 ppm, the measured deviations are acceptable.

Figure 6.5 *a* and *b* show the flame structures, flame height above burner (HAB) and flame length (FL), over different flame temperatures. During the two measurement days, the maximum HAB and FL deviations of 3.88 and 5.9 mm, respectively, are observed in the fuel-lean condition. The maximum deviations of the HAB and FL at the same operating point on the same day of measurement are 1.2 and 0.8 mm, respectively. It should be noted that the flame structural properties suffer from larger deviations than expected due differences in combustor heat and flame tube surface temperatures. Since the operating points were run in a randomized manner, the FL and HAB differences shown in Figure 6.5 *a* and *b* do not show a consistent trend.

The inherent accuracy of the ABB gas analyzer, the test bench infrastructure (MFCs, etc.), and most importantly, the variation in injector spray behavior at different fuel and air temperatures may be responsible for these variations. Reproducibility of results for all combustion performance indicators was found to be very adequate. This shows that the effects of the factors can be determined with a high degree of reliability.

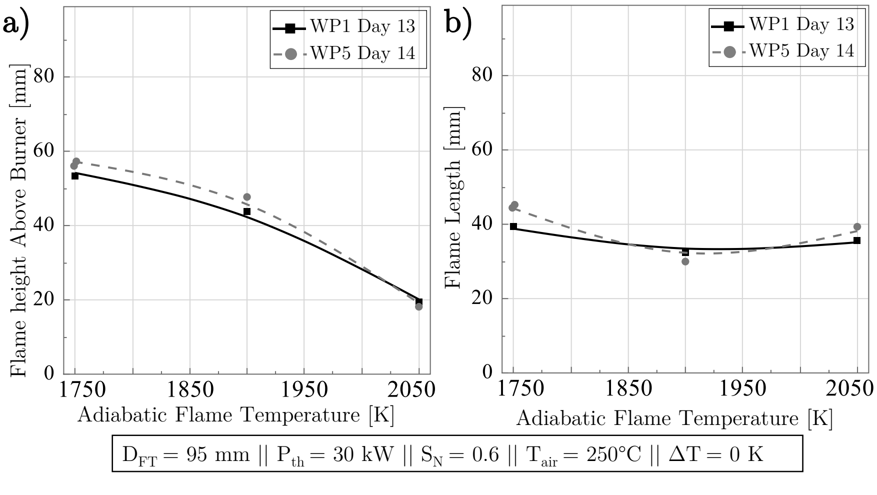

Figure 6.5: Flame Structure Reproducibility Test of Two Different Measurement Days: a) HAB and b) FL

6.4 Influence of Superheated Injection

In comparison to a gaseous fuel, there are additional factors in a liquid fuel combustion process that have an impact on the flame performance. Among other effects (see Section 3.2 for more details), fuel atomization, evaporation, spray-wall interaction and fuel thermophysical properties play a key role in determining the level of pollutant formation.

The effect of increasing fuel superheat level (ΔT) on emissions and flame structure is analyzed in this section. Increasing the fuel temperature during combustion can be beneficial as discussed in section 3.3. It has the effect of a reduction in fuel viscosity and the promotion of finer atomization. However, as discussed in Appendix A, high fuel temperatures can also lead to oxidation reactions that form deposits. These deposits can distort the fuel spray, cause uneven spray patterns, and even block the fuel flow.

The NO_x, CO and UHC emissions for different flame temperatures are shown in Figure 6.6 *a*, *b* and *c*, respectively. Flame tube diameter (D_{FT} = 120 mm), air nozzle diameter (D_{AN} = 25.2 mm), thermal power (P_{th} = 22.5 kW), swirl number (S_N = 0.6), and air temperature (T_{air} = 250°C) are held constant at baseline conditions (see Table 4.1 for design space matrix). Level of preheat ΔT values of +50 K (255°C), 0 K (205°C), and -50 K (155°C) represent, superheated, saturated, and sprayed Jet A-1 conditions, respectively.

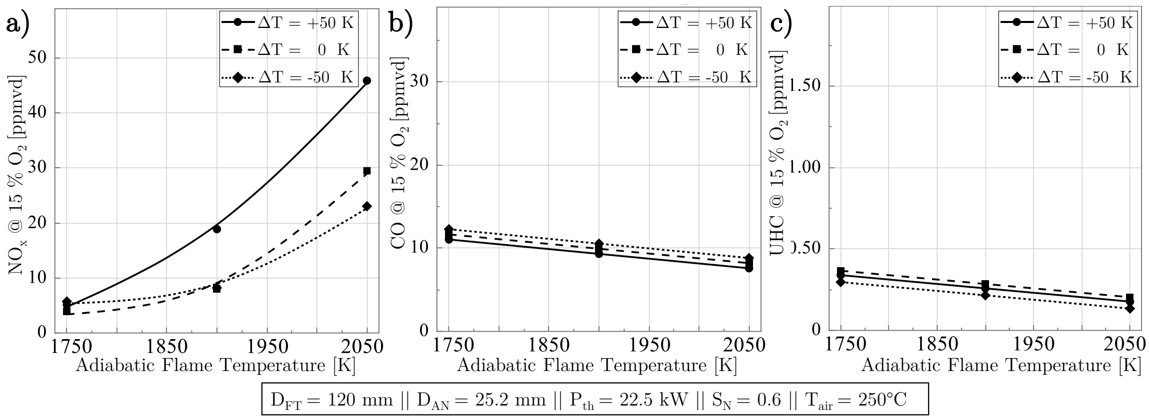

Figure 6.6: Effect of Level of Superheat ΔT on a) NO_x, b) CO and c) UHC Emissions for D_{AN} = 25.2 mm

The NO_x emissions appear to be similar at about 5 ppm for all superheat levels at fuel-lean conditions (T_{ad} = 1750 K). As the flame temperature increases from 1750–1900 K, the NO_x levels tend to increase as well. This is because the Zeldovich effect starts becoming dominant as NO formation rate increases. At 1900 K, the emission of both ΔT = -50 K and 0 K remain similar at ≈ 8 ppm. The NO_x value of the superheated condition (ΔT = +50 K) increases to 19 ppm. The NO_x levels increase further to 23, 29 and 46 ppm for the spray, saturated and superheated fuel, respectively, as the flame temperature reaches 2050 K. The NO_x values of ΔT = 0 K and

+50 K tend to be higher than the spray condition, contrary to the expectation that improving the droplet size or even pre-vaporizing the liquid fuel should decrease the NO_x level.

It appears that at 2050 K, where the bulk velocity decreases due to the decreasing air flow at constant fuel mass flow rate, the mixing of fuel and air has deteriorated. The recirculation intensity within the flame tube may be influenced by a decrease in bulk velocity. Additionally, the rapid axial expansion of the superheated fuel at $\Delta T = +50$ K may reduce the radial penetration depth of the fuel into the air flow (see Section 6.4.2), affecting mixing. These factors could contribute to the observed increase in NO_x levels. Further investigation is needed to explain this phenomenon at this time. Therefore, follow-up experiments have been carried out for investigation of:

- The effect of increased bulk velocity by decreasing the air nozzle diameter (see Section 6.4.1)
- Non-reactive Mie scattering measurements for detailed characterization of both spray and superheated fuel injection (see Section 6.4.2)
- The effect of primary atomization method by substituting the pressure-swirl atomizer with a plain-orifice injector (see Section 6.4.2)
- Isolation of the fuel and air temperature effect on the combustion performance (see Section 6.4.3)
- The effect of the combustor core components on the fuel evaporation, flame emissions, flame structure and lean blowout limits (see Section 6.4.4)
- The effect of fuel thermophysical properties by testing fuels of various origins and saturation temperatures (see Section 6.4.5)

Figure 6.6 *b* shows the CO emissions from the flames. The graph shows a fairly constant CO behavior over the whole temperature range of the flames from 1750-2050 K with about 8–12 ppm. The negligible difference in the CO levels between the flames at ΔT = -50 to 50 K is found to be about 1.3 ppm. These low CO levels may be evidence that there is sufficient residence time for the chemical reaction of CO to CO_2 and that the lean blowout limit has not yet been reached at approximately 1545–1625 K for all ΔT levels. Note that the exhaust gas probe was placed a distance of 566 mm. This may be one of the underlying reasons behind the low and constant CO levels. The insensitivity of CO to the variation of ΔT indicates that at these relatively low flame tube bulk velocities of 5.6–6.3 m/s and the corresponding mean residence times of 28.7–25.4 ms, the size of the fuel droplets has only a minor effect on the incomplete combustion of the fuel.

The mean residence time was calculated using the volume of the flame tube (D80 mm x H160 mm) excluding the volume of the rectangular combustion chamber shown in Figure 4.3, since the reaction zone took place only in the fame tube.

Figure 6.6 *c* shows the UHC levels of the tested flames. Similar to the CO emissions, the UHC emissions remain at a constant level of 0.16-0.3 ppm over the entire temperature range of the flames. Due to sufficient residence time of the exhaust gases, almost all UHCs are oxidized to CO_2. For all investigated factor combinations such low UHC values were observed. The measured UHC values are below ABB's UHC measurement accuracy of ±0.37 ppm. Therefore, the possible influence of the characterized factors on the UHC behavior is not analyzed and will be neglected.

The flame heights above burner (HAB) for various flame temperatures and fuel preheat levels are shown in Figure 6.7 *a*. Due to faster chemical reaction rates and higher reactivity of the fuel-rich mixture, the HAB values for all ΔT levels decrease sequentially with increasing flame temperature. In addition, HAB values increase with decreasing fuel preheat ΔT, where liquid fuel evaporation is enhanced because atomization occurs in a superheated state. The lowest HAB value of 30.5 mm at T_{ad} = 2050 K can be seen at ΔT = +50 K, and the highest HAB value is measured at 72 mm at T_{ad} = 1750 and ΔT = -50 K.

The measured flame lengths in Figure 6.7 *b* show a relatively constant behavior (33–43 mm) over the entire tested range of flame temperature and velocity from 1750–2050 K and 34.4–45.1 m/s. The slight decrease in flame length at the fuel-richer condition (2050 K) can be attributed to the lower bulk velocity and the higher temperature of the heat release zone, which leads to an accelerated evaporation of the fuel. At such a relatively low jet velocity range, the flame length appears to be insensitive to ΔT. To gain more insight into this phenomenon and to verify that this behavior is consistent at higher jet velocities, follow-up experiments at higher bulk velocities were carried out (refer to Section 6.4.1).

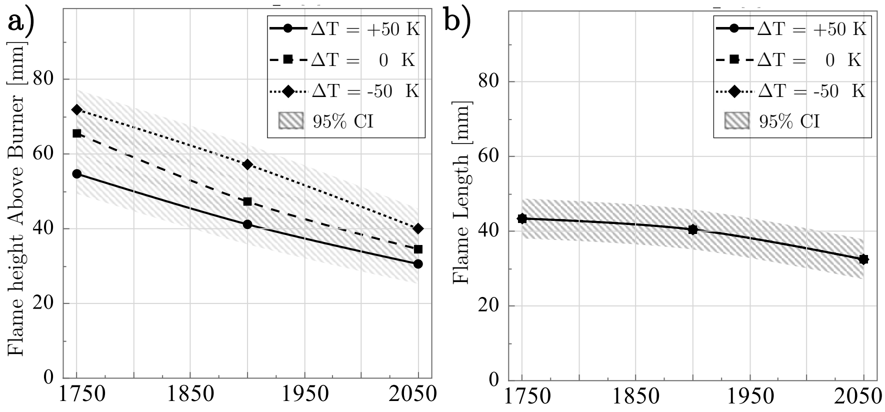

D_{FT} = 120 mm || D_{AN} = 25.2 mm || P_{th} = 22.5 kW || S_N = 0.6 || T_{air} = 250°C

Figure 6.7: Effect of Level of Superheat ΔT on a) HAB and b) FL for D_{AN} = 25.2 mm

Summary

In this section, the effect of various liquid fuel superheat level (ΔT = -50 to +50 K) on the exhaust gas emissions (NO_x, CO and UHC) of the novel combustor was tested. It was assumed that by avoiding the hot pockets in the reaction zone, NO_x levels could be reduced by increasing the fuel temperature and thus injecting it in a pre-vaporized state.

At fuel lean conditions (T_{ad} = 1750 K), NO_x emissions appeared to be similar at approximately 5 ppm for all superheat levels. NO_x levels tended to increase as the flame temperature increased from 1750–1900 K. The NO_x values of ΔT = 0 K and +50 K showed higher levels than the spray condition, contrary to the expectation that improving the droplet size or even pre-vaporizing the liquid fuel should decrease the NO_x level. The CO level was found to be fairly constant at about 8 to 12 ppm over an entire flame temperature range of 1750–2050 K. At ΔT = -50 to +50 K, there is a negligible difference of about 1.3 ppm in the CO levels. These low CO concentrations indicate the presence of enough residence time to convert CO to CO_2. The UHC values of the operating points were below the range of accuracy of the emission analyzer. Therefore, their analysis is neglected in this study.

HAB values for all ΔT levels decrease sequentially with increasing flame temperature due to faster chemical reaction rates and higher reactivity of the fuel-rich mixture. Furthermore, HAB values increase with decreasing fuel preheat ΔT, where liquid fuel evaporation is enhanced due to the overheated atomization. The measured flame lengths showed a relatively constant trend (33–43 mm) over the entire tested range of flame temperature from 1750 to 2050 K. The slight decrease in flame length at the higher fuel temperature (2050 K) is caused by the lower bulk velocity and the higher temperature of the heat release zone, resulting in faster fuel evaporation.

6.4.1 Follow-up Experiment: Influence of Air Nozzle Diameter

In all the follow-up experiments, some of the combustor design parameters such as S_N and P_{th} were kept constant at 0.6 and 22.5 kW, respectively, as they asserted a lesser effect on the combustion performance of the combustor (see section 6.5 and 6.6). The flame tube diameter D_{FT} was also kept constant at 120 mm because the laser sheet reflection was observed to be lowest due to its larger radius compared to D80 and D95.

The objective of this follow-up experiment is the analysis of the bulk velocity by reducing the air nozzle diameter from D_{AN} = 25.2 to 16 mm. This results in an increase in the dump area ratio from 4.77 to 7.5. This also increases the available volume/area for the recirculation zone. More volume means more residence time and mixing for fuel, air and exhaust gases. This should affect both flame emissions and flame structure. The Reynolds number increased from 20,000–26,500

(∅25.2) to 33,000–43,000 (∅16). The air nozzle bulk velocity increased from 34.4–45.1 m/s for ∅25.2 to 85.3–111.5 m/s for ∅16 mm, resulting in an increased level of turbulence and pressure drop [1].

The same flame and fuel temperature sweep as in Figure 6.6 was replicated with the air nozzle D_{AN} = 16 mm. To test the effect of the colder fuel temperature in this detailed test, the level of the preheat range was increased to include ΔT = -100 K (105°C). To allow a seamless comparison of the two velocity changes, other parameters such as D_{FT}, P_{th}, S_N, and T_{air} were kept constant (see Figure 6.8 legend).

The NO_x levels versus adiabatic flame temperature for D_{AN} = 16 mm are shown in Figure 6.8 *a*. The expected increase in the NO_x levels with increasing T_{ad} that was observed in Figure 6.6 *a* for D_{AN} = 25.2 mm is also reflected here. However, not only is the magnitude of the NO_x levels reduced, but so is the slope of the increase in NO_x levels with increase in T_{ad}. At ΔT = +50 K, as T_{ad} increases from 1800 to 2050 K, the NO_x levels increase by mere 7.4 ppm for D_{AN} = 16 mm compared to 39 ppm for D_{AN} = 25.2 mm.

In addition, the ΔT effect on NO_x seems to disappear at all T_{ad} levels. This is due to improved fuel-air mixing with increasing turbulence. The additional turbulence generated by the higher velocities (Reynolds number) has also led to an improved recirculation zone. This results in better mixing of fresh and exhaust gases. Fuel atomization, dispersion, and vaporization are also improved due to stronger shear forces at higher bulk air velocities. It is interesting to note that the flames at ΔT = -100 K show the same trend and levels as those at ΔT = +50 K, which proves the existence of other auxiliary factors that led to the improved fuel atomization. See Section 6.4.3 for a detailed analysis of the effect of fuel and air temperature on fuel evaporation. At the same combustor and operating parameters, the combustor total pressure loss was increased from 1.05% to 3.75% at T_{ad} = 1900 K for increasing the jet velocity from 37.7 m/s to 93.7 m/s, respectively.

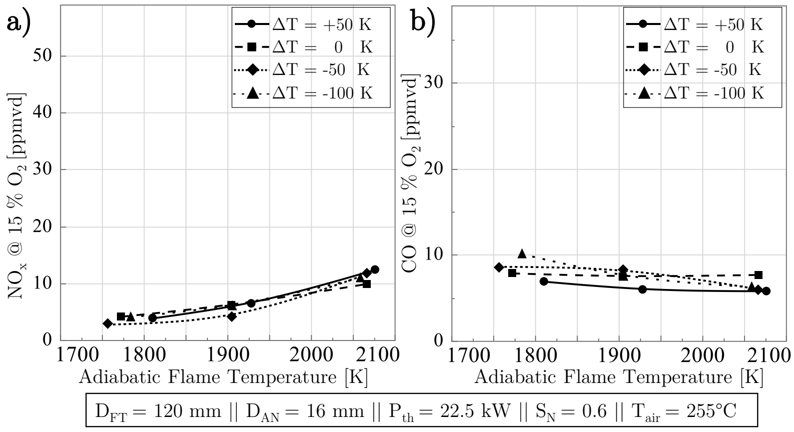

Figure 6.8: Effect of Level of Superheat ΔT on a) NO_x and b) CO for D_{AN} = 16 mm

Figure 6.8 *b* shows the CO levels measured at D_{AN} = 16 mm. CO remains insensitive to T_{ad} and for the most part insensitive to ΔT variation; similar to the previously discussed CO levels at D_{AN} = 25.2 mm. The maximum CO measured at the fuel-leanest point 1756 K is 10.2 ppm (at ΔT = -100 K). The maximum CO measured at the fuel-richest point 2066 K is 7.7 ppm (at ΔT = 0 K). The CO levels measured at ΔT = +50 K are consistently the lowest. This is due to improved evaporation of the liquid fuel.

The OH* image matrix of D_{AN} = 16 mm for different T_{ad} (1780–2070 K) and ΔT (-100 to +50 K) is shown in Figure 6.9. It can be seen that the intensity and propagation of the heat release zone is strongly dependent on the flame temperature when comparing the first column with ΔT = - 100 K. The flame size decreases with increasing T_{ad} as the air-fuel ratio decreases and the flame becomes more reactive. In addition, the axial and radial expansion of the reaction zone is influenced by the higher bulk velocity, shorter residence time and reduced reactivity of the mixture at fuel-leaner conditions.

Observing the rows of Figure 6.9, it is clear that the flames at ΔT = -100 K and -50 K appear more symmetrical than the flames at ΔT = 0 K and especially at +50 K, where a different state dominates due to the superheated fuel injection. The images shown at T_{ad} = 1900 and 2070 K show flame roots at ΔT = -100 to 0 K due to not fully vaporized fuel exiting the air nozzle. The flame root completely disappears at ΔT = +50 K. This may be due to improved fuel evaporation leading to shorted flame length.

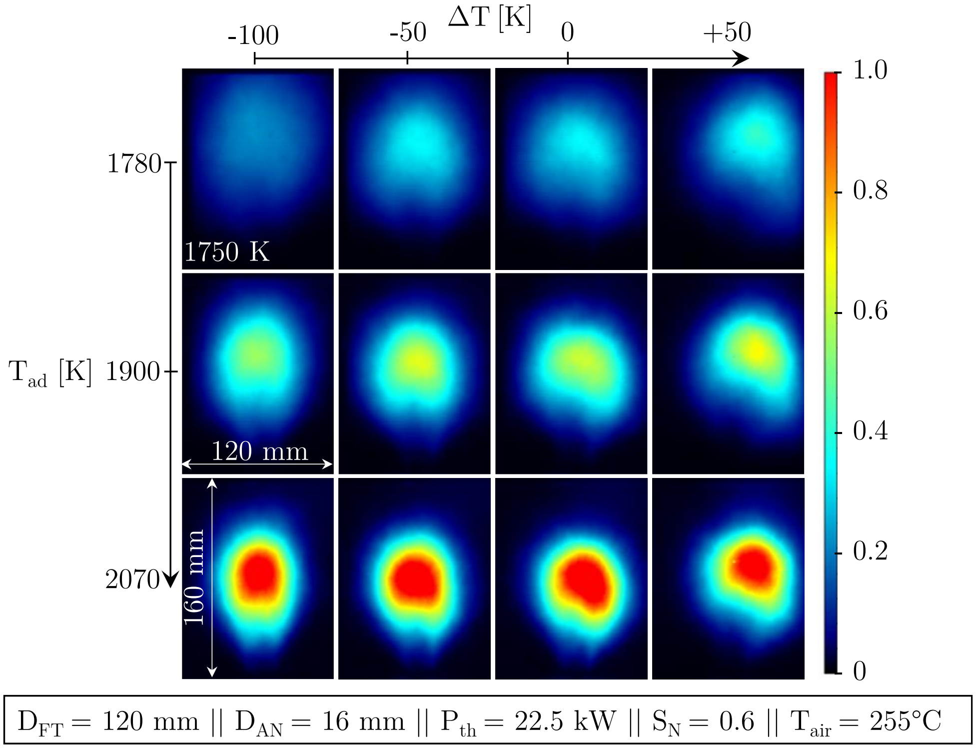

Figure 6.9: OH* Images of D_{AN} = 16 mm at Various T_{ad} and ΔT

The corresponding HAB values are shown in Figure 6.10 *a*. A similar trend to that seen for the HAB level at D_{AN} = 25.2 mm can be seen here as well. As the T_{ad} decreases, the measured HAB decreases due to the higher reactivity of the fuel-air mixture at the fuel-richer conditions. It is evident that the magnitude of the HAB levels is higher with 75 mm compared to 41 mm for D_{AN} = 25.2 and 16 mm, respectively, at T_{ad} = 1950 K and ΔT = +50 K. This is due to the higher bulk velocities and reduced mixture reactivity as a result of dilution of the fresh gas and exhaust gases at the flame root for D_{AN} = 16 mm.

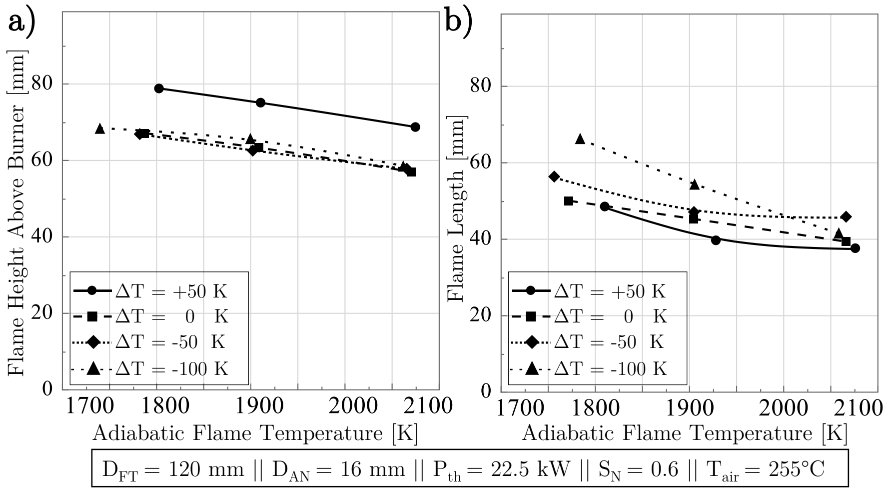

Figure 6.10: Effect of Level of Superheat ΔT on a) HAB and b) FL for D_{AN} = 16 mm

The slope in which the HAB decreases as T_{ad} increases is also reduced, indicating a reduced T_{ad} effect on HAB. This may be because of increased turbulence, a more improved recirculation zone, and improved fuel-air mixing. Due to the reduced quality of fuel-air mixing as a result of the large axial expansion of the evaporating superheated fuel and its relatively narrow injection path (reduced radial fuel penetration), the HAB appears to be higher at ΔT = +50 K. This higher HAB is a result of the lower reactivity of the fuel-air mixture entering the flame tube, which results in a delay in flame stabilization. The absence of this effect at lower jet velocity seen in Figure 6.7 *a* may indicate the interactivity of the jet velocity and ΔT level. It appears that at lower jet velocities, a more reactive fuel-air mixture is produced with increasing ΔT levels, whereas at higher velocities, this interaction effect is largely decoupled.

A reversed effect of ΔT on the HAB levels can also be observed when comparing Figure 6.10 *a* and Figure 6.7 *a*. At higher jet velocities (Figure 6.10 *a*), it appears that the highest HAB levels occur at ΔT =+50 K, whereas at lower jet velocities, the highest HAB levels were observed at ΔT =-50 K (Figure 6.7 *a*). It may be due to the tendency of the flame at lower velocity and higher ΔT levels to form flame mode *B* (see Section 6.2), which showed a significantly lower HAB levels.

The measured FL for $D_{AN} = 16$ mm is shown in Figure 6.10 *b*. The decrease in flame length observed at fuel-richer conditions is indicative of higher flame temperatures leading to higher heat radiation and consequently improved fuel droplet evaporation and shorter reaction zones. Different ΔT levels appear to cause FL changes up to 10 mm for $\Delta T = -50$ to 50 K. However, for the coldest fuel case at $\Delta T = -100$ K, FL appears to increase more steeply than the other ΔT levels. This shows that due to the lower fuel temperatures at $\Delta T = -100$ K, larger droplets are formed that take longer to evaporate thus leading to higher FL values at fuel-lean conditions.

An important objective of the study is to maximize the combustor operating range. In this regard, lean blowout limit (LBO) tests were conducted at constant combustor operating conditions (D_{FT}, D_{AN}, P_{th}, S_N, and T_{air}) as the air mass flow rate was increased. Each LBO test was replicated three times to gain statistical confidence. The air mass flow rate was manually increased at a rate of 0.02 g per second ($\Delta T_{ad} = 2$ K/s).

One such LBO limit test for various ΔT is shown in Figure 6.11. It is clearly visible that except for $\Delta T = -100$ K, the remaining ΔT values have negligible effect on the T_{ad} LBO limit of 1560–1570 K at about $v_{bulk} = 130$ m/s. In the case of $\Delta T = -100$ K, the T_{ad} LBO limit is reduced by about 50 K to 1520 K. This phenomenon can be attributed to the formation of larger fuel droplets at $\Delta T = -100$ K. These larger droplets exhibit slower rates of evaporation and combustion within the reaction zone. As combustion progresses, these droplets release a higher concentration of radical species, which are essential for sustaining chain reactions. These radicals significantly enhance the local reactivity of the mixture, facilitating rapid re-ignition and ensuring robust and stable flame propagation. Furthermore, the larger droplets contribute to a more distributed heat release, which aids in maintaining flame stability by preventing localized extinction and supporting continuous combustion. [1]

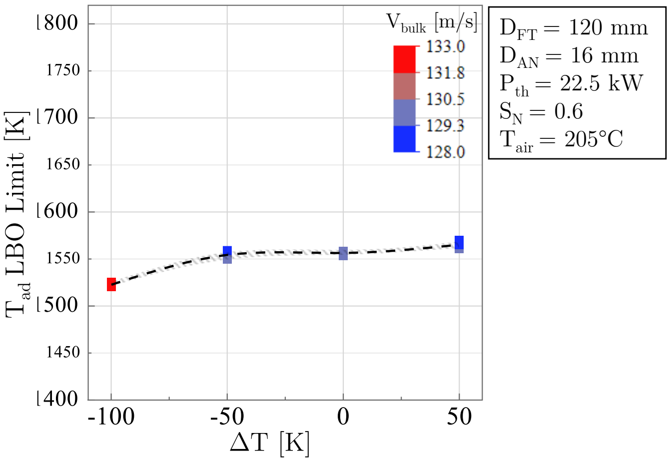

Figure 6.11: LBO Limits for Different ΔT at $D_{AN} = 16$ mm

While eliminating the flame hysteresis behavior described in Section 6.2, combustion performance can be significantly affected by increasing the bulk velocity at the air nozzle level by reducing the air nozzle diameter. As described in section 4.3.2, for a constant flame tube diameter of D_{FT} = 120 mm, the dump area ratio varied from 7.5, 6 and 4.77 for the tested air nozzle diameters D_{AN} = 16, 20 and 25.2 mm.

Summary

In the previous section, it was found that at lower air mass flow rates (lower jet velocities), the NO_x levels increased with increasing ΔT. Therefore, in this section, the jet velocity of the combustor was increased by decreasing the air nozzle diameter D_{AN} by 36% (from D_{AN} = 25.2 to 16 mm) to improve the recirculation zone and achieve higher fuel-air mixing rates needed for reducing temperature peaks in the reaction zone.

By increasing the jet velocity, not only was the level of NO_x concentrations lower, but also the steepness of the increase in NO_x with increasing T_{ad}. At superheated condition and with increasing T_{ad}, the NO_x values at D_{AN} = 16 mm increased by only 7.4 ppm, whereas at D_{AN} = 25.2 mm the NO_x increased by 39 ppm. At all T_{ad} values, the effect of ΔT on NO_x also disappeared. This was perhaps a result of the improvement in air-fuel mixing with the increase in turbulence. The recirculation zone may have also improved by the additional turbulence. Other influencing factors may be the higher shear forces at higher air velocities, which improve fuel atomization, distribution and vaporization.

The flames at spray condition appeared more symmetric than the flames at ΔT = 0 K and especially at +50 K. The root of the flame completely disappeared at ΔT = +50 K. This may be a consequence of the improved vaporization of the fuel, which leads to a shortening of the length of the flame.

The HAB trend of D_{AN} = 16 mm was similar to the values of D_{AN} = 25.2 mm. Due to the higher reactivity of the fuel-air mixture at fuel-richer conditions, the measured HAB value decreased with decreasing T_{ad}. The decrease in flame length observed under fuel-richer conditions is indicative of higher flame temperatures, which result in greater heat radiation and, therefore, better vaporization of the fuel droplets and shorter reaction zones. A slight decrease in FL values was observed with increasing ΔT level, which can be attributed to increased fuel droplet evaporation rate and thus shorter reaction zone at higher ΔT.

With the exception of ΔT = -100 K, the other ΔT values have a negligible effect on the Tad-LBO limit of 1560–1570 K. This may be due to the larger droplets formed at ΔT = -100 K, which burn at near-stoichiometric condition, providing radical species that lead to rapid re-ignition and improved stable flame propagation.

6.4.2 Follow-up Experiment: Fuel Injector Type Effect

In this section, two fuel injectors based on pressure swirl and plain orifice, as detailed in section 4.3.4, are characterized to test the effect of their atomization quality on the combustion performance of the flames. Combustion performance can be significantly affected by the quality of the fuel spray in a combustion process. Some of the most important effects of spray quality on the combustion performance are: a) emissions, b) heat release intensity, and c) flame stability. All these aspects are considered in the performed analysis in this section.

The spray shape and angle, the radial and axial penetration depth of the fuel, and finally the liquid/gas phase distinction needed to be determined in order to be able to characterize the combustion. For this purpose, a Mie scattering measurement (see section 5.2 and Figure 5.5) (W20 x H25 mm^2) was performed for a wide range of fuel temperatures (150–300°C) at atmospheric backpressure for both injector types. A selected range (190–280°C) is shown in Figure 6.12. The atomization behavior of the fuel remained constant from 150–200°C for both injector types. The Mie scattering measurement was performed in a non-reactive setup excluding the flame effect. The afterburner was turned on during the test and allowed the emerging jet A-1 to react in the rectangular part of the combustion chamber. However, due to the distance, this flame has no effect on the spray.

For the pressure-swirl injector, the expected injection regime of mechanical fuel breakup as a spray is dominant from room temperature up to 200–210°C. This is where the transition to the superheated regime occurs. At atmospheric backpressure, thermal fuel breakup essentially begins at about 220°C. The spray cone angle (SCA) appears to decrease steadily from about 100° at room temperature to 80°, 70°, and 30° at 150°C, 200°C, and 250°C, respectively. The hollow cone gradually changes into a solid spray cone with increasing fuel temperature after the transition to the superheated regime. The transition temperature was analytically determined and represents the accumulated Mie signal curve with the maximum intensity (see Figure 5.7 and Appendix Figure E.4). The transition occurs due to the rapid formation of bubbles near the injector outlet. The bubbles grow and then collide with each other, forming a fine plume. The absence of the hollow spray cone reduces the radial penetration of the fuel and can significantly degrade fuel-air mixing.

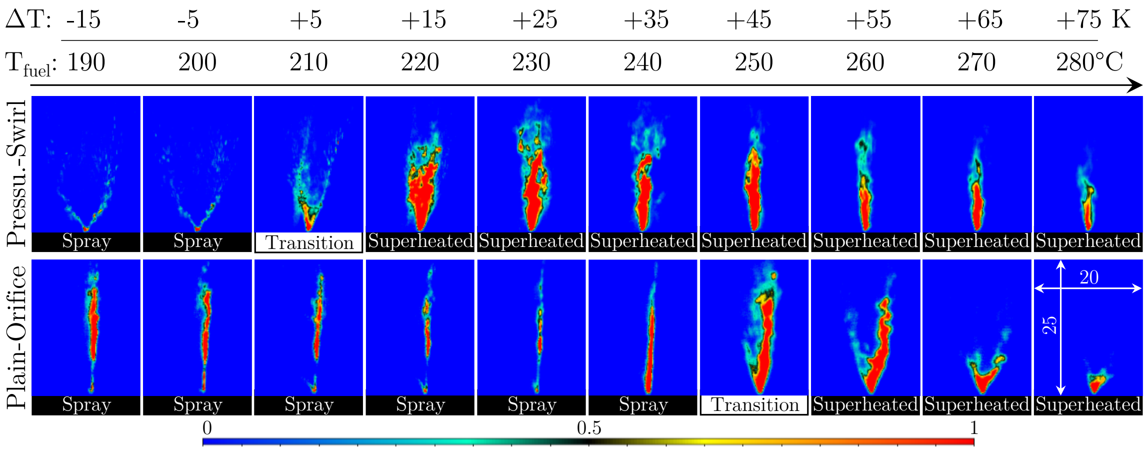

Figure 6.12: Instantaneous Mie Scattering Images of the Fuel Injectors for Various Fuel Temperatures [122]

For both fuel injectors, the transition of the liquid fuel to the gaseous phase can be well observed as the Mie scattering signal decreases with increasing fuel temperature. The gradual decrease in the axial penetration of the liquid phase is clearly visible. This indicates increased fuel evaporation. As the liquid fuel evaporates, it expands and accelerates downstream of the flow. If not slowed by a baffle, this will result in a narrow stream of vaporized fuel entering the reaction zone. This unobstructed flow of fuel can lead to localized fuel-rich pockets. The inhomogeneous mixing of fuel and air can result in a reduction of the flame stability range and thus higher flame temperatures and can facilitate increased NO_x formation.

The Mie signals of the fuel with the plain-orifice injector are shown in the bottom row. The required injector pressure loss of 2–3 bar at a temperature range of 150–240°C was not sufficient to cause any significant mechanical breakup of the liquid fuel at the nozzle exit, since the injector orifice diameter was relatively large at 500 µm and the fuel mass flow was relatively small at 0.52 g/s. Therefore, a jet of liquid fuel was dominant for most of the fuel temperature range up to 240°C. Note that some of the instantaneous images show interrupted Mie signals due to the off-centered liquid fuel jet from the laser sheet.

The transition point, the point at which the jet becomes a plume, for the plain-orifice nozzle is measured at 250°C. This could be due to the lack of swirling motion of the fuel in the injector and the resulting spray sheet. The superheated regime, characterized by a highly turbulent fuel plume, covers more of the laser sheet area and emits more signal to the camera, similar to the pressure-swirl injector. This plume decreases in volume at a faster rate than the pressure-swirl injector because the superheated fuel undergoes rapid thermal breakup into fine droplets that evaporate at high rates. The axial penetration depth of the fuel plume at 280°C appears to be shorter compared to the pressure-swirled injector.

The Jet A-1 spray behavior with increasing fuel temperature was demonstrated in the previously discussed non-reactive tests for both injector types. The injector was returned to its original position in the combustor for reactive tests (see Figure 5.4 *b*).

Figure 6.13 *a* shows the NO_x emissions as a function of the flame adiabatic temperature T_{ad} = 1730–2350 K and the level of preheat ΔT = -50 to 0 K for the pressure-swirl and the plain-orifice injector. Due to the partial evaporation of the fuel in the plain-orifice nozzle, it was not possible to operate at ΔT = +50 K, since the pressure drop of the fuel was much lower at 2–3 bar as compared to 13–15 bar for the pressure-swirl injector. The lower injector pressure drop means a lower saturation temperature of the pressurized fuel. At higher fuel temperatures (> 220°C), this resulted in nozzle choking due to gaseous fuel ejected through the 500 µm orifice. In the non-reactive tests shown in Figure 6.12, much higher fuel preheating temperatures were possible because the nozzle orifice was partially blocked by coking. This allowed the injector pressure drop to increase to 10 bar, allowing higher fuel temperatures without risking fuel vaporization in the nozzle and thus choking.

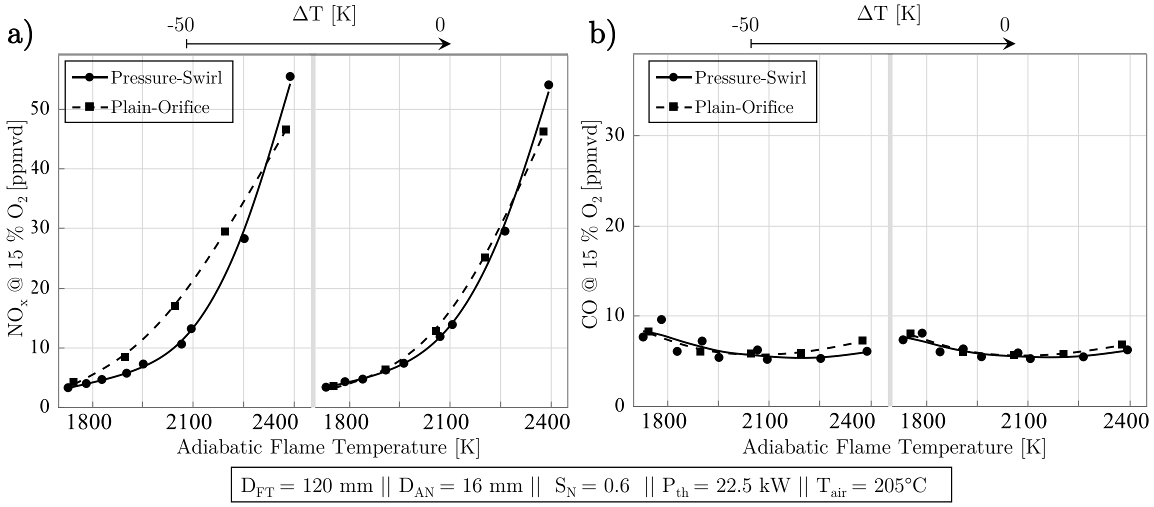

Figure 6.13: Exhaust Gas Emission Values of Fuel Injector Variation vs. T_{ad} vs. ΔT for a) NO_x and b) CO. [122]

The general progression of the NO_x values with increasing T_{ad} seems to be similar for both types of injectors at both ΔT, however, the NO_x trend of the plain-orifice at ΔT = -50 K seems to be increase at faster slope. At T_{ad} = 1730 K and ΔT = -50 K, where the fuel-air mixture is at its leanest and the spray is mostly liquid, the two NO_x values differ negligibly by only 1 ppm. The plain orifice has the higher value at 4.3 ppm. This is because, at higher air equivalence ratios, the velocity in the prefilmer channel is the highest at 17 m/s, leading to an increased airblast effect on the swirler leading and trailing edges. The result is a similar mixing quality of the spray produced by both injectors with air.

The NO_x difference increases to 6.5 ppm at T_{ad} = 2065 K, with NO_x = 17 ppm for the plain orifice. As the velocity in the prefilmer channel decreases to 13.1 m/s, the impingement of the fuel jet on the swirler hub and the subsequent secondary atomization by air blast become insufficient for the formation of fine fuel droplets and fuel-air mixing. As the flame temperature reaches its highest value at ≈ 2350 K, the pressure swirl NO_x level surpasses the plain-orifice with a difference of 9 ppm, with the pressure swirl NO_x at 55.5 ppm. As shown in Figure 6.14 *a*, the reaction zone of the pressure-swirl injector is much more concentrated due to improved mixing and fuel atomization. The reaction zones of the plain–orifice injector appear to be more spread out and less concentrated.

The NO_x levels for $\Delta T = 0$ K for both injector types appear to follow a similar trend in both rate and magnitude. This is due to the reduced fuel droplet size of the plain-orifice injector at higher fuel temperatures at $\Delta T = 0$ K ($T_{fuel} = 205°C$). An increase in fuel temperature not only results in a faster rate of fuel evaporation, but also a decrease in viscosity, which improves the fuel spray quality.

Despite the poorer atomization quality of the plain-orifice injector, the NO_x values of the flames are largely comparable for both injector types, mainly due to the additional internal parts of the combustor (prefilmer and swirler). The difference would certainly be much more pronounced if the straight fuel jet did not hit the swirler hub. However, this also means that the quality of the primary atomization is not the decisive factor for this type of combustor.

As shown in Figure 6.14 *b*, the CO emissions for both injector types remain constant at all ΔT levels and in the entire T_{ad} range due to sufficient mixing and atomization produced under both conditions at a high of 9.5 ppm and a low of 6.1 ppm.

Figure 6.14 *a* shows an OH* image (W120 x H160 mm^2) matrix of the reaction zone for the plain orifice (top row) and pressure-swirl atomizers (bottom row) for a range of $\Delta T = -50$ to $+50$ K. Among other parameters (see figure legend), T_{ad} is kept constant at 2350 K. For each of the injector types, an increase in ΔT leads to a slight change in flame shape and position, while the emitted OH* emission differs significantly between both injectors due to the different compactness of the reaction zone. Because the fuel droplet created by the pressure-swirl is smaller, it evaporates more quickly, resulting in a more concentrated and compact reaction zone. This could be the reason behind increased NO_x levels of the flame of the pressure-swirl at $T_{ad} = 2350$ K.

The LBO limits for both injector types are shown in the combustor operating range in Figure 6.14 *b*. Overall, the pressure swirl injector flames exhibited a constant LBO range over the tested ΔT levels at 1550 K. However, this limit decreased from 1600 K to 1632 K for the plain orifice with increasing ΔT from -50 to 0 K, respectively. The 50 K difference in the LBO limit of the injector types at $\Delta T = -50$ K is due to the larger droplets formed by the plain-orifice injector, resulting in longer droplet evaporation time and decreasing fuel-air mixing. The small increase of 32 K in the LBO limit of the plain-orifice flame by increasing ΔT from -50 to 0 K can be explained by the degradation of fuel-air mixing at near-superheated conditions.

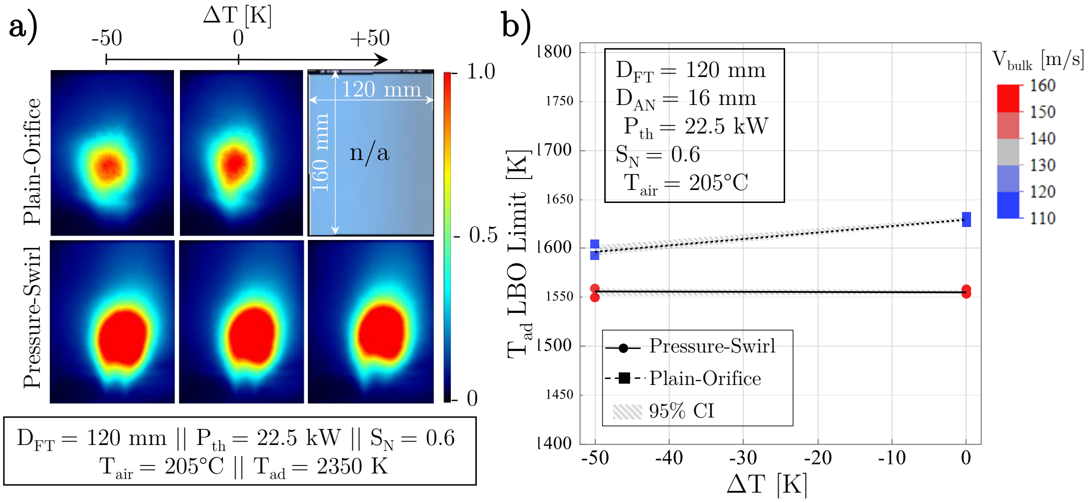

Figure 6.14: a) OH* Images and b) LBO Limits for Different ΔT and Fuel Injectors [122]

Figure 6.15 *a* shows the flame height above the burner behavior of the injectors. Significant differences in the HAB can be observed at ΔT = -50 K T_{ad} < 2200 K with the lowest value of 33 mm at T_{ad} = 2046 K for the plain orifice injector. The larger droplets formed with the plain orifice injector are entrained into the outer recirculation zone. This creates a local fuel-richer condition that reduces the ignition delay time of the mixture. Additionally, the larger fuel droplets increase the time for the fuel droplet to evaporate before forming the reaction zone.

The plain-orifice flame stabilizes closer to the combustor head. This may be due to degraded fuel-air mixture quality and premature ignition of the mixture. The produced larger droplets burn at near stoichiometric conditions, which promotes the production of the radical species necessary to initiate and propagate the chain reaction in the combustion process [118]. This condition leads to faster stabilization of the flame. At ΔT = 0 K, the HAB values for the plain-orifice injector become similar to those of the pressure-swirl atomizer. This is because the fuel droplet size and its mixing with air become comparable to that produced by the pressure-swirl injector.

The flame length values are shown in Figure 6.15 *b* for both ΔT levels. The FL values for the flames with the plain-orifice appear to be consistently higher than the values for the pressure swirl by a maximum of 13 mm. As T_{ad} increases, the FL values converge. At higher flame temperatures, fuel evaporation is enhanced due to increased heat release, resulting in lower FL values. The gap between the FL values of the injector types decreases as the fuel temperature increases. This is due to improved evaporation and atomization of the plain-orifice injector.

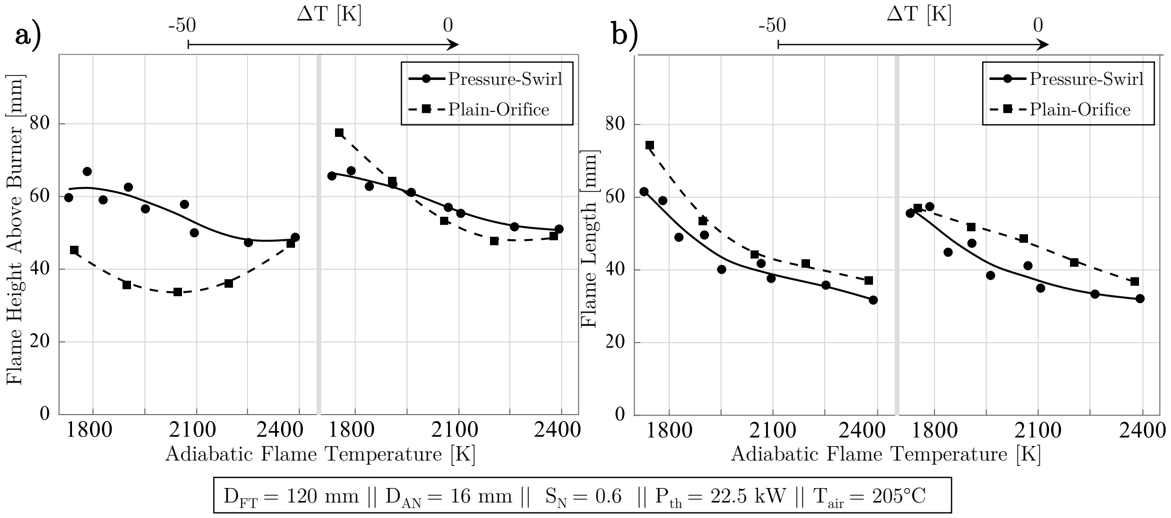

Figure 6.15: Flame Structural Values for Fuel Injector Variation vs. T_{ad} vs. ΔT for a) HAB and b) FL

Summary

By varying the injector type: pressure-swirl and plain-orifice, the effect of spray droplet size on emissions and flame size was investigated. A significant fuel injection behavior change was observed by preliminary non-reactive Mie scattering measurements. While fine droplets of fuel were formed with the pressure-swirl injector, a straight jet of fuel was formed with the plain-orifice injector. The transition temperature from spray to superheated injection regime also differed at T_{fuel} = 210 and 250°C for pressure-swirl and plain-orifice, respectively. The overall liquid phase penetration depth was similar once in the superheated injection regime.

The NO_x levels at T_{ad} = 2050 K for the plain orifice in the sprayed condition exceeded the pressure-swirl injector levels by 6.5 ppm. At the transition temperature (ΔT = 0 K), this difference was reduced to 1.5 ppm. This showed the large independence of the NO_x levels from the primary atomization quality of the fuel for the characterized combustor.

6.4.3 Follow-up Experiment: Fuel Evaporation Characterization

An in-depth study of the effect of fuel and air temperatures on the evaporation of the fuel and the subsequent effect on the size and position of the flame is given in this section. For this reactive test, the pressure-swirl atomizer is placed at its original position in the combustor as shown in Figure 5.4 *b*.

Figure 6.16 shows a matrix of time-averaged images of Mie signals (W18 x H17 mm^2) for an air temperature T_{air} range of 155 to 255°C (columns) and a fuel preheat level ΔT range of -100 to 50 K (rows) in reactive tests. The graphs on the left-hand side represent the accumulated Mie signal intensities plotted against the horizontal x-axis for the different T_{air} levels. See Section 5.2 for a description of the Mie setup.

The signal-to-noise ratio of the reactive tests shown in Figure 6.16 was measured to be half of what was achieved in non-reactive tests shown in Figure 6.12. this is mainly due to smaller fuel droplets exiting the combustor nozzle and thus reduced Mie scattering signal detected by the camera sensor in the reactive tests.

The fuel appears to enter the flame tube circumferentially from the air nozzle because the fuel nozzle sprays directly against the inner walls of the prefilmer and the axial swirler vane surfaces. The swirler hub and the swirling motion of the mixture prevent the fuel from leaving at the near-axis of the air nozzle.

The effect of the T_{air} at a constant ΔT = -100 K is visualized by the decrease in the intensity of the fuel Mie signal as the air temperature increases from 155 to 255°C. It appears that the signal intensities for all three T_{air} levels are asymmetric when looking at the first plot on the left. This asymmetry varies from the left image to the middle image, where more liquid is detected on the left side than on the right side. One explanation for this behavior is an asymmetric spray formation of the fuel nozzle. Also, decreased signal is detected on the right side of the image due to laser energy absorption by the fuel droplets on the left.

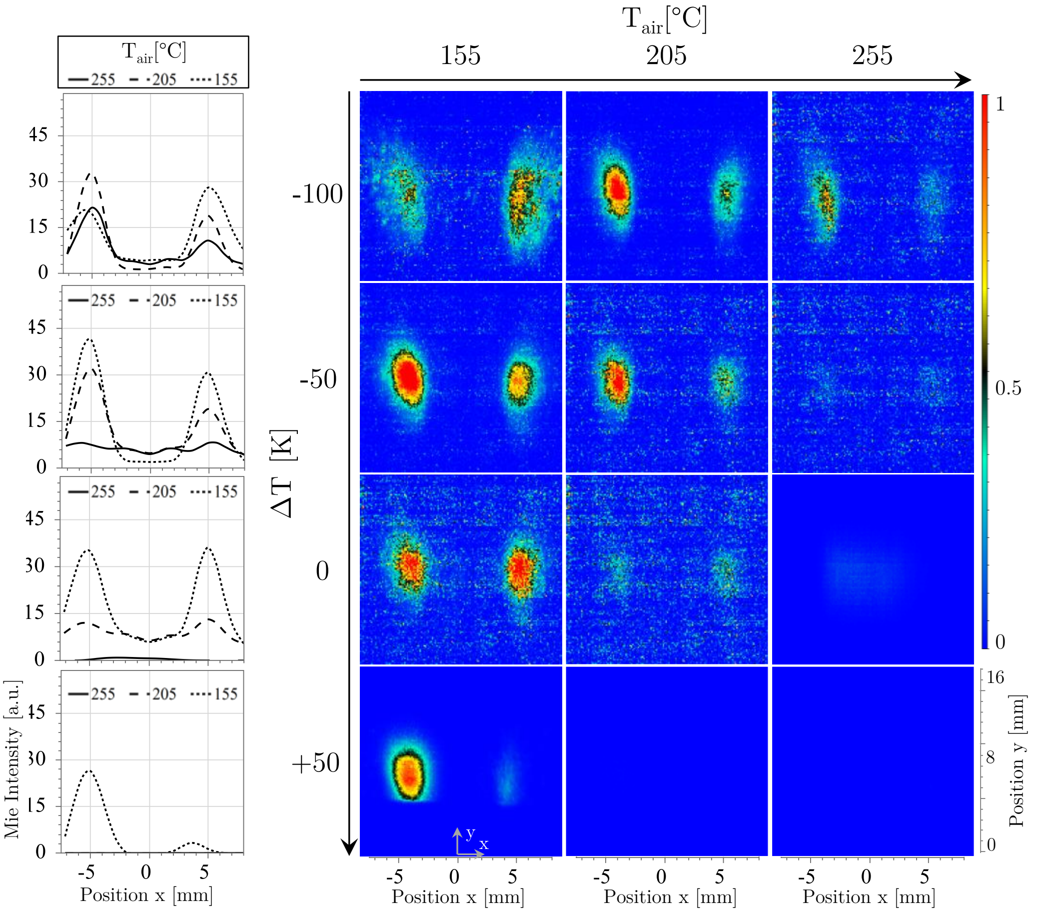

Full-Config || D_{FT} = 120 mm || D_{AN} = 16 mm || P_{th} = 22.5 kW || S_N = 0.6 || T_{ad} = 1900 K

Figure 6.16: Time-Averaged Mie Scattering Image of Jet A-1 in the Reactive Test. Adapted from [122]

At ΔT = -100 K and T_{air} = 155°C, most of the fuel was in the liquid phase. This is because ΔT is below the Jet A-1 initial boiling point (IBP) of 141.1°C (see Appendix Table C.1 for fuel distillation data). An increase in ΔT = -100 to 50 K at T_{air} = 155°C is shown in the left column. A significant change occurs when the ΔT reaches +50 K, where the fuel almost disappears from the right-hand side of the figure. Despite superheated injection of the fuel and its subsequent evaporation (see Figure 6.12), fuel in liquid phase can be observed. The superheated injected fuel at ΔT = +50 K may cool and potentially condense on the inner surfaces of the mixing chamber and in the flowing air, given the relatively lower air temperature of T_{air} = 155°C.The temperature combination of ΔT = +50 K and T_{air} = 205°C shows the lowest air temperature required for complete fuel evaporation without fuel condensation. The air temperature should be maintained above 155°C for complete fuel evaporation.

A corresponding matrix of OH* images for the operating conditions tested in Figure 6.16 is shown in Figure 6.17 *a* at T_{ad} = 1900 K. The derived HAB and FL values are shown in Figure 6.17 *b* and *c*, respectively. It is clearly shown that the reaction zone gains in OH* intensity as T_{air} increases from 155 to 255°C at all ΔT levels. The symmetry of the reaction zone gradually disappears with the increase of ΔT from 0 to +50 K. The lift-off height also increases in this range of ΔT. This indicates that the superheated fuel injection results in a different reduced fuel-air mixture.

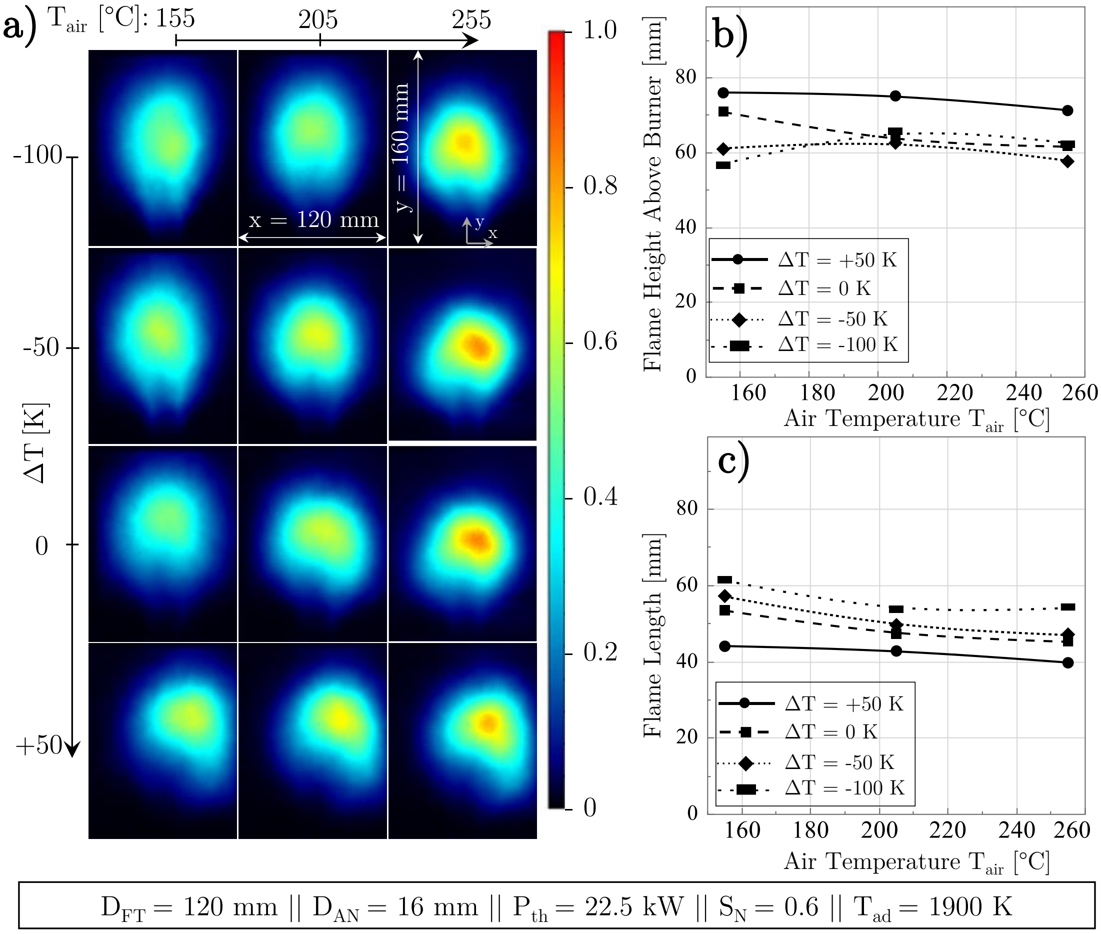

Figure 6.17: a) OH* Images, b) HAB and c) FL at Different ΔT and T_{air}. Adapted from [122]

At T_{air} = 155°C, an increase in ΔT from -100 to +50 K results in a large increase in HAB from 56.5 to 75.2 mm as a result of reduced fuel-air mixedness and reactivity. However, at ΔT = -100 K, an increase in T_{air} from 155 to 255°C results in a relatively small increase in HAB (56.5–62 mm). This behavior proves the existence of an additional effect during fuel evaporation via an increase in T_{fuel} (ΔT). The diminished quality of fuel and air mixing arises from reduced fuel penetration into the coaxial airflow and the concurrent rapid axial expansion of the fuel. The degraded mixing quality should be mitigated by the implementation of an axial swirler.

The flame length values shown in Figure 6.17 *c* indicate a moderate decrease in FL from 61.5 to 44 mm and a minor decrease in FL from 61.5 to 54 mm with increasing ΔT and T_{air}. It appears that fuel temperature has a more significant effect on flame length reduction than air temperature. While an increase in ΔT affects the fuel evaporation, an increase in T_{air} from 155°C to 255°C results in an increase in fuel evaporation and bulk velocity of 15 m/s, which can counteract the effect of fuel evaporation on FL reduction.

Summary

Two operating parameters: air and fuel temperatures were varied to study the degree of fuel evaporation prior to the reaction zone using Mie scattering in a reactive test. At different air temperatures (T_{air} = 155–255°C), the fuel temperature was increased (ΔT = -100 to +50 K). The effect of fuel and air temperature on fuel evaporation in the combustor could therefore be observed independently. The results showed that liquid fuel droplets were visible at the combustor head due to fuel recondensation at the lowest air temperature, even though the fuel temperature exceeded its saturation temperature by 50 K. At the air temperature T_{air} = 205°C and the highest fuel temperature ΔT = +50 K, complete fuel evaporation was achieved. Variation of T_{air} did not majorly affect NO_x and CO emissions. However, the increase in ΔT resulted in a slight increase in NO_x due to degraded fuel-air mixture quality.

The HAB increased (≈ 15 mm) with superheated injection (ΔT = +50 K). This may have been due to the rapid axial expansion of the superheated fuel. The result was a decrease in reactivity and a decrease in the mixture of fuel and air entering the reaction zone. The OH*-CL data showed a stronger decrease in FL with increasing ΔT than T_{air} levels as a result of stronger fuel evaporation effect with increasing ΔT.

6.4.4 Follow-up Experiment: Influence of Combustor Core Components

It is necessary to understand the influence of each of the combustor core components on the flame shape, the operating range of the combustor, the fuel evaporation, and the quality of the exhaust gas emissions. For this purpose, as shown in Figure 6.18, additional detailed experiments are performed in the absence and presence of some of the combustor core components.

The liquid fuel spray path is shown in light blue in Figure 6.18. The areas where fuel is atomized due to secondary atomization (air-blast effect) are colored light green. Pink is the area where the fuel droplets impinge structure surfaces.

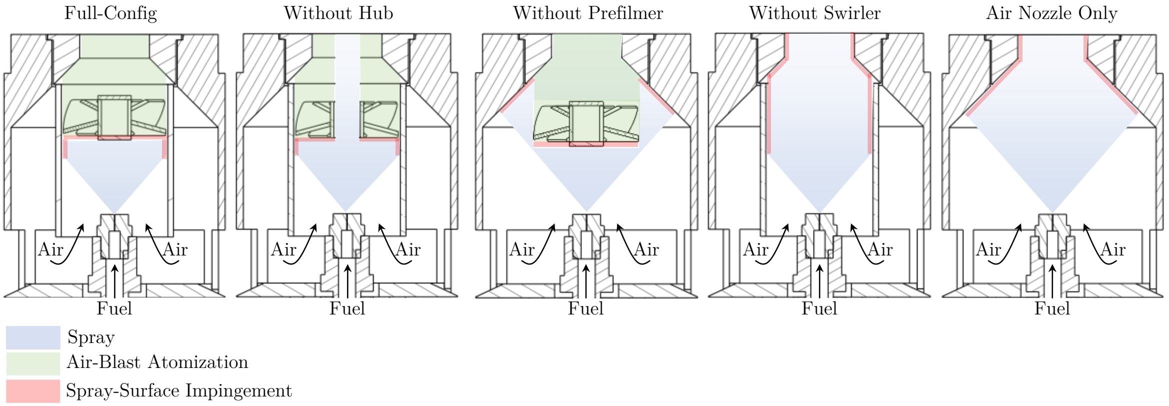

Figure 6.18: Illustration of the Swirl-Assisted Jet-Stabilized Combustor Core Components Variation Tests. Adapted from [122]

Reactive tests are performed using Mie, OH*, and emission diagnostic methods. The swirl-assisted jet-stabilized combustor with all its original components is used as the reference case. This is referred to as the “Full-Config” combustor configuration. The swirler hub is then removed to allow unobstructed fuel and air flow through the swirler center in both spray and superheated conditions. This is referred to as a “w/o Hub” combustor configuration.

In the third combustor modification, the swirler hub was placed back to its original position and the prefilmer channel was removed to isolate its influence on combustion performance. This is referred to as the “w/o prefilmer” combustor configuration. In the fourth configuration, the prefilmer is placed back and the axial swirler is removed. This is to study prefilmer’s effect on flame characteristics and fuel evaporation. This is referred to as the “w/o Swirler” combustor configuration. The last and final step was similar to the unmodified single-jet stabilized combustor tested in previous studies [6,7,46]. However, the air nozzle diameter was reduced to D_{AN} = 16 mm. This is referred to as the “Air Nozzle Only” combustor configuration.

Figure 6.19 *a* shows an OH* image matrix for the described combustor configurations at three T_{ad} levels of 1750, 1900, and 2050 K and $\Delta T = 0$ K. Due to the significantly reduced operating range of the “w/o Swirler” and “Air Nozzle Only” configurations, only one flame condition at T_{ad} = 2350 K was stably operable. Due to the presence of unvaporized fuel droplets in the flame tube and after the reaction zone, no emission measurement was performed for these two configurations. These unvaporized fuel droplets would have adversely affected the ABB gas analyzer as they passed through the probe. The data derived from the OH* measurement (HAB and FL) of the last two configurations could also not be considered. This was due to the resulting long reaction zones that extended beyond the camera field of view into the rectangular part of the combustion chamber.

At all T_{ad} levels, the Full-Config combustor has the most compact heat release zone among the other configurations. This is due to the increased fuel-air mixing and atomizing quality of the Full-Config. The reaction zone for the w/o Hub configuration appears to be more axially extended. To the extent that it leaves the 160 mm long flame tube. Due to the more volumetric flame propagation, the intensity of these flames appears to be reduced. The w/o Prefilmer flames show a less intense OH* compared to the full-config flames. However, they are slightly more axially stretched. This is due to larger fuel droplets entering the reaction zone, which have a longer evaporation time.

In the lower right of the image matrix, the expected long reaction zones are shown for both the w/o Swirler and Air Nozzle Only configurations. Note that due to the reduced operating range of the flames, these flames were operated at T_{ad} = 2350 K. It appears that the w/o Swirler flame is lifted more than the Air Nozzle Only configuration. This is due to the better fuel evaporation of the air nozzle only configuration. Apparently, better heat transfer between the larger inner wall surfaces and the accumulated fuel film results from the heavier and more thermally conductive combustor housing (see Figure 6.18). It is worth noting that the prefilmer mainly led to an increase of the air velocity through the swirler and thus helping to improve the air-blast atomization. Only when the swirler is installed does the installation of the prefilmer make sense.

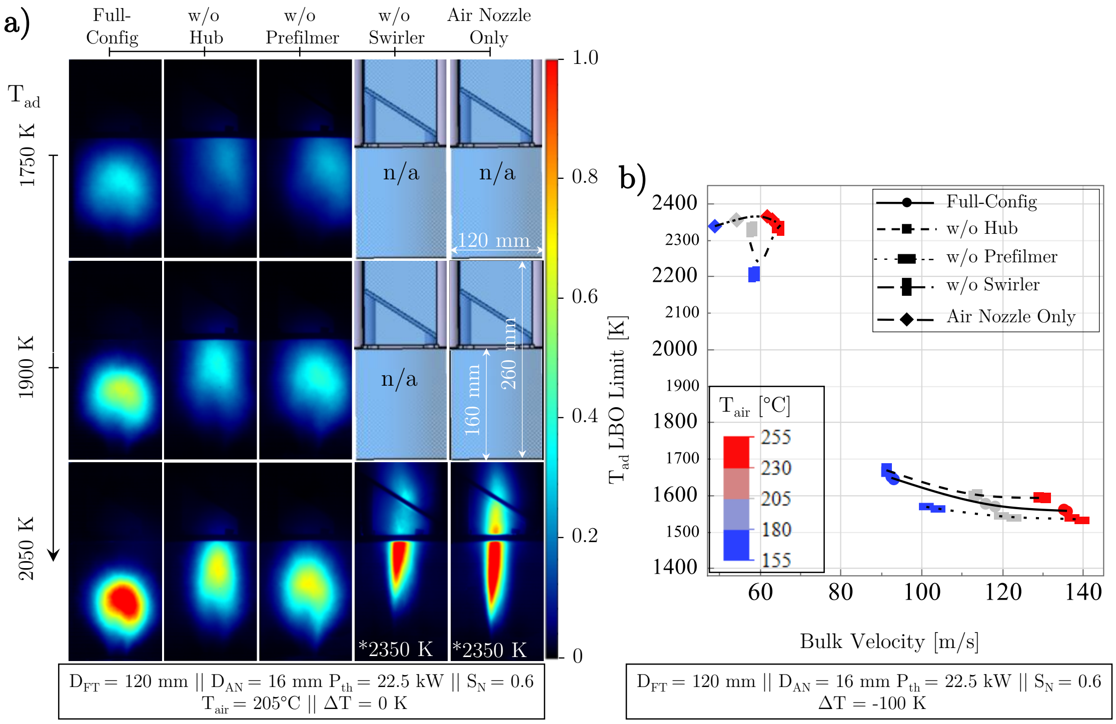

Figure 6.19: a) Matrix of OH* Images for all Five Combustor Configurations and b) Operating Range Plot for Different Configurations. Adapted from [122]

The operating range of the tested configurations is plotted in Figure 6.19 *b* as a function of bulk velocity at ΔT = -100 K. The air temperatures at which the T_{ad} LBO limits were recorded are color-coded: blue symbols for T_{air} = 155°C, pink symbols for 205°C, and red symbols for 255°C. A lower T_{ad} LBO means a wider range of flame stability. This is because the flame was able to maintain its operation at lower temperatures. The Air Nozzle Only configuration had the lowest LBO limit at T_{air} = 155°C and T_{ad} = 2338 K. A slight increase in LBO limit was observed for the w/o Swirler configuration at T_{ad} = 2205 K. At higher air temperatures, this slight advantage of the w/o Swirler configuration disappears as its LBO limits are equal to the limits of the Air Nozzle Only configuration. The hot zones at the flame root that help stabilize the flame also disappear as the large fuel droplets disappear at higher air temperatures.

The bulk velocity range where LBO limits occurred was 91–140 m/s for Full-Config, w/o Hub and w/o Prefilmer. The widest operating range was shown by the w/o Prefilmer, which consistently had a lower T_{ad} LBO at T_{air} = 155°C than the Full-Config, with a margin of 74 K at

1570 K. This margin was reduced to only 18 K at T_{air} = 255°C. The primary reason the w/o Prefilmer had a higher LBO margin was due to the formation of larger fuel droplets than the Full-Config at lower air temperatures. This resulted in “envelope” flames that formed around the larger droplets and burned in a diffusion mode at high temperatures. Also, w/o Prefilmer fuel droplet sizes approached the Full-Config condition as T_{air} increased.

The operating range of the w/o Hub flames showed a slightly lower flame stability of 30–37 K compared to the full configuration at T_{air} = 155–255°C. Originally, the swirler and its hub were installed to block the expansion of the fuel and improve its mixing with the air at superheated injection regime. At T_{air} = 205°C and an increase in ΔT from -50 to +50 K, the flame stability range decreased by 47 K (data not shown here). This means that the swirler hub leads to an increased flame stability at superheated fuel injection regime by improving the mixing of fuel and air prior to the reaction zone.

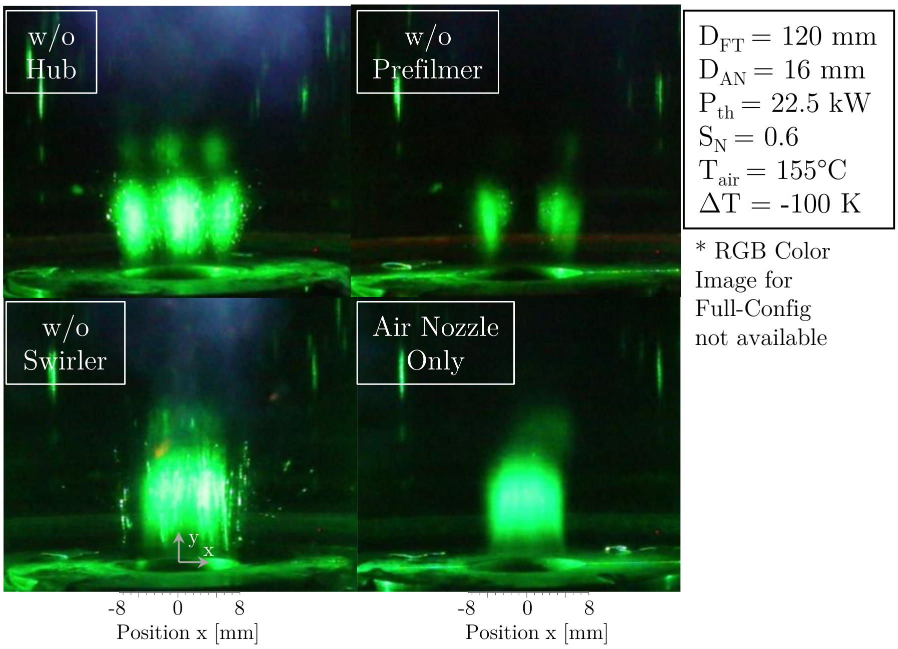

* RGB Color Image for Full-Config not available

Figure 6.20: Instantaneous Jet A-1 Mie Scattering Images Captured by Single-Lens Reflex Camera for Different Combustor Configurations. Adapted from [122]

To investigate the effect of fuel and air as a function of combustor configuration, Mie scattering measurements were performed as shown in Figure 5.4 *a* and *b*. Different degrees of fuel evaporation and droplet patterns were produced by each of the configurations tested (Figure 6.20).

Time-averaged Mie signal images (W18 x H17 mm^2) using a high-speed camera are shown in Figure 6.21 *a*, where ΔT is varied from -50 to +50 K (columns) for all five combustor configurations (rows) at a constant T_{air} = 205°C and T_{ad} = 2050 K. The air and fuel mass flow rates are also kept constant. Although the laser sheet height was mechanically trimmed from 25 mm to 17 mm to allow a more intense and homogeneous signal to pass through the measurement area, it appears that only the middle ≈ 10 mm of the field of view is visible. This is the reason for the elevation of the Mie images. The laser photon energy is blocked by the liquid fuel as it travels from the left to the right side of the image, resulting in the less intense signals seen on the right side of the images.

The different patterns that the liquid fuel has on its way out of the combustion chamber can be seen in different colors. Dark blue is the background. It represents the gaseous fuel phase and air. The light green, black, yellow, and red areas show different Mie intensities captured by the camera from lower to higher. These signal intensities are a qualitative description of the fuel droplet size and density in the vicinity of the combustor head. At $\Delta T = +50$ K, there appear to be some signals visible for the w/o Hub and w/o Swirler configurations, in contrast to the Full-Config, w/o Prefilmer, and Air Nozzle Only configurations.

In both w/o Hub and w/o Swirler configurations, the prefilmer is installed. The visible fuel plume at $\Delta T = +50$ K is due to reduced fuel evaporation. This was caused by the installation of the prefilmer. The installation of the prefilmer reduced the cross-sectional area by a factor of 3.77 and increased the fuel-air velocity through the swirler by the same factor. This reduced the residence time of the fuel droplets in the mixing channel. In the w/o Hub configuration, by slowing the axial flow of the fuel-air mixture, the swirler increases the residence time of the fuel droplets and their mixing with the air. This results in increased evaporation compared to the w/o Swirler configuration.

The other combustor configurations show different patterns of exiting liquid fuel except for the w/o Swirler and Air Nozzle Only configurations where the Mie signal intensities are largely similar. The only difference is at $\Delta T = +50$ K, where the Mie intensity is still visible for w/o Swirler. In the case of Air Nozzle Only, completely vaporized fuel exits the nozzle. In the Air Nozzle Only configuration, the fuel droplet residence time is longer than in the w/o Swirler configuration due to decreased fuel-air mixture velocity in the mixing channel. As a result, the evaporation of the fuel droplets is increased, resulting in complete vaporization of the fuel (see Figure 6.18).

For example, as shown in the Full-Config images, fuel exits the combustor nozzle edge circumferentially because the swirler and its hub block the high-speed exit of fuel from the center of the nozzle. In the w/o Hub configuration, larger and denser fuel droplets exit the center of the nozzle when the swirler hub is removed. The result is a reduction in the amount of fuel exiting the nozzle rim.

At the exit of the nozzle, the w/o Prefilmer configuration shows a more extended Mie signal than the full configuration. At $\Delta T = 0$ K, less Mie signal is observed for the full configuration than for the w/o Prefilmer. This indicates improved evaporation for the full configuration. Initially, to allow combustion under conditions without large fuel droplets burning diffusively in the reaction zone, the prefilmer was installed around the axial swirler. It was observed that the flame without the prefilmer contained burning fuel droplets that were exiting the combustion chamber. By installing the prefilmer, the cross-sectional area around the swirler was reduced by 377% (see Figure 6.18). As a result, the velocity of the mixture through the swirler was increased by the same amount. This increase in velocity increased the air-blast effect on the leading and trailing edges of the swirler vanes resulted in improved secondary fuel atomization.

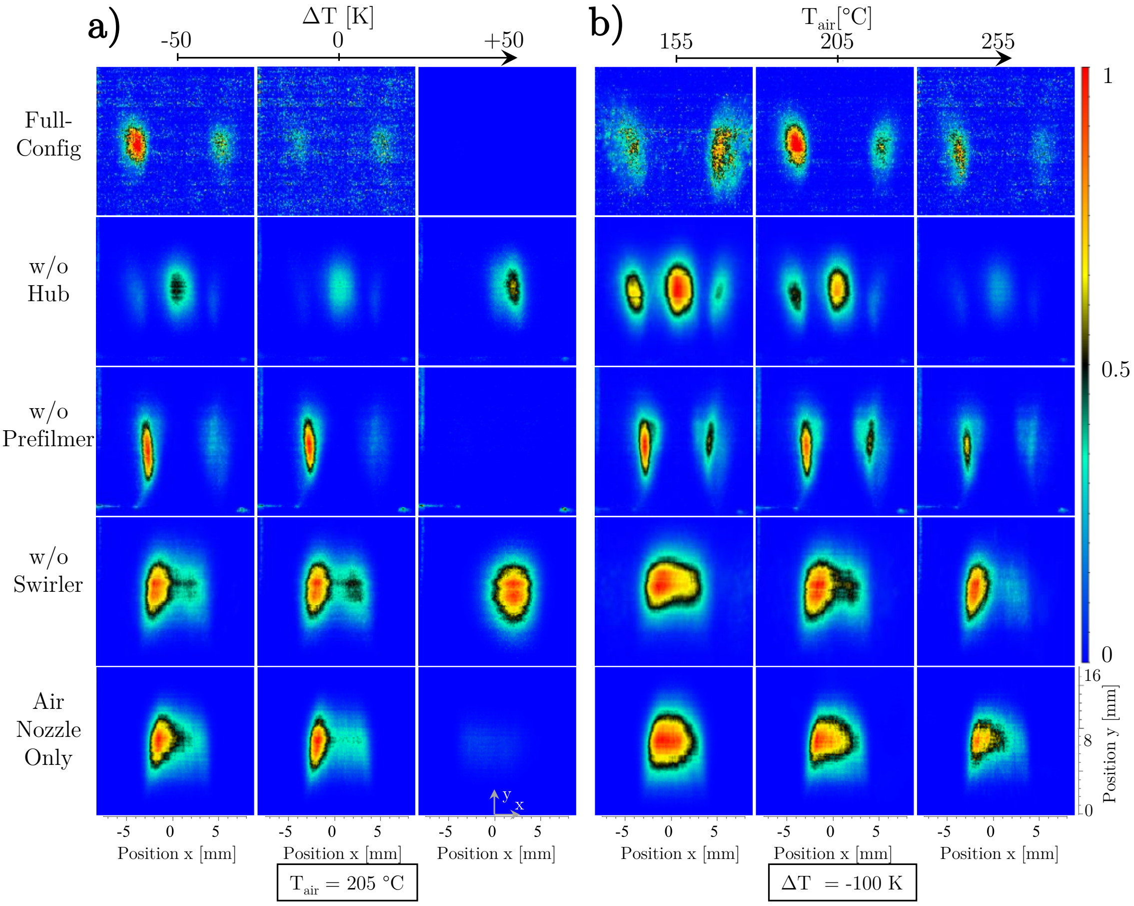

Figure 6.21: Time-Averaged Mie Signals for All Configurations at T_{ad} = 2050 K for a) ΔT Variation at T_{air} = 205°C and b) T_{air} variation at ΔT = -100 K. Adapted from [122]

The Mie signal intensity images shown in Figure 6.21 *b* show the degree of liquid fuel evaporation at a relatively low fuel temperature of ΔT = -100 K (T_{fuel} = 105°C) at different T_{air} = 155–255°C (columns) for the tested combustor configurations (rows). Here, the influence of T_{air} on the fuel spray can be characterized. At first sight, it is obvious that the fuel has not been completely vaporized for any of the T_{air} values. The same fuel droplet pattern is seen here than Figure 6.21 *a*, but with a higher intensity. This is due to less evaporated and larger fuel droplets exiting the air nozzle. It seems that there is a significant interaction effect between the ΔT and the T_{air} on the evaporation of the fuel (as previously seen in OH*-CL images in Figure 6.17 *a*). The liquid fuel can only enter the reaction zone completely vaporized if both parameters are high enough, i.e. above 205°C (ΔT = 0 K).

The resulting degree of fuel evaporation due to increasing fuel ΔT on the NO_x emissions at various T_{ad} for Full-Config, w/o Hub and w/o Prefilmer are shown in Figure 6.22. Note that the scales of the x- and y-axes in Figure 6.22 differ from those in Figure 6.13. Specifically, the x-axis range has been narrowed to focus on the adiabatic flame temperatures relevant to the operating conditions of interest, while the y-axis has been refined to provide greater resolution in depicting the measured NOx emissions. For all configurations and ΔT levels, NO_x emissions increase with increasing T_{ad}. This is due to the higher flame temperature and the resulting increase in thermal NO formation rate. The full configuration consistently shows higher NO_x levels (maximum 4.5 ppm) than the other configurations at all fuel preheat levels (different ΔT levels). This is largely due to the more compact reaction zones of the Full-Config. This leads to a higher concentration of the heat release zone (see Figure 6.19 *a*).

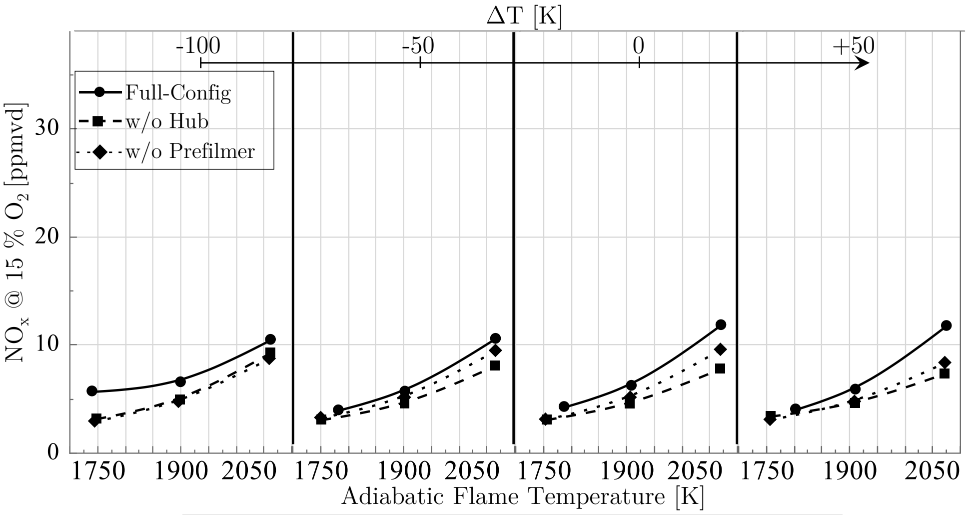

D_{FT} = 120 mm || D_{AN} = 16 mm || S_N = 0.6 || T_{air} = 205°C

Figure 6.22: NO_x Plots for Various ΔT Levels and Combustor Configurations. Adapted from [122]

The emitted NO_x levels for all configurations appear to be largely independent of the fuel temperature (ΔT) and the atomization regime, with a slight change in the NO_x levels as ΔT is increased above -50 K at T_{ad} > 2000 K. For the Full-Config at fuel-leanest point (T_{ad} = 1750 K), by increasing the ΔT from -100 to -50 K, the NO_x levels decrease from 5.7 to 4 ppm due to improved fuel droplet size. For ΔT from -50 to 0 K and at T_{ad} = 2050 K, Full-Config NO_x increases minimally by 1.3 ppm from 10.6 to 11.9 ppm and remains constant up to ΔT = +50 K.

At T_{ad} = 2050 K and for w/o Prefilmer configuration, increasing ΔT from -50 to +50 K results in a 1.1 ppm decrease in NO_x from 9.5 to 8.4 ppm. More propagated reaction zone for w/o Hub and w/o Prefilmer may play a role in the reduced NO_x levels (see OH* images in Figure 6.19 *a*).

The NO_x values are very low over the whole range studied in all configurations. They do not show any extreme increase with respect to T_{ad}. Therefore, the NO_x emissions will not play a major role in the evaluation of the configurations, since the NO_x emissions do not largely vary.

Although the configurations cause a minimal change in NO_x levels, they appear to have a significant effect on CO emissions. This is shown in Figure 6.23. The gradient of CO increase with decreasing T_{ad} is clearly visible. The highest levels of CO for the entire range of T_{ad} and for all the ΔT levels are emitted by the w/o Hub flames. Due to the larger droplets formed by the injector and the reduced fuel evaporation at lower fuel temperature (ΔT = -100 K) and fuel-leaner conditions (T_{ad} = 1750 K), the CO levels are highest (81 ppm).

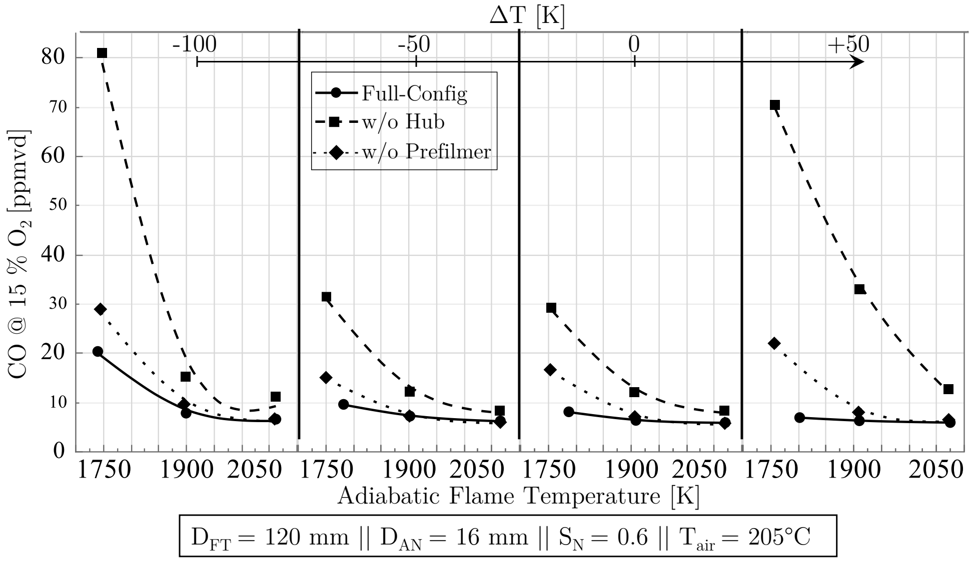

Figure 6.23: CO Plots for Various ΔT Levels and Combustor Configurations. Adapted from [122]

The w/o Prefilmer CO values at $T_{ad} \geq 1900$ K seem to be quite similar to the full configuration at all ΔT levels. However, at the leanest fuel condition (T_{ad} = 1750 K), the w/o Prefilmer configuration shows consistently higher CO levels, e.g. by a maximum margin of 15 ppm at ΔT = +50 K. Insufficient oxidation of CO to CO_2 is caused by longer evaporation time due to larger fuel droplets. While the w/o Prefilmer CO levels decrease to almost the same level at ΔT = -50 K, it increases again to as high as 22 ppm at ΔT = +50 K and T_{ad} = 1750 K. The decrease in CO at ΔT = -50 K is due to reduced fuel droplet size at spray conditions. The increase in CO at ΔT = +50 K is due to the rapid expansion of the evaporating fuel after superheated injection and subsequent degradation of fuel-air mixing. This sharp increase in the CO level is not present in the full configuration. It is evident that the fuel and air mixing downstream of the swirler has been improved by the higher velocity in the mixing channel caused by the prefilmer.

The w/o Hub, on the other hand, due to its inability to block most of the expanding fuel at ΔT = +50 K and T_{ad} = 1750 K, shows a significantly higher CO of 70.4 ppm compared to the w/o Prefilmer and Full-Config at 22 and 7 ppm, respectively. It appears that the swirler hub had significant effect on CO levels due to lower fuel-air mixedness at the superheated conditions. For the Full-Config however, as the fuel temperature increases ΔT ≥ -50 K, the fuel temperature effect decreases on the CO levels. This is due to improved fuel-air mixing and improved blockage of the rapidly expanding fuel at superheated conditions.

The effect of the variation of the configuration on the flame HAB at different ΔT is shown in Figure 6.24. Essentially, by increasing the fuel evaporation rate and improving the fuel-air mixture, the reactivity of the mixture should be increased. This should result in earlier flame stabilization and thus lower flame HAB levels. As previously described, at a constant ΔT = -100 K (see Figure 6.17 *b*), fuel evaporation as a result of increasing air temperature resulted in a minimal decrease in HAB of 5 mm.

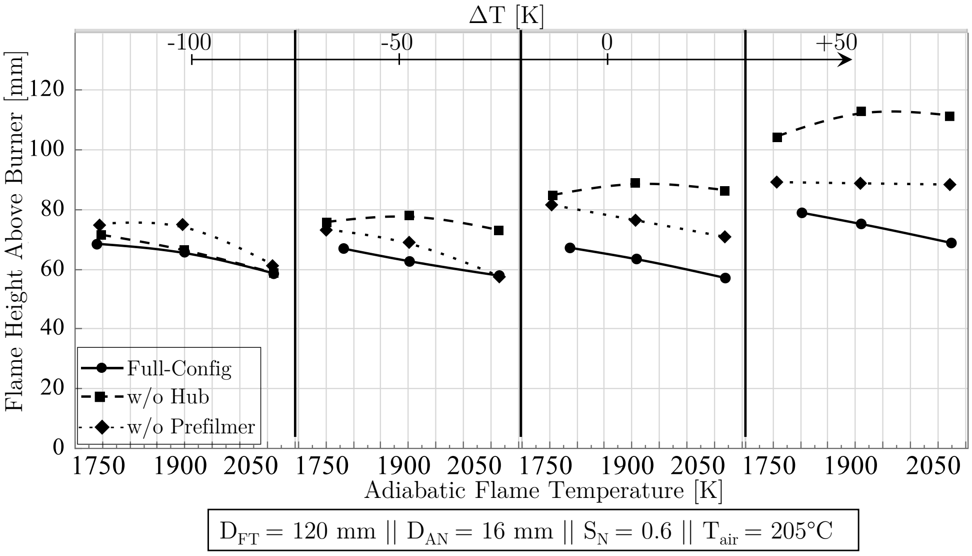

Figure 6.24: HAB Plots for Various ΔT Levels and Combustor Configurations. Adapted from [122]

Nevertheless, the successive increase in HAB as ΔT increases for all configurations, but at different rates, is shown in Figure 6.24. The improved mixing and ability of the Full-Config to block most of the expanding fuel as ΔT increases (-100 to +50 K) is reflected in its lowest rate of increase in HAB from 65.7 to 75.2 mm at T_{ad} = 1900 K. This can be compared to the w/o Prefilmer and w/o Hub configurations whose HAB increases by 14 and 46.4 mm respectively for the same ΔT increase. The prefilmer not only helps direct the combustion air axially through the swirlers. It also increases the velocity to allow for better mixing of fuel and air.

Figure 6.25 shows the flame length data for the tested configurations as a function of ΔT and T_{ad}. The lower FL values are due to better fuel-air mixing, improved fuel droplet evaporation and lower axial velocity. As the flame temperature increases, the FL values decrease. Under fuel-richer conditions, a more reactive mixture and higher rate of fuel evaporation in the reacting zone leads to shorter flames. As ΔT increases, the FL values decrease as the initial time for fuel droplets to evaporate decreases. The result is a shortening of the reaction zone. At all ΔT levels, the full configuration consistently shows the lowest FL values. The leanest fuel conditions, where velocity is highest and heat release rate is lowest, produce highest FL values for all configurations.

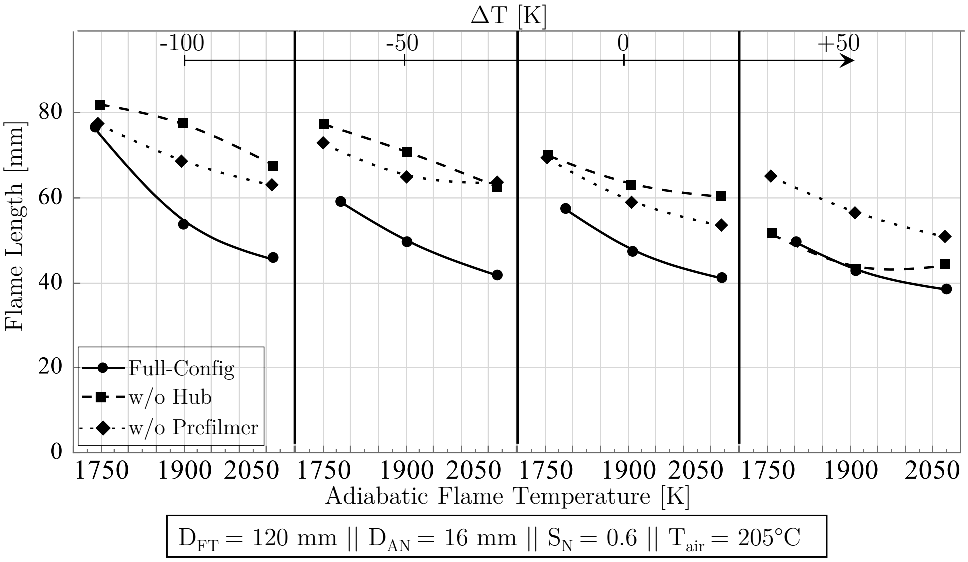

Figure 6.25: FL Plots for Various ΔT Levels and Combustor Configurations. Adapted from [122]

The FL of the w/o hub configuration decreases steadily as ΔT increases from -100 to 0 K by 14.6 mm at T_{ad} = 1900 K. Once the fuel is injected in the superheated condition (ΔT = +50 K), its FL value decreases by 20 mm compared to ΔT = 0 K.

The difference in fuel-air mixing quality of the configurations is responsible for the consistently higher FL values of the w/o Prefilmer than the full configuration at all ΔT levels. The flames at ΔT = -50 K differs in size and intensity for both configurations as shown in Figure 6.21 *a*. The larger fuel droplets and longer evaporation time result from the higher liquid phase concentration. At ΔT = 0 K, the FL gap between Full-Config and w/o Hub continues to widen with increasing T_{ad}. This is due to the improved fuel-air mixing resulting from the smaller fuel droplets in the Full-Config.

Summary

The full and four purposely modified configurations of the combustor were tested regarding their influence on fuel evaporation, emissions, flame operating range and heat release zone shape. It was shown that due to improved mixing and recirculation zone, the combustor full configuration had the most compact reaction zone with lowest overall CO emissions. The configuration without the swirler hub showed rather axially stretched reaction zone with the least NO_x emissions due to shorter residence time in the flame tube.

By blocking large fuel droplets entering the reaction zone, the swirler hub allowed for lower CO emissions at all ΔT levels. The prefilmer increased the fuel-air velocity in the mixing channel. This resulted in improved fuel vaporization and CO levels. The NO_x levels of the Full-Config were slightly higher than the w/o Hub and w/o Prefilmer configurations. This was due to the more compact reaction zones and therefore higher local temperatures. The flame operating range of the Full-Config was similar to the w/o Hub and w/o Prefilmer configurations. However, the HAB and FL levels of the Full-Config were much lower. The data showed that the swirler contributed significantly to flame stabilization due to improved formation of the recirculation zone. The w/o Swirler and Air Nozzle Only configurations had very narrow operating ranges. This was due to the absence of the swirler, which contributed significantly to flame stabilization.

It can be concluded that due to the consistently and significantly lower CO, HAB and FL values of the Full-Config at all fuel preheat levels, the incorporation of the prefilmer, swirler and its hub resulted in improved combustor performance. The slightly reduced operating range and slightly higher NO_x values of the Full Config are offset by the above benefits.

6.4.5 Follow-up Experiment: Influence of Liquid Fuels

A systematic variation of the fuel and thus of its thermal properties, such as the saturation temperature T_{sat}, is required to experimentally study the influence of the degree of preheating ΔT on different liquid fuels.

In an experimental study conducted by Lefebvre [75] on a range of liquid fuels, fuel properties were found to be of secondary importance, with liner pressure drop and furnace operating conditions having the greatest effect on combustion performance. He determined that fuel chemistry, specifically hydrogen and aromatic compounds, had an important influence on flame radiation, liner wall temperature and smoke emission. However, fuel chemistry had a limited effect on combustion efficiency, NO_x and CO emissions. Differences in calorific values were responsible for the small effect observed on combustion temperature. Fuel ignition, weak extinction limits, combustion efficiency and CO emissions were affected by different fuel physical properties (density, surface tension and viscosity), which affect atomization quality and evaporation rate. Changes in fuel physical properties had less effect on parameters such as NO_x and smoke emissions.

Fuel Properties

It is well known that the fuel properties have an effect on the combustion process and thus on the flame characteristic parameters such as exhaust gas emission, stability and flame shape. The selection of fuels with different saturation temperatures, which is one of the main factors influencing the superheated injection behavior, is not easy. To analyze the effect of fuel T_{sat}, it is desired that only the fuel saturation temperature varies. The rest of the chemical, thermal, and physical properties should remain the same. However, since these properties are strongly correlated with each other, a change in one fuel property will result in a change in the other properties [157]. Therefore, 4 different liquid fuels were selected. They differ in saturation temperature, origin, chemical composition, and thermal properties.

As shown in Table 6.2, in addition to fossil-based Jet A-1 as the reference fuel, a hydroprocessed esters and fatty acids (HEFA) [158] fuel equivalent to Jet A-1 but without aromatics, a Fischer-Tropsch [159] surrogate fuel called Future Fuel (FF), and finally a fossil-based heating oil extra light (HEL) were used in the experiments. The effect of the fuel chemical composition on the superheated injection behavior was evaluated by testing HEFA and FF. Refer to Appendix C for fuel surrogate compositions.

In addition, to affect the spraying characteristics of the Jet A-1, an additive: Adizol T-6 (manufacturer: ADIOZ, Kiev, Ukraine) was used at a dose of 3.6 ml/100 l_{fuel}. The use of the additive was claimed to improve the fuel economy of a diesel engine in a paper by Komitov et al. [160]. The manufacturer claimed that the additive leads to a reduction of the fuel viscosity. However, a negligible increase in viscosity from 4.41 to 4.50 mm^2/s was observed in the kinematic viscosity measurement of the fuel without and with the additive, respectively. The ASTM D7042 :2021 method was used to measure kinematic viscosity at -20°C. A maximum viscosity of 8.0 mm^2/s is allowed by the Standard Specification for Aviation Turbine Fuels (ASTM D1655:2022). The measured surface tension of Jet A-1 with and without additive at 15°C was 26.22 and 26.25 N/mm, respectively, a negligible difference of 0.03 N/mm. In the following, the Jet A-1 fuel with the additive is referred to as Jet A-1 (+).

As listed in Table 6.2 and for the fuels tested, the maximum difference in the volume average boiling point (VABP) is 63.3°C. This should have a noticeable effect on the superheated injection behavior of the fuels. The hydrogen content directly determines the required air-fuel ratio (AFR) for stoichiometric oxidation of the fuel. This affects the flame temperature and the combustion products. The aromatics content of the fuels varies considerably, with a difference of 28.6 vol%. This value should have a measurable effect on the particulate emission of the fuels, which was measured using a MCPC device (see Section 5.4 for more details). The density of a fluid is another characteristic parameter in mechanical breakup. Here, the maximum density deviation is 85.5 kg/m^3. And the net heat of combustion (net calorific value) of the fuels is in the range of 42.8 – 44.2 MJ/kg. See Appendix Figure E.3 for the distillation curves of the fuels. Jet A-1 with and without the additive exhibited identical VABP values. The other parameters shown in Table 6.2 were not analyzed for Jet A-1 (+) as they are assumed to be similar to those of base fuel Jet A-1.

Table 6.2: Thermochemical Properties of the Tested Liquid Fuels

Fuel	**VABP**	**Hydrogen Con.**	**Aromatics Con.**	**Density**	**Heat of Combustion**
Unit	°C	[mass%]	[vol%]	at 15°C [kg/m3]	[MJ/kg] (Net)
Method	ASTM D	ASTM D7171	ASTM D6379	ASTM 4042	ASTM D 4809
Jet A-1	206.9	13.65	19.2	814.7	43.138
HEFA	204.2	15.37	<0.5	752.7	44.184
FF	242.8	15.20	0	761.5	43.969
HEL	267.5	13.28	28.6	838.2	42.763

The VABP of the FF (242.8°C) and HEL (267.5°C) is significantly higher than the reference fuel Jet A-1 (206.9°C). Therefore, a higher fuel temperature would be required for a consistent ΔT test. The maximum achievable fuel temperature was 280°C due to insufficient heating power of the electric fuel heater and the maximum available pressure capacity of the liquid fuel supply pump. Therefore, to ensure better comparability of results, a T_{fuel} variation was performed instead of a ΔT variation of the fuels, which would require preheat temperatures above 317.5°C. Actual fuel temperatures required for a ΔT sweep are calculated and listed in Table 6.3, assuming VABP is the fuel saturation temperature.

Calculated laminar flame velocities (s_L) [142] for the tested fuels at the same experimental conditions of atmospheric pressure and air preheat temperature of 205°C are shown in Figure 6.26 *a*. There appears to be two groups of fuels that exhibit different s_L values over the entire range of the air to fuel ratio. Jet A-1 and HEL, with the lower laminar flame speeds, due to their lower hydrogen content and HEFA and FF with their slightly higher s_L values.

Table 6.3: Required Temperatures for ΔT Variation of -50 to +50 K for all Liquid Fuels

Fuel	**VABP**	**ΔT [K]**		
		-50	0	+50
Jet A-1	206.9	156.9	206.9	256.9
HEFA	204.2	154.2	204.2	254.2
FF	242.8	192.8	242.8	292.8
HEL	267.5	217.5	267.5	317.5

At higher temperatures $T > 1500$ K, very small differences in ignition delay times (IDT) are observed for all fuels in Figure 6.26 *b*. At $T = 900$ K, the same grouping trend is observed as in s_L. Jet A-1 and HEL take slightly longer to ignite. The slope at which the IDT progresses with decreasing temperature is relatively constant for all the fuels, which indicates that the activation energy of the reactions that occur is comparable. Overall, the reactivity of the fuels is in agreement with each other. The s_L and IDT values were calculated using the fuel surrogates listed in Appendix C. A Cantera code [161] used to calculated the s_L and IDT values.

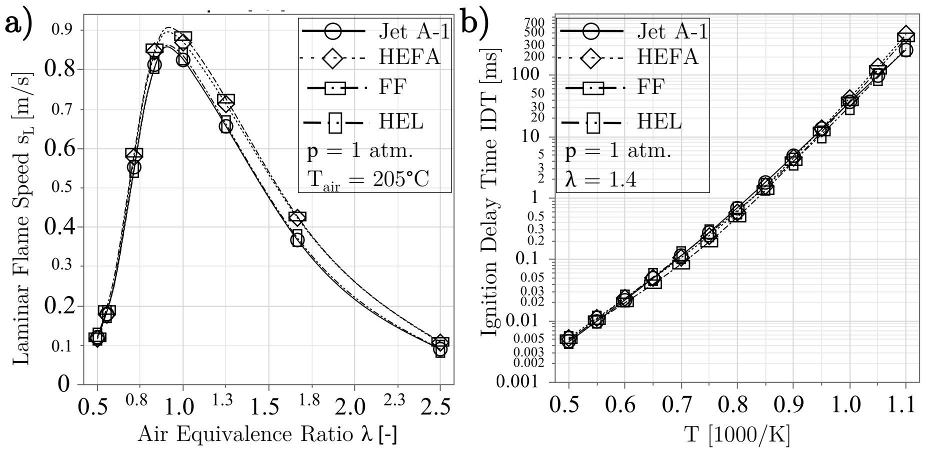

Figure 6.26: a) Laminar Flame Speeds and b) Ignition Delay Times of the Liquid Fuels. Adapted from [142]

Influence of Fuel Properties on the Injection Behavior

Mie scattering measurements were performed in a range of fuel temperatures from 150–280°C for all considered liquid fuels. As described in Section 5.2, for these non-reactive tests, the fuel injector was extended out of the flame tube (see Figure 5.5). A 1 mm thick laser sheet was passed through the injector orifice. The injected fuel in liquid phase and its penetration depth in axial (y) and radial (x) directions are shown in the instantaneous Mie images (W20 x H25 mm^2) in Figure 6.27. Assuming the VABP resembles the saturation temperature of HEFA, FF and HEL, the approximate ΔT values are shown in white script above each of the Mie images. For Jet A-1 and Jet A-1 (+), the saturation temperature T_{sat} (p = 1 atm) ≈ 205°C was used which was calculated using Antoine Equation 3.35, as suggested by Rachner [109] (see Section 3.5).

A transition to the superheated regime occurs at an intermediate fuel temperature range, which varies with different fuels and different VABP values. At higher fuel temperatures, usually close to the VABP, the spray formation mechanism collapses. Instead, a plume of very fine fuel droplets is formed. As fuel temperatures approach the final boiling point (FBP), this superheated fuel injection leads to rapid evaporation and expansion of the fuel (see Appendix Table C.1).

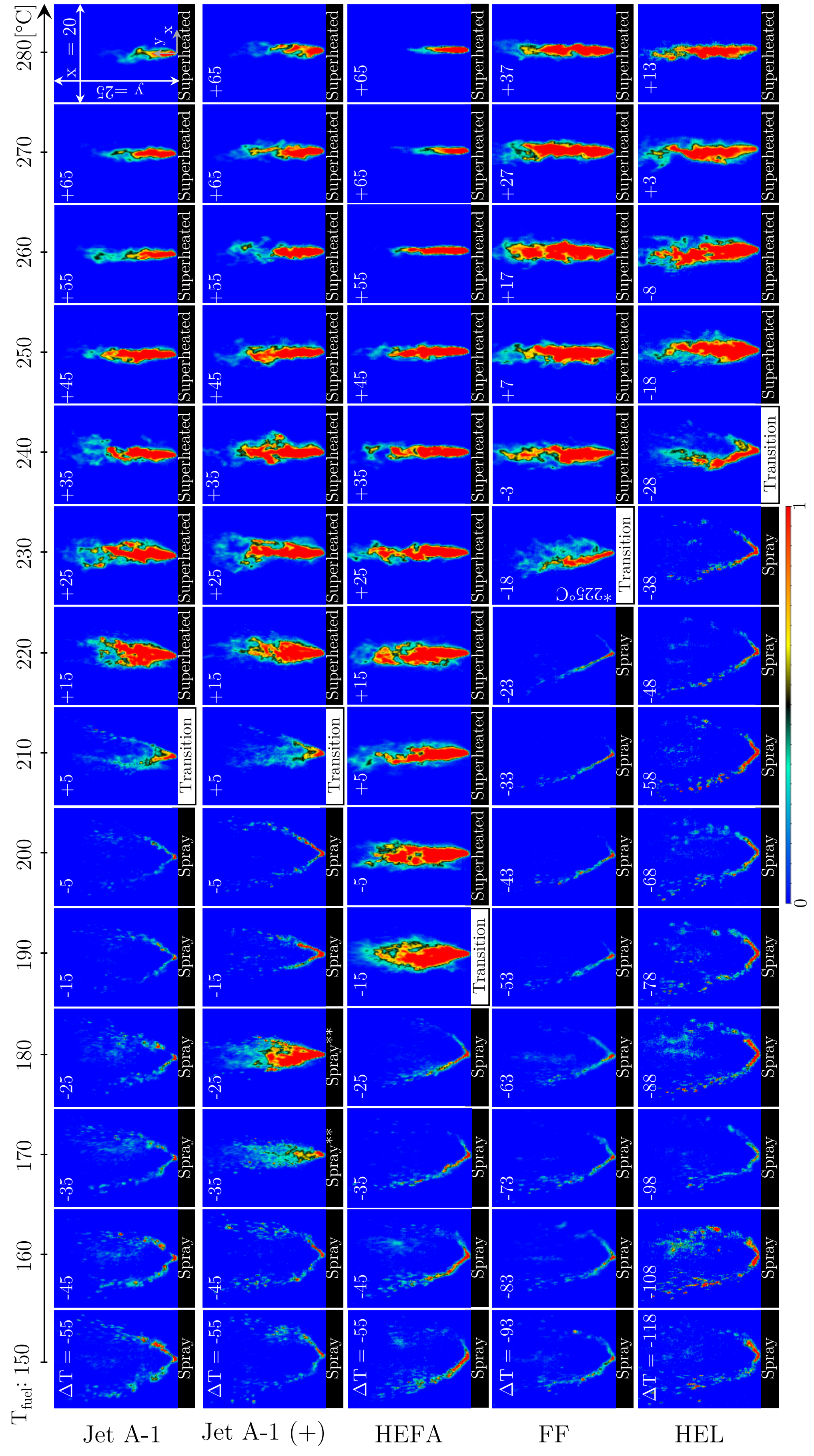

Figure 6.27: Instantaneous Mie Scattering Images for Various Fuel Temperatures of the Liquid Fuels [142]

In general, the injected fuel atomization regimes can be divided into three categories. At low fuel temperatures, the mechanical breakup of the liquid mass leads to the formation of fuel ribbons and then droplets due to the high kinetic energy of the liquid exiting the fuel nozzle. The spray regime extends up to $T_{fuel} \approx 210°C$ for Jet A-1 and Jet A-1 (+). At this temperature, the spray suddenly changes to a plume. It can be observed that the spray patterns for both Jet A-1 and Jet A-1 (+) are comparable. The only visible difference between Jet A-1 and Jet A-1 (+) is in the spray regime. The spray cone angle (SCA) of Jet A-1 (+) is consistently wider by 15° for $T_{fuel} = 150–170°C$. In addition, Jet A-1 (+) spray showed similar injection characteristics to the "transition regime" at $T_{fuel} = 170–180°C$. Note that this spray behavior was persistent in all 1000 Mie images of $T_{fuel} = 170$ and 180°C. When T_{fuel} was increased above 185°C, injection behavior was reversed to spray regime. The additive may be responsible for the increase in SCA and the immature "transition regime" injection, but with the available diagnostic methods it was not possible to explain this behavior.

For the fuel HEFA, the spray injection regime continues only up to $T_{fuel} \approx 190°C$, although it has similar T50 and VABP of ≈ 202°C and ≈ 205°C, respectively, to Jet A-1. The fuel plume at 280°C for HEFA appears identical with the fuel Jet A-1. The spray characteristics of the FF seems symmetrical up to $T_{fuel} = 180°C$. At higher T_{fuel}, the spray appears to be one-sided from $T_{fuel} = 190–220°C$. A possible blockage of an injector swirler channel could be a reason for this behavior. The heating oil HEL, has the longest spray range with up to $T_{fuel} = 230°C$, since HEL has the highest VABP value of 267.5°C among the rest of the fuels.

The spray regime is characterized by a hollow cone of fuel ribbons and droplets. The advantage of this spray regime is that fuel-air mixing is improved due to extended fuel penetration in the radial direction. This is generally desirable. This is because the fuel-air mixing channels are normally limited in length. The radial encounter of the fuel with the air is reduced by the transition to the superheated injection regime, where atomization occurs by thermal decomposition of the fuel, leading to a reduction in radial mixing quality. The result can be a deterioration in emission levels as well as longer HAB and FL.

As described in section 3.5, sudden fuel vaporization at high temperatures results in a high velocity fuel jet. If not slowed, this would result in higher NO_x, CO and HAB. The air temperature can be increased to achieve the same degree of evaporation while injecting the fuel in spray form. This eliminates the undesirable axial expansion effect of fuel due to superheated injection. For this purpose, a separate experiment was conducted to isolate the effect of air and fuel temperature on fuel vaporization and combustion performance (see section 6.4.3).

Analysis of penetration depth for spray conditions is not possible due to the limited camera field of view in the radial direction (x) and the increased radial penetration of the spray. Figure 6.28 shows the penetration depths for all fuels in axial direction (y) at superheated injection regime. The graph shows the axial distance at which a threshold is reached where the Mie intensity drops below 5 counts. Usually, penetration depth is measured at a point where the Mie intensity decreases to zero counts (absence of fuel droplets). However, for HEL and FF, at high T_{fuel} = 270–280°C, Mie signal was still observed even at the y = 25 mm. Therefore, Mie signal intensity of 5 counts was chosen for all tested fuels to allow for a better comparability (See Figure 5.7 and Appendix Figure E.4 for more details.)

At T_{fuel} = 200°C, only HEFA has reached the superheated injection regime. This is followed by Jet A-1 and Jet A-1 (+) at T_{fuel} = 220°C. As the fuel temperature increases, the fuels vaporize and as a result, the liquid phase length decreases. The penetration depths of liquid FF and HEL are much greater. This is due to their higher VABP values. At 280°C, the injected Jet A-1 and HEL have a penetration depth of 7 and 24 mm, respectively.

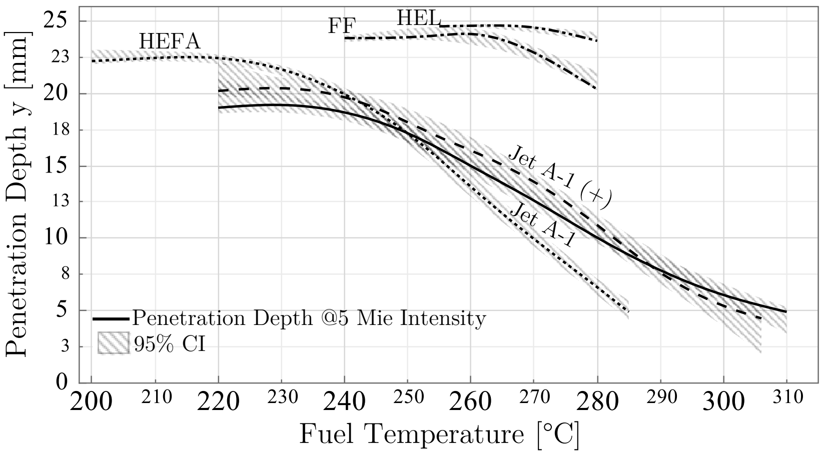

Figure 6.28: Penetration Depth of the Liquid Fuels at Various Fuel Temperatures. Adapted from [142]

Influence of Fuel Properties on the Reaction Zone

Figure 6.29 *a* shows a matrix of OH* images for the liquid fuels tested (columns) at various T_{fuel} = 155–255°C (rows) and a constant T_{ad} = 2050 K. The OH* images of the Jet A-1 fuel show significantly higher intensities than the rest of the fuel. Since Jet A-1 was the first fuel tested and several high temperature stoichiometric flames were run for at least 5 minutes each during the experiments, the cylindrical quartz glass flame tube lost its clear opacity and became cloudy. Therefore, the flames for the other fuels appear to have lower OH* intensities, among other fuel-specific reasons. Therefore, the maximum OH*-CL intensities cannot be compared between the fuels.

An increase in T_{fuel} appears to have some effect on the reaction zone shape, leading to more compact flames. The Jet A-1 and HEFA flames gradually lose their symmetry and stabilize more downstream of the flow as T_{fuel} increases from 155 to 255°C. The flames for Jet A-1 and Jet A-1 (+) differ not only in intensity but also in shape and size. The flame of Jet A-1 (+) seems to be more elongated. The flame shape of Jet A-1(+) is an indication that the vaporization of the fuel droplets is less than with Jet A-1 flames. However, this cannot be explained by the investigated characteristics of Jet A-1(+). At T_{fuel} = 155–205°C the flames of HEFA and FF are remarkably similar. The operation of a stable flame at T_{fuel} = 255°C was not possible due to choking and immature evaporation of the FF in the fuel nozzle, which led to intermittent combustion of the fuel. Therefore, LBO, emission and flame position data for FF at T_{fuel} = 255°C are not available. Compared to the Jet A-1 flames, the HEL flames appear to be more volumetric. This is due to the higher 60.6°C VABP and increased evaporation time of the fuel droplets within the reaction zone. The OH* image matrix of the fuels as a function of T_{ad} is shown in Appendix Figure E.5.

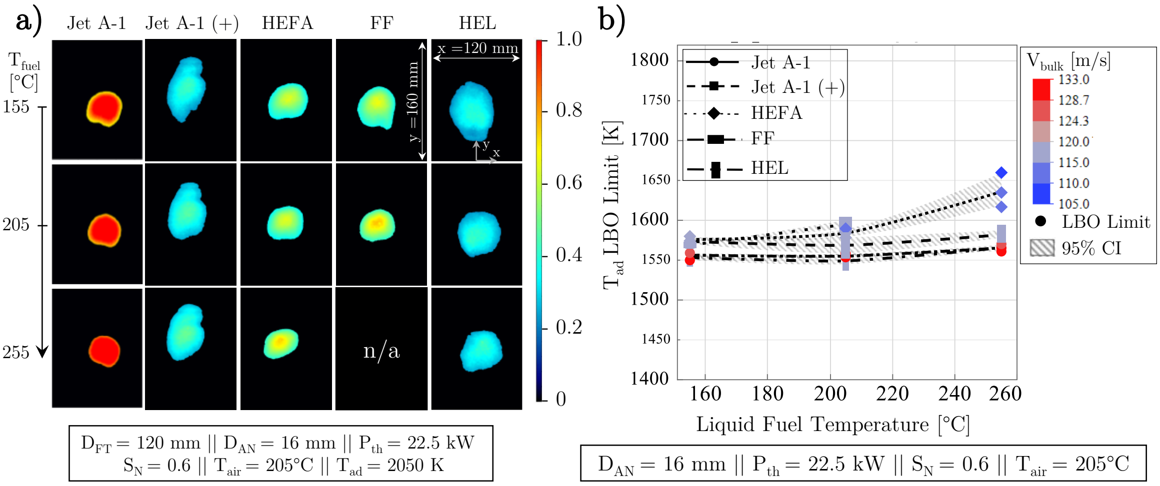

Figure 6.29: a) OH* Images and b) LBO Limits for Different T_{fuel} and liquid Fuels. Adapted from [142]

Figure 6.29 *b* shows the maximum operating range for the liquid fuels. Lower T_{ad} LBO meant higher vbulk values with increasing air mass flow rate. There are two effects that play a role here. First, a very low reaction temperature at which the chain reactions cannot be sustained, resulting in the flame blowing out. Second, higher v_{bulk} results in a velocity profile and recirculation zone that is not ideal for flame anchorage within the flame tube. The first is the more dominant factor here.

The HEFA and FF flames showed a slightly higher T_{ad} LBO limit of ≈ 15 K at T_{fuel} = 155°C than Jet A-1, despite being slightly more reactive (higher flame speed). For HEFA, with increasing T_{fuel}, this gap widened to ≈ 30 K and 70–90 K at T_{fuel} = 205 and 255°C, respectively. Several mechanisms may be behind this behavior. First, the VABP of FF is higher than that of Jet A-1. This results in a longer fuel vaporization time required for stable combustion. Second, despite the blocking effect of the axial swirler, the mixing of fuel and air quality is degraded by axial expansion of the fuel due to the faster transition of the HEFA to the superheated injection regime. Jet A-1 and HEL flames had similar LBO limits at T_{ad} = 1550–1570 K over the entire T_{fuel} range.

The HAB values for a wide T_{ad} range of 1750–2350 K and T_{fuel} values of 155–255°C are shown for the fuels in Figure 6.30 *a*. As the fuel-air mixture becomes more reactive at fuel-richer conditions, the HAB values decrease for all fuels. In general, the HAB levels decrease with decreasing T_{fuel}. This leads to diffusive burning of large fuel droplets, which helps to stabilize the flame as it develops. As described earlier, in addition to the reduced fuel droplet size and enhanced vaporization effect of superheated injection, radial fuel penetration is mostly reduced. Instead, axial, high-speed fuel vapor dominates. The effect of T_{fuel} on HAB values appears to be similar for all fuels.

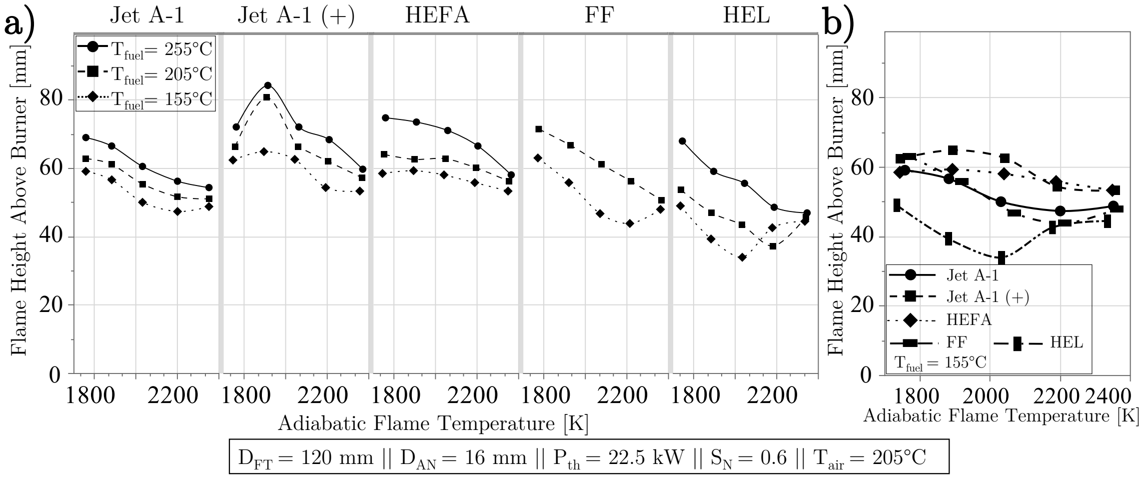

Figure 6.30: HAB Plots: a) for Various Fuel Temperatures and b) for Various Liquid Fuels. Adapted from [142]

For ease of comparison, the fuel-specific HAB values at a constant T_{fuel} = 155°C are shown in Figure 6.30 *b*. At this relatively low temperature, it is expected that most of the fuel exiting the air nozzle is still liquid. The fuel temperature of 155°C is close to the initial boiling points of the fuels of 141, 152, 133, and 177°C for Jet A-1, HEFA, FF, and HEL, respectively (see Appendix Table C.1 for more details). The FF and the Jet A-1 have relatively similar HAB values, while the HEFA and the Jet A-1 (+) have consistently higher HAB values (maximum difference: 12 mm) than the Jet A-1. With the currently available data, the difference between Jet A-1 and HEFA HAB values cannot be explained.

Contrary to the reported observation in the literature [45,162], the flames of HEL show consistently lower HAB values than Jet A-1 flames over the entire T_{ad} range. This is despite identical flame speed and ignition delay characteristics. Due to the low volatility and high density of HEL, the evaporation time of the HEL droplets should increase, leading to an increased HAB. Instead, the larger HEL droplets seem to lead to formation of an extended flame brush at its root, extending the flame upstream of the flow (see Figure 6.29 *a* for visual observation). The currently available data cannot explain this behavior of HEL.

Figure 6.31 *a* shows flame length plots as a function of T_{fuel} and T_{ad} for the various fuels. FL values decrease as the flame temperature increases due to higher reaction zone temperatures. There is a consistent and visible effect of T_{fuel} on the FL values. As T_{fuel} increases, the FL values decrease because the evaporation time of the fuel droplets is reduced, resulting in a faster oxidation of the fuel and a shorter reaction zone length.

Due to the relatively low IBP of Jet A-1, HEFA and FF, their flame length ranges appear similar. Jet A-1 values are lowest in the 32–50 mm range. The flame length values of Jet A-1 (+) are significantly different from those of its base fuel, Jet A-1. Fuel droplet size would be an important factor in the expansion of the reaction zone. However, qualitative non-reactive analysis of the Mie images showed similar spray patterns for both Jet A-1 with and without the additive. The longest FL values can be attributed to Jet A-1 (+) and HEL flames. For the HEL flames, this is due to its low volatility and higher VABP. The significantly higher Jet A-1 (+) FL values than Jet A-1 could be a result of reduced evaporation of the fuel droplets, but the Mie measurement data suggested that the evaporation was similar for both fuels.

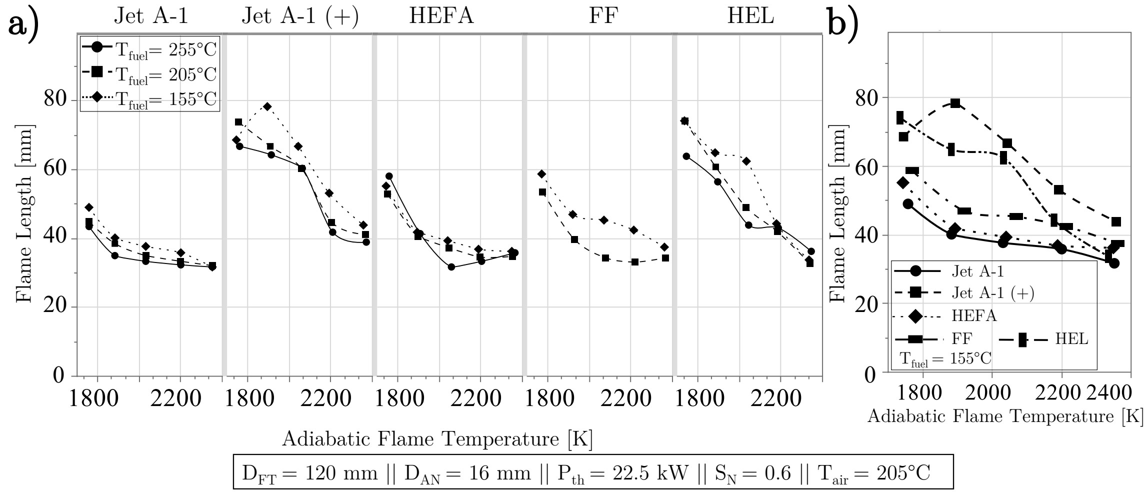

Figure 6.31: FL Plots: a) for Various Fuel Temperatures and b) for Various Liquid Fuels

For ease of comparison, Figure 6.31 *b* shows a plot of flame lengths for the different fuels at a constant T_{fuel} = 155°C. At the highest air-to-fuel ratio, where the fuel temperature is lowest (≈1750 K), the greatest variation in FL for the different fuels can be seen. The fuel evaporation time increases and the flame extends as the reaction zone temperature decreases.

The fuel specific effect diminishes as the T_{ad} reaches its highest value at 2350 K, because the high combustion temperature provides enough heat for the evaporation of the fuels with different

VABP. The chemical reaction rate of the fuel plays a more dominant role in flame length at this point.

Excluding the behavior of Jet A-1 (+) and assuming that the FL differences of Jet A-1 and HEFA are negligible, the lowest to highest FL values can be attributed to Jet A-1 (and HEFA), FF, and HEL. This directly correlates to the order VABP values of the fuels (see Table 6.2).

Influence of Fuel Properties on the Exhaust Gas Emissions

Figure 6.32 *a* shows the NO_x behavior as a function of T_{ad} and T_{fuel} for the tested liquid fuels. As expected, an increase in flame temperature leads to an exponential increase in NO_x formation. This is due to the Zeldovich NO_x formation mechanism. It appears that for none of the fuels, the variation in T_{fuel} has a significant effect on the NO_x levels. This is due to sufficient mixing of fuel and air in the mixing channel through the action of the prefilmer and swirler.

Figure 6.32 *b* shows a separate NO_x plot for each of the fuels at a constant T_{fuel} = 155°C for a better comparison. At T_{ad} = 1750 K, the HEFA and HEL flames emit the lowest (3 ppm) and highest (8.6 ppm) NO_x values, respectively. This trend remains constant throughout the T_{ad} range up to 2350 K, where the NO_x values of Jet A-1 and HEL approximately equalize at 55.5 and 54.5 ppm, respectively. In addition to the different composition of the HEL fuel, its reaction zone may have contained hot pockets. This leads to a local increase in temperature, resulting in increased thermal NO formation. This study also confirms the positive effect of additive on NO_x emissions reported by the literature [163] for Jet A-1(+). However, the dominance of this effect is not justified by the investigations carried out.

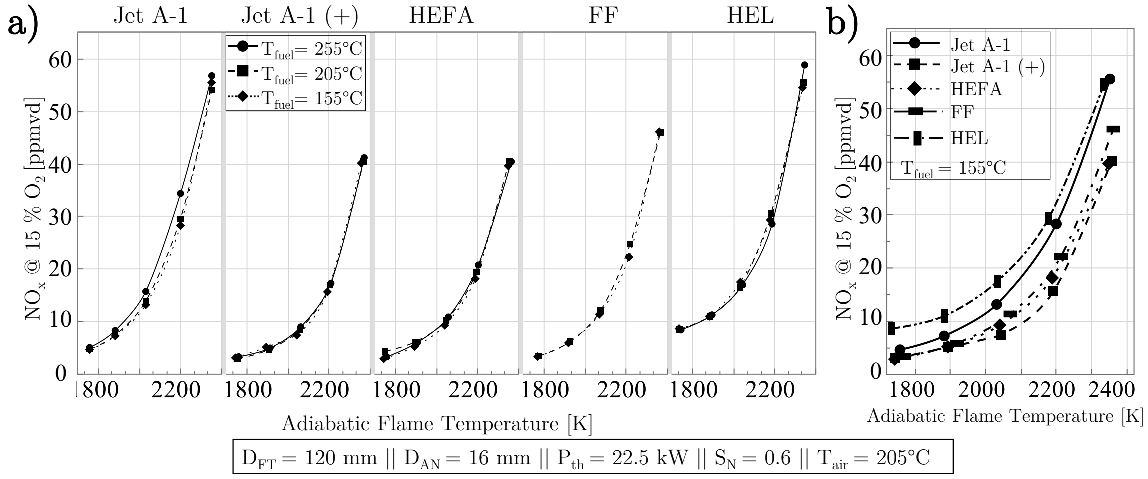

Figure 6.32: NO_x Plots: a) for Various Fuel Temperatures and b) for Various Liquid Fuels. Adapted from [142]

Figure 6.33 *a* shows the CO emissions from the flames for the liquid fuels, adiabatic flame and fuel temperatures. It appears that the flame temperature has a minimal effect on the CO emissions at fuel rich conditions (> 2050 K). The effect of the T_{fuel} on the Jet A-1 fuel is almost nonexistent. The CO levels of Jet A-1 (+), HEL, and FF are at their highest levels at $T_{fuel} = 205°C$. This temperature is similar to the temperature at the transition point from spray to superheat regime for Jet A-1 (+). However, both FF and HEL are injected in spray mode (see Figure 6.27) at $T_{fuel} = 205°C$.

The increase of CO levels of HEL at $T_{fuel} = 205°C$ and $T_{ad} = 1750$ K seems inconsistent and cannot be explained using the current available data. The reduced residence time of fuel droplets leads to reduced evaporation at higher air mass flow rates. This results in incomplete oxidation of CO to CO_2 and thus the sharp increase in CO emissions from FF and HEL flames at the fuel-leanest conditions.

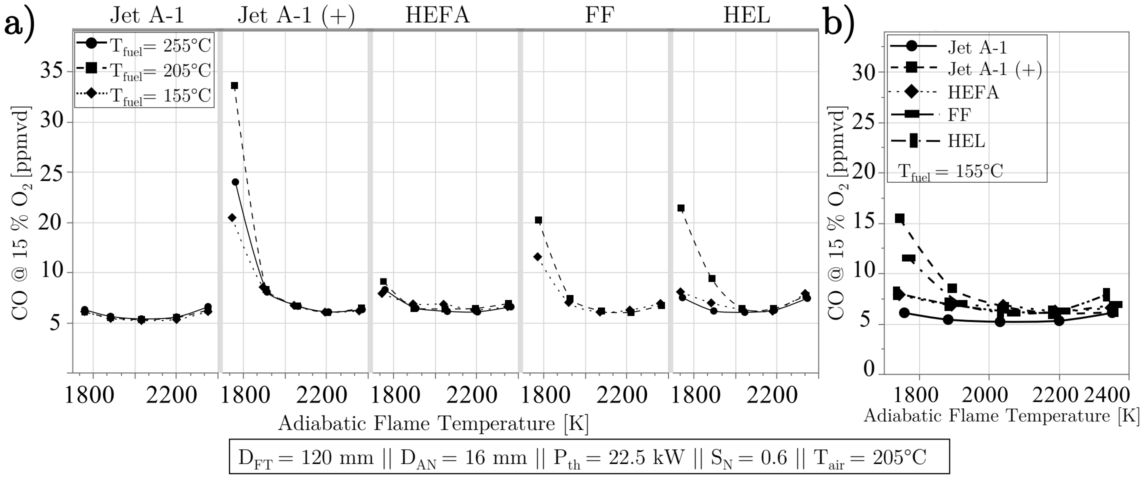

Figure 6.33: CO Plots: a) for Various Fuel Temperatures and b) for Various Liquid Fuels. Adapted from [142]

Figure 6.33 *b* is presented for better comparability of fuel specific CO emissions at $T_{fuel} = 155°C$. For the most part the operating range, the CO values of all the fuels resemble the CO values of Jet A-1. The slightly smaller operating range (LBO) of HEFA is reflected here with a CO difference of 1.8 ppm from Jet A-1. Due to excessive lean conditions and reduced fuel droplet evaporation, FF and Jet A-1 (+) flames show higher levels of CO emissions at $T_{ad} < 2050$ K than Jet A-1. The T_{ad} LBO limits of FF and HEL were fairly similar with Jet A-1 by differed only by 19 and 5 K, respectively. Due higher VABP, the CO emissions of HEL were shown to deviate from Jet A-1 emissions by maximum 2 ppm in the entire operating range of the flames. Higher VABP results in longer fuel vaporization time and therefore shorter time for CO to oxidize to CO_2 for the same droplet residence time.

Visual soot was virtually absent under all operating conditions and fuels. This led to an interest in measuring particulate emissions at various fuel temperatures and for all fuel types. Figure 6.34 shows the number of particles emitted. It was measured using a mixing condensation particle counter (MCPC) described in Section 5.4. This method allows the measurement of particulate matter (PM) in the 7–2000 nm size range in the flame exhaust. However, this technique cannot determine the size distribution of the measured particles.

The goal is to compare the PM levels for each liquid fuel at various adiabatic flame temperatures (T_{ad} = 1750–2350 K) and fuel temperatures (T_{fuel} = 155–255°C). During the measurement tests, 180 samples over 3 minutes were taken. These data were subsequently time-averaged and plotted. The standard deviation of the averaged points are also shown as error bars, which show the spread of the data during the tests. The fuel chemical composition, fuel property, combustion condition and fuel preparation have the most influence on the emission of PM [1]. Due to technical issues, the PM emissions of Jet A-1 at T_{fuel} = 155 and 205°C are not available. However, as seen in the right graph in Figure 6.34, both Jet A-1 and Jet A-1 (+) emit similar PM at T_{fuel} = 255°C and T_{ad} = 1900–2200 K. Therefore, the emissions of Jet A-1 (+) will be used as the reference for the T_{fuel} = 155–205°C cases.

As shown in Figure 6.34, the PM emission of Jet A-1 (+) is progressively reduced as T_{fuel} increases from 155 to 255°C. This is due to smaller fuel droplet size and evaporation at higher T_{fuel} levels leading to reduced emitted particles. At fuel-richer conditions, due to higher flame temperatures, fuel evaporation increases but also formation of soot particles. Furthermore, at higher flame temperatures, the thermal decomposition of fuel molecules leads to the formation of more complex and larger particulate matter. The larger variation of the PM measurement data could partially explain the oscillatory behavior of Jet A-1 and Jet A-1 (+) at T_{fuel} = 255°C with increasing flame adiabatic temperature. However, the available measurement data cannot explain the reason for the partly large standard deviation of the measured particle counts at some of adiabatic flame temperatures.

Interestingly, although HEL has an aromatics content of 28.6 vol%, its PM emissions remain constant at low level over the entire T_{ad} range, except for the colder fuel temperature of T_{fuel} = 155°C, where its PM emissions increase with increasing T_{ad} from 2050 to 2350 K. Here, larger fuel droplet size due to lower T_{fuel} and lower bulk velocity could be the cause of this behavior. At T_{fuel} = 155°C, the PM emitted by the FF flames remains constant for most of the operating range, except for T_{ad} = 2200 K. This increase in PM with T_{ad} is more pronounced at T_{fuel} = 205°C, where the standard deviation is also the largest. With an average counts of 35,600 and a standard deviation of ±48,400, it is very difficult to consider the measurement point as reliable. Sufficient data to explain the extremely high PM variance of FF at T_{ad} = 2200 K is not available at this time.

The synthetically produced fuels, HEFA and FF, show the lowest and constant PM emission regardless of T_{ad} and T_{fuel} variation. These two fuels are the only fuels with zero aromatic content.

The measured exhaust gas emissions and heat release zone data have shown that the swirl-assisted jet-stabilized combustor is capable of combusting a variety of liquid fuels with different compositions and properties. With low emissions and compact reaction zones, the combustor is very well adapted to a wide range of different fuels.

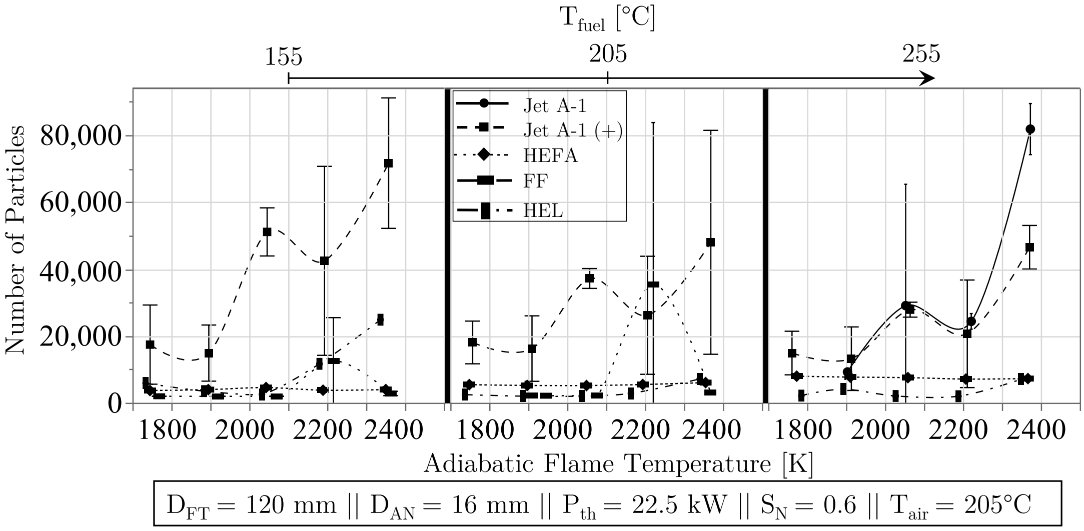

Figure 6.34: Particle Count Measurement Using MCPC for All Fuels and Various T_{fuel}. Adapted from [142]

Summary

In this section, a set of four different liquid fuels of different origin and thermochemical properties were selected to evaluate their spray and combustion behavior with increasing fuel temperature (150–280°C). Jet A-1 as a reference fuel and hydroprocessed esters and fatty acids (HEFA) with similar volume average boiling points (VABP) of 206.9 and 204.2°C, respectively, allowed to evaluate the effect of the fuel chemical composition on the superheated injection behavior. A commercial additive was added to the Jet A-1 at a dose of 36 ppm. This was used to reduce the viscosity and thus improve the atomization of the Jet A-1. Future Fuel (FF) as a surrogate crude oil and Heating Oil Extra Light (HEL), both with higher VABP than Jet A-1 at 242.8 and 267.5°C, respectively, were also tested to evaluate the different thermal effect on the superheated injection. Both fossil fuels Jet A-1 and HEL contained 19.2 and 28.6 vol% aromatics, respectively, while FF and HEFA contained less than 0.5 vol% aromatics.

Mie scattering measurements were performed in a non-reactive test for all liquid fuels considered. It was observed that the spray formation mechanism collapsed at higher fuel temperatures. Instead, a fine plume of fuel drops was generated. Subsequently, as the fuel temperature approached the final boiling point, superheated fuel injection caused rapid evaporation and expansion of the fuel. Spraying was characterized by a hollow cone of droplets, whereas superheated injection occurred in a much narrower solid cone. HEL and FF were shown to penetrate the liquid phase to the greatest depth.

It appeared that increasing T_{fuel} affected the shape of the reaction zone, resulting in a more compact flame. As the fuel injection transitioned from spray to superheat, the Jet A-1 and HEFA flames gradually lost their symmetry and moved downstream of the flow. The flame shape of the Jet A-1 (+) indicated that reduced vaporization of fuel droplets had taken place than in the Jet A-1 flames due to its elongated shape. The flames of HEFA and FF were remarkably similar at lower fuel temperatures. Compared to the Jet A-1 flames, the HEL flames appeared more volumetric. This may have been due to the higher VABP of 60.6°C and the longer time required for the HEL droplets to evaporate in the reaction zone.

As the fuel-air mixture became more reactive under fuel-richer conditions, the flame height above the burner decreased for all fuels. The FF and Jet A-1 had relatively similar HAB values, while the HEFA and Jet A-1 (+) had consistently higher HAB levels than the Jet A-1. Throughout the T_{ad} range, the HEL flames had consistently lower HAB levels than the Jet A-1 flames. This occurred despite the flames having the same velocity.

Under fuel-lean conditions, the HEFA and HEL flames emitted the lowest and highest NO_x values, respectively. This trend remained constant over the entire Tad range up to 2350 K, where the NO_x values of Jet A-1 and HEL were approximately equal at about 55 ppm. For most of the operating range, the CO values of all fuels were similar to those of Jet A-1.

The PM emission of Jet A-1 (+) gradually decreased as T_{fuel} increased from 155 to 255°C. This was due to the smaller size of the fuel droplets and the evaporation at higher T_{fuel} levels, which resulted in lower particulate emissions. Higher flame temperatures increased fuel evaporation but also increased soot formation as the mixture became richer.

An increasingly important feature of modern gas turbine combustors is fuel flexibility. It is also essential for the combustor to be able to burn a variety of fuels with comparable high combustion performance. Based on measured exhaust emissions and heat release zone data, the swirl-assisted jet-stabilized combustor is capable of burning a wide variety of liquid fuels with different compositions and properties. It has been demonstrated that the combustion technology in place can have low emissions and has a wide range of flame stability.

6.5 Influence of Thermal Power

In this section, the influence of various thermal power of the combustor is analyzed. It is assumed that with the increase of the thermal power, the atomization quality will be improved due to higher pressure loss of the fuel injector. In addition, for a constant adiabatic flame temperature, a higher thermal power means a higher air mass flow rate. This results in a higher jet velocity, which can lead to an improved recirculation zone in the flame tube.

The influence of thermal power (P_{th} = 15 to 30 kW) on NO_x at different fuels (ΔT = -50 to +50 K) and flame temperatures (T_{ad} = 1750 to 2050 K) is shown in Figure 6.35. An increase in T_{ad} from 1750 to 2050 K leads to an increase in NO_x values. This is due to an increase in thermal NO formation at higher fuel temperatures.

At ΔT = -50 K, while the liquid fuel is injected in the spray regime, there appears to be a negligible difference in NO_x levels of at most 1.5 ppm between P_{th} = 15–30 kW. A reduction of NO_x levels at P_{th} = 30 kW was expected, as seen in a previous study [6] in a single-nozzle jet-stabilized combustor. With a simplex pressure-swirl atomizer, an increase in mass flow rate results in a decrease in fuel droplet size, which in turn improves fuel evaporation and thus reduces NO_x levels. However, the swirl-assisted jet-stabilized combustor shows an independence of the emitted NO_x and CO emissions from the primary atomization quality, as described in section 6.4.2. The reason behind this phenomenon is the fact that most of the fuel spray interacts with the combustor inner component (swirler) surfaces, which then atomize efficiently as a result of air-blast effect. Despite the general expectation that higher air velocities at increased thermal power would lead to smaller droplet sizes (D_{32}) due to greater shear forces, resulting in more efficient combustion and potentially higher NO_x and CO emissions, the swirl-assisted jet-stabilized combustor shows an unusual independence of these emissions from the primary atomization quality. Consequently, the emissions remain stable even with variations in air velocity and thermal power at ΔT = -50 K.

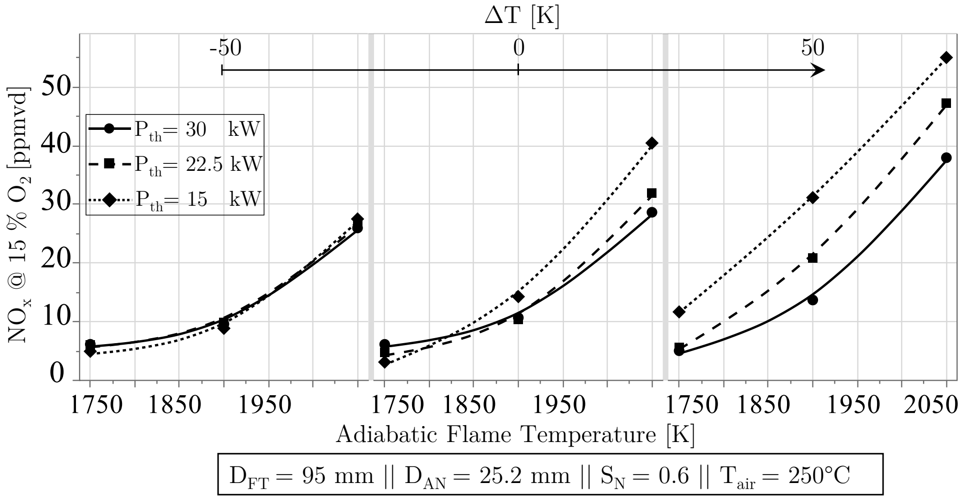

Figure 6.35: NO_x Plots of Various Thermal Power

At ΔT = 0 K and T_{ad} = 2050 K, as the injection regime changes from spray to superheated, increasing P_{th} = 15 to 30 kW leads to a reduction of NO_x levels by 11.9 ppm from 40.5 to 28.6 ppm, respectively. As shown in Section 6.4.2, the injected Jet A-1 at ΔT = 0 K is at transition regime, where some radial fuel-air mixing can still occur. However, some of the more volatile fuel components (about 50 vol%) evaporate and rapidly expand axially leading to reducing fuel-air mixing.

At $\Delta T = +50$ K, the gap between the NO_x emissions increases to 17 ppm for an increase of $P_{th} = 15–30$ kW as the fuel injection occurs at superheated regime. At this fuel temperature, about 95 vol% of the fuel rapidly expands axially while evaporating. This leads to deterioration of the fuel-air mixture as a result of the reduction of the radial penetration of the fuel and the high velocity axial expansion of the superheated fuel.

There was a minimal decrease of 1.2 ppm in CO emissions over the entire T_{ad} range with an increase in $P_{th} = 15$ to 30 kW. The HAB values increased by 7.7 mm with increasing P_{th} due to increased bulk velocity and decreased reactivity of the fuel-air mixture. The FL values also had a negligible increase of 6 mm with the increase in P_{th}. Higher heat output requires an increased fuel mass flow rate, which can lead to a longer evaporation time for the fuel droplets due to the greater volume of fuel needing to evaporate before combustion. The result is an increase in flame length at higher velocity and a decrease in droplets residence time.

Summary

In this section, the potential decrease in emissions due to improved fuel atomization quality was analyzed by varying the thermal power in a range of $P_{th} = 15$ to 30 kW. In addition, the fuel level of superheat ΔT was varied from -50 to +50 K to assess the prevaporization degree of the fuel at different load points.

In the spray injection condition, the NO_x values were not affected by increasing P_{th}. In the transient and superheated conditions, the NO_x levels increased with decreasing P_{th}. This may have been due to lower bulk velocities as a result of lower thermal power and rapid expansion of the superheated fuel, which could result in poorer fuel-air mixing quality.

6.6 Influence of Swirl Number

Increasing the swirl number directly affects the mixing of fuel and air and the recirculation rate, as discussed in Section 3.7. Improved fuel-air mixing can result in improved fuel vaporization and therefore lower NO_x and CO emissions and a more stable flame with a wider operating range. The use of a swirler can also result in a more compact reaction zone and a shorter and less lifted flame. The measured total pressure losses of $S_N = 0.5$, 0.6, and 0.7 were 0.9, 1.1, and 1.3%, respectively, under the baseline operating conditions and with the $D_{AN} = 25.2$ mm.

Flame height above burner (HAB) and flame length (FL) values for three levels of swirl numbers (S_N = 0.5–0.7) and adiabatic flame temperatures (T_{ad} = 1750–2050 K) are shown in Figure 6.36 *a* and *b*. Since the level of preheat ΔT did not affect the HAB and FL data in any significant way, the entire fuel level of preheat $-50 \leq \Delta T \leq +50$ K is included in the graphs. The previously described decrease in HAB with increasing T_{ad} is clearly shown. This is due to the more reactive mixture at fuel-richer conditions. The weak swirl intensity produced by S_N = 0.5 is reflected in the graph by consistently higher HAB values than S_N = 0.6–0.7. The degree of fuel-air mixing and the recirculation rate of the two S_N = 0.6–0.7 seem to be similar. Their HABs follow a similar trend of 55–29.5 mm at 1750–2050 K, respectively.

The slight decrease in the FL values (10–15 mm) with increasing T_{ad} in Figure 6.36 *b* is due to the higher heat release at fuel-richer conditions which leads to a decrease of fuel evaporation time. Swirl numbers 0.5 and 0.6 show similar FL values (31.5–29 mm) at $T_{ad} \geq 1900$ K, while the resulting FL of S_N = 0.7 shows consistently lower values of 6 mm than S_N = 0.6. The relatively stronger swirling motion of the fuel-air mixture at S_N = 0.7 produces stronger vortex breakdown with more pronounced shear regions, increased turbulence and enhanced mixing rates in the flame tube [1]. This, in return, enhances the combustion process and shortens the reaction zone. The effect of different swirl numbers on FL values can be neglected considering a prediction accuracy of the model of ±5.5 mm.

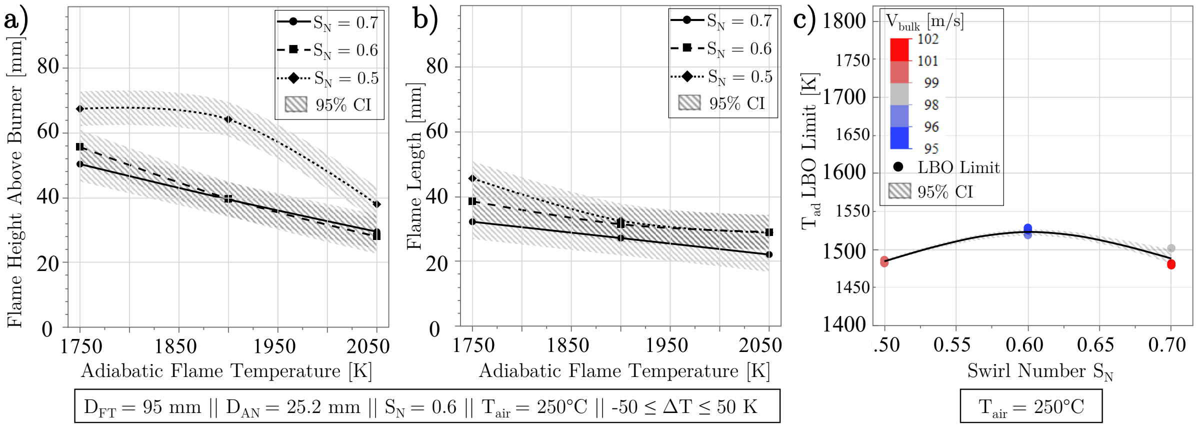

Figure 6.36: a) HAB, b) FL and c) Operating Range Plots of Various Swirl Numbers

The effect of different swirl numbers on flame emissions was virtually nonexistent. This is due to the similar mean residence time of fuel and air mixture and the secondary atomization effect of all swirl numbers. The operating range in terms of T_{ad} LBO for the tested swirl numbers is shown in Figure 6.36 *c* for the conditions shown in Figure 6.36 *a* and *b*, but at T_{air} 250°C. Overall, for the different swirl numbers, a small difference in operating range was observed. The averaged measured T_{ad} LBO limits for S_N = 0.5, 0.6 and 0.7 were 1485, 1523 and 1488 K, respectively.

For the follow-up experiments, the $S_N = 0.6$ was chosen because the total pressure loss differed from the $S_N = 0.5$ only by +10%, while its difference from the $S_N = 0.7$ was +38%. The choice of $S_N = 0.6$ for the follow-up experiments was also based on the similar HAB values to $S_N = 0.7$ due to the comparable fuel-air mixing capability as shown in Figure 6.36 *a*.

Summary

This section discussed the effect of the variation of the swirl number $S_N = 0.5$–0.7 on the performance of the combustor. Increasing the swirl number (S_N) did not have a major effect on NO_x and CO in part due to sufficient fuel-air mixing at $S_N = 0.5$. However, the position and shape of the reaction zone were moderately affected. The HAB values of $S_N = 0.6$–0.7 remained unchanged, while the HAB for $S_N = 0.5$ was higher by 24 mm than $S_N = 0.6$–0.7 at $T_{ad} = 1900$ K. This may have been due to reduced mixture reactivity and dissimilar recirculation zone. The FL values decreased by 4 mm with increasing $S_N = 0.6$–0.7, which could be as a result of better mixture quality by improved fuel droplet dispersion and evaporation. The operating range was not significantly affected by the variation in S_N levels. It was perhaps due to fairly similar secondary atomization and mixture quality at different swirl numbers.

6.7 Influence of Flame Tube Diameter

The size of the gas turbine flame tube diameter D_{FT} must be carefully selected. It can significantly affect fuel-air mixing, residence time, flame operating range, and emissions. In this section, a brief review of the most notable effect of the D_{FT} on a selected set of combustion performance indicators will be presented. As shown in section 4.3.1, the characterized $D_{FT} = 80$, 95, and 120 mm lead to an increase in the dump area ratio of 3.12, 3.77, and 4.77 for a constant air nozzle diameter $D_{AN} = 25.2$ mm. Considering the baseline conditions of air mass flow rate of 12.5 g/s, $T_{ad} = 1900$ K ($\lambda = 1.644$), $T_{air} = 250°C$, and $P_{th} = 22.5$ kW (0.52 g/s Jet A-1), an increase in the D_{FT} from 80–120 mm results in a decrease in flame tube bulk velocities of 13.3, 9.4, and 5.9 m/s, respectively. These bulk velocities yield residence times of 12, 17, and 27 ms in the cylindrical flame tube (see Table 6.4). Although the residence time is highly variable at different GT load points, a typical residence time in a gas turbine combustor is between 15 and 25 ms [164,165]. The flame tube (D120 mm, L160 mm) volume was divided by the volumetric flow rate of the combustion gas to calculate the residence time (see Equation 6.1). The product gas density was calculated by NASA CEA [55] at equilibrium and adiabatic temperatures.

$$\tau = \frac{V}{\dot{V}} = \frac{\rho V}{\dot{m}} \tag{6.1}$$

Table 6.4: Flame Tube Bulk Velocity and Residence Time for Various Flame Tube Diameters

D_{FT} [mm]	$\dot{m}_{air}$ [g/s]	$\dot{m}_{fuel}$ [g/s]	Aspect Ratio	$v_{bulk\ @\ Flame\ Tube}$ [m/s]	$t_{residence}$ [ms]
80	10.9–14.4	0.52	3.12	12.6–14.2	12.8–11.3
95	10.9–14.4	0.52	3.77	8.9–10	18–16
120	10.9–14.4	0.52	4.77	5.6–6.3	28.7–25.4

Changing the D_{FT} tends to have a more pronounced effect on the flow field [165]. It is expected that the smaller D_{FT} will have a relatively shorter recirculation zone, and thus a lower recirculation rate, and vice versa.

The HAB values for each of the flame tube diameters at different adiabatic flame temperatures are shown in Figure 6.37 *a*. The D_{FT} = 120 mm flames consistently showed the highest HAB values for the entire T_{ad} range, contrary to the expectation that a larger flame tube diameter should result in a lower HAB value due to reduced velocity gradient and longer residence time in the cylindrical combustion chamber. For example, at T_{ad} = 1900 K, the HAB levels of D_{FT} = 120 mm were consistently higher than D_{FT} = 80 and 95 mm by 17 and 10 mm, respectively. Reduced entrainment of recirculated exhaust gas into the fresh gas mixture results in reduced dilution of the fresh gas at the root of the flame for the D120.

Due to larger volume available in the D120 flame tube, the reaction zone further propagates leading to more extended flame. This behavior is shown in Figure 6.37 *b*, where the measured flame lengths of D120 were consistently higher than D95 and D80 at 40.5, 31.5 and 24.8 mm, respectively at T_{ad} = 1900 K. A possible explanation would be that due to increased dump area ratio, flame and chamber wall interaction could be reduced which leads to reduced flame quenching and thus larger reaction zone.

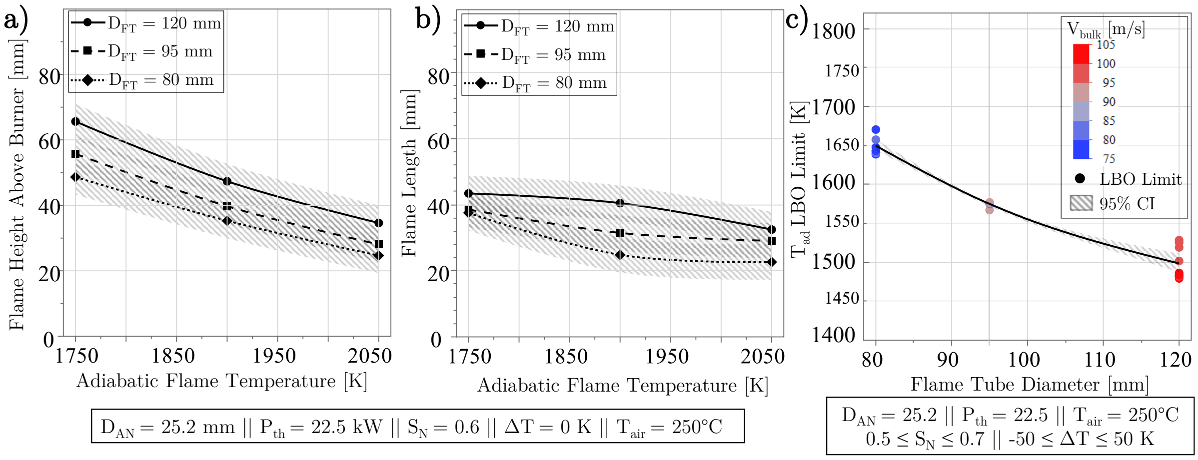

Figure 6.37: Flame Tube Diameter D_{FT} Effect on a) HAB, b) FL and c) LBO Limit

The LBO limits for the three tested flame tube diameters are shown in Figure 6.37 *c* at T_{air} = 250°C. For each of the flame tube diameters, several LBO limit tests were conducted. The graphed LBO limits also include the test points at different ΔT (-50 to +50 K) and S_N levels (0.5 to 0.7). The calculated bulk velocities v_{bulk} (75 to 105 m/s) are color coded. It is expected that by increasing the bulk velocity in the flame tube with increasing flow rate, the recirculation strain rate is increased that can influence the flame stability.

The widest flame operating range was observed with D120 at an averaged LBO limit $T_{ad} = 1498 \pm 19.3$ K and $v_{bulk} = 99 \pm 2.1$ m/s due to the increased residence time of the required radicals in the reaction zone needed to sustain the flame. The change in the fresh gas jets and the exhaust gas mixing could be a possible effect. If more exhaust gas is entrained into the fresh gas jets at larger D_{FT}, then leaner conditions could prevail, which would result in an LBO at a lower T_{ad}.

A larger dump area ratio provided more space for the fuel-air to mix and react, resulting in more stable combustion and preventing flameout at higher flow rates. Reduced residence time in D80 of 18–24.5 ms, which is about one-third of D120, reduces fuel-air mixing and the time needed for the fuel to react with the air. Increased quenching due to the lower dump area ratio of D80 can also result in premature flameout near the tube wall. Averaged LBO limits for D80 were observed at $T_{ad} = 1649.7 \pm 10.3$ K and $v_{bulk} = 79.6 \pm 3.2$ m/s, which is approximately 152 K lower than the D120 LBO limit.

While there was a noticeable effect at the LBO limit (see Figure 6.37 *c*), a decrease of 5.7 ppm NO_x was observed with increasing $D_{FT} = 80$–120 mm at $\Delta T = 0$ K and $T_{ad} = 2050$ K. At the same fuel temperature and $T_{ad} = 1750$ K, this change was reduced to 0.5 ppm because the NO formation rate at fuel-lean conditions is so low that the behavior becomes less dependent on the residence time. The CO emissions were not significantly affected by the D_{FT} variation. This was due to the adequate recirculation zone and residence time provided by all three flame tube diameters. See Appendix Figure E.6 for combustion emission data.

For the follow-up experiments, the D120 was the choice, as the laser sheet reflection was minimal due to its larger diameter. To further minimize NO_x emissions, the D120 flame tube also had the largest operating range.

Summary

This section discussed the effect of the variation of the flame tube diameter $D_{FT} = 80$–120 mm.

Variation of the flame tube diameter (D_{FT}) mainly affected the mean residence time, the bulk velocity in the flame tube, and the recirculation shape and rate. Primarily, the reaction zones HAB and FL were affected. Despite the longer residence time and slower bulk velocity, the HAB values increased by 17 mm with increasing $D_{FT} = 80$–120 mm. The entrainment of the recirculated hot exhaust with the fuel-air mixture at the flame root had occurred at a higher rate for the D80, resulting in higher mixture reactivity and faster flame stabilization.

Flame length values also increased with increasing D_{FT} due to the increased dump area ratio, which reduced flame tube chamber wall interaction. This resulted in reduced flame extinction and a larger reaction zone. The operating range was significantly increased by 152 K with increasing $D_{FT} = 80$–120 mm. This could be due to decreased residence time of the required radicals in the reaction zone needed to sustain the flame. In addition, a larger dump area ratio provided more space for the fuel-air mixture to mix and react, resulting in more stable combustion and preventing flameout at higher flow rates.

6.8 Influence of Steam Injection

The purpose of this section is to characterize the resistance of the developed swirl-assisted jet-stabilized combustor to external perturbations such as the dilution of the combustion air with inert gases such as steam. In addition, the experiments are intended to show that the combustor can be operated with both liquid and gaseous fuels. These tests will evaluate the effect of Jet A-1 and natural gas (NG) (as reference fuel with $AFR_{stoich} = 16.25$, $LHV = 47.36$ MJ/kg, see Appendix C for composition details) on flame emissions, stability and shape. In addition, since there are many researches related to steam injection in NG flames, a better comparison with literature work can be made by testing with NG. A ∅1.3 mm plain-orifice injector was used as the fuel nozzle for the NG experiments.

Steam injection is an alternative method of diluting the reactant mixture and reducing the flame temperature, as described in Section 3.6. Mainly due to the thermal effect of the steam acting as a heat sink, the flame temperature is reduced. Steam injection also has the advantage of not significantly disturbing the flow profile, thus maintaining the combustion stability performance.

Experimental Conditions

At first, water (at 25°C) was injected into the preheated air flow in the mixing tube about 1000 mm prior the air nozzle outlet (see Figure 4.3). However, at water mass flow rates greater than 0.8 g/s, incomplete evaporation of water was observed even at $T_{air} = 255$°C. As a result, the decision was made to inject the water in a prevaporized state (steam).

Table 6.5: Boundary Conditions of Steam Injection at T_{air} = 305°C, P_{th} = 22.5 kW, ΔT = -100 K and λ = 1.0

$\dot{m}_{air}$ [g/s]	$\dot{m}_{H_2O}$ [g/s]	WGR [%]	NG T_{ad} [K]	Jet A-1 T_{ad} [K]
7.6	0	0	2343.7	2385.1
7.6	0.66	8	2170.2	2216.4
7.6	1.32	16	1993	2052.5

For these tests, the preheat air temperature was kept constant at T_{air} = 305°C. This is high enough to prevent condensation of water in the mixing channel. In addition, the water was heated up to ≈ 105–115°C under 3–4 bar pressure using a 3.6 kW electric heater. The water was injected through a pressure-swirl nozzle in a superheated state. The injection technique was similar to that used for liquid fuel injection. This was done to ensure its evaporation and complete mixing with the air before entering the combustion chamber.

The air equivalence ratio, λ, was increased from 1.0 in 0.2 increments up to near-LBO limit. To measure the effect of water vapor content on combustion performance, the water-to-gas ratio (WGR) was varied from 0 to 16% in 8% steps. A constant 22.5 kW thermal fuel power was maintained. D_{FT} = 120 mm and D_{AN} = 16 mm were selected as the flame tube and air nozzle diameters, respectively. To evaluate the effect of WGR variation on liquid and gaseous fuel combustion performance, Jet A-1 and natural gas were selected (see Table 6.5).

For the steam injection tests, the previously electrical liquid fuel preheater was used for heating up the water. Therefore, in these tests, the liquid fuel was supplied only at room temperature. However, the injected Jet A-1 at the nozzle had a T_{fuel} = 105°C (ΔT = -100 K), due to heat transfer between preheated combustion air and fuel lines in the combustor plenum.

The chemical kinetic effects of the presence of water vapor in the reaction zone can be evaluated by plotting the emission values as a function of adiabatic flame temperature as shown in Figure 6.39 *a* and *b*. These chemical effects include both the changes in the concentration of the species and the third body effects of the H_2O. Separately, NO_x and CO values as a function of air equivalence ratio λ are shown in Appendix Figure E.7, which illustrates the combined thermal (temperature) and chemical effects of steam on emissions.

Flame Exhaust Gas Emissions

The wide, stable and low emissions operating range of the combustor for both NG and Jet A-1 show the fuel flexibility of the combustor at dry conditions WGR = 0% (see Figure 6.38 *a* and *b*). Similar to the results obtained by Snyder et al. [64] (see Figure 3.5 *a*), the NO_x emissions of Jet A-1 appear to be higher (+15 ppm) than those of NG at λ = 1.0. The higher stoichiometric

T$_{ad}$ of Jet A-1 and hot combustion temperatures of the liquid fuel around the droplets may account for this [1]. However, the results of the current study show nearly equal NO$_x$ and CO values for both fuels at T$_{ad}$ < 2300 K, in contrast to the results of higher NO$_x$ for the liquid fuel at identical flame temperatures shown by Snyder et al. [64]. This may be due to similar combustion conditions and comparable mixing of both fuels with air in the reaction zone. Another reason for this phenomenon could be the reduced effect of localized near-stoichiometric burning of the liquid fuel, which approximates the combustion conditions of both liquid and gaseous fuels [1]. The higher T$_{ad}$ LBO limit of NG and the localized quenching of the reactions leading to increased incomplete combustion are responsible for the sharp increase in CO levels in the fuel-leaner conditions (T$_{ad}$ < 1900 K).

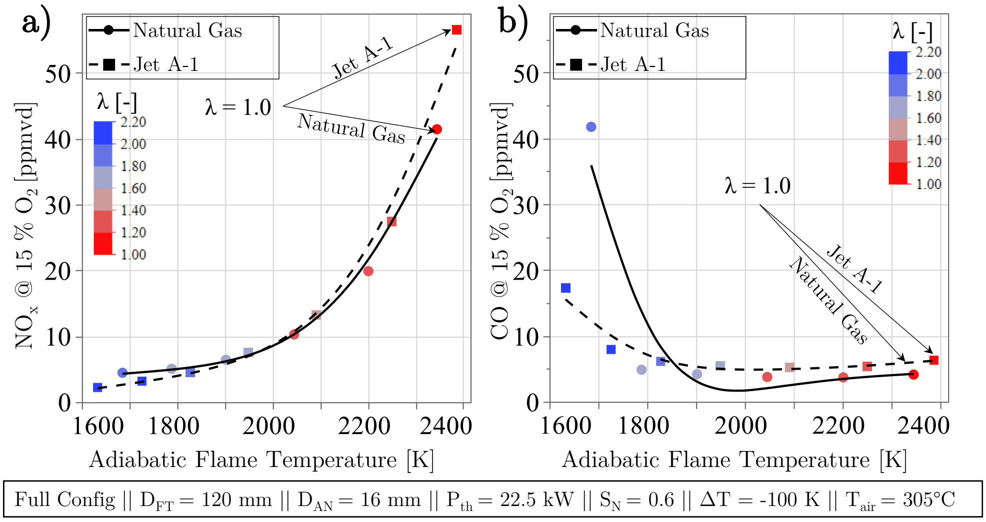

Figure 6.38: a) NO$_x$ and b) CO Emissions for Different Jet A-1 and NG at WGR = 0%. Adapted from [140]

The evaluated results in Figure 6.39 *a* show that by increasing the WGR = 0 to 16%, the NO$_x$ levels decrease from 56.6 to 10.1 ppm (-82%) and from 41.5 to 0 ppm (-100%) at $\lambda = \varphi = 1.0$ for Jet A-1 and NG, respectively. This is mainly due to thermal effects, i.e. flame temperature reduction from T$_{ad}$ = 2385 to 2052 K at WGR = 0 to 16% for Jet A-1 and T$_{ad}$ = 2343 to 1993 K for NG. It appears that at T$_{ad}$ ≥ 2050 K, the chemical effect (kinetics and third body effects) dominates the NO$_x$ formation for liquid Jet A-1, while for NG, the chemical effect rather dominates at T$_{ad}$ ≤ 2050 K. Chemical effects stem from the kinetics of the reaction, as opposed to thermal effects, where the introduction of steam into the reaction zone increases the heat capacity of the mixture and reduces the temperature of the combustion process.

In addition to the dilution effect of steam injection on the fresh gas and limiting the availability of oxygen, the third body role of water molecules can also promote the formation of free radicals needed to enhance fuel oxidation. In addition, under conditions where O$_2$ and O radical concentrations are higher, steam reduces NO_x formation by reducing the formation of oxygen radicals, which are the primary source of NO_x formation. [166]

The NG behavior is confirmed by Cong et al. [166], who reported that the chemical effect of steam on NO_x formation is higher under fuel-lean conditions than under stoichiometric conditions for methane combustion. Under fuel-lean conditions, the concentrations of O_2 and O radical are higher than at $\lambda = 1$ mixtures. According to Cong et al. [166], the formation of NO_x is reduced by steam through the reduction of O radical formation.

At WGR = 16%, the NG flames showed a T_{ad} LBO limit of 1830 K. The two operating points measured at T_{ad} = 1930 K and 1993 K showed 0 ppm NO_x. This behavior was shifted to lower T_{ad} levels as steam content was reduced to WGR = 8%. Here, while the NG flames showed a T_{ad} LBO limit of 1700 K, the emitted NO_x levels were at 0 ppm at T_{ad} = 1750 and 1850 K. Inhibition of NO_x emissions by increasing steam concentration is primarily due to reduced flame temperature, which leads to reduced thermal NO formation. Dilution and reduction on N_2 concentration are other factors influencing this behavior [166].

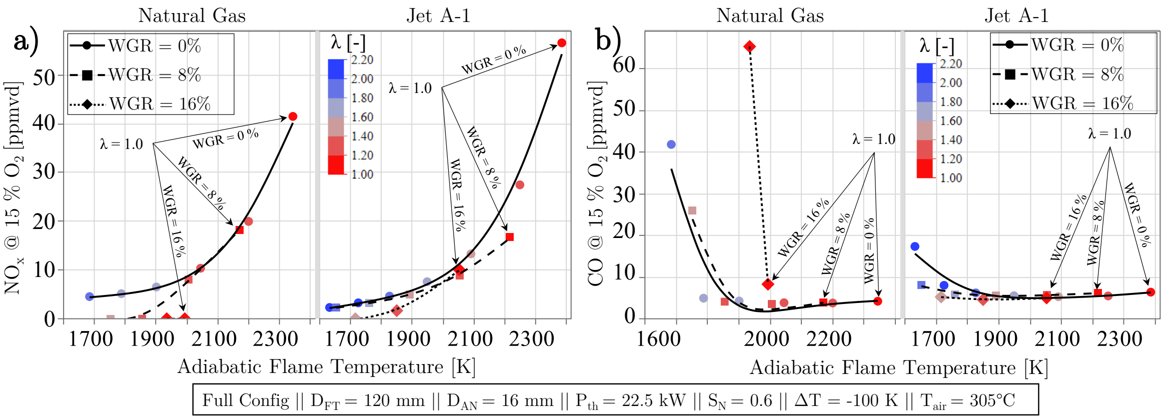

Figure 6.39: a) NO_x and b) CO Emissions for Different T_{ad}, Water-to-Gas Ratios and Fuels. Adapted from [140]

Figure 6.39 *b* shows the measured CO emission levels of the corresponding operating points with WGR variation for Jet A-1 and NG. The CO levels remain constant at 5.8 ±0.74 ppm for all WGR levels for Jet A-1 and at stoichiometric conditions. At fuel-lean conditions up to T_{ad} = 1700 K, this constant level of CO is maintained to a large extent with an average level of CO = 5.8 ±0.84 ppm for all WGR levels. CO levels increase to a maximum of 17.3 ppm at WGR = 0% at lower flame temperatures of T_{ad} < 1700 K due to flame quenching effects near-LBO limit.

For the natural gas flames, the emitted CO concentrations are not significantly affected by WGR = 0–8%. However, at WGR = 16%, due to the proximity of the T_{ad} LBO limit, the operable points at T_{ad} = 1993 and 1935 K have the greatest deviation in CO levels with +5 and +61 ppm. Here, the low flame temperatures and the local quenching in the reaction zone cause the CO not to oxidize to CO_2. The CO values measured in this study remain constant over a wide operating range, which is in contrast to the CO values reported in the literature [165] for a steam injected premixed swirl-stabilized combustor operated with NG.

Flame Size and Shape

Figure 6.40 *a* and *b* show the OH* images for different steam loads for Jet A-1 and NG. The effect of mixing fuel and air prior to the reaction zone is the same for both dry and wet conditions due to identical air equivalence ratios and but slightly increased bulk velocities (rows). What varies with increasing WGR (columns) are the flame temperature (shown above each OH* plot) and the chemical kinetics.

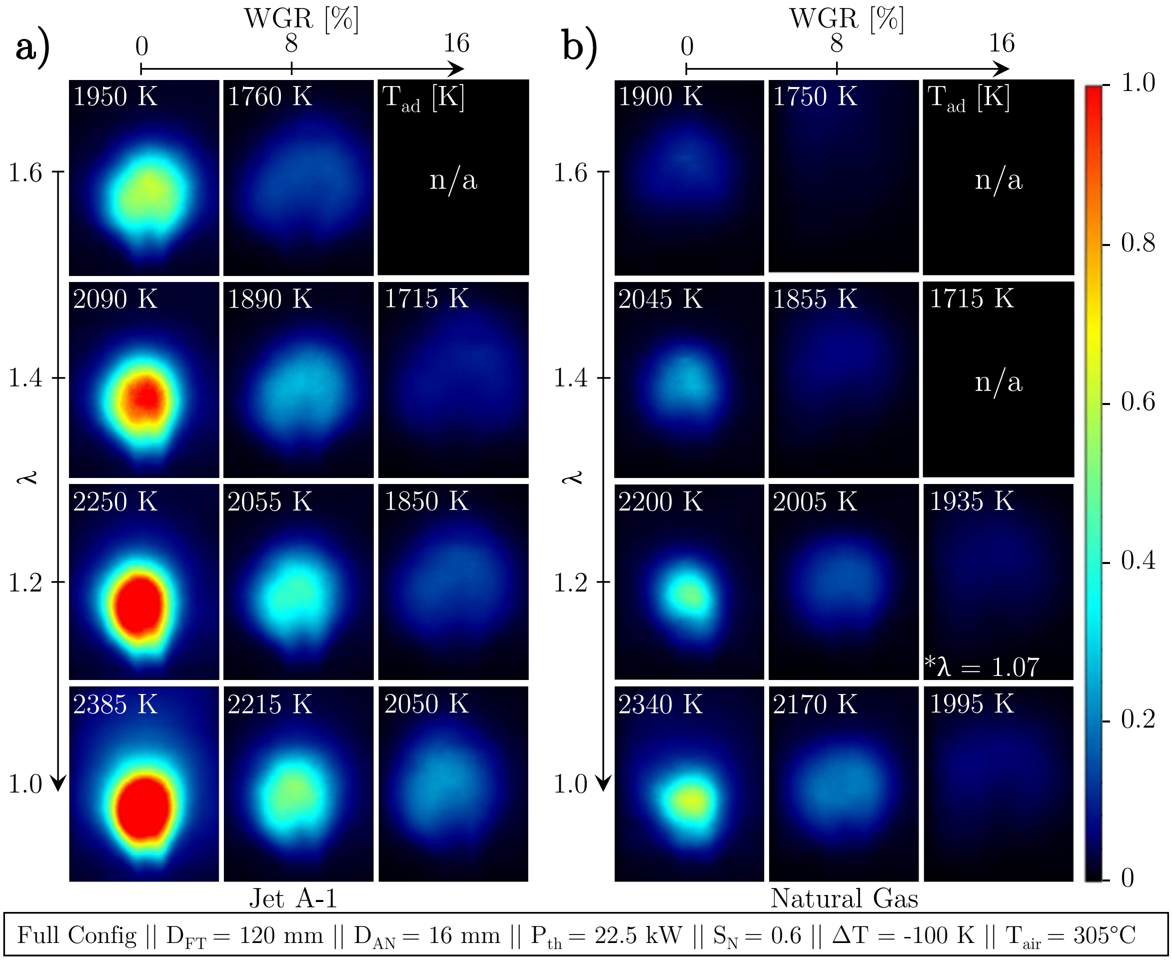

Figure 6.40: OH* Image Matrix at Different λ and Water-to-Gas Ratios for a) Jet A-1 and b) Natural Gas. Adapted from [140]

Increasing the steam concentration at $\lambda = 1.0$ in the mixture from WGR = 0–16% results in a wider and less concentrated reaction zone. This is due to the lower flame temperature (2385 to 2050 K) and increased bulk velocity (66.9 to 78.5 m/s) caused by the injected steam. In addition, the reactivity of the fresh gas mixture is reduced. This leads to a slight shift of the reaction zone downstream of the flow and its further propagation towards the flame tube walls. To achieve the same adiabatic flame temperature as the WGR increases, the air equivalence ratio λ must be reduced. Therefore, by looking at the plots diagonally (figures from left to lower right), an approximately similar T_{ad} can be obtained. In this way, the OH* images can be compared at similar T_{ad} values as the WGR increases.

Lellek et al. [167] investigated the influence of water injection on the heat release zone at constant adiabatic flame temperature using NG as fuel. Their results showed almost no change in the shape or intensity of the heat release zone when water was injected. In contrast, the presently measured more volumetric and substantially reduced OH* signal intensities at similar T_{ad} (max. ±60 K) with increasing WGR levels (see diagonal figures from left to lower right), which is in agreement with the results of Göke [165]. This proves that at constant T_{ad} and decreasing air equivalence ratio, a chemical kinetic effect is involved (in addition to the thermal effects due to the T_{ad} ±60 K difference).

The O_2 concentration in the fresh gas is lower at higher WGR levels. As a result, the reactivity of the mixture decreases. This causes the reactions to slow down and the heat release rate to be reduced. An important role can also be played by local effects such as mixing. Bulk velocity and the associated mixing effects between fresh gas and exhaust gas may also be a factor.

The fuel phase in which they are injected into the reaction zone and their different chemical compositions are the main reasons for the different intensity of the Jet A-1 and NG flames. Among other reasons, locally rich regions where rapid evaporation and combustion of fuel droplets occur are responsible for the high intensity zones of the Jet A-1 flames. Mixture effects after Jet A-1 injection may also play a role. The gaseous fuel mixes differently with the steam-air flow than it does with the A-1 spray injection.

The flame height above burner (HAB) for the measured operating points at various WGR levels is shown in Figure 6.41 *a*. The HAB values at WGR = 0 to 8% remain similar with a maximum deviation of 7 mm over the entire T_{ad} range for both the liquid fuel Jet A-1 and the gaseous fuel NG. However, at WGR = 16%, the HAB values increase by a maximum of 10.7 and 26.5 mm for Jet A-1 and NG, respectively, due to the lower flame speed and lower reactivity of the mixture. The thermal effects reduce the burning velocity of hydrocarbon flames [166,168,169].

Due to the much larger operating range of Jet A-1 than NG flames, their HABs remain largely constant over the tested T_{ad} levels. Natural gas HABs increase significantly with decreasing T_{ad}. It appears that the Jet A-1 flames maintain a similar level of reactivity potentially due to the presence of hot burning fuel droplets.

The flame length data derived from the averaged OH* images for different levels of WGR are shown in Figure 6.41 *b* for both Jet A-1 and NG. Flame lengths for both fuels increase with decreasing T_{ad} due to increased bulk velocities at higher air equivalence ratios λ. The lower global reactivity of the fuel-air mixture and the shorter residence times in fuel-leaner conditions contribute to slower evaporation of Jet A-1 droplets. This also results in longer flame lengths.

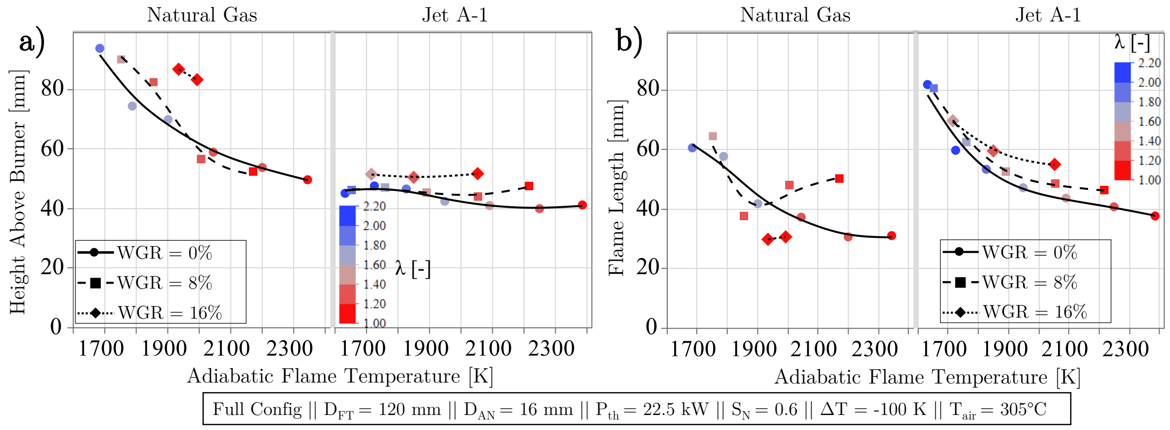

Figure 6.41: a) HAB and b) FL for Different T_{ad}, Water-to-Gas Ratios and Fuels. Adapted from [140]

It appears that Jet A-1 flame lengths become increasingly insensitive to WGR values as T_{ad} levels decrease. An analysis of the FL values in relation to the air equivalence ratio λ showed a clear increase in FL with increasing WGR for all the λ values (data not shown here). This is an indication that the adiabatic flame temperature has a more dominant effect on the flame length than the WGR.

Increasing the WGR levels results in an increase in FL for Jet A-1 flames consistently from FL = 44, 48.8, and 55.8 mm at $T_{ad} = 2050$ K. This difference decreases to 1.2 mm at fuel-leaner conditions due to reduced chemical kinetic effect and similar mixture reactivity. The FL for NG flames at WGR = 0% shows increasing values with decreasing T_{ad} levels due to increasing bulk velocity and reduced residence time. This is in accordance with the expectation. However, their FL values at WGR = 8–16% do not show a consistent trend. A visual analysis of the OH* images showed that due to the very low intensity of the OH* signal at higher WGR levels, the macro software used to evaluate the OH* data was not able to adequately assess the contour of the reaction zone. Therefore, the presented data should be analyzed with caution.

The measured T_{ad} LBO limits (y-axis) of both Jet A-1 and NG as a function of WGR (x-axis) are shown in Figure 6.42 *a*. The same values, but plotted against the air equivalence ratio λ (y-axis), are shown in Figure 6.42 *b* for comparison. For the LBO tests, the air mass flow rate was incrementally increased by 2 K per second at a constant thermal power (fuel mass flow rate) of 22.5 kW. Simultaneously, to keep the WGR at a constant level, the water mass flow rate was adjusted with increasing air mass flow rate. To gain statistical confidence, the lowest possible LBO limit T_{ad} was run three times for each WGR level.

Different combustion characteristics of the fuels and their interactions with steam are indicated by the more gradual incline of the Jet A-1 T_{ad} LBO limits with increasing WGR levels compared to the NG LBO limits with a notably steeper incline (see Figure 6.42 *a*). Both thermal and chemical effects of steam injection may account for the relatively narrower operating range of NG flames at identical WGR levels shown in Figure 6.42 *b*. It appears that the increase in WGR has a more pronounced effect on NG combustion than on Jet A-1 flames, which may contain fuel droplets burning at near-stoichiometric conditions.

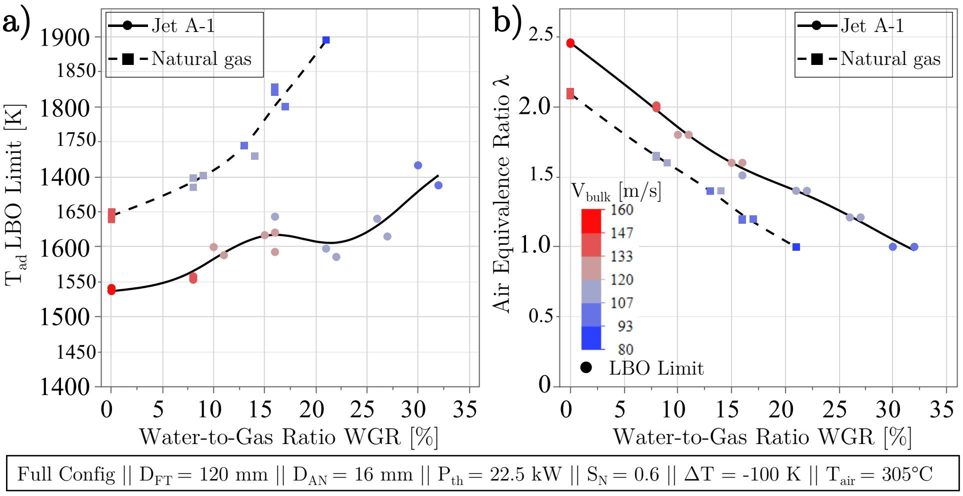

Figure 6.42: Operating Range in Terms of a) T_{ad} LBO Limits and b) λ for Various WGR Levels. Adapted from [140]

The air equivalence ratio must be reduced to maintain a stable flame with increasing WGR. As the fresh gas mixture becomes fuel-richer, the concentration of OH radicals increase. This in turn leads to a higher global reaction rate and higher flame speeds [170]. Under dry conditions, Jet A-1 flames showed an average T_{ad} LBO limit of 1538 ±2.5 K, which is 107 K lower than that of NG flames. This is due to the chemical composition of the fuels. For example, methane, the major constituent (91.12 % mol) of the tested NG, requires higher temperature to crack and participate in the combustion process due to its stronger molecular bond.

The maximum WGR content at $\lambda = 1.0$ was found to be at WGR ≈ 32% ($T_{ad} \approx 1688$ K) and at WGR ≈ 21% ($T_{ad} \approx 1895$ K) for Jet A-1 and NG, respectively. The LBO limits of pre-vaporized kerosene flames were investigated and compared with those of methane flames by Pathania et al. [171]. In their study, they found that the low-temperature reactions in the Jet A flame were more pronounced than those in the methane flame. A slightly higher intensity of CH_2O was observed in Jet A flames than in methane flames using the CH_2O-PLIF measurement technique. This higher intensity results in mixing of CH_2O with fresh reactants in the recirculation zones, which may have resulted in more stable Jet A flames.

Summary

It has been demonstrated that the swirl-assisted, jet-stabilized combustor is capable of operating at high steam loads while maintaining the improved performance of the combustor at dry conditions. NO_x levels were suppressed by diluting the air-fuel mixture with steam, while the CO levels were kept largely constant.

For both Jet A-1 and NG combustion, the injection of steam as an external perturbation into the swirl-assisted jet-stabilized combustor led to minimizing NO_x emissions by reducing the adiabatic flame temperature. However, at a constant T_{ad}, some reduction in NO_x emissions due to chemical kinetics and third body effects was also observed. Increasing the steam content had little effect on the CO emissions. The heat release zone became more volumetric and its intensity (OH*) was reduced even at similar T_{ad} values with increasing WGR levels.

With increasing WGR from 0 to 8%, the analyzed HAB values for Jet A-1 and NG did not change significantly. The HAB levels increased only at WGR = 16% for both fuels. Since the adiabatic flame temperature played a more dominant role in changing the reaction zone shape, the flame length of Jet A-1 showed minimal change with increasing WGR at $T < 1900$ K. Compared to NG flames, with increasing WGR, the operating range of Jet A-1 flames decreased more gradually. This indicated that, even in the wet conditions, the influence of combustion characteristics of Jet A-1 and NG, local mixing and the presence of fuel droplets on the extension of the operating range was significant.

For a GT engine combustor application, steam injection can have several effects. In particular, it can affect emissions and operating range. Steam injection can reduce NO_x emissions while operating the GT combustor at a similar turbine inlet temperature. The method can also result in heat absorption and a reduction in peak temperature, which can have the effect of extending liner life.

It is also possible to increase the operating range of the GT at part-load operation. This is achieved by allowing the GT to operate at higher power settings without exceeding the temperature limits set by the liner wall and the turbine blades. This can be particularly useful in hot and dry environments where the combustor inlet temperature is higher, where the engine is limited at operating at higher loads.

The added engineering and operational considerations must also be taken into account. For example, the additional steam injection system, the potential effects of the steam on the GT components due to the increased moisture content and its effect on the overall complexity of the system. Therefore, before designing or redesigning a GT combustion system, a complete cost-benefit analysis must be performed.

7 Conclusions

A brief overview of the conducted research is presented in this section. In conclusion, the future research that is required to increase the technology readiness level (TRL) of the developed combustor system will be given.

7.1 Combustor Development Iteration

As previously discussed (see Section 1.2), the objective of this research was to develop a liquid-fueled combustor concept with low-NO_x, compact reaction zone and high fuel flexibility with a wide operating range for various applications. A single-nozzle, jet-stabilized combustor was selected to improve combustion performance in terms of emissions, operating range, and shorten the flame size. The design required several iterative steps, resulting in low NO_x and CO emissions, a wide range of combustor operability, and a relatively compact reaction zone. Figure 7.1 illustrates the steps that led to the development of the swirl-assisted jet-stabilized combustor in both spray and superheated conditions. These steps are summarized below:

- Iteration I (reference combustor described in Section 6.1): Unmodified single-nozzle jet-stabilized combustor with fuel spray operation. The combustor operating range was limited to a maximum flame blowout limit of $\lambda = 1.55$ ($T_{ad} = 2080$ K). The length of the flame was more than 200 mm, which had to be reduced.
- Iteration II: Superheated fuel injection was used in an unmodified single-nozzle jet-stabilized combustor. The operating range of the flame decreased to a maximum of $\lambda = 1.2$ due to combustion instability. When the fuel temperature exceeded 205°C, the flame height above the burner was observed to increase.
- Iteration III: Modified jet-stabilized combustor operating with superheated fuel injection and a blocking body to inhibit vaporizing liquid fuel axial expansion during superheated injection. The modification resulted in increasing the blowout limit to $\lambda = 1.45$. At this point, it was clear that the expansion of the fuel resulting from the superheated injection had to be compensated via a blocking body.
- Iteration IV: Modified jet-stabilized combustor operating in a liquid-sprayed condition. This version of the combustor incorporated a static mixer, which both blocked the axial expansion of the evaporating liquid fuel (at superheated injection) and improved fuel-air mixing. The introduction of the static mixer increased the lean blowout (LBO) limit to

$\lambda = 2.1$ at superheated injection, but resulted in the formation of large fuel droplets at spray conditions. Figure 7.1 (iteration IV) shows the burning droplets leaving the combustor.

- Iteration V: Modified jet-stabilized combustor with spray fuel injection. This step included a prefilmer channel and a static mixer. They improved fuel vaporization and fuel-air mixing. This step, while maintaining an LBO limit of $\lambda = 2.1$, allowed the combustor to operate at both spray and superheated fuel injection. However, a further improvement of fuel-air mixing was required as the flame length was still over 150 mm.
- Iteration VI: Modified jet-stabilized combustor operating with superheated injected fuel. In this final step, a moderate swirler (swirl number = 0.6) was used to intensify mixing and reduce the flame length to 50 mm while maintaining the operating range ($\lambda_{\mathrm{LBO}} = 2.1$) and pollutant emission levels below 10 ppm. This configuration also allowed the combustor to operate at both spray and superheated fuel injection

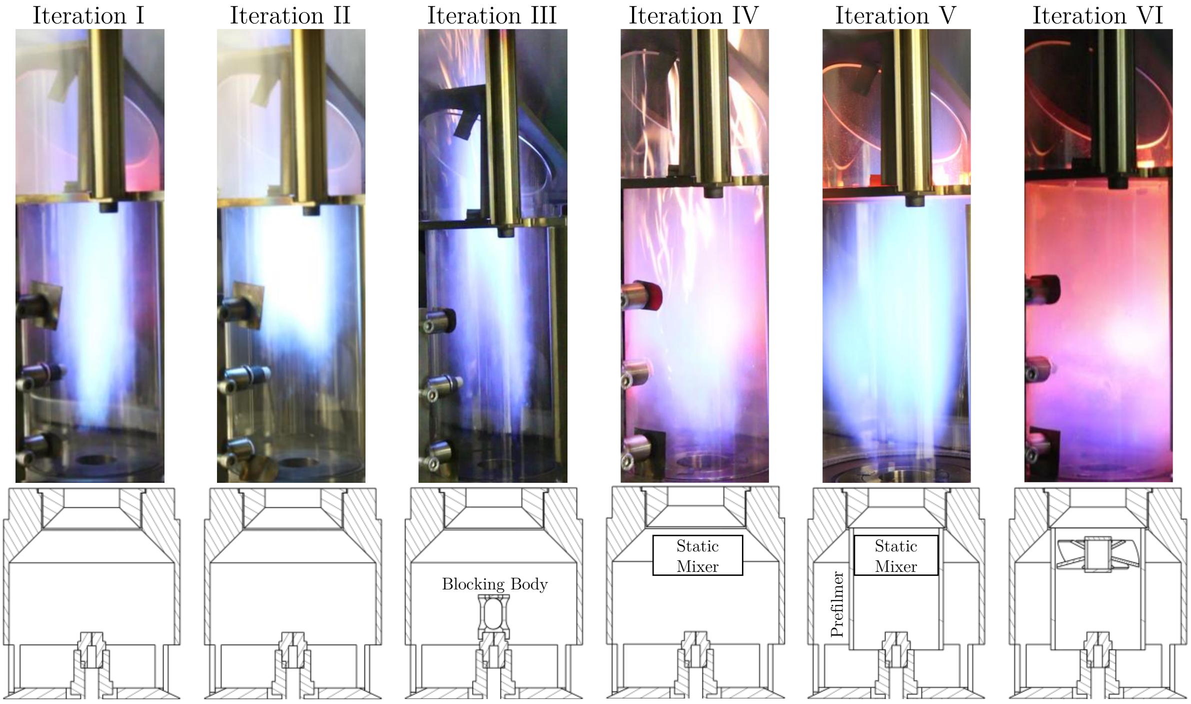

Figure 7.1: Combustor Development Iteration Steps

7.2 Summary and Conclusion

The influence of various operational and geometric parameters on NO_x, CO, heat release zone shape, lean blowout limits and fuel evaporation have been characterized and a thorough and comprehensive experimental data set has been generated. Due to the complexity of the spray combustion simulation and the prediction of the related interaction effects, an accurate understanding of the occurring phenomena has been shown to be possible on a relatively low-cost atmospheric test rig.

In a liquid fuel combustion process, the vaporization of the fuel and its mixing prior to the reaction zone play a significant role in determining the flame exhaust gas emissions, the shape of the heat release zone and the operating range of the combustor. It was essential to investigate the effect of a variety of combustor operational and geometric factors on flame characteristics to better understand the combustion phenomena of the novel swirl-assisted and jet-stabilized combustor concept.

In this context, an atmospheric experimental investigation was performed on a modified single-nozzle jet-stabilized combustor using a moderate swirler. OH* chemiluminescence and Mie scattering measurements were performed in the flame tube, which was optically accessible. Design of experiments was used to systematically vary experimental settings such as combustor configuration, air and fuel flow rates and preheat temperatures.

Technically relevant performance indicators such as NO_x, CO, UHC, heat release zone shape and intensity, fuel evaporation and lean blow-off limits were characterized over a wide range of parameters. The operational parameters included thermal power (P_{th} = 15–30 kW), preheated air temperature (T_{air} = 155–255°C), fuel preheating level (ΔT = -100 to +50 K) and adiabatic flame temperature (T_{ad} = 1650–2350 K). Geometric parameters included swirl number (S_N = 0.5–0.7), flame tube diameter (D_{FT} = 80–120 mm), air nozzle diameter (D_{AN} = 16 and 25.2 mm), fuel injector type (pressure-swirl and plain-orifice) and combustor core components such as axial swirler, pre-filmer and swirler hub. These operational and geometric parameters under investigation were specifically selected on the basis of their potential effect on combustion behavior. The air and fuel preheat temperature range was varied to include both liquid (spray) and gaseous (superheated) phases of the Jet A-1 under test. The combustor core components were varied based on their effect on fuel-air mixing and fuel evaporation.

Based on the results presented in Section 6.4 regarding the impact of superheated injection, it was expected that improving droplet size by superheating the liquid fuel could lead to a reduction in NO_x emissions. However, the NO_x values at ΔT = 0 K and +50 K were higher than those observed in the spray condition. While the level of superheat affected fuel evaporation, it probably led to a decrease in fuel-air mixing and mixture reactivity due to the rapid expansion of evaporating fuel in the mixing channel. Additionally, a bimodal flame behavior was observed that needed to be addressed due to its significant impact on the combustor's performance. As a result, follow-up experiments (section 6.4.1 to 6.4.5) were conducted to better understand the physical and combustion phenomena resulting from the newly designed combustor concept under sprayed and superheated conditions.

As discussed in Section 6.4.1, reducing the diameter of the air nozzle and increasing the jet velocity likely enhanced fuel-air mixing. The bimodal behavior of the flame was eliminated and the NO_x emissions were significantly improved due to the increased turbulence in the flame tube caused by the higher jet velocity at the air nozzle. As the air nozzle diameter was reduced, the effect of superheated injection on NO_x disappeared to a large extent. This may have been due to the improved recirculation zone and fuel-air mixing. Due to similar residence times, no effect of bulk velocity on CO emissions was observed. It can be concluded that the benefit of preheating the Jet A-1 reaches its maximum effect at $\Delta T = -50$ K ($T_{fuel} = 155°C$), and thus superheat injection of the fuel, although leading to its complete vaporization, does not necessarily lead to improved NO_x, CO and LBO limits for the developed combustor concept.

The results discussed in Section 6.4.2 showed that despite the significantly lower primary atomization quality of the plain-orifice injector, the small differences in NO_x emissions could be reduced by increasing the fuel temperature. Since the primary spray generated by the plain-orifice injector was significantly poorer, the effect of fuel evaporation as a result of higher fuel temperature was more pronounced.

The study discussed in Section 6.4.3 observed the independent effect of fuel and air temperature on fuel evaporation in the combustor. The results indicated that liquid fuel droplets were visible at the combustor head due to fuel recondensation at the lowest air temperature, despite the fuel temperature exceeding its saturation temperature by 50 K. In addition, the variation of T_{air} did not significantly affect CO emissions. However, the increase in fuel temperature resulted in a slight increase in NO_x due to degraded fuel-air mixture quality.

The in-depth characterization of the combustor core components discussed in Section 6.4.4 demonstrated that the combustor's full configuration had the most compact reaction zone and the lowest overall CO emissions probably due to improved mixing of fuel and air and enhanced recirculation zones. The configuration without the swirler hub had a rather axially stretched reaction zone and the least NO_x emissions likely due to a shorter residence time in the flame tube. The swirler hub effectively reduced CO emissions at all ΔT levels by preventing larger fuel droplets from entering the reaction zone. The prefilmer multiplied the velocity of the air and fuel droplets through the swirler. This probably resulted in improved secondary atomization due to the air-blast effect. The Full-Config showed slightly higher NO_x levels compared to the w/o Hub and w/o Prefilmer configurations due to its more compact reaction zones and higher local temperatures. The resulted decreased flame length demonstrated the positive influence of the swirler and its hub on fuel evaporation and recirculation zone. The swirler hub also provided improved fuel-air mixing under superheated injection conditions. This was evidenced by reduced flame height above the burner.

To evaluate the different thermal properties of various multi-component liquid fuels, a synthetic crude oil (Future Fuel) and heating oil extra light (HEL) were used (see Section 6.4.5). These fuels have final boiling points well above that of the Jet A-1 reference fuel. In addition, HEFA and Jet A-1 (+) with an additive were used to test their behavior with spray and superheated injection. As a result of more propagated reaction zones, the measurements showed lower NO_x levels for Jet A-1 (+) and HEFA. To evaluate the liquid fuel pattern and vaporization quality in the flame tube, both reacting and non-reacting tests were conducted. These tests covered a wide range of liquid fuel temperatures from 150 to 280°C. The tests included both spray and superheated injection regimes. The data obtained provided a qualitative insight into the spray distribution and the depth of penetration of the liquid fuel at different operating conditions. Due to the higher volume average boiling point of FF and heating oil extra light, their transition to the superheated regime occurred at higher temperatures than Jet A-1. This resulted in longer liquid phase penetration depths.

The higher boiling point of HEL, and thus decreased evaporation rate, may have been responsible for the maximum difference of +4 ppm in NO_x levels between the HEL and Jet A-1 flames. A literature review also showed that the chemical properties of the fuel are of secondary importance for NO_x and CO emissions, and that the heating value of the fuel is a more dominant factor. All tested liquid fuels showed negligible differences in NO_x, CO and LBO limits at higher fuel temperatures. Regarding fuel flexibility, the combustor concept was able to achieve comparable emission levels, flame geometry characteristics and operating ranges due to sufficient fuel-air mixing, fuel vaporization and comparable recirculation zone.

The study of the thermal power (P_{th}) variation effect on the combustion performance presented in Section 6.5 showed that increasing P_{th} did not affect the NO_x values. However, in the transient and superheated conditions, the NO_x levels increased as P_{th} decreased. This could be attributed to lower bulk velocities resulting from lower thermal power at a constant T_{ad} and rapid expansion of the superheated fuel, which could lead to poorer fuel-air mixing quality.

The results discussed in Section 6.6 showed that increasing the swirl number (S_N) had no significant effect on NO_x and CO, likely due to sufficient fuel-air mixing at $S_N = 0.5$. However, it moderately affected the reaction zone position and shape. The test results presented in Section 6.7 showed that the mean residence time and bulk velocity in the flame tube were primarily affected by variation of the flame tube diameter (D_{FT}). In particular, the reaction zone HAB and

FL were affected, possibly due to changes in recirculation rate and shape. In spite of the longer residence time and the slower bulk velocity, the HAB values increased by 17 mm as the D_{FT} was increased from 80 to 120 mm. The mixing of the recirculated hot exhaust gas with the fuel-air mixture at the root of the flame occurred more rapidly for the D80, resulting in an increased reactivity of the mixture and a faster stabilization of the flame.

In the wet tests shown in Section 6.8, both thermal and chemical kinetic effects on NO_x formation were observed. Under stoichiometric conditions $\lambda = 1.0$, the NO_x emission was reduced by - 82% and -100% with increasing WGR = 0 to 16% for the Jet A-1 and NG flames, respectively. The thermal effects and the reduction of the flame temperature were mainly responsible for this. The maximum water vapor content at which a flame was still operable was found to be WGR ≈ 32% and WGR ≈ 21% for Jet A-1 and NG, respectively. The combustor's ability to tolerate high water-to-gas ratios levels allows the GT to operate at a similar turbine inlet temperature but increase power output due to increased mass flow through the turbine. The process also provides heat absorption and a reduction in peak temperature that can extend the life of the liner and reduce NO_x levels.

Compared to other combustor concepts introduced in this thesis, the studied combustor concept offers simplicity while maintaining competitive combustion performance. The CO emissions were constant over a wide adiabatic flame temperature range, allowing the combustor to operate at very lean fuel conditions. This in turn led to further reduced NO_x emissions without the need to operate the combustor too close to the LBO limits. The compact shape of the reaction zone has the potential of reducing the GT liner volume, in case of its application in an aero engine. The total pressure loss across the combustor is also kept in a favorable range of 2 to 4 percent.

The question remains as to whether the increase in fuel temperature, and thus the improvement in fuel evaporation rate, will have the same negligible effect on the combustion characteristics of other combustor designs. It is conceivable that the effects could be very different, given that the current combustor core components significantly affect fuel-air mixing and fuel evaporation.

7.3 Recommendations and Future Research

The research performed in this thesis introduced the concept and basic principles of the swirl-assisted jet-stabilized combustor and achieved the technology readiness level (TRL) 1–2. Preliminary experimental characterization of a single-nozzle version of the combustor in terms of emissions, LBO testing and reaction zone position at atmospheric pressure was performed. However, the combustor needs to be tested at high pressure and in the significantly higher power range to meet the TRL 3 requirement. For an aircraft engine application, the required testing power would be in the megawatt range, but for a smaller gas turbine application, a range of a few hundred kilowatts can be considered.

Although high nozzle velocity operation (80–143 m/s) have been incorporated into the combustor design, if necessary, modification of the mixing channel length may be required with respect to flashback risk at higher combustor pressures.

To deepen the understanding of the underlying superheated fuel expansion phenomena in the mixing channel, detailed CFD simulations are required. Simulation tools should also be used to further investigate the state of the fuel-air mixture prior to the air nozzle exit in the superheated injection regime.

To quantify the mixture quality at the nozzle outlet, but also to determine the mixture between the fresh gas jet and the recirculated exhaust gas and to understand its influence on the target variables, a mixture characterization experiment is also recommended.

After validation of the combustion performance under higher pressure conditions, integration of the developed combustor as a single nozzle configuration into a gas turbine seems to be conceivable with the current configuration. For a higher turndown ratio, a piloted version of the combustor in a circular arrangement would be advantageous. Whether and how the combustor interacts with other swirl-assisted nozzles is currently unclear. Investigation is needed to determine if the stabilization mechanism works or is compromised by a multi-jet configuration. This would extend the operating range of the combustor at different GT power loads. Therefore, it is recommended that the combustor be tested in a multi-jet configuration.

In the current combustor configuration, it has been shown that a fuel preheat temperature above 155°C does not have a significant effect on combustion performance. This behavior has been validated for a variety of liquid fuels with different chemical compositions and different thermophysical properties. Therefore, when using a pressure-swirl atomizer, it can be recommended not to preheat the fuel above 155°C in order to avoid the related coking problems that have sometimes compromised the reliable operation of the combustor. If a plain-orifice injector is used, the fuel preheat can be increased to 205°C. In this case, comparable NO_x results can be achieved.

8 References

[1] Lefebvre A. H., and Ballal D. R., 2010. *Gas Turbine Combustion*, CRC Press: Taylor & Francis Group, Boca Raton, FL.

[2] Richard C. Miake-Lye (Aerodyne Research), INNOVATION FOR A GREEN TRANSITION: ICAO Environmental Report 2022.

[3] Liu Y., Sun X., Sethi V., Nalianda D., Li Y.-G., and Wang L., 2017,“Review of modern low emissions combustion technologies for aero gas turbine engines,” Progress in Aerospace Sciences, **94**, pp. 12–45.

[4] Lee D. S., Fahey D. W., Skowron A., Allen M. R., and Burkhardt U., 2021,“The contribution of global aviation to anthropogenic climate forcing for 2000 to 2018,” Atmospheric environment (Oxford, England 1994), **244**, p. 117834.

[5] Pardowitz B., Tapken U., Knobloch K., Bake F., Bouty E., Davis I., and Bennett G. J., 2014, Core noise - Identification of broadband noise sources of a turbo-shaft engine, *20th AIAA/CEAS Aeroacoustics Conference*, American Institute of Aeronautics and Astronautics.

[6] Izadi S., Zanger J., Kislat O., Enderle B., Grimm F., Kutne P., and Aigner M., 2021,“Experimental Investigation of the Combustion Behavior of Single-Nozzle Liquid-FLOX®-Based Burners on an Atmospheric Test Rig,” 0742-4795, **143**(7).

[7] Izadi S., Zanger J., Kislat O., Enderle B., Grimm F., Kutne P., Aigner M., and Kraus C., 2021,“A Design of Experiments Based Investigation of the Influence of Hot Cross-Flow Gas on a FLOX®-Based Single-Nozzle Liquid Burner,” American Society of Mechanical Engineers, International Gas Turbine Institute et al. 2021 – Proceedings of the ASME Turbo(GT2021-59029).

[8] Mongia Hukan D. W., 2004,“Low Emissions Propulsion Engine Combustor Technology Evolution Past, Present and Future,”

[9] H. H. CHIU, and T. M. LIU, 1977,“Group Combustion of Liquid Droplets,” Combustion Science and Technology, **17**(3-4), pp. 127–142.

[10] Lefebvre A. H., 1995,“The Role of Fuel Preparation in Low-Emission Combustion,” Journal of Engineering for Gas Turbines and Power, **117**(4), pp. 617–654.

[11] Rokke P. E., and Hustad J. E., 2005,“Exhaust gas recirculation in gas turbines for reduction of CO2 emissions; combustion testing with focus on stability and emissions,” International Journal of Thermodynamics, **8**(5), 167–173.

[12]Hatch M., Sowa W., Samuelsen G., and Holdeman J., 1995,"Influence of Geometry and Flow Variations on NO Formation in the Quick Mixer of a Staged Combustor: NASA Technical Reports Server (NTRS). https://ntrs.nasa.gov/citations/19960013915,"

[13]Pierce R. M., Mosier S. A., Smith C. E., and Hinton B. S., 1980,"Advanced combustion systems for stationary gas turbine engines. Volume II. Bench scale evaluation. Final report September 1976-January 1978," United States.

[14]Samuelsen G., Brouwer J., Vardakas M., and Holdeman J., 2012,"Experimental and modeling investigation of the effect of air preheat on the formation of NOx in an RQL combustor," Heat and Mass Transfer, **49**.

[15]MOURA D. M., and REZVANI R.,"COMBUSTOR FOR GAS TURBINE ENGINE WITH QUENCH JET PATTERN: EUROPEAN PATENT," EP 4 242 520 A2.

[16]Rosfjord T. J., Padget F. C., and Tacina R. R., 2001,"Experimental Assessment of the Emissions Control Potential of a Rich/Quench/Lean Combustor for High Speed Civil Transport Aircraft Engines," E-12572.

[17]Bräunling W. J. G., 2015. *Flugzeugtriebwerke*, Springer Nature.

[18]Reddy D. R., and Lee C.-M., Eds., 2016. *An Overview of Low-Emission Combustion Research at NASA Glenn*.

[19]Baklanov A., 2021,"Influence of the Fuel Distribution in Double Annular Combustors on the Emissions," Russian Engineering Research, **41**, pp. 582–585.

[20]Richard E. Stenger,"Double annular combustor configuration," US4194358A.

[21]Jeong G., and Ahn K., 2021,"One-Dimensional Analysis of Double Annular Combustor for Reducing Harmful Emissions," Energies, **14**, p. 3930.

[22]Hegde G., Khandelwal B., Sethi V., and Singh R., 2012,"Design, Evaluation and Performance Analysis of Staged Low Emission Combustor," Journal of Engineering for Gas Turbines and Power, **136**.

[23]Ren X., Brady K. B., Xue X., Sung C.-J., and Mongia H. C., 2022,"Swirl rotation direction effects on lean direct injection pilot mixer performance: Experiments and LES modeling," Aerospace Science and Technology, **129**(C).

[24]General Electric, 2013,"TAPS II Technology Final Report – Technology Assessment: Report: Continuous Lower Energy, Emissions and Noise (CLEEN) Program," DTFAWA-10-C-00046.

[25]Mongia H., 2003. *TAPS: A Fourth Generation Propulsion Combustor Technology for Low Emissions*.

[26]Dr. A. R. Wadia, 2014,"GE Aviation ,Technologies for the Next Engine Generation,"

[27]Nickolaus D., Crocker D., Black D., and Smith C., 2002,“Development of a Lean Direct Fuel Injector for Low Emission Aero Gas Turbines,” American Society of Mechanical Engineers, International Gas Turbine Institute, Turbo Expo (Publication) IGTI, **1**.

[28]David S. Crocker, Daniel A. Nickolaus, and Clifford E. Smith,“PILOTED AIRBLAST LEAN DIRECT FUEL INJECTOR: United States Patent,” US 6,272,840 B1.

[29]Shen Y., Ghulam M., Zhang K., Gutmark E., and Duwig C., 2020,“Vortex breakdown of the swirling flow in a Lean Direct Injection burner,” Physics of Fluids, **32**, p. 125118.

[30]Marek C. J., Smith T. D., and Kundu K., 2005,“Low emission hydrogen combustors for gas turbines using Lean Direct Injection,” *41st AIAA/ASME/SAE/ASEE Joint Propulsion Conference & Exhibit*, American Institute of Aeronautics and Astronautics, Reston, Virigina.

[31]Behrendt T., Heinze J., and Hassa C., Eds., 2003. *Experimental Investigation of a New LPP Injector Concept for Aero Engines at Elevated Pressures*.

[32]S.L. Plee, and A.M. Mellor, 1978,“Review of flashback reported in prevaporizing/premixing combustors,” Combustion and Flame, **32**, pp. 193–203.

[33]Nakamura S., McDonell V., and Samuelsen S., 2008,“The Effect of Liquid-Fuel Preparation on Gas Turbine Emissions,” Journal of Engineering for Gas Turbines and Power, **130**(2), p. 21506.

[34]Harth S., 2017,“Entwicklung und Untersuchung eines LPP Brennerkonzeptes für Druckverbrennung mit geringen Schadstoffemissionen,” Ph.D. thesis.

[35]Wünning J. G., Ed., 2003. *FLOX® - Flameless Combustion*.

[36]J.A. Wünning, and J.G. Wünning, 1997,“Flameless oxidation to reduce thermal no-formation,” Progress in Energy and Combustion Science, **23**(1), pp. 81–94.

[37]Lammel O., Schütz H., Schmitz G., Lückerath R., Stöhr M., Noll B., Aigner M., Hase M., and Krebs W., 2010,“FLOX® Combustion at High Power Density and High Flame Temperatures,” J. Eng. Gas Turbines Power, **132**(12), 1–10.

[38]Lammel O., Ax H., Severin M., and Aigner M., 2016,“FLOX Wobbe - Entwicklung von BrennBrennstoff für erweiterte Brennstoffflexibilität,”

[39]Lammel O., Stöhr M., Kutne P., Dem C., Meier W., and Aigner M., 2012,“Experimental Analysis of Confined Jet Flames by Laser Measurement Techniques,” J. Eng. Gas Turbines Power, **134**(4), 041506–041506-9.

[40]Zornek T., Monz T., and Aigner M., 2015,“Performance analysis of the micro gas turbine Turbec T100 with a new FLOX-combustion system for low calorific fuels,” Applied Energy, **159**, pp. 276–284.

[41]Lammel O., Lückerath R., and Institut für Verbrennungstechnik, 2017. *FLOX Wobbe: Entwicklung von Brennstoffdüsen für erweiterte Brennstoffflexibilität Charakterisierung des*

Verbrennungssystems im Labormaß Verbundprojekt Siemens Clean Energy Center - Entwicklung von Verbrennungstechnologien für die klimaschonende Energieerzeugung, Teilprojekt 1.4/1D, Deutsches Zentrum für Luft- und Raumfahrt e.V. (DLR), Institut für Verbrennungstechnik (VT).

[42]Hohloch M., Lingstädt T., and Kutne P., 2023,"Experimental Analysis of the Hydrogen Capability of a Fuel Flexible Jet Stabilized Syngas Micro Gas Turbine Combustor under Atmospheric Conditions," *Proceedings of the ASME Turbo Expo: Turbomachinery Technical Conference and Exposition - 2023: June 26-30, 2023, Boston MA*, The American Society of Mechanical Engineers, New York, N.Y.

[43]Zanger J., 2016,"Experimentelle Charakterisierung eines atmosphärisch betriebenen, jet-stabilisierten Mikrogasturbinenbrenners für Erdgas," Stuttgart, Universität.

[44]Severin M., 2019,"Analyse der Flammenstabilisierung intensiv mischender Jetflammen für Gasturbinenbrennkammern," PHD Thesis, Institut der Verbrennungstechnik der Luft- und Raumfahrt (IVLR), Universität Stuttgart, Stuttgart.

[45]Zizin A., Lammel O., Severin M., Ax H., and Aigner M., 2015,"Development of a Jet-Stabilized Low-Emission Combustor for Liquid Fuels," *Proceedings of the ASME Turbo Expo: Turbine Technical Conference and Exposition - 2015: Presented at the ASME 2015 Turbo Expo: Turbine Technical Conference and Exposition, June 15 - 19, 2015, Montreal, Quebec, Canada*, ASME, New York, NY.

[46]Saeed Izadi, 2018. *Characterization of Pressure Atomizers for a Single Nozzle Liquid FLOX® Burner Using Optical and Laser Diagnostics: Master Thesis*, Institute of Combustion Technology for Aerospace Engineering (IVLR), University of Stuttgart.

[47]Schäfer D., Gounder J. D., Lammel O., Ax H., Lückerath R., and Aigner M., 2019,"High Momentum Jet Flames at Elevated Pressure: Part D — Simultaneous Measurements of OH/PAH PLIF and Mie Scattering on Liquid Fuels," *Proceedings of the ASME Turbo Expo: Turbomachinery Technical Conference and Exposition - 2019: Presented at the ASME Turbo Expo 2019: Turbomachinery Technical Conference and Exposition, June 17-21, 2019, Phoenix, Arizona, USA*, The American Society of Mechanical Engineers, New York, N.Y.

[48]Gounder J. D., Zizin A., Lammel O., Rachner M., Aigner M., and Kulkarni S. R., 2016,"Experimental and numerical investigation of spray characteristics in a new FLOX ® based combustor for liquid fuels for Micro Gas Turbine Range Extender (MGT-REX)," *52nd AIAA/SAE/ASEE Joint Propulsion Conference*, American Institute of Aeronautics and Astronautics, Reston, Virginia.

[49]Krebs W., Schulz A., Witzel B., Johnson C., Laster W., Pent J., Schilp R., Wasif S., and Weaver A., 2022,"Advanced Combustion System for High Efficiency (ACE) of the New

SGT5/6- 9000HL Gas Turbine," *Proceedings of the ASME Turbo Expo: Turbomachinery Technical Conference and Exposition - 2022: June 13-17, 2022, Rotterdam, The Netherlands*, The American Society of Mechanical Engineers, New York, N.Y.

[50]Banihabib R., Lingstädt T., Wersland M., Kutne P., and Assadi M., 2024,"Development and testing of a 100 kW fuel-flexible micro gas turbine running on 100% hydrogen," International Journal of Hydrogen Energy, **49**, pp. 92–111.

[51]"ICAO Aircraft Emissions Databank Issue 30 [23 July 2024]," Sourced on 13.02.2025. www.easa.europa.eu/en/domains/environment/icao-aircraft-engine-emissions-databank.

[52]Icao,"Annex 16 to the Convention on International Civil Aviation: Environmental Protection Volume II - Aircraft Engine Emissions, Fourth Edition, July 2017," https://ffac.ch/wp-content/uploads/2020/10/ICAO-Annex-16-Environmental-protection-Vol-II-Aircraft-Engine-Emissions.pdf sourced: 14.02.2025.

[53]Icao,"Introduction to the ICAO Engine Emissions Databank (06/2023): https://www.easa.europa.eu/en/downloads/45576/en sourced: 14.02.2025,"

[54]Kathrotia T., Oßwald P., Zinsmeister J., Methling T., and Köhler M., 2021,"Combustion kinetics of alternative jet fuels, Part-III: Fuel modeling and surrogate strategy," Fuel, **302**, p. 120737.

[55]McBride B. J., and Zehe M. J., 1994,"Software: Chemical Equilibrium Applications (CEA): Reference Number LEW-17687-1,"

[56]Turns S. R., 2012. *An Introduction to Combustion: Concepts and Applications*, McGraw-Hill.

[57]Aigner M., and Riedel U., 2018. *Einfuhrung in die Verbrennung: Lecture script: University of Stuttgart: Institute of Combustion Technology for Aerospace Engineering (IVLR)*, Version 1.16.

[58]2003. *Low Emission Gas Turbine Combustors Based on Flameless Combustion.*

[59]2012. *Handbook for Evaluating Emissions and Costs of APUs and Alternative Systems*, Transportation Research Board, Washington, D.C.

[60]Adachi S., Iwamoto A., Hayashi S., Yamada H., and Kaneko S., 2007,"Emissions in combustion of lean methane-air and biomass-air mixtures supported by primary hot burned gas in a multi-stage gas turbine combustor," Proceedings of the Combustion Institute, **31**(2), 3131–3138-3131–3138.

[61]Baessler S., Mo?sl K. G., and Sattelmayer T., 2006,"NOx Emissions of a Premixed Partially Vaporized Kerosene Spray Flame," *Proceedings of the ASME Turbo Expo: Power for Land, Sea and Air - 2006: Presented at the 2006 ASME Turbo Expo, May 6 - 11, 2006, Barcelona, Spain*, ASME, New York, NY.

[62] Peter Glarborg, James A. Miller, Branko Ruscic, and Stephen J. Klippenstein, 2018,"Modeling nitrogen chemistry in combustion," Progress in Energy and Combustion Science, **67**, pp. 31–68.

[63] Joos F., 2006. *Technische Verbrennung - Verbrennungstechnik, Verbrennungsmodellierung, Emissionen*, Springer-Verlag Berlin Heidelberg.

[64] Snyder T. S., Rosfjord T. J., McVey J. B., and Chiappetta L. M., Eds., 1994. *Comparison of Liquid Fuel/Air Mixing and NOx Emissions for a Tangential Entry Nozzle*.

[65] Lefebvre A. H., Ed., 1995. *The Role of Fuel Preparation in Low Emissions Combustion*.

[66] Christian H. Beck, 2009,"Analyse der Stickoxidbildung in mageren Sprayflammen mit partieller Vorverdunstung," Dissertation, ISBN: 978-3-8325-2321-3, Universität Karlsruhe. Lehrstuhl und Institut für Thermische Strömungsmaschine.

[67] Baulch D., Bowman C., Cobos C., Cox R., Just T., Kerr J., Pilling M., Stocker D., Troe J., Tsang W., Walker R., and Warnatz J., 2005,"Evaluated Kinetic Data for Combustion Modeling: Supplement II," Journal of Physical and Chemical Reference Data - J PHYS CHEM REF DATA, **34**.

[68] David G. Nicol, Philip C. Malte, Jenkin Lai, Nick N. Marinov, David T. Pratt, and Robert A. Corr, 1992,"NOx Sensitivities for Gas Turbine Engines Operated on Lean-Premixed Combustion and Conventional Diffusion Flames,"

[69] Warnatz J., Maas U., and Dibble R. W., 2006. *Combustion: physical and chemical fundamentals, modeling and simulation, experiments, pollutant formation*, Springer.

[70] Wolfrum J., 1972,"Bildung von Stickstoffoxiden bei der Verbrennung," Chemie Ingenieur Technik, **44**(10), pp. 656–659.

[71] Nikolaus D. Spyra, 2010. *Dissertation: Entwicklung und Untersuchung eines neuartigen Brennstoffaufbereitungssystems für kleine Gasturbinen: Fakultät Maschinenwesen der Technischen Universität München*.

[72] Hupfer A., 2007,"Kraftstoffeinspritzsysteme für Vormischbrenner kleiner Fluggasturbinen," Technische Universität München.

[73] Jones R. E., La Diehl, Da Petrash, and Grobman J., 1978,"Results and status of the NASA aircraft engine emission reduction technology programs,"

[74] Naegeli D. W., and Moses C. A., 1980. *Effect of fuel molecular structure on soot formation in gas turbine engines*, American Society of Mechanical Engineers.

[75] A. H. Lefebvre, 1983,"FUEL EFFECTS ON GAS TURBINE COMBUSTION: AFWAL-TR-83-2004," Combustion Laboratory, Thermal Science and Propulsion Center, Purdue University, West Lafayette, Indiana 47907.

[76] Rink K. K., and Lefebvre A. H., 1986,"Influence of fuel drop size and combustor operating conditions on pollutant emissions," SAE Technical Paper.

[77]Lefebvre A. H., and McDonell V. G., 2017. *Atomization and sprays*, CRC Press Taylor & Francis Group, Boca Raton, London, New York.

[78]Lefebvre A. H., 1985,“Fuel Effects on Gas Turbine Combustion—Ignition, Stability, and Combustion Efficiency,” Journal of Engineering for Gas Turbines and Power, **107**(1), pp. 24–37.

[79]Suyari M., and Lefebvre A. H., 1986,“Film thickness measurements in a simplex swirl atomizer,” Journal of Propulsion and Power, **2**(6), pp. 528–533.

[80]Castleman, R A Jr, 1933,“The Mechanism of Atomization Accompanying Solid Injection,” NACA-TR-440.

[81]Lorenzetto G. E., and Lefebvre A. H., 1977,“Measurements of drop size on a plain-jet airblast atomizer,” AIAA Journal, **15**(7), pp. 1006–1010.

[82]Dipanjay DEWANJI, 2012. *Flow Characteristics in Lean Direct Injection Combustors: Dissertation: Technische Universtiteit Delft*.

[83]G.L. Hubbard, V.E. Denny, and A.F. Mills, 1975,“Droplet evaporation: Effects of transients and variable properties,” International Journal of Heat and Mass Transfer, **18**(9), pp. 1003–1008.

[84]Sahu S., Hardalupas Y., and Taylor A., 2018,“Interaction of droplet dispersion and evaporation in a polydispersed spray,” Journal of Fluid Mechanics, **846**, pp. 37–81.

[85]Pichard C., Michou Y., Chauveau C., and Gökalp L., 2002,“Average droplet vaporization rates in partially prevaporized turbulent spray flames,” Proceedings of the Combustion Institute, **29**(1), pp. 527–533.

[86]Abouelmagd Abdelsamie, and Dominique Thévenin, 2017,“Direct numerical simulation of spray evaporation and autoignition in a temporally-evolving jet,” Proceedings of the Combustion Institute, **36**(2), pp. 2493–2502.

[87]Wolff M. C., Meisl J., Koch R., and Wittig S., 1998,“The influence of evaporation on the autoignition-delay of n-heptane air mixtures under gas turbine conditions,” Symposium (International) on Combustion, **27**(2), pp. 2025–2031.

[88]Harrison III W. E., Mongia H. C., Heneghan S. P., and Ballal, 1995. *Advanced Jet Fuels—JP-4 Through JP-8 and Beyond*, American Society of Mechanical Engineers.

[89]McAllister S., Chen J. Y., and Fernandez-Pello A. C., 2011. *Fundamentals of Combustion Processes*, Springer New York.

[90]EMANUEL N. M., The problem of the control of the chain reactions taking place in the liquid-phase oxidation of hydrocarbons, *The Oxidation of Hydrocarbons*, pp. 1–31.

[91]M. BRANDAUER, A. SCHULZ, A. PFEIFFER, and WITIIG S., 1993,“Experimental Study of Coke Deposition under Gas Turbine Combustor Conditions,” Combustion Science and Technology, **89**(1-4), pp. 265–273.

[92]Mayo F. R., Kirshen N. A., Richardson H., and Stringham R. S., 1972,“The chemistry of fuel deposits and their precursors,” Final Report NASC contract(00019).

[93]Szetela E. J., and Chiappetta L., 1980,“External fuel vaporization study, phase 1, NASA Technical Reports Server (NTRS),” https://ntrs.nasa.gov/citations/19800016957.

[94]Mongia H.,“Engineering aspects of complex gas turbine combustion mixers Part IV: Swirl cup,” *9th Annual International Energy Conversion Engineering Conference*, p. 5526.

[95]General Electric Co, Timothy James Held, Jun Xu, and Mark Anthony Mueller,“Method and Apparatus to Decrease Combustor Emissions: General Electric Co,”

[96]Watt J. J., Evans A., and Hibbard R. R., 1968. *Fouling characteristics of ASTM Jet a fuel when heated to 700° F in a simulated heat exchanger tube*, National Aeronautics and Space Administration.

[97]Wiest H. K., and Heister S. D., 2014,“Experimental Study of Gas Turbine Combustion With Elevated Fuel Temperatures,” Journal of Engineering for Gas Turbines and Power, **136**(12).

[98]Smith L. L., Dai Z., Lee J. C., Fotache C. G., Cohen J. M., and Hautman D. J., 2013,“Advanced Combustor Concepts for Low Emissions Supersonic Propulsion,” Journal of Engineering for Gas Turbines and Power, **135**(5).

[99]Taylor W. F., and ESSO RESEARCH AND ENGINEERING CO LINDEN NJ GOVERNMENT RESEARCH LAB, 1969,“The Study of Hydrocarbon Fuel Vapor Deposits,” GR-lo-VDP-69, Esso Research and Engineering Co.

[100] Smith J. D., 1969,“Fuel for the Supersonic Transport,” Industrial & Engineering Chemistry Process Design and Development, **8**(3), pp. 299–308.

[101] Le Faith, Ackerman G. H., and Henderson H. T., 1971,“Heat sink capability of Jet A fuel: heat transfer and coking studies,” Shell Development Co., S–14115, NASA CR–72951.

[102] Szetela E., Ed., 1976. *Deposits From Heated Gas Turbine Fuels: ASME 1976 International Gas Turbine and Fluids Engineering Conference*, V01AT01A009.

[103] Anderson D., 1975. *Effects of equivalence ratio and dwell time on exhaust emissions from an experimental premixing prevaporizing burner*, American Society of Mechanical Engineers.

[104] Leonard G., and Stegmaier J., 1994,“Development of an Aeroderivative Gas Turbine Dry Low Emissions Combustion System,” Journal of Engineering for Gas Turbines and Power, **116**(3), pp. 542–546.

[105] Eran Sher, Tali Bar-Kohany, and Alexander Rashkovan, 2008,“Flash-boiling atomization,” Progress in Energy and Combustion Science, **34**(4), pp. 417–439.

[106] Senda J., Wada Y., Kawano D., and Fujimoto H., 2008,“Improvement of combustion and emissions in diesel engines by means of enhanced mixture formation based on flash

boiling of mixed fuel,” International Journal of Engine Research - INT J ENGINE RES, **9**, pp. 15–27.

[107] Rees A., Araneo L., Salzmann H., Lamanna G., Sender J., and Oschwald M., 2020,“Droplet velocity and diameter distributions in flash boiling liquid nitrogen jets by means of phase Doppler diagnostics,” Exp Fluids, **61**(8), pp. 1–18.

[108] Grazia Lamanna, Hend Kamoun, Bernhard Weigand, and Johan Steelant, 2014,“Towards a unified treatment of fully flashing sprays,” International Journal of Multiphase Flow, **58**, pp. 168–184.

[109] Rachner M., 1998. *Die Stoffeigenschaften von Kerosin Jet A-1*, DLR, Abt. Unternehmensorganisation und -information.

[110] Reid Robert C., Prausnitz John M., and Poling Bruce E., 1987,“The properties of gases and liquids,” Journal of Women s Health.

[111] Iyengar V., Simmons H., Ransom D., and Rakopoulos C. D., 2012,“Flash Atomization: A New Concept to Control Combustion Instability in Water-Injected Gas Turbines,” Journal of Combustion, **2012**, p. 718202.

[112] W Yang W. B., Ed., 2003. *Effects of fuel temperature and flame locations on emissions of nitrogen oxides in combustion with high temperature air*.

[113] Yin Z., Kutne P., Eichhorn J., and Meier W., 2021,“Experimental Investigations of Superheated and Supercritical Injections of Liquid Fuels,” Journal of Engineering for Gas Turbines and Power, **143**(4).

[114] Marcellan A., Henke M., Schuldt S., Maas P., and Göhler-Stroh A., A numerical investigation of the Water-Enhanced Turbofan A numerical investigation of the Water-Enhanced Turbofan laboratory-scale ground demonstrator, *AIAA SciTech Forum 2022*.

[115] Marian Hiestermann, Marco Konle, and Ludovic de Guillebon, 2022,“NUMERICAL INVESTIGATION OF THE EFFECT OF HIGH STEAM LOADS ON THE COMBUSTION OF AN ACADEMIC PREMIXED SWIRL STABILIZED COMBUSTOR,” Proceedings of Global Power & Propulsion Society.

[116] Roointon Pavri, and Gerald D. Moore, 2001,“Gas Turbine Emissions and Control: GE Energy Services: GER-4211,”

[117] Kaiser S., Schmitz O., Ziegler P., and Klingels H., 2022,“The Water-Enhanced Turbofan as Enabler for Climate-Neutral Aviation,” Applied Sciences, **12**(23), p. 12431.

[118] Matthew J. Degges, J. Eric Boyer, Kenneth K. Kuo, and Luca Basini, 2010,“Influence of steam on the flammability limits of premixed natural gas/oxygen/steam mixtures,” Chemical Engineering Journal, **165**(2), pp. 633–638.

[119] Balakrishnan P., and Srinivasan K., 2017,“Pipe jet noise reduction using co-axial swirl pipe,” Aeronaut. j., **121**(1238), pp. 488–514.

[120] Guillaume Vignat, Daniel Durox, and Sébastien Candel, 2022,“The suitability of different swirl number definitions for describing swirl flows: Accurate, common and (over-) simplified formulations,” Progress in Energy and Combustion Science, **89**, p. 100969.

[121] C. A. Martin, 1987,“Aspects of the Design of Swirlers as used in Fuel Injectors for Gas Turbine Combustors,”

[122] Izadi S., Zanger J., Seliger-Ost H., Kutne P., and Aigner M., 2024,“Experimental Evaluation of Combustor Configuration's Impact on a Swirl-Assisted Jet-Stabilized Combustor Performance: ASME. J. Eng. Gas Turbines Power. January 2025,” 0742-4795, **146**(12).

[123] Chanaud R. C., 1965,“Observations of oscillatory motion in certain swirling flows,” Journal of Fluid Mechanics, **21**(1), pp. 111–127.

[124] Gupta A. K., Lilley D. G., and Syred N., 1984,“Swirl flows,” Tunbridge Wells.

[125] Liu L., 2016, Developments in Combustion Technology: Phenomenological Modeling of Combustion Process in Diesel Engines Based on Stochastic Method, *Developments in Combustion Technology*, IntechOpen London, UK.

[126] Bevilaqua P. M., and Lykoudis P. S., 1977,“Some observations on the mechanism of entrainment,” AIAA Journal, **15**(8), pp. 1194–1196.

[127] S.H. Park, and H.D. Shin, 1993,“Measurements of entrainment characteristics of swirling jets,” International Journal of Heat and Mass Transfer, **36**(16), pp. 4009–4018.

[128] Reichel T. G., 2017,“Flashback prevention in lean-premixed hydrogen combustion,” Technische Universität Berlin.

[129] Fisher R. A., 1935,“The design of experiments ((1935, 1st),” Edinburgh: Oliver and Boyde.

[130] Montgomery D., and St C., 2022. *Design and Analysis of Experiments, 9th Edition.*

[131] Gatti C., 2014. *Design of experiments for reinforcement learning*, Springer.

[132] Dean A., Morris M., Stufken J., and Bingham D., 2015. *Handbook of Design and Analysis of Experiments*, CRC Press.

[133] Dean A., Voss D., and Draguljić D., 2017. *Design and Analysis of Experiments*, Springer International Publishing.

[134] Sall J., Stephens M. L., Lehman A., and Loring S., 2017. *JMP Start Statistics: A Guide to Statistics and Data Analysis Using JMP, Sixth Edition*, SAS Institute.

[135] White Paper, 2016. *The JMP Design of Experiments Advantage: http://www.jmp.com/content/dam/jmp/documents/en/white-papers/jmp-doe-advantage.pdf.*

[136] Proust M., and SAS Institute, 2022. *JMP 17 Multivariate Methods*, JMP, a business unit of SAS.

[137] Hair J. F., Black W. C., Babin B. J., and Anderson R. E., 2013. *Multivariate Data Analysis*, Pearson Education Limited.

[138] Douglas C. Montgomery, 2017. *Applied Statistics and Probability for Engineers, 7E*, John Wiley & Sons, Incorporated.

[139] Izadi S., Zanger J., Kislat O., Enderle B., Grimm F., Kutne P., and Aigner M., 2021,“Experimental Investigation of the Combustion Behavior of Single-Nozzle Liquid-FLOX®-Based Burners on an Atmospheric Test Rig,” Journal of Engineering for Gas Turbines and Power, **143**(7).

[140] Izadi S., Kislat O., Zanger J., Seliger-Ost H., Kutne P., and Aigner M., 2024,“Investigating the Impact of Steam Enhancement on Combustion in a Swirl-Assisted Jet-Stabilized Gas Turbine Combustor: ASME. J. Eng. Gas Turbines Power. January 2025,” 0742-4795, **147**(1).

[141] Kislat O., Römgens J., Schuldt S., Zanger J., Jakobs N., Henke M., Kraus C., Moosbrugger A., Asmi M. A., and Aigner M., 2024,“Development and Testing of a Gas Turbine Test Rig Setup for Demonstrating New Aviation Propulsion Concepts,” Aerospace, **11**(7).

[142] Izadi S., Zanger J., Baggio M., Seliger-Ost H., Kutne P., and Aigner M., 2024,“Experimental Investigation of the Effect of Superheated Liquid Fuel Injection On the Combustion Characteristics of Lean Premixed Flames,” ASME. J. Eng. Gas Turbines Power(146), pp. 1–13.

[143] Kilik E., 1976,“The influence of swirler design parameters on the Aerodynamics of downstream recirculation region,” School of Mechanical Engineering, Cranfiel Institute of Technology, Cranfield.

[144] Leo M. de, Saveliev A., Kennedy L. A., and Zelepouga S. A., 2007,“OH and CH luminescence in opposed flow methane oxy-flames,” Combustion and Flame, **149**(4), pp. 435–447.

[145] Kathrotia T., 2011,“Reaction Kinetics Modeling of OH($*$), CH($*$), and C2($*$) Chemiluminescence,” Heidelberg, Ruprecht-Karls-Universität.

[146] Krishnamachari S., and Broida H. P., 1961,“Effect of Molecular Oxygen on the Emission Spectra of Atomic Oxygen-Acetylene Flames,” The Journal of Chemical Physics, **34**(5), pp. 1709–1711.

[147] Gaydon A. G., 1974. *The Spectroscopy of Flames*, John Wiley and Sons, New York.

[148] T. Kathrotia, M. Fikri, M. Bozkurt, M. Hartmann, U. Riedel, and C. Schulz, 2010,“Study of the H+O+M reaction forming OH$*$: Kinetics of OH$*$ chemiluminescence in hydrogen combustion systems,” Combustion and Flame, **157**(7), pp. 1261–1273.

[149] Najm H. N., Paul P. H., Mueller C. J., and Wyckoff P. S., 1998,“On the Adequacy of Certain Experimental Observables as Measurements of Flame Burning Rate,” Combustion and Flame, **113**(3), pp. 312–332.

[150] Albregtsen F., 2008,“Reflection, refraction, diffraction, and scattering,” University of Oslo: Oslo, Norway.

[151] Singham S. B., and Bohren C. F., 1993,“Scattering of unpolarized and polarized light by particle aggregates of different size and fractal dimension,” Langmuir, **9**(5), pp. 1431–1435.

[152] Zanger, J., Zornek, T., Monz,“Entnahmesonde und Verfahren zur Entnahme von Abgas,” Patent reg. Nr.: DE 10 2017 102 046 A1: 2018.08.02.

[153] David Green, 2023,“VIDEO: How Condensation Particle Counters Work: https://www.pmeasuring.com/video/video-how-condensation-particle-counters-work/,”

[154] 2016,“Brechtel Manufacturing Incorporated Model 1720 Mixing Condensation Particle Counter Manual Version 2.2: MCPC Manual Part Number 901803001,”

[155] Blesinger G., 2022,“Flammenrückschlag durch verbrennungsinduziertes Wirbelaufplatzen: Ähnlichkeitsanalyse unter Berücksichtigung von Baugröße und Brennstoffeigenschaften,”

[156] Izadi S., Zanger J., Baggio M., Seliger-Ost H., Kutne P., and Aigner M., 2023,“Experimental Investigation of the Effect of Superheated Liquid Fuel Injection on the Combustion Chracteristics of Lean Premixed Flames,” *Proceedings of the ASME Turbo Expo: Turbomachinery Technical Conference and Exposition - 2023: June 26-30, 2023, Boston MA*, The American Society of Mechanical Engineers, New York, N.Y.

[157] A.H.Lefebvre, Ed., 1985. *Influence of Fuel Properties on Gas Turbine Combustion Performance: AFWAL-TR-94-2104*.

[158] Oßwald P., Zinsmeister J., Kathrotia T., Alves Fortunato M., Burger V., Westhuizen R., Viljoen C., Lehto K., Sallinen R., Sandberg K., Aigner M., Le Clercq P., and Köhler M., 2021,“Combustion Kinetics of Alternative Jet Fuels, Part-I Experimental Flow Reactor Study,” Fuel, **302**, p. 120735.

[159] Jürgens S., Oßwald P., Selinsek M., Piermartini P., Schwab J., Pfeifer P., Bauder U., Ruoff S., Rauch B., and Köhler M., 2019,“Assessment of combustion properties of non-hydroprocessed Fischer-Tropsch fuels for aviation,” Fuel Processing Technology, **193**, pp. 232–243.

[160] G Komitov D. K., Ed., 2019. *Comparative research of diesel engine at working with anamegators*, EDP Sciences.

[161] David G. Goodwin and Harry K. Moffat and Ingmar Schoegl and Raymond L. Speth and Bryan W. Weber, 2023,“Cantera: An Object-oriented Software Toolkit for Chemical, https://www.cantera.org, 10.5281/zenodo.8137090,”

[162] Gimeno J., Martí-Aldaraví P., Carreres M., and Cardona S., 2021,“Experimental investigation of the lift-off height and soot formation of a spray flame for different co-flow conditions and fuels,” Combustion and Flame, **233**, p. 111589.

[163] Rajendran S., 2020,“Effect of antioxidant additives on oxides of nitrogen (NOx) emission reduction from Annona biodiesel operated diesel engine,” Renewable Energy, **148**, pp. 1321–1326.

[164] Yang H., Zhang Z., and Li K., 2022,“Suggestion on Axial Staged Mild Combustion considering the variable load,”

[165] Göke S., 2012,“Ultra Wet Combustion: An Experimental and Numerical Study,”

[166] Le Cong T., and Dagaut P., 2009,“Experimental and detailed modeling study of the effect of water vapor on the kinetics of combustion of hydrogen and natural gas, impact on NO x,” Energy & Fuels, **23**(2), pp. 725–734.

[167] Lellek S., and Sattelmayer T., 2015,“Influence of Water Injection on Heat Release Distribution, Lean Blowout and Emissions of a Premixed Swirl Flame in a Tubular Combustor,”

[168] Müller-Dethlefs K., and af Schlader, 1976,“The effect of steam on flame temperature, burning velocity and carbon formation in hydrocarbon flames,” Combustion and Flame, **27**, pp. 205–215.

[169] Babkin V. S., and V'yun A. V., 1971,“Effect of water vapor on the normal burning velocity of a methane-air mixture at high pressures,” Combustion, Explosion and Shock Waves, **7**(3), pp. 339–341.

[170] Griebel P., Boschek E., and Jansohn P., 2006,“Lean Blowout Limits and NOx Emissions of Turbulent, Lean Premixed, Hydrogen-Enriched Methane/Air Flames at High Pressure,” 0742-4795, **129**(2), pp. 404–410.

[171] Pathania R. S., Helou I. E., Skiba A. W., Ciardiello R., and Mastorakos E., 2023,“Lean blow-off of premixed swirl-stabilised flames with vapourised kerosene,” Proceedings of the Combustion Institute, **39**(2), pp. 2229–2238.

[172] Spadaccini L. J., and Huang H., Eds., 2002. *On-Line Fuel Deoxygenation for Coke Suppression.*

[173] Robert Morris, Jeremiah Miller, and Santosh Limaye, Fuel Deoxygenation and Aircraft Thermal Management, *4th International Energy Conversion Engineering Conference and Exhibit (IECEC).*

[174] VRANOS A., MARTENEY P., and KNIGHT B., 1981,“Determination of Coking Rate in Jet Fuel,” Combustion Science and Technology - COMBUST SCI TECHNOL, **26**, pp. 171–175.

[175] Wang H., Jin B., Wang X., and Tang G., 2019,“Formation and Evolution Mechanism for Carbonaceous Deposits on the Surface of a Coking Chamber,” Processes, **7**(8), p. 508.

9 Appendices

Appendix A : Fuel Injector Carbon Deposition and Coking

The deposits formed in this work have been studied using an optical microscopy and scanning electron microscopy (SEM), which has revealed particles sizes as large as 3 mm and as small as 10 µm (see Appendix Figure A.1 *a* and Appendix Figure A.3 *a*). These particles are arranged in twisted and fragmented chunks of carbon residues (see Appendix Figure A.1 *b*–*c*). The dry and extremely brittle particles were collected after each measurement day while purging the fuel lines with pressurized air. It appears that these particles were formed while residual liquid fuel was trapped in the fuel preheater in the cooling-down time.

The inner wall of the injector is shown in Appendix Figure A.1 *b*. These sporadically distributed carbon deposits were formed during operation due to the very high surface temperature of the injector walls. The deposits were largely removed using an ultrasonic bath with isopropanol solvent. The carbon deposits could also be scratched off manually using a hard object.

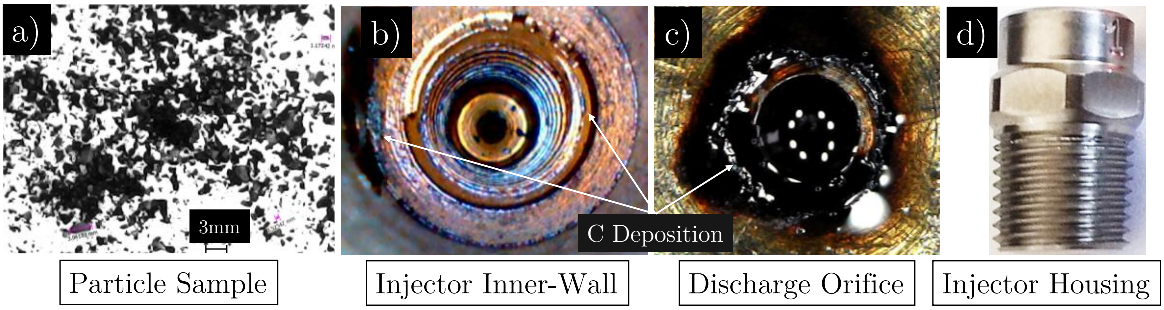

Appendix Figure A.1: Images of a) Sample of Particles Resulted from Coking, b) Injector Inner-Wall, c) Injector Discharge Orifice and d) Injector Housing. Adapted from [142]

The build-up of carbon in the fuel lines and in the fuel nozzle occurred steadily during the operation of all of the tested fuels, particularly during the heat-up period of FF. This may be related to the chemical composition of the fuel FF. It is worth noting that FF was found to exhibit the lowest IBP of all the fuels at 133.55°C. Coking consistently occurred during or after combustor shutdown despite purging of the fuel and its feed assembly. Some solutions to prevent coking have been presented in the literature, such as membrane-based fuel deaerators [172] and catalytic deoxygenation [173]. However, in the current study, liquid fuel deoxygenation by nitrogen sparging was tested and results were unsatisfactory because coking was still present. Both the fuel lance and the injector were purged with pressurized nitrogen gas for 180 seconds after the combustor shutdown as an effective method to mitigate coking. This method of limiting coking in the fuel supply system proved to be the most effective.

Sticky and tar-like substances were also observed in the current experiments on the injector swirl body due to both T_{fuel} and T_{air} reaching 255 and 450°C, respectively (see Appendix Figure A.2). In some severe cases during the combustor operation, at higher air and fuel temperatures, the deposits had completely blocked the fuel lines and clogged the injectors. This resulted in poor spray performance and flame out.

To gain more insight into the constituents of the recovered coke particles, Energy Dispersive X-ray Analysis (EDX) was performed. It was found that the majority of the particle constituents were carbon (C). Some percentages were copper (Cu), oxygen (O), sulfur (S) and chromium (Cr), which are similar to the results reported by [93]. These small traces of could be due to external contamination of the fuel itself and its supply lines. A total of three analyses were performed on different coking samples. The samples were collected from the liquid fuel line and the spray nozzle housing/swirler. The results of these analyses are presented in Appendix Table A.1.

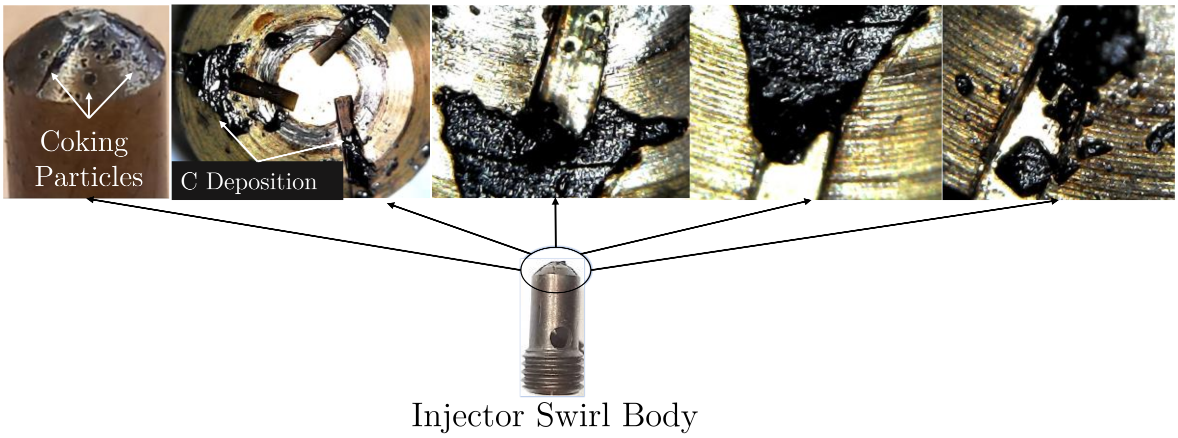

Appendix Figure A.2: Images of Coking Instances on the Current Work's Injector Swirl Body with three Tangential Fuel Channels. Adapted from [142]

Appendix Table A.1: EDX of Jet A-1 Coking Sample Analysis Results

Sample	Content [mass%]				
	Carbon	Copper	Oxygen	Sulfur	Chrome
Pipeline A	54.7	28.7	8.6	6.2	1.8
Pipeline B	70.5	13.2	13.3	2.9	n. a.
Injector	61.7	24.8	9.5	2.6	1.5

In a study by Vranos et al. [174] on determination of coking rate in jet fuel showed that deposits are composed of layers of various clusters of black, hard, brittle deposits (see Appendix Figure A.3 *b*–*e*). The morphology of the deposits suggests that they are formed by the precipitation of particles in the liquid fuel. There has also been evidence that very low levels of precursors can lead to formation of deposits and particulate matter.

Scanning electron microscopy (SEM) was used to study the morphology of the various carbonaceous deposits on the surface of the fuel line. The hard, black, intertwined and coiled filaments with a rough surface are revealed. Appendix Figure A.3 *a–e* show randomly distributed patterns of mainly carbon, copper and sulfur surfaces. The images show the carbonaceous deposit obtained after the decomposition the fuels. The surface structure of the particles is similar to a form of disordered and crusty in texture material. The formation of carbon strings is indicated by some long and stringy threads.

Similar to the observations were made by Wang et al. [175], where a carbonaceous sample was characterized via SEM. The coking sample of the current study is shown in Appendix Figure A.3 *a*. The figure shows the morphology of a particle sample at low magnification. It appears to be roughly structured with many perforations. Appendix Figure A.3 *b* shows the sample at high magnification with a relatively coarse surface. Structures as small as 1–5 microns were found. They may be the result of reduction of hydrocarbons during the coking process. Appendix Figure A.3 *c* shows that the cluster structure consists of carbon particles. The length of the carbon fiber is 10 to 100 µm. They were easily able to break down into smaller carbon particles. These particles probably are capable of further splitting and combining with each other to form a lump of carbonaceous deposit. A rough structure with many cavities can be seen in high magnification of sample Appendix Figure A.3 *d*. The release of molecules at high temperatures may have caused this. A high magnification of a carbon fiber is shown in Appendix Figure A.3 *e*. It appears that residues of hydrocarbon are condensed on the fiber surface at high fuel temperatures. [175]

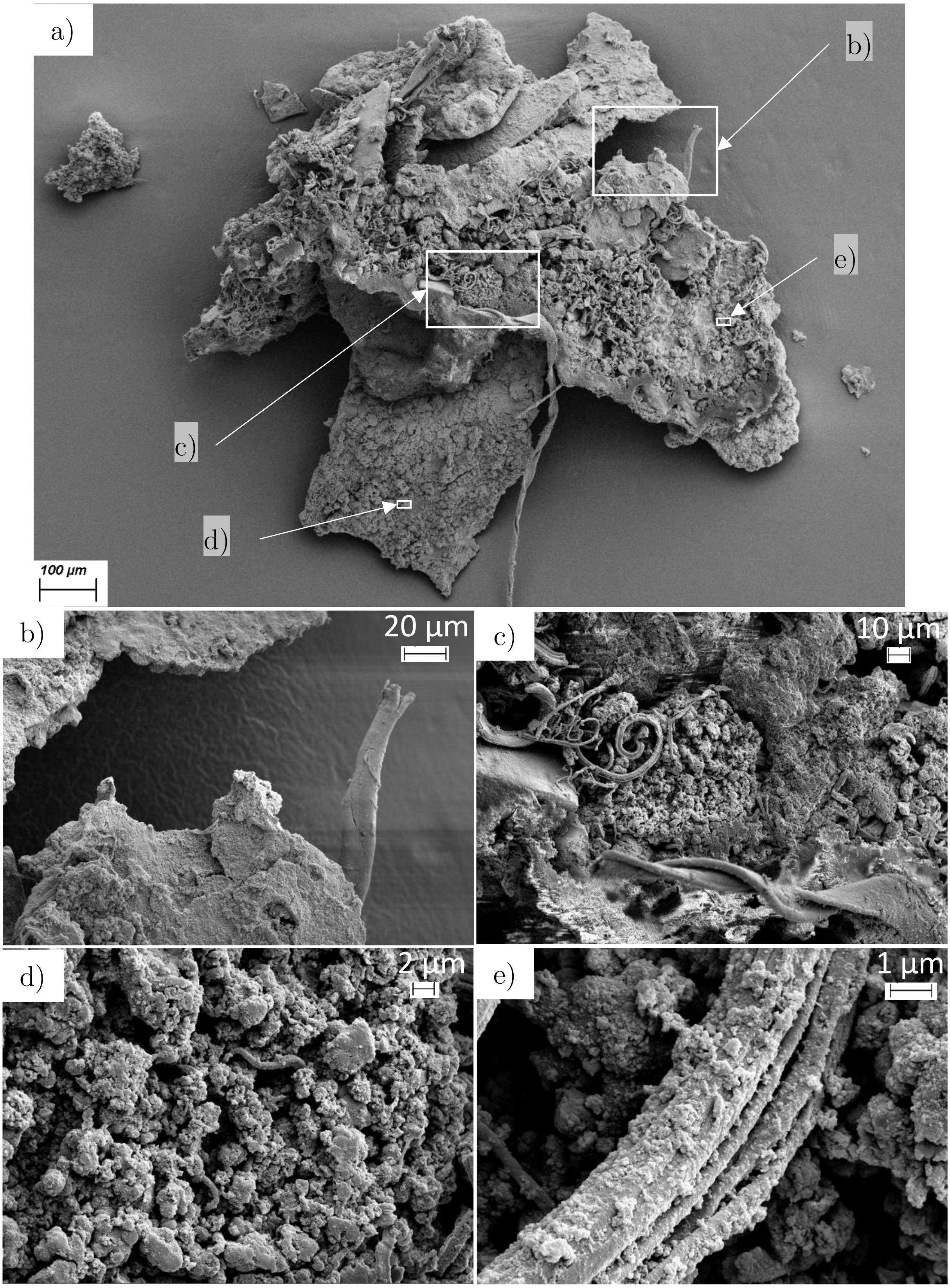

Appendix Figure A.3: SEM Images of a Particle Structure Resulted from Jet A-1 Coking at Different Scales, a) 100 µm, b) 20 µm, c) 10 µm, d) 2 µm, e) 1 µm. Adapted from [142]

Appendix B : NASA Chemical Equilibrium for Applications (CEA) Code

Jet A-1 Surrogate

```
prob  hp
  phi(eq.ratio) = 1.0 p(bar) = 1
react
  fuel=C10H22(L)_RMG  wt%= 0.120226   t,c= 155
  fuel=C11H24(L)_RMG  wt%= 0.258486   t,c= 155
  fuel=C9H18(L)_RMG  wt%= 0.236445   t,c= 155
  fuel=C10H18(L)_RMG  wt%= 0.158298   t,c= 155
  fuel=C9H12(L)_RMG  wt%= 0.136256   t,c= 155
  fuel=C9H8(L)_RMG  wt%= 0.013024   t,c= 155
  fuel=C10H12(L)_RMG  wt%= 0.056105   t,c= 155
  fuel=C10H8(L)_RMG  wt%= 0.002004   t,c= 155
  fuel=C11H10(L)_RMG  wt%= 0.017032   t,c= 155
  fuel=C12H10(L)_RMG  wt%= 0.002004   t,c= 155
  fuel=C12H8(L)_RMG  wt%= 0.00012   t,c= 155
  oxid=Air  wt%=13.89  t,c= 206.048
output
    plot CO2 CO NO NO2 H2O O2 t phi,eq.ratio
end
```

HEFA Surrogate

```
prob  hp
  phi(eq.ratio) = 1.0 p(bar) = 1
react
  fuel=C12H26(L)_RMG  wt%= 0.823225   t,c= 155
  fuel=C9H18(L)_RMG  wt%= 0.017211   t,c= 155
  fuel=C10H18(L)_RMG  wt%= 0.00413   t,c= 155
  fuel=C9H12(L)_RMG  wt%= 0.00238   t,c= 155
  fuel=C9H10(L)_RMG  wt%= 0.00014   t,c= 155
  fuel=C10H12(L)_RMG  wt%= 0.00026   t,c= 155
  fuel=C11H24(L)_RMG  wt%= 0.152655   t,c= 155
  oxid=Air  wt%=13.9  t,c= 206.037
output
    plot CO2 CO NO NO2 H2O O2 t phi,eq.ratio
end
```

FF Surrogate

```
prob  hp
  phi(eq.ratio) = 1.0  p(bar) = 1
react
  fuel=C8H16(g)_RMG  wt%= 0.0395   t,c= 155
  fuel=C10H20(g)_RMG  wt%= 0.04675   t,c= 155
  fuel=C12H24(L)_RMG  wt%= 0.043   t,c= 155
  fuel=C8H18nOKT(g)_RMG  wt%= 0.07225   t,c= 155
  fuel=C10H22(g)_RMG  wt%= 0.11425   t,c= 155
  fuel=C12H26(L)_RMG  wt%= 0.136   t,c= 155
  fuel=C14H30(L)_RMG  wt%= 0.13475   t,c= 155
  fuel=C16H34(L)_RMG  wt%= 0.11775   t,c= 155
  fuel=C17H36(L)_RMG  wt%= 0.10525   t,c= 155
  fuel=C18H38(L)_RMG  wt%= 0.0905   t,c= 155
  fuel=C20H42(L)_RMG  wt%= 0.06425   t,c= 155
  fuel=C22H46(L)_RMG  wt%= 0.03575   t,c= 155
  oxid=Air  wt%=13.89  t,c= 206.762
output
    plot CO2 CO NO NO2 H2O O2 t phi,eq.ratio
end
```

HEL Surrogate

```
  phi(eq.ratio) = 1.0 p(bar) = 1
react
  fuel=C10H22(L)_RMG  wt%= 0.027368   t,c= 155
  fuel=C12H26(L)_RMG  wt%= 0.085183   t,c= 155
  fuel=C16H34(L)_RMG  wt%= 0.138727   t,c= 155
  fuel=C8H18(g)_RMG  wt%= 0.075828   t,c= 155
  fuel=C16H34(L)_RMG  wt%= 0.188057   t,c= 155
  fuel=C6H12(g)_RMG  wt%= 0.001563   t,c= 155
  fuel=C7H14(g)_RMG  wt%= 0.166916   t,c= 155
  fuel=C10H18(L)_RMG  wt%= 0.052495   t,c= 155
  fuel=C7H8(g)_RMG  wt%= 0.007641   t,c= 155
  fuel=C9H12-TM(L)_RMG  wt%= 0.180798   t,c= 155
  fuel=C11H10(L)_RMG  wt%= 0.068553   t,c= 155
  fuel=C14H10(L)_RMG  wt%= 0.006871   t,c= 155
  oxid=Air  wt%=13.9  t,c= 205.871
output
    plot CO2 CO NO NO2 H2O O2 t phi,eq.ratio
end
```

Appendix C : Fuels and Surrogates Composition

Appendix Table C.1: Liquid Fuels' Distillation Curve Characteristic Values

Fuel	**IBP**	**T50**	**FBP**	**VABP**
Unit	**°C**	**°C**	**°C**	**°C**
Method	**ASTM D 86**	**ASTM D 86**	**ASTM D 86**	
Jet A-1	141.13	202.78	270.35	206.9
HEFA	152.22	202.01	258.39	204.2
FF	133.55	246.92	328.99	242.8
HEL	171	269.58	333.10	267.5

IBP: Initial Boiling Point

FBP: Final Boiling Point

VABP: ASTM volume average boiling point = $1/5(T_1+T_3+T_5+T_7+T_9)$

Appendix Table C.2: Jet A-1 Surrogate Composition

	Jet A-1		
Surrogate Component	Formula	CAS R.N.	%m/m
n-decane	n-C_{10}	124-18-5	12
2-methyl decane	i-C_{11}	6975-98-0	25.8
n-propylcyclohexane	C_9H_{18}	1678-92-8	23.6
decalin	$C_{10}H_{18}$	91-17-8	15.8
propylbenzene	C_9H_{12}	103-65-1	13.6
indene	C_9H_8	95-13-6	1.3
tetralin	$C_{10}H_{12}$	119-64-2	5.6
naphthalene	$C_{10}H_8$	91-20-3	0.2
1-methylnaphthalene	$C_{11}H_{10}$	90-12-0	1.7
biphenyl	$C_{12}H_{10}$	92-52-4	0.2
acenaphthylene	$C_{12}H_8$	208-96-8	0.012
AFR_{stoich}	14.62		
Lower heating value	43.138 MJ/kg		

Appendix Table C.3: Hydroprocessed Esters and Fatty Acids Surrogate Composition

Hydroprocessed Esters and Fatty Acids (HEFA)			
Surrogate Component	Formula	CAS R.N.	%m/m
n-Dodecane	$C_{12}H_{26}$	112-40-3	82.323
Cyclohexane, propyl-	C_9H_{18}	1678-92-8	1.721
Naphthalene, decahydro-	$C_{10}H_{18}$	91-17-8	0.413
Benzene, propyl-	C_9H_{12}	103-65-1	0.238
Indane	C_9H_{10}	496-11-7	0.014
Tetralin / Naphthalene, 1,2,3,4-tetrahydro-	$C_{10}H_{12}$	119-64-2	0.026
Decane, 2-methyl-	$C_{11}H_{24}$	6975-98-0	15.266
AFR_{stoich}	15.01		
Lower heating value	44.184 MJ/kg		

Appendix Table C.4: Future Fuel Surrogate Composition

Future Fuel (FF)			
Surrogate Component	Formula	CAS R.N.	%m/m
1-Octene	C_8H_{16}	111-66-0	3.950
1-Decene	$C_{10}H_{20}$	872-05-9	4.675
1-Dodecene	$C_{12}H_{24}$	112-41-4	4.300
n-Octane	C_8H_{18}	111-65-9	7.225
n-Decane	$C_{10}H_{22}$	124-18-5	11.425
n-Dodecane	$C_{12}H_{26}$	112-40-3	13.600
n-Tetradecane	$C_{14}H_{30}$	629-59-4	13.475
n-Hexadecane	$C_{16}H_{34}$	544-76-3	11.775
n-Heptadecane	$C_{17}H_{36}$	629-78-7	10.525
n-Octadecane	$C_{18}H_{38}$	593-45-3	9.050
n-Eicosane	$C_{20}H_{42}$	112-95-8	6.425
n-Docosane	$C_{22}H_{46}$	629-97-0	3.575
AFR_{stoich}	14.97		
Lower heating value	43.969 MJ/kg		

Appendix Table C.5: Heating Oil Extra Light Surrogate Composition

Heating Oil Extra Light (HEL)			
Surrogate Component	Formula	CAS R.N.	%m/m
Decane	$C_{10}H_{22}$	124-18-5	2.737
n-Dodecane	$C_{12}H_{26}$	112-40-3	8.518
Hexadecane	$C_{16}H_{34}$	544-76-3	13.873
Pentane, 2,2,4-trimethyl-	C_8H_{18}	540-84-1	7.583
Nonane, 2,2,4,4,6,8,8-heptamethyl-	$C_{16}H_{34}$	4390-04-9	18.806
Cyclohexane	C_6H_{12}	110-82-7	0.156
Cyclohexane, methyl-	C_7H_{12}	591-49-1	16.692
decalin	$C_{10}H_{18}$	91-17-8	5.250
Toluene	C_7H_8	108-88-3	0.764
1,2,4-Trimethylbenzene	C_9H_{12}-TM	95-36-3	18.080
alpha.-methylnaphthalene	$C_{11}H_{10}$	90-12-0	6.855
Phenanthrene	$C_{14}H_{10}$	85-01-8	0.687
AFR_{stoich}	14.54		
Lower heating value	42.763 MJ/kg		

Appendix Table C.6: Natural Gas Composition of Stuttgart as of June 2023

Natural Gas (NG)		
Component	Formula	%mol/mol
Methane	CH_4	91.120
Ethane	C_2H_6	5.113
Propane	C_3H_8	0.880
Iso-Butane	i-C_4H_{10}	0.259
n-Butane	n-C4H_{10}	0.085
n-Hexane	n-C_6H_{14}	0.166
Carbon dioxide	CO_2	1.139
AFR_{stoich}		16.25
Lower heating value		47.36 MJ/kg

Appendix D : Error Evaluations

In order to accurately classify and evaluate the results, it is vital to know the measurement uncertainties of the sensors and data acquisition. For this reason, the measurement uncertainties of all the sensors in use, as well as the errors of the variables derived from them, are discussed below. The resulted maximum deviations on NO_x, CO, HAB and FL as a result of errors inherent to the measurement technique and devices are calculated.

Data Acquisition

The measured data recorded by the Delphin modules include analog and digital input and output signals for valves and pressure transducer control and measurement. The “TopMessage” modules are also equipped with thermocouple voltage measurement capability. The modules used were AAST (master) and ADGT, ADVT, DIOT, and IOIT (slaves). The conversion polynomials for thermoelectric conversion to temperature are implemented within the modules. Since the voltage data is converted to temperature values, there are errors associated with the data acquisition. These errors must be added to the inaccuracies of the sensors. The operating manual of the modules produced by the original equipment manufacturer states a measurement accuracy of ±0.1% of the measurement range after sensor compensation, which amounts to ±1.15°C for N-Type thermocouples.

Thermocouples

All built-in temperature sensors were Type N, Class 1, manufactured by TC Mess- und Regeltechnik GmbH, Mönchengladbach, Germany, with an accuracy of:

- ±1.5°C (-40°C ≤ T < +375°C) and
- ±0.4% · |T| ((+375°C ≤ T ≤ +1000°C)

Four thermocouples were used to measure and control the preheated air temperature. The values were then averaged and used for calculation of the adiabatic flame temperature.

$$T_{air(mean)} = \frac{T_1 + T_2 + T_3 + T_4}{4}$$

Mass flow Controllers

The air mass flow controller (described in Section 4.1) had a capacity of 150 g/s and an accuracy of 0.1 % of full scale. The fuel and water mass flow controllers had capacities of 2.5 and 6.11 g/s and an accuracy of 0.2 % of full scale.

Error Calculation

An overview of the variations caused by different measurement and control equipment is given in Appendix Table D.1. The table shows that when the uncertainty of each operating parameter is considered, some variations in T_{ad}, NO_x, CO, etc. models can be expected.

The variation in terms of adiabatic flame temperature T_{ad} was calculated using Jet A-1 and air with NASA CEA software [55], taking into account the accuracy range of the sensors/equipment. The calculated T_{ad} was then fed into the multivariate models generated for the experiments. The corresponding changes in the responses (NO_x, CO, HAB, FL) were then calculated. The bulk velocity (v_{bulk}) at the air nozzle was calculated by assuming the exiting fuel-air mixture to be an ideal gas. The ideal gas law was used for its calculation.

Appendix Table D.1: Calculated Error from Temperatures and Mass Flow Rates on KPIs

Parameter	Unit	Accuracy	Maximum Error					
			T_{ad} [K]	NO_x [ppm]	CO [ppm]	HAB [mm]	FL [mm]	v_{bulk} [m/s]
T_{air} (TC)	[°C]	±1.5°C	±0.900	±0.058	±0,013	±0.031	±0.048	±0.144
T_{air} (DA)	[°C]	±1.15°C	±0.690	±0.044	±0.010	±0.024	±0.037	±0.110
T_{fuel} (TC)	[°C]	±1.5°C	±0.100	±0.004	±0,001	±0.003	±0.005	±0.000
T_{fuel} (DA)	[°C]	±1.15°C	±0.077	±0.003	±0.001	±0.002	±0.004	±0.000
m_{air}	[g/s]	±0.15 g/s	±17.500	±0.727	±0,235	±0.540	±0.842	±0.586
m_{fuel}	[g/s]	±0.005 g/s	±11.300	±0.469	±0,152	±0.349	±0.543	±0.020
m_{water}	[g/s]	±0.0122 g/s	±2.400	±0.100	±0,032	±0.074	±0.115	±0.047
Grand Total				±1.405	±0.444	±1.023	±1.594	±0.907

TC: Thermocouple

DA: Data Acquisition

Appendix E : Miscellaneous Figures

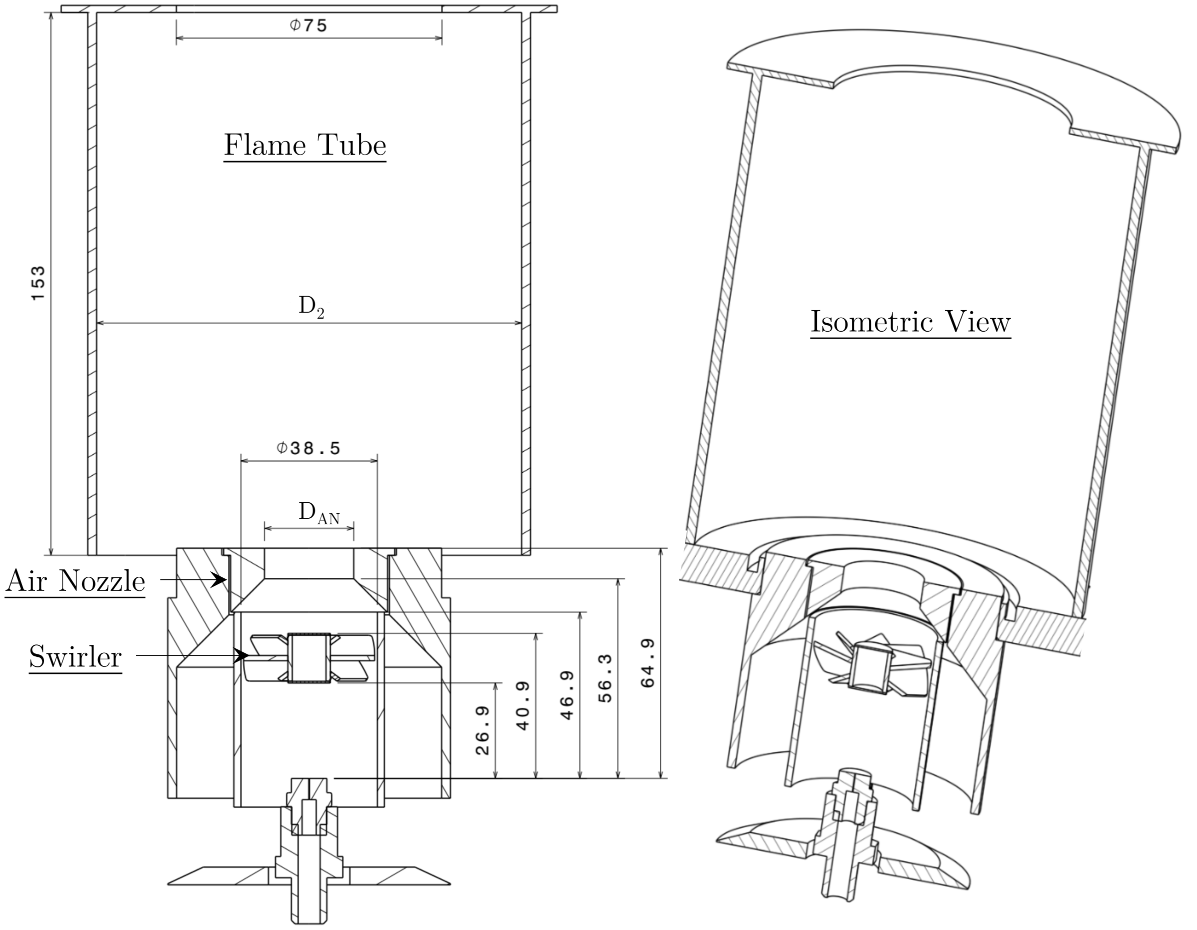

Appendix Figure E.1: Dimensions of the Studied Combustor, with Swirler, Air Nozzle and Flame Tube. Adapted from [140]

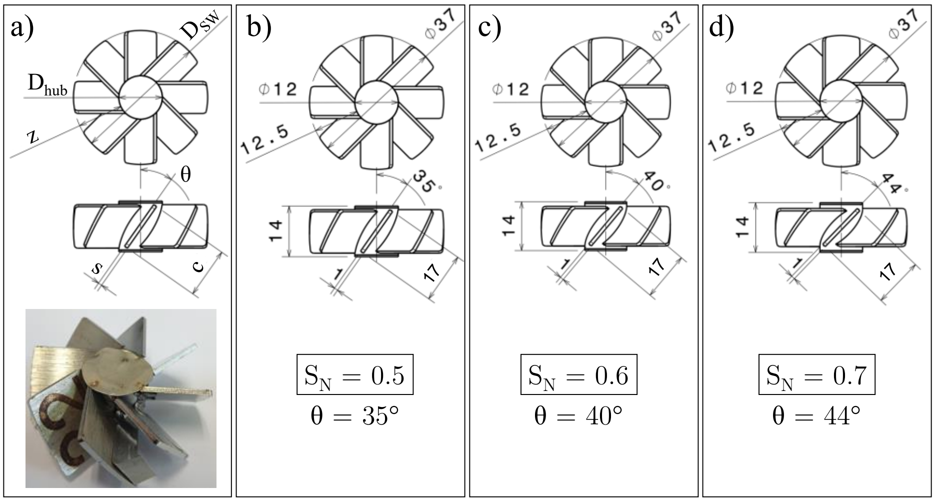

Appendix Figure E.2: a) Top and Side View of a Flat Vane Swirler Used in the Study, Tested Swirlers with b) $S_N = 0.5$, c) $S_N = 0.6$ and d) $S_N = 0.7$. Adapted from [140]

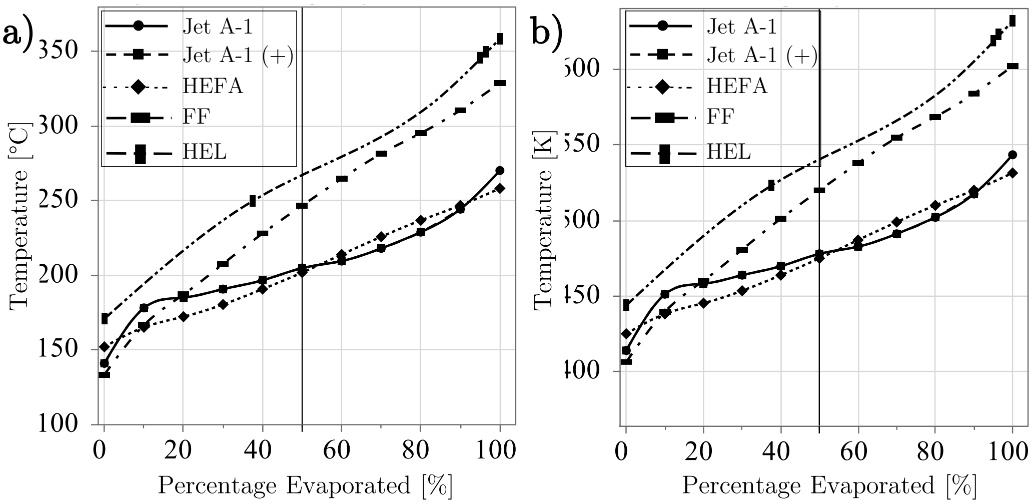

Appendix Figure E.3: ASTM D-86 Distillation Curves for Various Fuels, a) in °C and b) in K

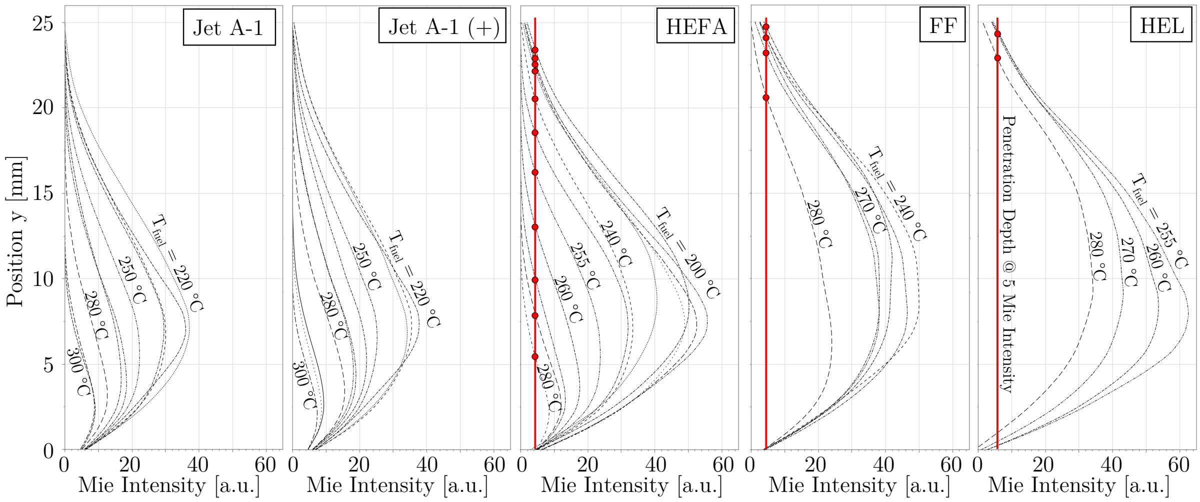

Appendix Figure E.4: Evaporation Behavior and Penetration Depth of Various T_{fuel} and Fuels

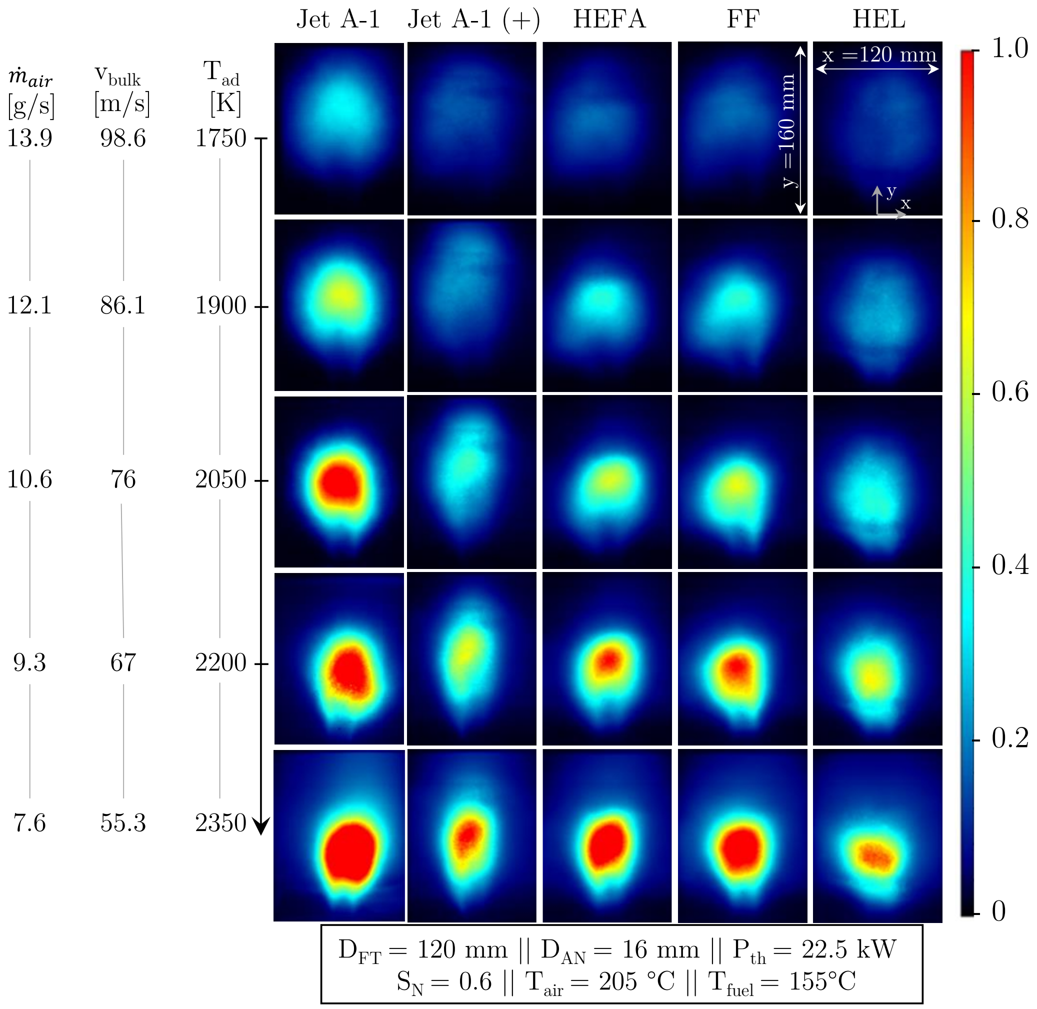

Appendix Figure E.5. OH* Images for Different T_{ad} and liquid Fuels

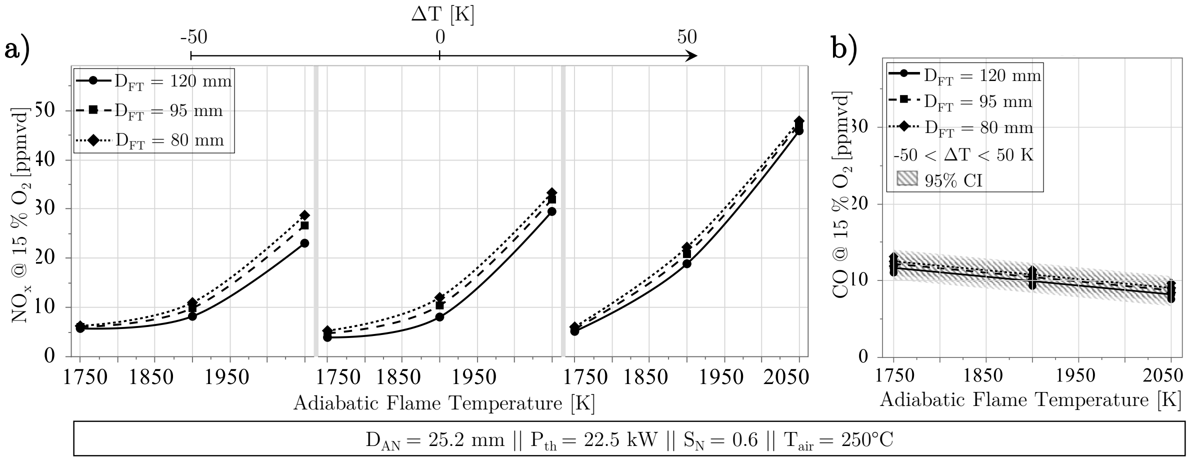

Appendix Figure E.6: a) NOx and b) Plots for Flame Tube Diameter Variation

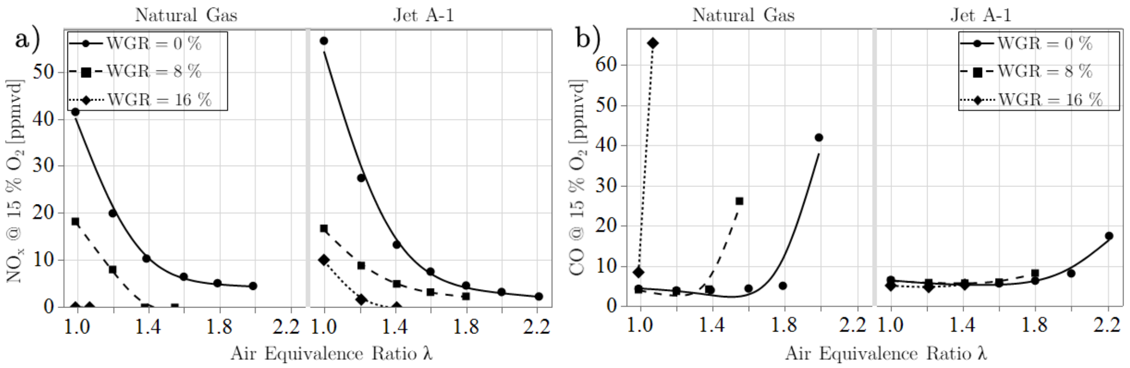

Appendix Figure E.7: a) NOx and b) CO Emissions in ppm for Different λ, Water-to-Gas Ratios and Fuels

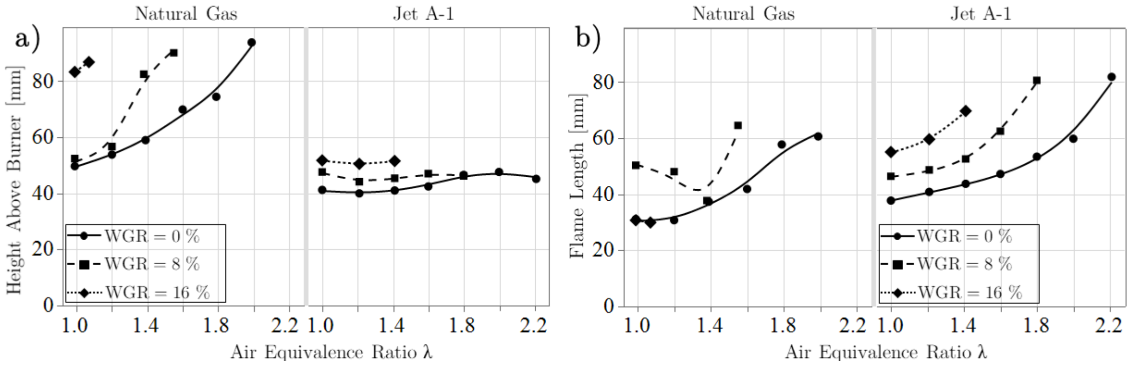

Appendix Figure E.8: a) HAB and b) FL Emissions in ppm for Different λ, Water-to-Gas Ratios and Fuels

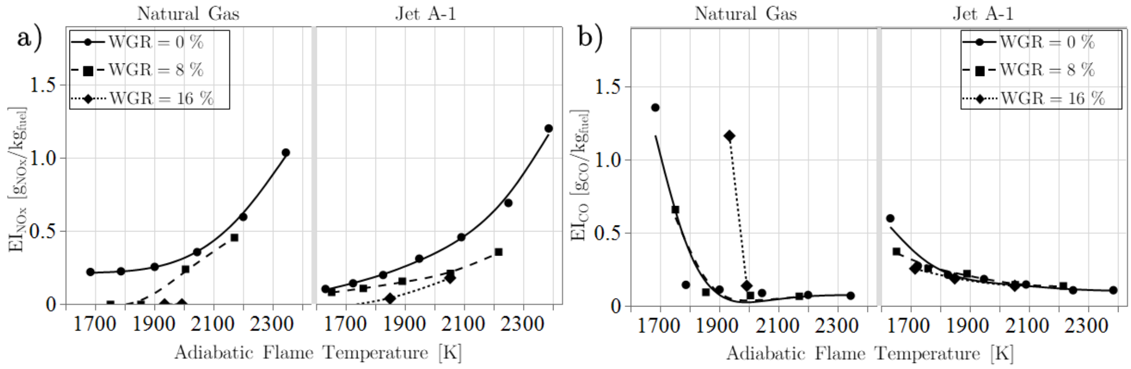

Appendix Figure E.9: a) EI_{NOx} and b) EI_{CO} Emissions in ppm for Different T_{ad}, Water-to-Gas Ratios and Fuels

Publications

Izadi, Saeed; Zanger, Jan; Baggio, Martina; Seliger-Ost, Hannah; Kutne, Peter; Aigner, Manfred (2024): Experimental Investigation of the Effect of Superheated Liquid Fuel Injection on the Combustion Characteristics of Lean Premixed Flames. In: ASME. J. Eng. Gas Turbines Power (146), Article 051012, S. 1–13. DOI: 10.1115/1.4063772.

Izadi, Saeed; Zanger, Jan; Kislat, Oliver; Enderle, Benedict; Grimm, Felix; Kutne, Peter et al. (2021): A Design of Experiments Based Investigation of the Influence of Hot Cross-Flow Gas on a FLOX®-Based Single-Nozzle Liquid Burner. In: American Society of Mechanical Engineers, International Gas Turbine Institute et al. 2021 – Proceedings of the ASME Turbo (GT2021-59029).

Izadi, Saeed, Zanger, J., Kislat, O., Enderle, B., Grimm, F., Kutne, P., and Aigner, M. (March 31, 2021). "Experimental Investigation of the Combustion Behavior of Single-Nozzle Liquid-FLOX®-Based Burners on an Atmospheric Test Rig." ASME. J. Eng. Gas Turbines Power. July 2021; 143(7): 071021. https://doi.org/10.1115/1.4049166

Izadi, Saeed, Zanger, J., Seliger-Ost, H., Kutne, P., and Aigner, M. (September 6, 2024). "Experimental Evaluation of Combustor Configuration's Impact on a Swirl-Assisted Jet-Stabilized Combustor Performance." ASME. J. Eng. Gas Turbines Power. December 2024; 146(12): 121022. https://doi.org/10.1115/1.4066234

Izadi, Saeed, Kislat, O., Zanger, J., Seliger-Ost, H., Kutne, P., and Aigner, M. (September 6, 2024). "Investigating the Impact of Steam Enhancement on Combustion in a Swirl-Assisted Jet-Stabilized Gas Turbine Combustor." ASME. J. Eng. Gas Turbines Power. January 2025; 147(1): 011001. https://doi.org/10.1115/1.4066235

Izadi, Saeed, Seliger-Ost, H, Zanger, J, Kutne, P, & Aigner, M. "Analysis of Liquid Fuel Effect on Swirl-Assisted Jet-Stabilized Combustor Performance." Proceedings of the ASME Turbo Expo 2024: Turbomachinery Technical Conference and Exposition. Volume 3B: Combustion, Fuels, and Emissions. London, United Kingdom. June 24–28, 2024. V03BT04A019. ASME. https://doi.org/10.1115/GT2024-127721